K. V. L. Subramaniam
Mohd Ataullah Khan   *Editors*

Advances in Structural Engineering

Select Proceedings of FACE 2019

Lecture Notes in Civil Engineering

Volume 74

Lecture Notes in Civil Engineering (LNCE) publishes the latest developments in Civil Engineering—quickly, informally and in top quality. Though original research reported in proceedings and post-proceedings represents the core of LNCE, edited volumes of exceptionally high quality and interest may also be considered for publication. Volumes published in LNCE embrace all aspects and subfields of, as well as new challenges in, Civil Engineering. Topics in the series include:

- Construction and Structural Mechanics
- Building Materials
- Concrete, Steel and Timber Structures
- Geotechnical Engineering
- Earthquake Engineering
- Coastal Engineering
- Ocean and Offshore Engineering; Ships and Floating Structures
- Hydraulics, Hydrology and Water Resources Engineering
- Environmental Engineering and Sustainability
- Structural Health and Monitoring
- Surveying and Geographical Information Systems
- Indoor Environments
- Transportation and Traffic
- Risk Analysis
- Safety and Security

To submit a proposal or request further information, please contact the appropriate Springer Editor:

– Mr. Pierpaolo Riva at pierpaolo.riva@springer.com (Europe and Americas);
– Ms. Swati Meherishi at swati.meherishi@springer.com (Asia - except China, and Australia, New Zealand);
– Dr. Mengchu Huang at mengchu.huang@springer.com (China).

Indexed by Scopus and Compendex

More information about this series at http://www.springer.com/series/15087

K. V. L. Subramaniam · Mohd Ataullah Khan
Editors

Advances in Structural Engineering

Select Proceedings of FACE 2019

🐎 Springer

Editors
K. V. L. Subramaniam
Indian Institute of Technology Hyderabad
Sangareddy, India

Mohd Ataullah Khan
Mahindra Ecole Centrale
Hyderabad, India

Preface

The primary objective of this book is to bring excerpts from the structural engineering community comprising researchers and practitioners, inculcating the state of the art and state of the practice. This communication was established through the conference *Futuristic Approaches in Civil Engineering* (FACE) 2019 held at Mahindra Ecole Centrale, Hyderabad, during August 30–31, 2019. The papers submitted to the FACE 2019 are published in two volumes covering the subareas of structural, geotechnical and environmental engineering. These papers were peer-reviewed and concurrently independently reviewed by the editors for quality. Subsequently, Springer as a publisher went through a general quality and plagiarism check for the accepted papers. Finally, a total of twenty papers passed through the scrutiny of a thorough peer-review process to become a part of this book. This book is one of the two volumes from the papers accepted through a peer-review process, and it presents high-quality research papers for researchers and practitioners in the area of structural engineering.

It has been a delightful experience editing the vital contributions from FACE 2019 in the form of a book. The experimental evaluation has always been a key to capturing the mechanics of existing and novel structures while the structural modeling and simulation capabilities have been the catalyst in establishing their response. The state of the practice hinges on the confidence of the practicing engineers in the existing and developed techniques. In this book, research developed in the areas of construction materials, structural health monitoring, earthquake engineering, fiber-reinforced polymer composites is covered.

In the area of construction materials, the book covers a range of new knowledge on raw materials and manufacture of cement, mixing, rheology and hydration, admixtures, structural characteristics and performance of cement-based materials, characterization techniques and modeling, use of fiber in cement-based materials, degradation and repair of cement-based materials, novel testing techniques such as digital image correlation (DIC) and applications. In addition, performance assessment and suitability of sustainable alternatives to the present building materials are also covered. For example, a few chapters suggest geopolymer as a replacement for cement and one chapter presents the usage of recycled aggregates for concrete

production. Techniques such as fuzzy logic and artificial neural networks to understand the experiments and establish the response are also discussed.

In the area of earthquake engineering, papers related to the areas of seismic response of load-bearing unreinforced masonry wall, reinforced concrete frames, buildings with dampers are covered. The focus of these chapters is the numerical modeling driven by the material response of such structural components under earthquake stimuli. Additionally, there are chapters on structures subjected to vehicular impact and fire. Fundamental contributions toward bond behavior between steel and concrete at elevated temperatures and moment–curvature relationship are also included.

From the organizers and the editors of FACE 2019, we would like to express heartfelt gratitude toward the authors, for contributing chapters. The reviewers played a vital role in ensuring the quality of the papers by providing critical reviews. We would also like to thank Mahindra Ecole Centrale (MEC) in providing us the opportunity to organize FACE 2019. Lastly, we would like to thank our publisher, Springer, for accepting our proposal to publish the proceedings from FACE 2019 as a part of this book. The support from Dr. Akash Chakraborty (Associate Editor, Applied Science and Engineering, Springer), Mr. Daniel Joseph. G (Project Coordinator, Book Production, Springer) and Rekha Nimesh (Editorial Assistant, Applied Science and Engineering, Springer) is gratefully acknowledged.

Sangareddy, India   Dr. K. V. L. Subramaniam
Hyderabad, India   Dr. Mohd Ataullah Khan

Contents

About the Editors

Prof. K. V. L. Subramaniam is a Professor in the Department of Civil Engineering at Indian Institute of Technology Hyderabad (IITH). Prior to joining IITH, he was Professor and Catell Fellow in Department of Civil Engineering at the Grove School of Engineering, the City College of New York (CCNY). Dr. Subramaniam obtained a B.Tech. in Civil Engineering from IIT Delhi and Ph.D. in Structural Engineering and Materials from Northwestern University, Evanston. After graduation, Dr. Subramaniam worked as Research Associate at the NSF Center for Advanced Cement Based Materials. Dr. Subramaniam was awarded the Early Career Award from the National Science Foundation of USA for investigating the early-age changes in cementitious materials. He received the James Instrument Award from the American Concrete Institute (ACI) in 1999 for his research on nondestructive evaluation of concrete. He is the recipient of the outstanding young researcher award at the Grove School of Engineering in 2006. He was the Chairman, committee 215 on Fatigue of Concrete of the ACI. In 2009, he was elected Fellow of the American Concrete Institute for notable contribution in the area of fracture and fatigue of concrete. He has served on the Editorial Boards of the Journal of Materials in Civil Engineering and the Journal of Bridge Engineering of the American Society of Civil Engineers. He is a life member of the Indian Concrete Institute. Prof. Subramaniam is currently the Director of the Center of Excellence in Sustainable Urban Development of the Ministry of Human Resource Development at IIT Hyderabad. He is the Program leader for the Sustainable Development thrust in the Friendship program of the Japan International Cooperation Agency. He was the recipient of excellence in teaching award at IIT Hyderabad in 2011 and 2015.

Dr. Mohd Ataullah Khan is an Assistant Professor in the Department of Civil Engineering, Mahindra Ecole Centrale (MEC), Hyderabad, India. He has a master's in Structural Engineering from the Indian Institute of Science (IISc), Bangalore, India and a PhD in Interdisciplinary Engineering from the Khalifa University of Science and Technology (KUST), Abu dhabi. His PhD was funded by the Masdar institute (a part of KUST) – Massachusetts Institute of Technology (MI-MIT)

cooperative agreement. The doctoral work of Dr. Mohd was focused on theoretical and computational modeling, 3D printing and experimental evaluation of material-tailored multilayers. Dr. Mohd has published articles in the top quartile mechanics journals along with peer-reviewed conferences. His research interest lies in the areas of mechanics of adhesively bonded joints, micro-/nano- fibre-reinforced composites, novel bio-inspired composites and concrete 3D printing. Dr. Mohd also had experience working as structural engineer for the design of steel structures, prior to joining PhD.

Seismic Fragility Assessment of Unreinforced Masonry Shear Walls

Jayaprakash Vemuri and K. V. L. Subramaniam

1 Introduction

The Kutch region in the western part of India is seismically active and has been struck by destructive earthquakes in the past. The M_w 7.6 earthquake which struck Kutch on 26 January 2001 was the largest intraplate earthquake to strike in India [1]. Post-earthquake damage surveys reported intensity levels up to X on the Modified Mercalli Intensity (MMI) scale [2]. The epicentre lay about 9 km southwest of the village of Chobari in the Kutch district of Gujarat, India [3]. The earthquake caused widespread damage in the province of Gujarat. Overall, over a million structures were damaged, and the consequent economic loss was close to US$10 billion [4]. In the Kutch region, the earthquake destroyed several towns causing major devastation of low-rise unreinforced masonry (URM) structures [5]. Typically, URM structures in the region consist of load-bearing masonry shear walls made of low-strength bricks. The performance of shear walls greatly affects the vulnerability of masonry buildings, and it is imperative to assess their seismic fragility.

In India, 69% of buildings are constructed using unreinforced brick masonry [6]. However, barring a few classical studies [7, 8] the in-plane behaviour of URM walls has not received much attention [9, 10]. The research reported varies widely due to inconsistency in test practices [11]. While researchers have conducted nonlinear time-history analyses of URM structures, there is no available literature presenting the correlation between ground motion parameters and URM structural response. Also, the lack of recorded seismic data from major earthquakes of the Kutch region presents a major challenge to the seismic assessment. Even the available information

J. Vemuri (✉)
Mahindra Ecole Centrale, Hyderabad, India
e-mail: jayaprakash.vemuri@mechyd.ac.in

K. V. L. Subramaniam
Indian Institute of Technology Hyderabad, Sangareddy, India
e-mail: kvls@iith.ac.in

following the major Kutch earthquake (M_w 7.6 at 8:46 a.m. on 26 January 2001) is limited to recorded peak ground accelerations (PGA) at selected towns. Since the accuracy of seismic assessment depends on capturing the local soil effects, the absence of seismic records from the Kutch region complicates our understanding of the actual seismic hazard.

In this study, ground motions are generated at rock level by the modified stochastic finite-fault method. The PGAs of these synthetic ground motions generated at rock level are compared with bedrock-level PGAs, which are available at thirteen stations. After validation, strong ground motions are generated at surface level by accounting for varied local topography by using site amplification functions for various towns available in the literature [12]. The ground motions are generated at bedrock level and amplified to surface level using the soil amplification functions corresponding to each particular site. The cyclic response of masonry, which is generated using an analytical-based model for the shear response of masonry, is used to investigate the vulnerability of the masonry to different parameters of the ground motions.

2   Material and Geometric Properties of URM Walls

Under lateral forces, a URM wall may fail due to sliding, flexure/rocking or shear. Sliding occurs along bed and head joints under low values of normal stress. Masonry can also crack under direct tension. Walls with high aspect ratios typically exhibit flexural or rocking behaviour while those with moderate aspect ratios fail in shear. In shear failures of URM walls, pre-cracking behaviour is characterised by mild hysteresis. Flexural cracks originate first, and then diagonal cracks start close to the ultimate shear strength. Diagonal cracking is visible when the peak lateral force is achieved, followed by a degradation in strength. In the post-peak regime, strength and stiffness drop rapidly, and high level of energy is dissipated. The wall collapses by stepped cracking along mortar joints. Cyclic response of the wall is bounded by the monotonic shear–deformation ($V - \Delta$) envelope. To obtain the monotonic envelope for URM walls, an incremental procedure available in the literature [13, 14] is used, where the lateral force is increased in increments, and at each step, the shear and flexural deformations are combined to obtain the load–deformation curve ($V - \Delta$ curve). The flexural strength is computed [7] as:

$$V_r = \frac{pDt}{2\alpha_v}\left(1 - \frac{p}{kf_u}\right) \tag{1}$$

where $p = P/Ht$ is the vertical compressive stress and P is the vertical compressive force. H, D and t represent the height, length and thickness of the wall, f_u is the masonry strength in compression, k is a coefficient which accounts for vertical stress distribution at the compressed toe, $\alpha_v = M/(VD)$ is the shear ratio. The shear strength can be computed [7] as:

$$V_d = Dt\tau_u; \quad \tau_u = \text{minimum}(\tau_{cs}; \tau_{ws}; \tau_b) \tag{2}$$

τ_{cs} is the shear stress corresponding to the cracked section and is given by:

$$\tau_{cs} = \frac{1.5c + \mu p}{1 + \frac{3c\alpha_v}{p}} \tag{3}$$

τ_{ws} is the shear stress of the complete section and is given by:

$$\tau_{ws} = \frac{c + \mu p}{1 + \alpha_v} \tag{4}$$

τ_b is the shear stress based on brick cracking and is given by:

$$\tau_b = \frac{f_{bt}}{2.3}\sqrt{1 + \frac{p}{f_{bt}}} \tag{5}$$

where c is the joint cohesion, μ is the joint friction coefficient, f_{bt} is the tensile strength of brick. The expressions for joint cohesion and joint friction have been defined [15] as $c' = kc$ and $\mu' = k\mu$ where k is:

$$k = \frac{1}{1 + \mu 2 \frac{\Delta_y}{\Delta_x}} \tag{6}$$

where Δ_x and Δ_y are the height and length of the brick unit, respectively. Due to the absence of experimental data on shear walls from India, two shear walls [16, 17] were selected from literature, which are representative of the typical masonry construction in Kutch [18]. Table 1 shows the properties of the two URM walls. The monotonic backbone envelope is computed for both the walls.

The cyclic behaviour was modelled in SAP2000 [19] where the *link element* is chosen to model the URM wall. The multilinear-plastic pivot model is used to define the hysteresis loop. The four pivot parameters, $\alpha_1, \alpha_2, \beta_1$ and β_2, govern the shape of the cyclic loops and the degradation in strength and stiffness. The optimum values for the four parameters were obtained using the least-squares method to minimise the error concerning the values obtained from experiments. For the wall with lower axial stress, $\alpha_1, \beta_1, \alpha_2$ and β_2 are 0.90. The symmetrical response and no pinching resulted in the parameters to be equal in magnitude. The hysteresis behaviour obtained from the experiment matches well with the loops obtained from the pivot model (Fig. 1a). For the shear wall having higher axial stress, $\alpha_1, \beta_1, \alpha_2$ and β_2 were computed to be 0.90. Figure 1b shows the match between the experimental hysteresis loops of the wall and the loops obtained from the pivot model. Limit states corresponding to cracking, ultimate strength and collapse are noted for both walls.

Table 1 Properties of the two URM shear walls considered in the present study

Property	Wall-1	Wall-2
H (mm)	1350	3000
D (mm)	1000	1500
t (mm)	250	380
p (MPa)	0.6	1.24
f_b (MPa)	16	19.7
f_{bt} (MPa)	1.22	1.07
f_m (MPa)	3.31	4.33
f_u (MPa)	6.2	7.9
c (MPa)	0.23	0.21
c' (MPa)	0.17	0.14
μ	0.58	0.81
μ'	0.43	0.55
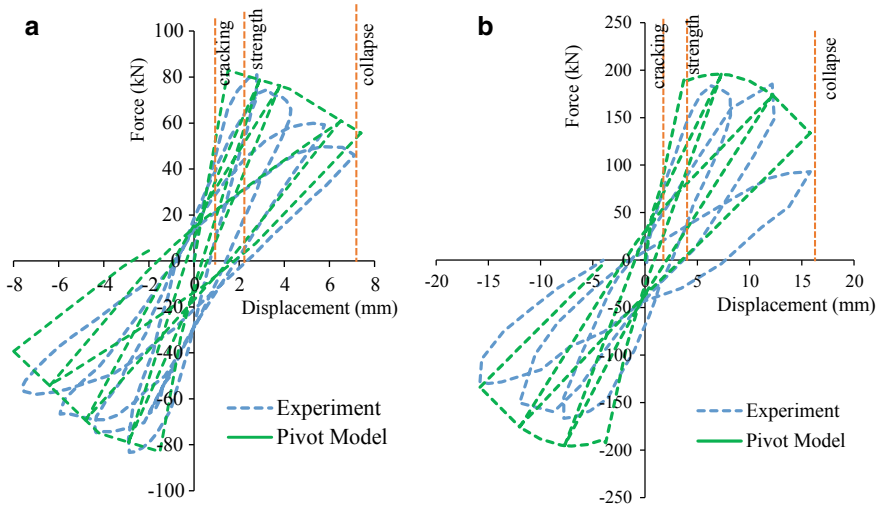
Fig. 1 Comparison between experiment and pivot model. **a** URM wall with diagonal shear cracking through mortar joints; **b** URM wall with shear–tensile cracking of bricks

3 Nonlinear Time-History Analyses Using Synthetic Ground Motions

Seismic records for the 2001 Kutch earthquake are not available. In such regions where a rich database of historical strong motions is unavailable, modified records may be obtained either by generating artificial records or by altering natural records.

The modified stochastic finite-fault method [20] has been used by researchers [21] to generate surface-level synthetic ground motions for the 2001 Kutch earthquake. From these synthetic accelerograms, ground motion characteristics such as PGA, PGV, predominant period, mean period, significant duration and response spectra are computed. Figure 2 shows the ground motions generated at surface level. At each site, ten synthetic ground motions were generated by conducting trials. The modified stochastic finite-fault method is extended to derive synthetic ground motions at surface level, for towns across various seismic zones. These synthetic ground motions are used for nonlinear time-history analyses.

The earthquake hazard in the province of Gujarat ranges from low to high. Based on the estimated hazard level, the seismic zoning map of India IS1893:2016 [22] has assigned four seismic zones to Gujarat, ranging from Zone 2 (low) to Zone 5 (high). The Kutch region has the highest earthquake hazard and lies in Zone 5 (SA at DBE level of 0.45 g), and intensity levels more than IX may be expected in this region. Zone 4 (SA at MCE level of 0.30 g) comprises regions from Saurashtra and Kutch, within a belt with a width of 60–70 km around Zone 5 and intensity VIII may be expected in this zone. Mainland Gujarat is assigned Zone 3 (SA at DBE level of 0.20 g) where intensity level of VII may be expected. Table 2 shows the characteristics of the surface-level synthetic ground motions generated for various towns in Gujarat. These towns are situated across various seismic zones as per the seismic zonation map of India (IS1893:2016). The epicentral distance of the station, the PGA, PGV, the significant duration and, the mean displacements for both walls are tabulated. The MMI data as observed from the earthquake isoseismals [23] to indicate the overall damage to structures in each town is also tabulated in Table 2. Additionally, in this study, two scalar measures, the predominant period, T_p, and the mean period, T_m, were used to assess frequency content in ground motion. Both scalar frequency parameters exhibited a weak correlation with the structural displacements of the two walls. Nevertheless, it is observed that ground motions at most sites exhibited very low predominant periods. From Table 2, it is observed that the mean periods of the ground motions are higher than predominant periods but higher than the natural periods of the walls. Observation of experimental hysteresis loops for wall-1 shows that the stiffness decreased by nine times, causing the fundamental period to increase three times. For wall-2, experimental hysteresis loops indicate that the stiffness decreased by three times. The increased natural period of both walls is close to the frequency content, indicated by T_m, in the ground motion. The low values of both frequency parameters indicate that the seismic energy of the ground motions generated due to the 2001 Kutch earthquake was concentrated in the low time period range. This makes the masonry structures vulnerable to collapse once there is an increase in time period due to damage in the walls.

From Table 2, it is observed that URM walls in Seismic Zone 5 witnessed high displacements which caused collapse. Most ground motions from Zone 5 have PGV values > 0.1 m/s and PGA values > 0.1 g and caused the walls to reach the collapse displacement levels. In Figs. 3 and 4, the PGA and the PGV are correlated with structural displacements of the two walls. The three limit states are marked for reference. Ground motions in the epicentral region, with PGAs > 0.1 g, caused a
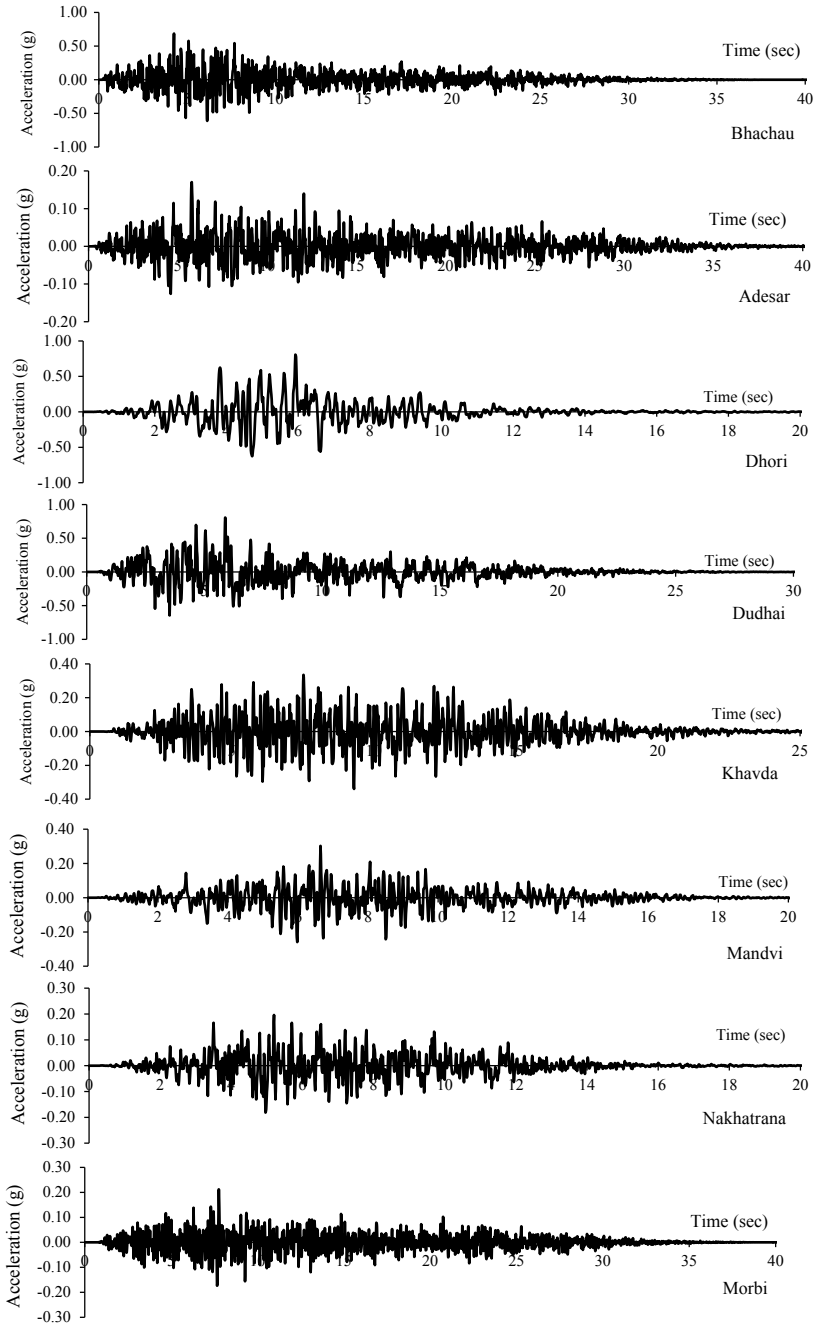
Fig. 2 Synthetic ground motions generated at surface-level using site amplification functions

Table 2 Results from nonlinear time-history analyses of URM walls using surface-level synthetic ground motions

S. No.	Station	Dist. (km)	MMI	PGA (g)	PGV (m/s)	T_p (s)	T_m (s)	Significant duration (s)	Disp. wall-1 (mm)	Disp. wall-2 (mm)
Sites in Zone 5 (IS1893:2016)—PSA(DBE) = 0.45 g										
1	Dudhai	15	X	0.74	0.87	0.21	0.55	12.81	7.5	16
2	Bhachau	19	X	0.64	0.54	0.10	0.31	18.08	7.5	16
3	Suvai	34	IX	0.38	0.32	0.22	0.35	21.38	7.5	16
4	Lakadia	36	IX	0.42	0.53	0.18	0.50	21.73	7.5	16
5	Rapar	46	IX	0.33	0.18	0.11	0.19	22.80	7.5	16
6	Dhori	49	X	0.74	0.63	0.26	0.40	5.92	7.5	16
7	Khavda	73	IX	0.35	0.18	0.15	0.23	12.24	7.5	16
8	Bela	77	IX	0.12	0.12	0.19	0.41	21.39	7.5	16
9	Adesar	78	VIII	0.15	0.13	0.19	0.38	22.88	7.5	16
10	Mandvi	111	VIII	0.24	0.17	0.14	0.26	9.26	7.5	16
11	Dayapur	141	VIII	0.13	0.09	0.16	0.29	7.80	7.5	13.6
12	Nakhtarana	155	VIII	0.20	0.16	0.13	0.33	8.31	7.5	16
13	Naliya	192	VIII	0.14	0.11	0.13	0.39	8.07	7.5	16
Sites in Zone 4 (IS1893:2016)—PSA(DBE) = 0.30 g										
14	Dwarka	183	VIII	0.03	0.03	0.25	0.46	9.95	3.4	3.99
15	Lalpur	122	VIII	0.09	0.05	0.11	0.18	13.67	6.11	6.19
16	Morbi	93	VIII	0.16	0.12	0.17	0.25	21.13	7.5	16
17	Radhanpur	148	VIII	0.06	0.07	0.30	0.49	24.33	7.5	10.81
18	Sipu	235	VIII	0.02	0.01	0.10	0.25	25.13	1.73	1.90

(continued)

Table 2 (continued)

S. No.	Station	Dist. (km)	MMI	PGA (g)	PGV (m/s)	T_p (s)	T_m (s)	Significant duration (s)	Disp. wall-1 (mm)	Disp. wall-2 (mm)
Sites in Zone 3 (IS1893:2016)—PSA(DBE) = 0.20 g										
19	Amreli	256	VII	0.017	0.006	0.08	0.13	20.51	2.91	1.04
20	Gandhinagar	248	VI	0.012	0.010	0.15	0.32	25.44	1.91	1.38
21	Jhagadia	354	VI	0.002	0.001	0.24	0.36	25.68	0.17	0.18
22	Junagadh	235	VII	0.019	0.010	0.09	0.17	18.45	1.71	1.37
23	Kadana	369	V	0.004	0.002	0.11	0.15	27.53	0.18	0.20
24	Kevadia	396	V	0.002	0.001	0.13	0.19	26.96	0.08	0.08
25	Rajkot	129	VII	0.065	0.074	0.45	0.54	19.16	7.5	9.80
26	Surendranagar	158	VII	0.047	0.041	0.21	0.36	23.34	5.21	5.41
27	Ukai	422	V	0.002	0.001	0.07	0.15	26.14	0.10	0.10
28	Una	280	V	0.009	0.005	0.17	0.24	19.61	1.41	0.63
29	Vadodara	321	V	0.004	0.003	0.22	0.32	25.61	0.33	0.35
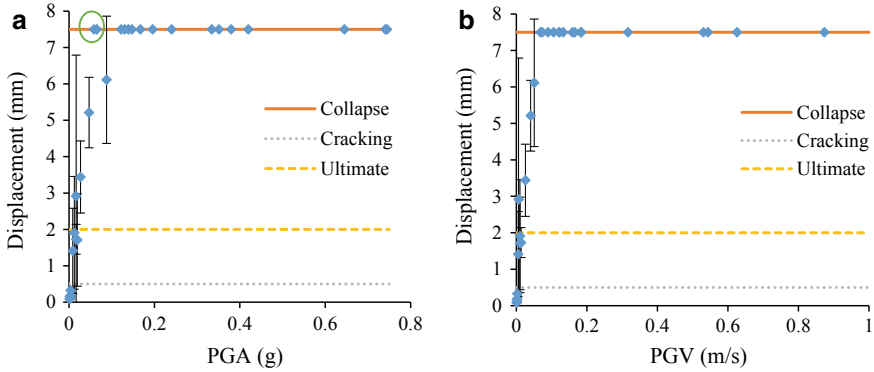
Fig. 3 **a** Displacement versus PGA (wall-1), **b** displacement versus PGV (wall-1)
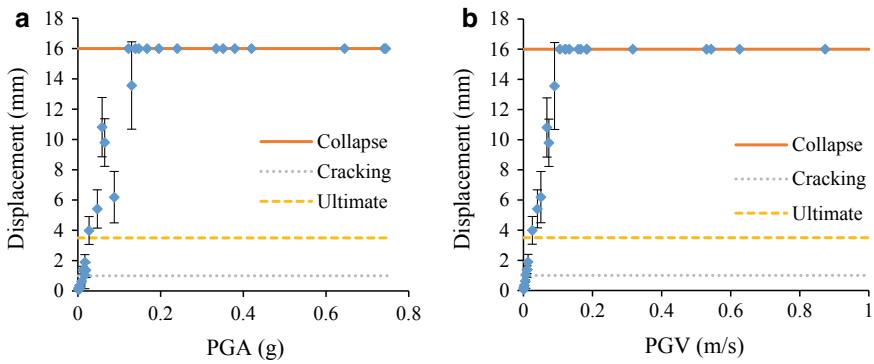
Fig. 4 **a** Displacement versus PGA (wall-2), **b** displacement versus PGV (wall-2)

collapse of the walls: this observation matches well with reconnaissance survey which reports catastrophic damage to low-rise masonry structures in this region. Figure 3 and Table 2 show that most towns in Seismic Zone 5 were assigned high MMI levels (X, IX and VIII) due to extensive damage observed to masonry structures [2, 5]. On the other extreme, ground motions from Zone 3 had very low PGA values and did not cause the collapse of the two URM walls. Some ground motions caused the walls to reach the cracking limit. This also corresponds well with data from reconnaissance surveys [2, 21] which show little or no damage to low-rise masonry construction in the 2001 Kutch earthquake. It is to be noted that the MMI levels for some towns in Zone 3 are higher due to high damage levels of mid-rise concrete buildings due to poor construction practices [2]. Ground motions in towns situated in Zone 4 caused the walls to exhibit displacements not exceeding the limit state of peak strength. Substantial damage to masonry structures was reported [5] in one particular town, Morbi, which is situated in Zone 4. In the current study, it is observed that surface-level ground motions in Morbi had high PGA values of 0.16 g, causing

both URM walls to collapse. The high PGAs observed in Morbi town are primarily due to site amplification [21].

The method of maximum likelihood has been recommended by several researchers [24–26] for fitting fragility curves for displacement data. The fitted fragility function is a lognormal cumulative distribution function, with a median, θ, and dispersion, β. Table 3 shows that for wall-1, the median values for cracking, ultimate strength and collapse are 0.01 g, 0.02 g and 0.06 g, respectively. For wall-2, the median values for cracking, ultimate strength and collapse are 0.01 g, 0.03 g and 0.12 g, respectively. In IS1893:2016, the peak spectral acceleration for design basis earthquake for seismic Zones 3, 4 and 5 are prescribed as 0.20 g, 0.30 g and 0.45 g, respectively. The median values are lower than expected seismic intensity indicating the high vulnerability of both walls.

Figure 5a, b show seismic demand fragility curves for both walls. The seismic intensity is represented by PGA. Figure 6 shows the fragility curves for the two walls, with PGV as the seismic intensity measure. The graphs provide a means to visually assess the vulnerability in terms of probability of exceedance of various limit states of the masonry shear walls, considering variability in demand. The damage state displacement thresholds were identified earlier, in Fig. 2, from the cyclic hysteric curves. The median values for achieving strength limit states for wall-1 and wall-2

Table 3 Fragility curves: median and dispersion

Damage state	Wall-1		Wall-2	
	Median, θ	Dispersion, β	Median, θ	Dispersion, β
Cracking	0.01	0.10	0.01	0.41
Strength	0.02	0.40	0.03	0.23
Collapse	0.06	0.52	0.12	0.26
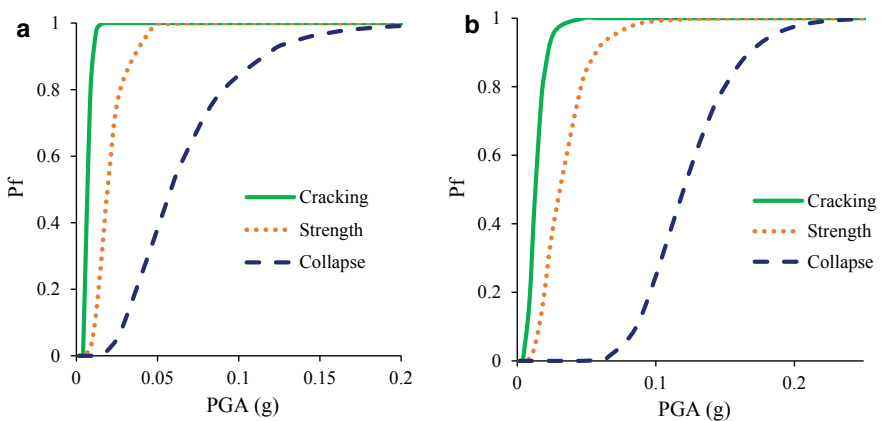
Fig. 5 a Seismic fragility curves (w.r.t. PGA) for wall-1, **b** seismic fragility curves (w.r.t. PGA) for wall-2
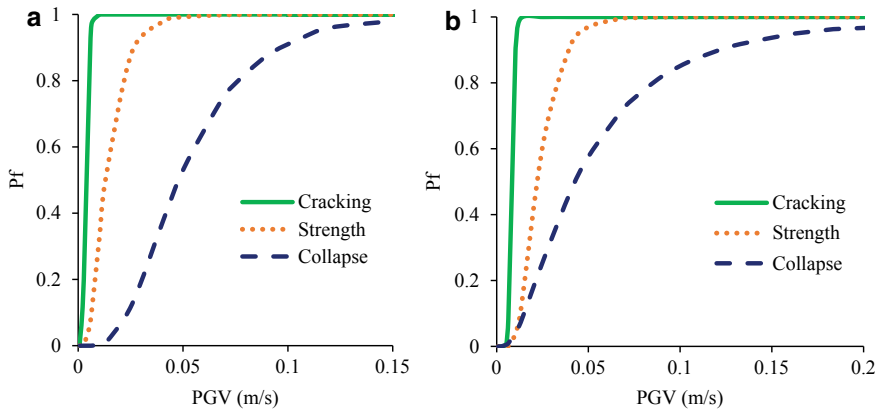
Fig. 6 a Seismic fragility curves (w.r.t. PGV) for wall-1, **b** seismic fragility curves (w.r.t. PGV) for wall-2

are 0.05 g and 0.1 g, respectively. The median values for achieving cracking limit for wall-1 and wall-2 are 0.01 g in both walls. The seismic fragility of the wall with higher axial load (wall-2) is only slightly lower than the wall with lower axial load (wall-1).

4 Anomalous Displacements/Outliers

In general, the wall displacement is observed to increase linearly with PGA, till collapse. However, it is observed that for two cases, Radhanpur (Zone 4) and Rajkot (Zone 3), the wall with lower axial load, differs slightly from the overall trend as the limit state of peak strength is reached at low PGA. These two outliers were shown, marked in Fig. 3. Figures 7 and 8 show velocity pulses from Radhanpur and Rajkot. Although the two records had low PGA, the occurrence of sharp velocity pulses triggered the collapse of the URM. The displacement time history in both cases shows that the velocity pulse imposed a high strength demand on the walls. Subsequently, there is a degradation in strength and stiffness of walls, leading to high displacements.

5 Summary and Conclusions

The 2001 Kutch earthquake was one of the most destructive intraplate earthquakes ever recorded. It had a moment magnitude of 7.6 and caused heavy damage to URM structures in the Kutch region. Unfortunately, no strong ground motions were
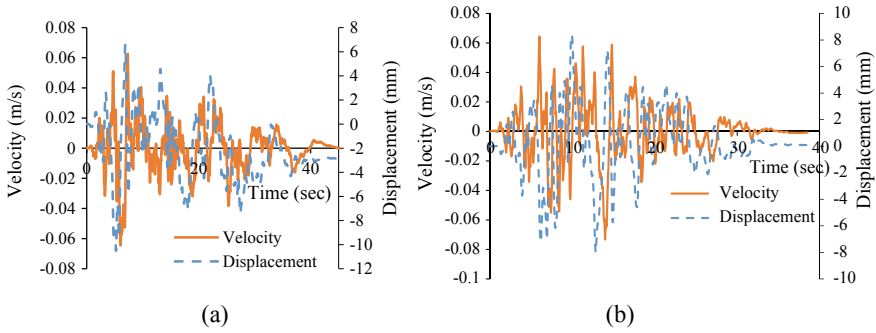
Fig. 7 **a** Radhanpur velocity pulse and displacement (wall-1), **b** Rajkot velocity pulse and displacement (wall-1)
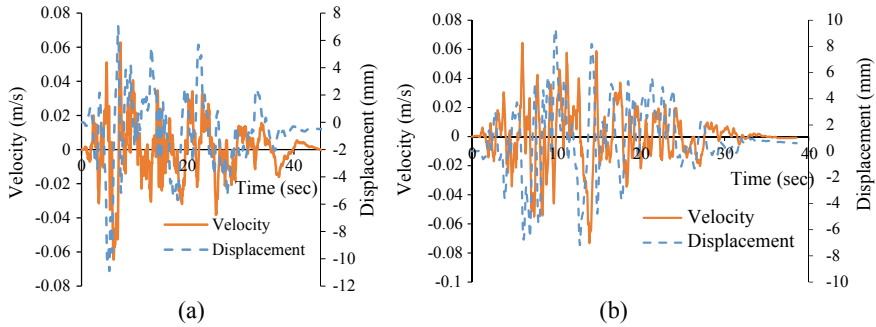
Fig. 8 **a** Radhanpur velocity pulse and displacement (wall-2), **b** Rajkot velocity pulse and displacement (wall-2)

recorded in this earthquake. Only PGA values from structural response recorders at thirteen sites are available. In this paper, nonlinear time-history analyses of URM walls are performed using surface-level synthetic ground motions. Characteristics of the ground motions such as PGA, PGV, frequency content and duration are tabulated. It is observed that ground motions have low values of predominant period. Such high-frequency ground motions could be particularly damaging to low-rise structures. A mechanics-based technique is used to develop the monotonic load envelope for two masonry shear walls. Using stress-based criteria, various displacement limit states are identified. Results from the dynamic analyses performed on calibrated hysteretic models were used to derive seismic fragility curves. Examination of the fragility curves indicates that the collapse limit state is reached for most towns in Zone 5, the highest seismic zone as per IS1893:2016. Most ground motions from Zone 5 have PGV values > 0.1 m/s and PGA values > 0.1 g and cause the walls to reach the collapse displacement levels. These results confirm satisfactorily with reconnaissance studies which report catastrophic damage to masonry structures in Zone 5, particularly in the epicentral region. Results from NTHA for towns situated in Seismic Zones 3 and 4

vary between no damage to collapse, which correlate well with post-earthquake field surveys carried out in these two zones, where varying levels of damage intensities were observed. The wall displacement is observed to vary linearly with PGA and PGV, until the collapse of the wall. Pulse ground motions from two distant sites, Radhanpur and Rajkot, had a destructive effect on the walls. It is concluded that URM structures with shear walls are highly vulnerable for expected ground motions in the Kutch region. Such URM structures existing in the Kutch region need to be upgraded to resist the expected level of seismic forces.

References

1. Nagamani, D., & Mandal, P. (2017). Estimation of earthquake source parameters in the Kachchh seismic zone, Gujarat, India, using three component S-wave spectra. *Journal of Earth System Science, 126*(5), 1–14.
2. Sinvhal, A., Bose, P. R., Prakash, V., Bose, A., Saraf, A. K., & Sinvhal, H. (2003). Isoseismals for the Kutch earthquake of 26th January 2001. *Journal of Earth System Science, 112*(3), 375–383.
3. Chopra, S., Kumar, D., & Rastogi, B. K. (2010). Estimation of strong ground motions for 2001 Bhuj (M_w 7.6), India earthquake. *Pure and Applied Geophysics, 167*(11), 1317–1330.
4. Rastogi, B. K., Gupta, H. K., Mandal, P., Satyanarayana, H. V. S., Kousalya, M., Raghavan, R., et al. (2001). The deadliest stable continental region earthquake occurred near Bhuj on 26 January 2001. *Journal of Seismology, 5*(4), 609–615.
5. Jagadish, K. (2003). Behaviour of masonry structures during the Bhuj earthquake of January 2001. *Journal of Earth System Science, 112*(3), 431–440.
6. WHE-PAGER Survey. (2007). Retrieved from http://www.world-housing.net/related-projects/whe-pager-project/about-this-project. Accessed July 2015.
7. Magenes, G., & Calvi, G. M. (1997). In-plane seismic response of brick masonry walls. *Earthquake Engineering and Structural Dynamics, 26,* 1091–1112.
8. Abrams, D. P. (1992). Strength and behavior of unreinforced masonry elements. In *Proceedings of the Tenth World Conference on Earthquake Engineering*, Madrid, Spain, July 19–24, 1992.
9. Vemuri, J., Ehteshamuddin, S., & Kolluru, S. (2018). Numerical simulation of soft brick unreinforced masonry walls subjected to lateral loads. *Cogent Engineering, 5*(1), 1551503.
10. Vemuri, J. P., & Kolluru, S. (2017). Seismic analysis of unreinforced masonry walls. *IDRiM Journal, 6*(2), 102–115.
11. Federal Emergency Management Agency (FEMA). (1999). *Evaluation of earthquake damaged concrete and masonry wall buildings: Technical resources* (FEMA P-307). Washington, DC.
12. Chopra, S., Kumar, D., Rastogi, B. K., Choudhury, P., & Yadav, R. B. S. (2012). Estimation of site amplification functions in Gujarat region, India. *Natural Hazards, 65*(2), 1135–1155.
13. Penelis, G. R. G. (2006). An efficient approach for pushover analysis of unreinforced masonry (URM) structures. *Journal of Earthquake Engineering, 10*(3), 359–379.
14. Vemuri, J., Ehteshamuddin, S., & Kolluru, S. V. L. (2018). Evaluation of seismic displacement demand for unreinforced masonry shear walls. *Cogent Engineering, 5*(1), 1480189.
15. Mann, W., & Muller, H. (1982). Failure of shear stressed masonry. An enlarged theory, tests and application to shear walls. *Proceedings of the British Ceramic Society, 30,* 223–235.
16. Anthoine, A., Magonette, G., & Magenes, G. (1995). Shear compression testing and analysis of brick masonry walls. In *Proceedings of the 10th European Conference on Earthquake Engineering*, August 28–September 02, 1994. Rotterdam: Balkema.
17. Magenes, G., & Calvi, G. M. (1992). Cyclic behaviour of brick masonry walls. In *Proceedings of the 10th World Conference on Earthquake Engineering*, Madrid, Spain, July 19–24, 1992.

18. BIS (Bureau of Indian Standards). (1991). *Handbook on masonry design and construction, SP:20*. New Delhi, India.
19. CSI (Computers and Structures Incorporated). (2012). *SAP2000 version 15, software*. Walnut Creek, California, USA.
20. Motazedian, D., & Atkinson, G. M. (2005). Stochastic finite-fault modelling based on dynamic corner frequency. *Bulletin Seismological Society of America, 95,* 995–1010.
21. Vemuri, J., Kolluru, S., & Chopra, S. (2018). Surface level synthetic ground motions for M7.6 2001 Gujarat earthquake. *Geosciences, 8*(12), 429.
22. Bureau of Indian Standards (BIS). (2016). *Indian Standard criteria for earthquake resistant design of structures: Part 1—General provisions and buildings, IS: 1893*. New Delhi, India.
23. Narayan, J. P., & Sharma, M. L. (2004). Effect of local geology on damage severity during Bhuj, India earthquake. In *Proceedings of the Thirteenth World Conference on Earthquake Engineering* (Paper No. 2042), Vancouver, Canada, August 1–4.
24. Baker, J. W., & Cornell, C. A. (2005). A vector-valued ground motion intensity measure consisting of spectral acceleration and epsilon. *Earthquake Engineering and Structural Dynamics, 34*(10), 1193–1217.
25. Cutfield, M. R., & Ma, Q. T. (2018). Solution strategies for three problems in empirical fragility curve derivation using the maximum likelihood method. *Journal of Earthquake Engineering, 22*(3), 435–453.
26. Straub, D., & Der Kiureghian, A. (2008). Improved seismic fragility modeling from empirical data. *Structural Safety, 30*(4), 320–336.

Axial Behaviour of Corroded CFST Columns Wrapped with GFRP Sheets—An Experimental Investigation

S. Vijaya Bhaskar Reddy and S. Sivasankar

1 Introduction

Corrosion causes severe deterioration both in reinforced concrete (RC) and steel structures like buildings, bridges and marine structures. Once they got corrosion, their structural performance and safety get reduced significantly. Recent days concrete-filled steel tubular (CFST) members are widely served as structural elements (beams, columns and slabs) both in onshore and offshore applications. Since, composite members have concrete and steel, resulting in a member that has the beneficial qualities of both materials [1]. Also, they have very good strength and ductility properties compare to reinforced concrete structures. Offshore structures are more prone to corrosion, since they are directly contacted with very severe environment like sea water. In offshore CFST members, steel is directly exposed to sea water, and therefore, they get deteriorated by corrosion due to long-term chloride ingress. As the amount of corrosion increases, CFST member starts loosing design strength, and finally, the structure fails as a whole. In addition, maintenance losses such as cost and time needed to make the replacements of corroded objects are incurred. The ancient and traditional method of retrofitting is providing additional plates on corrosion affected region by welding techniques. They increase the self-weight of the section further affecting the design strength. Also, the welded plates get further corrosion when it is exposed to the sea water. So, we need a permanent, easy to use and cost-effective solution to overcome these issues. For the past few decades, a lot of RC structural members were failed by corrosion and other severe environmental deterioration, and they are successfully repaired by fibre-reinforced polymers (FRP)

S. V. B. Reddy · S. Sivasankar (✉)
Department of Civil Engineering, CMR Technical Campus, Medchal, Hyderabad, Telangana 501401, India
e-mail: drsssphd@gmail.com

S. V. B. Reddy
e-mail: vbsgen06@gmail.com

composites [2–4]. FRP composites are made up of high-tensile strength fibres embedded in an epoxy matrix; they afford superior resistance to corrosion, low weight, high strength-to-weight ratio, impact resistance, high mechanical strength, fast and economical way of rehabilitation or repair of beams, columns and slabs [6]. Due to the superior mechanical and physical properties, FRP composites are widely used for external strengthening of RC columns [4–6], beams [2, 3, 8], slabs [7, 9], bridge decks [8], impact [10] and fatigue strength [11]. After the successful use of FRP composites in RC structures, researchers and engineers are now using FRP in steel structures for strengthening and retrofitting applications. Al-Saidy et al. [12] performed a study on corrosion damaged beam retrofitted with CFRP plates. Results showed that the strength and stiffness of beam retrofitted by CFRP plates increased significantly. Photiou et al. [13] studied the applications of high modulus CFRP composites for beams artificially corroded. Four beams were wrapped, two utilizing U-shaped prepreg units, whereas the other two beams used a flat plate prepreg. From the results, it was found that the beam wrapped by high modulus CFRP composite showed higher load-carrying capacity and ductility compared to unwrapped beam. Sundarraja and Sivasankar [14] did an experimental study on square steel tubular members strengthened by CFRP strips. It was found that the specimen wrapped by CFRP strips exhibited higher strength and ductility compared to control specimen. Teng and Hu [15] suggested the use of FRP sheets for circular steel specimens. Steel members were wrapped with one, two and three layers of GFRP sheets around the periphery throughout the height. Test results indicated that the specimen wrapped by three GFRP layers showed higher axial load-carrying capacity and stiffness compared to that of specimens wrapped with one and two layers of GFRP sheets. Also, it was found that the GFRP sheets significantly reduce the local buckling. Seica and Packer [16] performed study on retrofitting of steel members using CFRP composites for underwater and in-air applications. Two specimens were wrapped in normal condition and the remaining four were wrapped in underwater. Test results showed that the CFRP sheets significantly increase the load and stiffness of both in-air and underwater wrapped specimens. Also, they strongly recommended the CFRP sheets for underwater applications. Keykha et al. [17] done both investigational and numerical analyses on steel columns reinforced by CFRP sheets. Experimental and numerical studies results are close to each other.

From the previously published journal results, it has been found that the FRP is the most suitable composite materials for strengthening and retrofitting of RC and steel structures. To date, only a limited number of studies have specifically reported on corroded CFST members repaired with GFRP sheets. Nowadays, CFST members were broadly used in the marine and other structural applications. The prime goal is to experimentally explore the usefulness of GFRP (full wrapping) on corroded CFST column members subjected to axial compression.

2   Material Properties

2.1   Steel Tube

Circular hollow steel tube confirming to IS 1239-1983 having length and diameter 600 and 101.6 mm was used in this experiment. Thickness and height of the CCFST members are 3.6 mm and 600 mm, respectively. The yield strength provided by the manufacture is 250 N/mm^2.

2.2   Concrete Mix

Concrete strength of M$_{25}$ was achieved by using commercially available materials with mixing using vibrators and simple curing methods. The design proportion of 1: 1.62: 2.58 was used to attain a maximum strength of 25 N/mm^2 with w/c ratio as 0.45. The average compressive strength of 26.29 N/mm^2 was found at the end of 28 days.

2.3   Glass Fibre-Reinforced Polymer (GFRP) Sheet

The unidirectional webbed glass fibre was used in the experimental investigation. GFRP has Young's modulus of 50 GPa and tensile strength can be up to 1600 N/mm^2. The thickness and width of the glass fibre were 0.360 mm and 600 mm, respectively.

2.4   Adhesive

The most suitable adhesive material with GFRP fabrics with steel is epoxy resin. The adhesive material consists of two compounds, namely resin and hardener. These have a mixing ratio of 100: 10 (B: H) as specified by the manufacturer.

3   Experimental Investigation

A total of eight columns were used for this investigation. All the specimens are undergone corrosion by artificial corrosion process. Artificial corrosion was performed by adding 70 g of sodium chloride (NaCl) and 100 ml of acidic acid with one litre of portable water. Thereafter, all samples are immersed in the solution for a period of six weeks. To accelerate the corrosion, samples were taken out and cured in the ambient

Fig. 1 Samples before
corrosion

temperature for alternate days. Corrosion rate was calculated by weight loss method
at an interval of seven days. Samples before corrosion and after corrosion processes
were presented in Figs. 1 and 2. Corrosion rate calculation at seven days interval is
presented in Table 1.

3.1 Test Specimen Details

GFRP fabrics were used as continuous sheets wrapping around the peripheral of
the circular concrete-filled columns. Among the eight CCFST columns, two were
reference and rest of the specimens were confined with GFRP continuous sheets. For
easy identification, specimens were named such as CCFST-C, CCFST-1L, CCFST-2L
and CCFST-3L. For specimen CCFST-1L, CCFST denoted the corroded concrete-
filled steel tubes and 1L denoted the specimen confined by single layer of GFRP
sheets.

Fig. 2 Samples after corrosion

3.2 Application of GFRP Sheets on CCFST Columns

Prior bonding of CFRP strips surface preparation of specimen was done by sand-blasting [8]. This could avoid the debonding of CFRP strips. Before bonding, surface of the specimens was cleaned by acetone. This removes rust and impurities present on the surface. Resin and hardener were mixed well as per the mix ratio given by the manufacturer. Before wrapping the first layer, mixed resin is applied around the specimen using brush. Immediately after application of resin, initial layer is wrapped around the specimen and is presented in Fig. 3. Steel ribbed rollers were used for removing excess air present between the layers which are presented in Fig. 4. Similar procedure was repeated for second and third layer GFRP wrapping. Wrapped specimens were dried at room temperature for 2–3 days. The crushing tests were carried out in a 2000 kN universal testing machine shown in Fig. 5.

4 Experimental Results and Discussion

4.1 Failure of Specimens

Specimen with no wrapping (control specimen) failed by local buckling located at the top which is shown in Fig. 5. GFRP fabrics do not alter the actual failure mode; however, it is capable to postpone buckling and permit crushing strains reaching upper values therefore resulting in greater load-carrying capacity. Buckling of all

Table 1 Corrosion rate analysis

Sl. No.	Sample details	Initial weight in kg	Corrosion rate						Total weight loss in kg
			Wt. loss after 7 days	Wt. loss after 14 days	Wt. loss after 21 days	Wt. loss after 28 days	Wt. loss after 35 days	Wt. loss after 42 days	
1	CCFST-C-1	14.630	14.609	14.567	14.546	14.518	14.486	14.458	0.171
2	CCFST-C-2	14.680	14.649	14.616	14.571	14.532	14.482	14.447	0.233
3	CCFST-1L-1	14.500	14.479	14.428	14.336	14.310	14.279	14.234	0.266
4	CCFST-1L-2	14.530	14.522	14.508	14.477	14.449	14.427	14.408	0.122
5	CCFST-2L-1	14.570	14.554	14.527	14.481	14.457	14.431	14.403	0.167
6	CCFST-2L-2	14.600	14.581	14.562	14.529	14.492	14.461	14.428	0.172
7	CCFST-3L-1	14.470	14.455	14.431	14.399	14.356	14.332	14.310	0.160
8	CCFST-3L-2	14.500	14.481	14.454	14.422	14.394	14.367	14.332	0.168

Fig. 3 GFRP wrapping

Fig. 4 Air removal using rollers

Fig. 5 Failure of control column

confined columns is effectively resisted by GFRP; it is evident from the load incre-
ment associated with normal specimen is shown in Table 2. All confined columns,
rupture of GFRP and the peak load occur simultaneously. This ensures the effective-
ness and bonding of GFRP on corroded steel columns. Also it was observed from
failure pattern, all confined columns failed by rupture of GFRP alone and not by
fibre delamination. After the fibre rupture, there was a sudden drop in load occurs
in all confined columns. Photograph in Figs. 6, 7 and 8 shows the failure modes of
samples wrapped by unique, two and three GFRP layers.

Table 2 Ultimate compressive load and its increment comparison

Sl. No.	Specimen identification	Ultimate compressive strength (kN)	% Development in compressive strength compared to normal sample
1	CCFST-C-1	677.00	–
2	CCFST-C-2	671.00	–
3	CCFST-1L-1	702.85	3.82
4	CCFST-1L-2	713.00	5.32
5	CCFST-2L-1	728.85	7.66
6	CCFST-2L-2	734.00	8.42
7	CCFST-3L-1	746.00	10.19
8	CCFST-3L-2	741.00	9.45

Fig. 6 Failure of CCFST-1L

Fig. 7 Failure of CCFST-2L

Fig. 8 Failure of CCFST-3L

4.2 Ultimate Compressive Load

The gain in ultimate compressive load for all strengthened columns including control columns is given in Fig. 9 and Table 2. The percentage improvement in compressive load of GFRP confined columns compared with normal column was given in Table 2. For specimen CCFST-1L (one layer), the ultimate compressive load was 713 kN and the percentage gain compared control column was 5.32%. The ultimate compressive load observed for specimen CCFST-2L (two layers) was 734 kN which is 8.42% higher when related to normal sample. Similarly, the compressive strength for CCFST-3L (three layers) was 746 kN and the percentage gain was 10.19% compared to control column. The ultimate compressive strength of all confined columns increased with an increase in number of GFRP layers. But the increases are not twice compared with the ratios increased by single layer, similarly for three layers also. The reason was resin breakage takes place between the GFRP layers. Overall, there was an increase in strength compared to control column. These results confirm the effectiveness of GFRP sheets on corroded steel members.

4.3 Load–Deformation Relationship

Figure 10 presented the load–deformation curve of all tested specimens. It was observed that all the curves are similar (linear) in the initial stages. But in the second
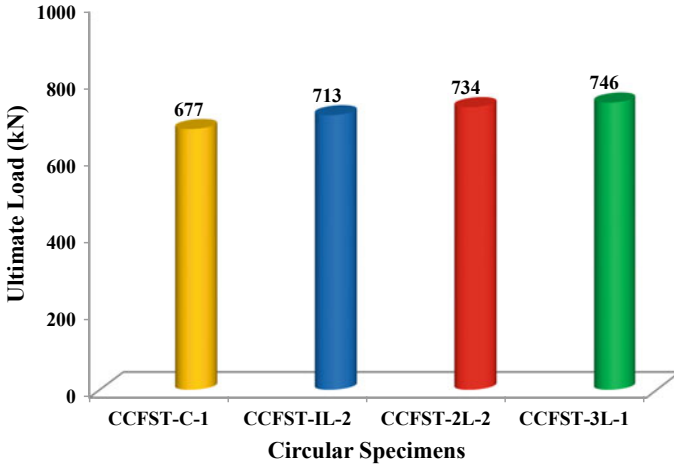
Fig. 9 Ultimate load comparison
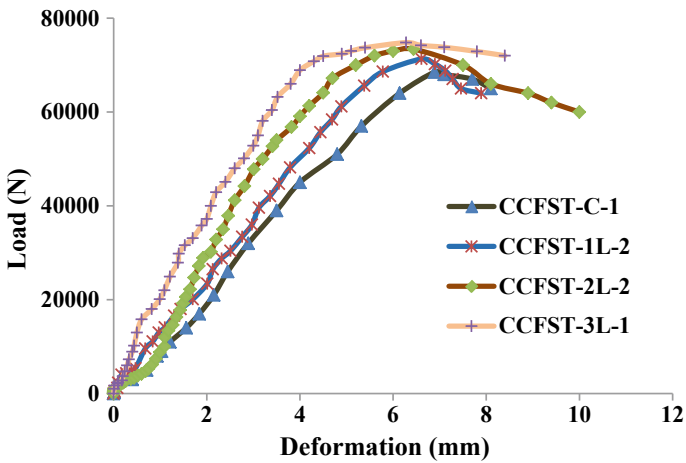
Fig. 10 Load versus deformation

stage, curves are different (nonlinear) because of stiffness provided by GFRP sheets. This phenomenon indicates that the load increment and reduction in deformation as the number of layers increased until the GFRP rupture. Deformation values for all tested specimens are presented in Fig. 11.
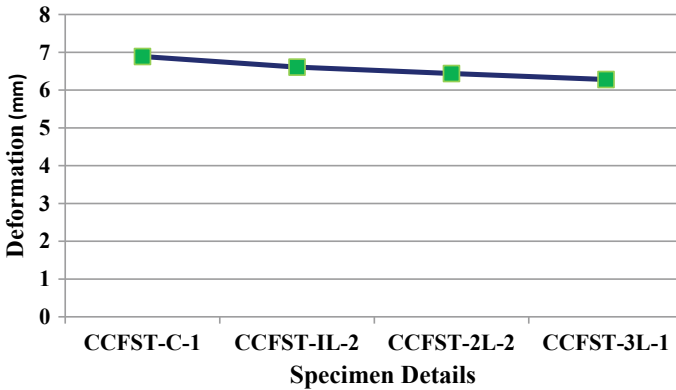
Fig. 11 Deformation curve for all specimens

4.4   Stress–Strain Relationship

Figure 12 represented the stress–strain relations of control column and GFRP confined columns. All confined columns exhibited same approach until reach as the normal samples highest strain value afterwards a massive difference in strain. Strain value for control column at peak is 0.01148, and for confined columns CCFST-1L-2, CCFST-2L-2 and CCFST-3L-1, the strain value is 0.01102, 0.010733 and 0.010467, respectively. The percentage of strain for confined columns (CCFST-1L-2, CCFST-2L-2 and CCFST-3L-1) compared to control column was 4%, 7.14% and 8.88%, respectively. From the above details, it can be seen that the percentage strain increase was not linear with increasing number of GFRP layers. This was mainly because of the resin breakage between CFRP layers.

Fig. 12 Stress–strain relationship
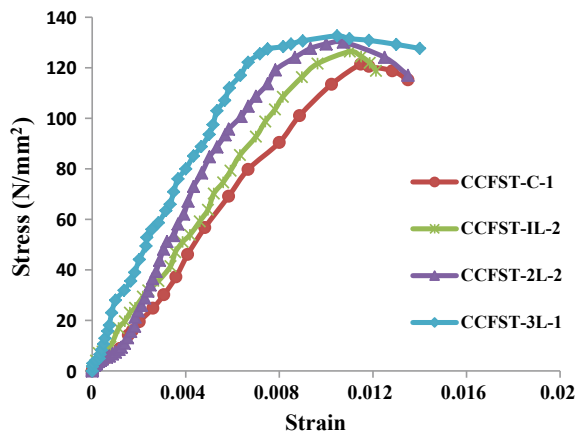
5 Conclusions

Six CCFST columns wrapped with different number of GFRP layers and two unwrapped specimens were tested in UTM machine. From the investigation, the following conclusions were summarized:

- Adding more number of GFRP sheets to steel samples significantly delayed the buckling and in that way raises the compressive strength.
- Failure of columns wrapped by GFRP sheets is purely by rupture only and no sign of delamination. This result concludes the superior attachment of GFRP sheets and CCFST tubes.
- All GFRP wrapped columns shown higher ultimate compressive load than the bare corroded steel column.
- Ultimate compressive load gain of columns wrapped with one, two and three GFRP layers CCFST-1L-2, CCFST-2L-2 and CCFST-3L-1 compared to CC2 was 5.32%, 8.41% and 10.19%, respectively.
- Axial deformation control for GFRP wrapped columns CCFST-1L-2, CCFST-2L-2 and CCFST-3L-1 was 4.06, 6.53 and 8.85% higher compared to CC2. The corresponding deformation at peak load was 6.61 mm, 6.44 mm and 6.28 mm, respectively.
- The strain values for columns CCFST-1L-2, CCFST-2L-2 and CCFST-3L-1 are 0.01102, 0.010733 and 0.010467, respectively at the peak load.
- It is recommended that the columns corroded by corrosion, wrapping with GFRP sheets are considered to be an effective technique to improve the compressive strength and stiffness.

Conflict of Interests The authors declare that there is no conflict of interests regarding the publication of this paper.

References

1. Gupta, P. K., Sarda, S. M., & Kumar, M. S. (2007). Experimental and computational study of concrete filled steel tubular columns under axial loads. *Journal of Constructional Steel Research, 63,* 182–193.
2. Pham, H., & Al-Mahaidi, R. (2004). Experimental investigation into flexural retrofitting of reinforced concrete bridge beams using FRP composites. *Composite Structures, 66*(1), 617–625.
3. Soudki, K., El-Salakawy, E., & Craig, B. (2007). Behavior of CFRP strengthened reinforced concrete beams in corrosive environment. *Journal of Composites for Construction, 11*(3), 291–298.
4. Saadatmanesh, I. I., & Ehsani, M. R. (1997). Repair of earthquake damaged reinforced concrete columns with FRP wraps. *ACI Structural Journal, 94*(2), 206–215.
5. Demers, K. W. (1999). Neale confinement of reinforced concrete columns with fiber reinforced composite sheets—An experimental study. *Canadian Journal of Civil Engineering, 34,* 226–241.

6. Li, J., & Hadi, M. N. S. (2003). Behaviour of externally confined high-strength concrete columns under eccentric loading. *Composite Structures, 62,* 145–153.
7. Mosallam, A. S., & Mosalam, K. M. (2003). Strengthening of two-way concrete slabs with FRP composite laminates. *Construction and Building Materials, 17,* 43–54.
8. Ghosh, K. K., & Karbhari, V. M. (2007). Evaluation of strengthening through laboratory testing of FRP rehabilitated bridge decks after in-service loading. *Composite Structures, 77,* 206–222.
9. Rochdi, E. H., Bigaud, D., Ferrier, E., & Hamelin, P. (2006). Ultimate behavior of CFRP strengthened RC flat slabs under a centrally applied load. *Composite Structures, 72,* 69–78.
10. Erki, M. A., & Meier, U. (1999). Impact loading of concrete beams externally strengthened with CFRP laminates. *Journal of Composites for Construction, 3,* 117–124.
11. Tavakkolizadeh, M., & Saadatmanesh, H. (2003). Fatigue strength of steel girders strengthened with carbon fiber reinforced polymer patch. *Journal of Structural Engineering, 129*(2), 186–196.
12. Al-Saidy, A. H., Klaiber, F. W., & Wipf, T. J. (2004). Repair of steel composites beams with carbon fibre reinforced polymer plates. *Journal of Composites for Construction, 8*(2), 163–172.
13. Photiou, N. K., Hollaway, L. C., & Chryssanthopoulos, M. K. (2006). Strengthening of an artificially degraded steel beam utilising a carbon/glass composite system. *Construction and Building Materials, 20,* 11–21.
14. Sundarraja, M. C., & Sivasankar, S. (2012). Axial behaviour of HSS tubular sections strengthened by CFRP strips—An experimental investigation. *Science and Engineering of Composite Materials, 19,* 159–168.
15. Teng, J. G., & Hu, Y. M. (2007). Behaviour of FRP-jacketed circular steel tubes and cylindrical shells under axial compression. *Construction and Building Materials, 21,* 827–838.
16. Seica, M. V., & Packer, J. A. (2007). FRP materials for the rehabilitation of tubular steel structures, for underwater applications. *Composite Structures, 80,* 440–450.
17. Keykha, A. H., Nekooei, M., & Rahgozar, R. (2016). Numerical and experimental investigation of hollow steel columns strengthened with carbon fiber reinforced polymer. *Journal of Structural and Construction Engineering, 3*(1), 49–58.

Tensile Membrane Structures: An Overview

Allan L. Marbaniang, Subhrajit Dutta, and Siddhartha Ghosh

1 Introduction and History

Tensile membrane structures (TMS) are excellent solutions for covering long spans efficiently. These days, TMS are commonly adopted as roofing solutions for different types of large open areas and are mostly seen in stadia, amphitheatres and airports (Fig. 1). Membrane tents have also been used as makeshift shelters and roof shades since ancient history, being used extensively for military purposes since the Roman times till the present day. Modern tensile membrane structures, however, have a level of sophistication in their design, construction technology and material properties that separate them considerably from their historical counterparts.

Most of the tension structures developed during the late nineteenth century were in bridges, and they were mostly buildings during the twentieth century [1]. The development of such structures in the early twentieth century was attributed to circus tents and the need for larger structures after the industrial age started [2]. The advantages for lightweight construction are plentiful with an obvious decrease in dead load, low costs and an efficient use of the material. Frei Otto was one of the pioneers in the field of lightweight structures, with his exploration of different types and forms of tensile structures [3]. One of the earliest notable tensile structures was his German Pavilion at the Expo 1967 in Montreal. His research at the Institute for Lightweight Structures in Germany created a firm base of experience, knowledge and direction, for future

A. L. Marbaniang (✉) · S. Ghosh
Indian Institute of Technology Bombay, Mumbai 400076, India
e-mail: allanmarbaniang@iitb.ac.in

S. Ghosh
e-mail: sghosh@civil.iitb.ac.in

S. Dutta
National Institute of Technology Silchar, Assam 788010, India
e-mail: subhrajit.nits@gmail.com

Fig. 1 Denver International Airport. *Source* Wikimedia commons

research and designs. Although physical models were popular those days, they are, however, costly and inaccurate for the use in large structures. This led to a push for computational methods for modelling tensile structures. During the construction of the large cable net roof for the Munich Olympic Stadium, different computational methods were used alongside physical models.

Digital designing has provided architects with powerful tools to come up with different shapes and forms. The focus has now shifted to construction materials and technologies that are more sustainable, cost-effective and which leave a lower carbon footprint. Tensile membranes are a popular choice due to their flexibility in shape, light material, free flowing and aesthetically pleasing nature. The increase in use of tensile membranes was complemented with better materials, computational modelling tools and construction techniques. The adoption of tensile membranes has, however, not been as common as expected when compared to some other popular materials like concrete or steel. Structural failures like the collapse of the fabric roof over Montreal's Olympic Stadium in 1999 [4], lack of technical know-how and an inadequate availability of code provisions slow down the wide adoption of such structures. Currently, there is a slight shift of architectural designs to flatter membrane shapes like the Millennium Dome [5]. The attempt to remove the anticlastic shapes may lead to unforeseen circumstances [6] which further complicate the design process. The few code provisions available and the limited number of architects or structural engineers with the knowledge of implementing effective and safe designs create a gap for fully utilizing such structures. The aim of this study is to therefore present a review on the design of TMS. The design of such structures is unconventional as the initial shape is not known beforehand. This central concept

of TMS is presented, along with a review of past research on form finding, analysis and patterning. The other challenges that need to be included during the design are emphasized which could improve the design of TMS in the future.

2 Tensile Membrane Structures

Tensile membranes are lightweight, efficient membranes, possessing no bending stiffness, and they resist any external loading only through in-plane stresses. The ability of the full cross section to be stressed uniformly over the whole domain results in the most efficient use of the material. The two most common fabrics used are the PVC-coated polyester and the PTFE Teflon-coated glass cloth [7]. The fabric material is generally formed by weaving fabrics with the *weft* yarns passed over and under fairly straight *warp* yarns, causing the material to behave differently along the yarn directions as seen in Fig. 2.

Cables behave similarly to tensile membranes and are many a times used along the TMS boundary to apply prestress. The membrane can also be stretched to fit a fixed boundary or a cable perimeter with a desirable prestress. This initial prestress used to stretch the membrane should be high enough so that wrinkling or slack is avoided without over-stressing or causing a tear in the material. The shape of the membrane changes on the application of external loads. External loading can occur in the form of wind or snow/rain loading, which may lead to higher stresses or ponding if not properly designed. Unique shapes are formed under different loads and boundary conditions. These shapes and corresponding prestress are not known beforehand but need to be found [6]. This process is different from conventional structures, where the initial shape is already known. The required shape is sometimes forcibly acquired

Fig. 2 Fibre material with weft and warp yarns
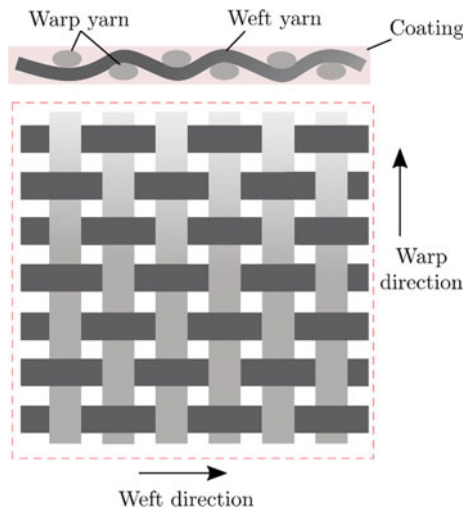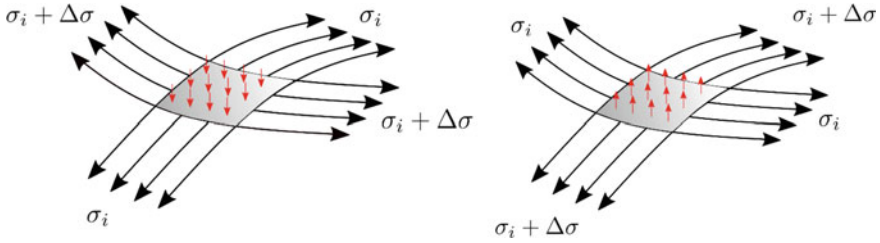
Fig. 3 Anticlastic shape under prestress σ_i providing stability and stiffness under loads in both directions

by applying uneven initial prestresses, which may be undesirable. Therefore, an inverse process of *form finding* is needed so that the initial equilibrium geometry is found under a particular prestress and the given boundary conditions. The form found shape should be anticlastic (i.e. principal curvatures are of opposite signs) [8], which provides the necessary stability as seen in Fig. 3.

The final design has to further undergo a patterning stage so that different pieces of membrane fabric can be seamed together. The patterned membrane needs to be compensated so that it forms the right geometry on the application of prestress [9]. The form found shape should also be analysed to check whether it can withstand environmental loads. These structures, however, possess highly nonlinear behaviours, that further complicate the form finding, analysis and patterning stages. A typical design of a tensile membrane structure from the initial form finding to the final patterning phase can be seen in Fig. 4.

3   Form Finding

A majority of research done on TMS is in finding different ways of solving the initial equilibrium problem by using different techniques. Frei Otto was a pioneer who obtained shapes for membranes and cable nets by physically using soap film models. The interest in moving toward computational methods started with the Munich Olympic Stadium, when scaled physical models of the cable net roof could not provide a desirable level of accuracy [10]. The use of physical models, however, gives a good intuition to the problem and should be used alongside numerical methods, according to many practitioners [6].

3.1   *Formulation*

In the form-finding stage, the membrane continuum is discretized using finite elements. This discretization can be done using equivalent cable elements. This approach
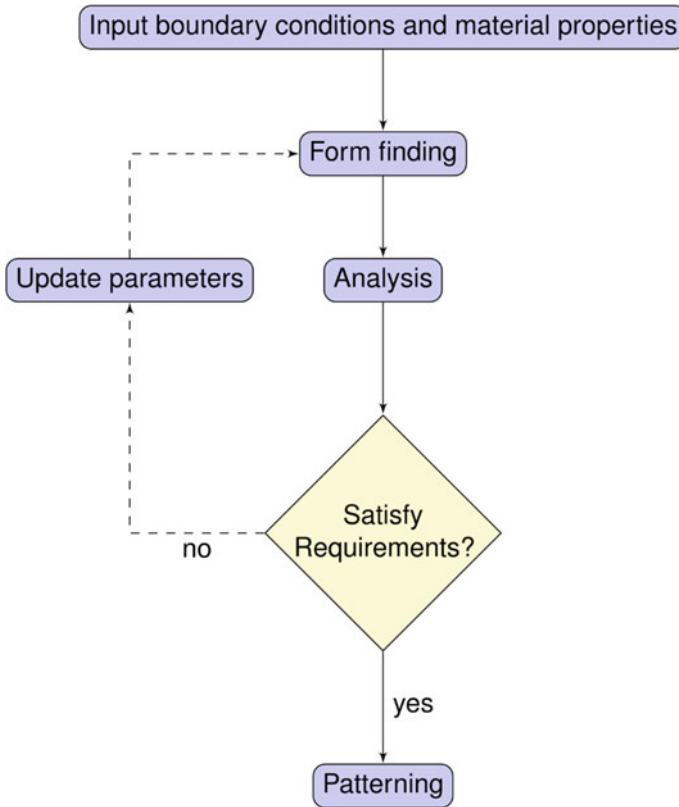
Fig. 4 Design process of tensile membrane structures

has, however, shown to be inaccurate due to the inability to model shear [9, 11]. The use of constant strain triangle elements (CST) is a popular choice to discretize the membrane domain as shown in Fig. 5b.

The equilibrium at each node i is given as

$$R_i = P_i + \sum \frac{T \Delta x}{L} \tag{1}$$

where at each node i, R_i is the residual due to the imbalance between external loads P_i and the prestress T in the neighbouring elements and $\Delta x/L$ is the direction cosine of the prestress force from each neighbouring element. During form finding, the residual is only due to the internal prestress without any external loading and material dependency [11]. The basis of form finding is then to numerically find a geometry in which the residual force at all the nodes is close to zero for a particular pretension and boundary condition, as shown in Fig. 5a.
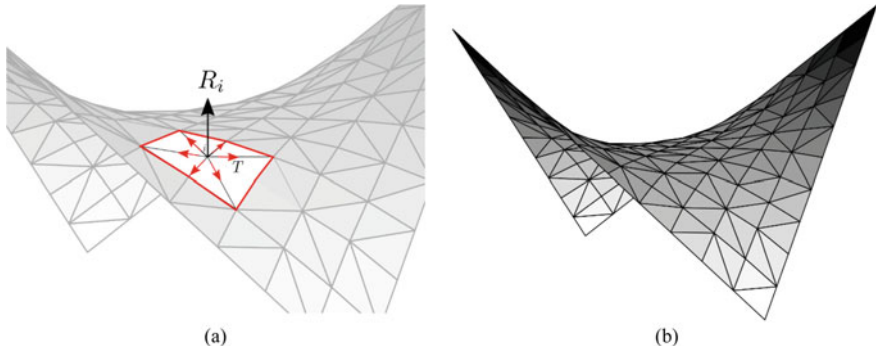
Fig. 5 **a** Equilibrium at node i without external loads, and **b** the final form found shape of a hypar TMS

Minimal surfaces having constant stresses are, however, more efficient as all sections in the membrane surface carry an equal amount of stress. This reduces the chance of occurrence of wrinkles and local stress concentrations. Physical soap films have been used to acquire minimal shapes over a certain boundary. The boundary conditions can sometimes not allow for minimal surfaces to be formed, and so pseudo-minimal surfaces are acquired. In that case, the prestress applied to acquire the shape is not constant which is not desirable.

3.2 Computational Methods

The force density method was used to find the shape for the cable net roof for the Munich Olympic Stadium [10, 12]. At the same time, Argyris et al. [13] used the natural form-finding method to also find the equilibrium shape of the same structure. The force density method linearized the nonlinear equilibrium equations by assuming the unknown parameters as force densities while the natural form-finding method used the stiffness method. Apart from static approaches to form-finding, dynamic methods such as the dynamic relaxation method have also been used [14]. The method is popular and robust where the system oscillates towards its equilibrium state under damping. Lewis [15] compared the transient stiffness method with dynamic relaxation methods. The dynamic relaxation method was found to be more efficient with the stability of iterations assured. Veenendaal and Block [11] performed an overall comparison of different types of form-finding methods within the same formulation. The different methods were categorized into stiffness matrix, geometric stiffness and dynamic equilibrium methods. It was found that geometric methods fare better when compared to dynamic and stiffness methods.

4 Analysis and Design

Analysis of tensile membrane structures under external loading is done by considering the material properties, external loading and finding the equilibrium shape. Wind loading and snow loading are usually the dominant forces with self-weight being largely negligible due to the lightweight material [4]. The form should also allow for drainage to avoid ponding under different load conditions. Wind loading is updated with the geometrically nonlinear deformation [14]. Barnes [14] used the dynamic relaxation method to find the static response. The use of viscous damping is more preferable with extreme environmental loads if it causes slackening which slows the overall convergence [16]. Tabarrok and Qin [17] used large deformation finite element analysis for the form finding and load analysis of structures made of cables, frames and membrane elements. Bridgens and Birchall [5] showed the response of different types (hypars, conic and saddles) of tensile membrane structures. Hypars show a low sensitivity to shear stiffness especially when the patterning is such that the yarns are in the direction of the opposite corners of the structure. Dutta et al. [18, 19] showed that by optimizing the initial prestress in the membrane, one could get shapes with better performance, particularly under uncertain wind loading. The dynamic relaxation method was used [20] along with heuristic optimization methods and metamodels to save computational time.

Since these structures show high geometric nonlinearity, a limit state approach is not suitable for designing as the geometry of the structure is dependent on the magnitude and the distribution of the loading [21]. This approach is followed in codes like ASCE [22] where stress factors are used as permissible limits. Gosling et al. [4] had kept the requirements of a design to fulfil the requirements of permissible stress limits, deflection and avoidance of ponding and wrinkles.

5 Patterning

The form found membrane shapes are doubly curved and cannot be easily projected on a two-dimensional plane. The cloth pieces used for the structure have to be seamed together from sheets of fabric material such that the desired shape can be formed as shown in Fig. 6. Some of the methods used to find the patterned shapes are physical, geometrical or based on equilibrium shapes [23]. Patterning can be done by finding the unstressed side lengths from the equilibrium shape along with cable slack lengths which can be independently unstressed [2]. The cutting pattern can be found using geodesic lines on the form found shape with compensation to allow for the actual stretching when it is installed [9]. If non-minimal forms are used, varying levels of compensation should be applied in different directions, which is rarely followed [21].
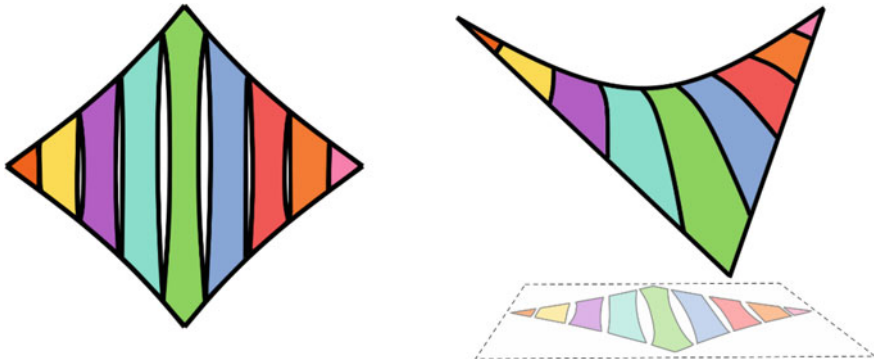
Fig. 6 Patterning along geodesic lines. Adapted from [24]

6 Challenges

6.1 Form Finding

Form finding is varied in its approaches and is dependent on the choice of different discretizations and the solving method used. Minimal shapes may not form within all boundary conditions. Bridgens and Birchall [5] showed that for conic structures, the minimal surface may neck off with unfeasible boundary conditions. This leads to pseudo-minimal surfaces with higher stresses at high curvature points, where the soap film would fail. In a round-robin exercise, it was found that a high variation in stresses, displacements and reactions was obtained from all the participants highlighting the challenges faced with benchmarking different methods and software packages [25].

The different computational methods available also present their own challenges that have to be considered such as computational time, stability and simplicity. Computational time is an important aspect of any numerical scheme, which can be intensive in some cases. The dynamic relaxation method improves with better descriptions of the initial shape close to the formed shape [6]. This may not always be known for surfaces with complex shapes and boundary conditions. Different parameters are required to control stability and convergence of dynamic equilibrium methods [11]. The stiffness methods unnecessarily require material properties which may be excluded. The linear force density method, which is in itself elegant and simple, can produce impractical or unwanted results, necessitating a nonlinear solution phase for proper results.

6.2 Uncertainty

The woven fabric material is highly nonlinear with uncertain mechanical properties. Assumptions in the material properties for a given fabric, that are usually adopted, can be very approximate [5]. Tensile membrane structures are highly sensitive to wind loading due to their lightweight nature. Wind loading in itself is stochastic in nature, and the current practice of taking critical static wind loads is unrepresentative of the actual behaviour. The nonlinear behaviour of the structure and wind loading is coupled, and this requires detailed fluid–structure interaction studies [26].

6.3 Design

The design process is made more difficult due to an inadequate availability of code provisions. While there is a standard guideline on TMS in the USA [22], there is no code yet established in Europe, while other existing codes provide only broad design principles [4]. The step to a Eurocode provision is, however, ongoing with the release of the "Science and Policy Report" [27] which provides a base for the formulation of a new standard in the near future [28]. India does not have any standard for TMS, and there are only a few capable practitioners.

The current general design practice is to provide a single stress reduction factor which tries to account for the uncertainty in material property, loading, durability and construction errors, which is unreasonable. The consideration of displacement as ultimate states within a reliability approach should be considered [4]. The reliability against uncertain loading can be increased by optimizing the initial prestress resulting in more stable structures [18]. Investigating the erection process is also important as the whole system may not be stable until the full process is completed and stresses during erection may also reach failure limits [9]. The prestress has to be maintained throughout the life of the structure, which needs to be monitored for a long-term creep behaviour [21].

6.4 Other Constraints

Membrane structures should satisfy various other constraints and requirements surplus to the general structural requirements. The structure should be able to discharge water (due to snow or rainwater) safely. One of the major advantages of tensile membranes is their capability of transmitting light. The translucency of the fabric should be an important factor while choosing the material for the structure. Uninsulated membranes are sensitive to changes in radiation, and they quickly heat up or cool down. This can make the structure behave as a hot or cold radiator over an area which

can be uncomfortable [7]. The fabric is thin and may not provide good acoustic insulation. Fire safety is also an important aspect, and while most membrane fabrics are at least fire-resistant, they should be tested [29]. Toxic fumes from PTFE fabrics at high temperatures require proper ventilation and sprinkler systems [7].

7 Conclusion

Tensile membrane structures are efficient and lightweight and are gaining in popularity for roofing large open areas. The adoption of TMS is, however, not straightforward due to an unfamiliar design process and lack of codes and resources. In this paper, a review of past research on the design of TMS is presented. Form finding is an integral part of the design of TMS, with numerical methods used to solve the nonlinear initial equilibrium problem. These methods are also used for analysis under external loads. The fabric needs to be patterned properly in order to acquire the desired prestress or shape upon construction. While computational methods are effective, most of the software packages and methods used in the design process need to be benchmarked and regularized. The computational cost associated with the existing numerical methods of form finding and load analysis is expected to drive future research towards more efficient algorithms. The future scope of TMS can be improved through the development of codes, resources and reliable software. Further research into the inclusion of material uncertainty and nonlinearity, stochastic loading and fluid–structure interaction need to be explored. The comparison of minimal shapes over non-minimal ones can follow with a detail investigation between various shapes.

References

1. Bradshaw, R., Campbell, D., Gargari, M., Mirmiran, A., Tripeny, P. (2002). Special structures: Past, present, and future. *Journal of Structural Engineering*, *128*. https://doi.org/10.1061/(asce)0733-9445(2002)128:6(691).
2. Topping, B., Ivanyi, P. (2007). *Computer aided design of cable membrane structures*. Saxe-Coburg Publications.
3. Drew, P. (1976). *Frei Otto: Form and structure*. London: Granada Publishing Limited.
4. Gosling, P., Bridgens, B., & Zhang, L. (2013). Adoption of a reliability approach for membrane structure analysis. *Structural Safety, 40,* 39–50. https://doi.org/10.1016/j.strusafe.2012.09.002.
5. Bridgens, B., & Birchall, M. (2012). Form and function: The significance of material properties in the design of tensile fabric structures. *Engineering Structures, 44,* 1–12. https://doi.org/10.1016/j.engstruct.2012.05.044.
6. Lewis, W. (2003). *Tension structures-form and behaviour*. London: Thomas Telford Publishing.
7. Chilton, J. (2010). Tensile structures—Textiles for architecture and design. In: G. Pohl (ed.), *Textiles, polymers and composites for buildings, Woodhead publishing series in textiles* (pp. 229–257). Woodhead Publishing. https://doi.org/10.1533/9780845699994.2.229.
8. Meek, J. L., & Xia, X. (1999). Computer shape finding of form structures. *International Journal of Space Structures, 14*(1), 35–55. https://doi.org/10.1260/0266351991494687.

9. Wakefield, D. S. (1999). Engineering analysis of tension structures: Theory and practice. *Engineering Structures, 21*(8), 680–690. https://doi.org/10.1016/S0141-0296(98)00023-6.

10. Gruendig, L., Moncrieff, E., Singer, P., Strbel, D (2000). A history of the principal developments and applications of the force density method in Germany 1970–1999. In *4th international colloquium on computation of shell and spatial structures* (IASS-IACM) (pp. 1–13). Chania-Crete, Greece.

11. Veenendaal, D., & Block, P. (2012). An overview and comparison of structural form finding methods for general networks. *International Journal of Solids and Structures, 49*(26), 3741–3753. https://doi.org/10.1016/j.ijsolstr.2012.08.008.

12. Schek, H. J. (1974). The force density method for form finding and computation of general networks. *Computer Methods in Applied Mechanics and Engineering*, *3*, 115–134. https://doi.org/10.1016/0045-7825(74)90045-0.

13. Argyris, J. H., Angelopoulos, T., & Bichat, B. (1974). A general method for the shape finding of lightweight tension structures. *Computer Methods in Applied Mechanics and Engineering, 3*(1), 135–149. https://doi.org/10.1016/0045-7825(74)90046-2.

14. Barnes, M. R. (1999). Form finding and analysis of tension structures by dynamic relaxation. *International Journal of Space Structures, 14*(2), 89–104. https://doi.org/10.1260/0266351991494722.

15. Lewis, W. J. (1989). The efficiency of numerical methods for the analysis of prestressed nets and pin-jointed frame structures. *Computers & Structures, 33*(3), 791–800. https://doi.org/10.1016/0045-7949(89)90254-X.

16. Barnes, M. R. (1988). Form-finding and analysis of prestressed nets and membranes. *Computers & Structures, 30,* 685–695. https://doi.org/10.1016/0045-7949(88)90304-5.

17. Tabarrok, B., & Qin, Z. (1992). Nonlinear analysis of tension structures. *Computers & Structures, 45,* 973–984. https://doi.org/10.1016/0045-7949(92)90056-6.

18. Dutta, S., Ghosh, S., Inamdar, M.M. (2017). Reliability-based design optimization of frame-supported tensile membrane structures. *ASCE-ASME Journal of Risk and Uncertainty in Engineering Systems*, *Part A: Civil Engineering, 3*(2). https://doi.org/10.1061/ajrua6.0000866.

19. Dutta, S., Ghosh, S., & Inamdar, M. M. (2018). Optimisation of tensile membrane structures under uncertain wind loads using PCE and kriging based metamodels. *Structural and Multidisciplinary Optimization, 57*(3), 1149–1161. https://doi.org/10.1007/s00158-017-1802-5.

20. Dutta, S., Ghosh, S. (2014). Numerical form-finding of a tensile membrane structure using dynamic relaxation method. In *Proceedings of the 5th International Congress on Computational Mechanics and Simulation* (ICCMS), Chennai, India.

21. Bridgens, B., Gosling, P., & Birchall, M. (2004). Tensile fabric structures: Concepts, practice and developments. *Structural Engineer, 82,* 21–27.

22. ASCE: ASCE/SEI 55-10. (2010). Tensile membrane structures. *American Society of Civil Engineers*.

23. Moncrieff, E., & Topping, B. (1990). Computer methods for the generation of membrane cutting patterns. *Computers & Structures, 37*(4), 441–450. https://doi.org/10.1016/0045-7949(90)90034-Y.

24. Veenendaal, D. (2017). *Design and form finding of flexible formed concrete shell structures* (Ph.D. Thesis).

25. Gosling, P. D., Bridgens, B. N., Albrecht, A., Alpermann, H., Angeleri, A., Barnes, M., et al. (2013). Analysis and design of membrane structures: Results of a round robin exercise. *Engineering Structures, 48,* 313–328. https://doi.org/10.1016/j.engstruct.2012.10.008.

26. Dutta, S., Ghosh, S. (2019). Analysis and design of tensile membrane structures: Challenges and recommendations. *Practice Periodical on Structural Design and Construction*, *24*(3). https://doi.org/10.1061/(asce)sc.1943-5576.0000426.

27. Stranghner, N., Uhlemann, J., Bilginoglu, F., Bletzinger, K. U., Bgner-Balz, H., Corne, E., Gibson, N., Gosling, P., Houtman, R., Llorens, J., Malinowsky, M., Marion, J. M., Mollaert, M., Nieger, M., Novati, G., Sahnoune, F., Siemens, P., Stimpfle, B., Tanev, V., Thomas, J. C. (2016). Prospect for European guidance for the structural design of tensile membrane structures, science and policy report (Sap-report). https://doi.org/10.1016/j.proeng.2016.08.027.

28. Stranghner, N., Uhlemann, J., & Mollaert, M. (2016). Background to the science and policy report for tensile membrane structures. *Procedia Engineering, 155,* 256–264. https://doi.org/10.1016/j.proeng.2016.08.027.
29. Huntington, C. G. (2013). Tensile fabric structures. *American Society of Civil Engineers*. https://doi.org/10.1061/9780784412893.

Investigation of Cold-Formed Steel Members Subjected to Extreme Low Temperatures Relevant to the Arctic Environment

Gaurav S. Chobe and Mahendrakumar Madhavan

1 Introduction

Metals tend to become hard and brittle under low-temperature condition. To meet the increasing demand of oil and natural gas, the exploration activities taking place in the Arctic region have expanded in the past decade due to the presence of 13% of the world's undiscovered oil and gas in the Arctic Circle [1]. However, the optimal design and operation of Polar Offshore structures face the risk of brittle fracture of the equipment due to extremely low temperatures (down to −50 °C).

Cold-formed steel (CFS) has an excellent combination of good strength-to-weight ratio and high corrosion resistance [2], which makes it suitable for the rapid and demountable construction of low-rise residential and industrial structures. Temperature induces a change in the mechanical properties of steel which affects the ultimate load-carrying capacity of a steel structure [3].

Much of the research study has been conducted to understand the behavior of the CFS at ambient and elevated temperature [4–8]. However, limited literature is available on its performance at low temperatures relevant to the structural applications [9–12]. According to Yu [3], when the temperature is lowered, the ultimate strength, yield strength, and the elastic modulus generally increase, and the ductility decreases. Hence, it is generally recommended to design CFS structures with great care.

In this study, results from a numerical investigation on the effect of temperature, slenderness ratio, and cross-sectional geometry on the ultimate load-carrying capacity of the unlipped CFS channel column are presented. A FE model was developed

G. S. Chobe (✉) · M. Madhavan
Department of Civil Engineering, Indian Institute of Technology Hyderabad, Hyderabad, India
e-mail: ce15btech11010@iith.ac.in

M. Madhavan
e-mail: mkm@iith.ac.in

41

and analyzed using ANSYS 15.0 software package. Specimen temperature was varied from −60 to 20 °C at an interval of 20 °C to encompass the temperature variations experienced in Polar Regions. The model was verified against the test results provided by Young and Yan [7]. FE results were found to be in good agreement with the experimental data; hence, the model was used for the further parametric study to analyze the behavior of different CFS channel columns at low temperatures. Finally, the results obtained from the FE analysis were compared with the design strength calculated using the Direct Strength Method (DSM) with modified material properties at low temperatures. Suitable graphs are drawn to demonstrate the effect of low temperature on the load-carrying capacity of the column.

2 Background

Inadequate literature is available which aims to study the performance of steel structures at sub-zero temperatures relevant to structural applications. Polyzois et al. [9] studied the compressive behavior of cold-formed angles in a temperature range of −45 to 25 °C. They found that the capacity of angles at temperatures below −40 °C was 8% higher than the capacity at room temperature. In a study conducted by Abdel-Rahim and Polyzois [10], it was found that yield strength, ultimate strength, and elastic modulus of the CFS coupon increased by as much as 13.3%, 14%, and 24%, respectively, at −50 °C compared to the room temperature. However, the maximum percentage elongation decreased by as much as 35% at −50 °C. The research conducted by Ritakallio and Björk [11] demonstrated that the Charpy-V impact toughness decreased by approximately 50% at −50 °C compared to room temperature for both corner portion and the flat portion of the hollow section EN10219.

3 Finite Element Modeling Details

3.1 Description of Material

The mechanical properties of CFS at low temperatures were obtained from the research conducted by Abdel-Rahim and Polyzois [10]. Stress–strain curves were generated for the material at temperatures ranging from −60 to 20 °C at an interval of 20 °C. Mechanical properties like ultimate strength, yield strength, elastic modulus, and maximum elongation were obtained for each temperature. Table 1 lists the mechanical properties of CFS at different low temperatures.

Bilinear elastic–plastic stress–strain curve was assumed for modeling the material.

Table 1 Mechanical properties of CFS at low temperatures

Temperature (°C)	Yield strength (MPa)	Ultimate strength (MPa)	Elastic modulus (GPa)	Maximum strain (%)
−60	514.16	608.82	235.68	17.11
−40	501.59	592.59	229.78	18.66
−20	489.03	575.51	224.32	20.13
0	475.57	561.05	218.42	21.76
+20	463.89	543.97	213.39	23.16

3.2 Development of Finite Element Model

A three-dimensional nonlinear FE model was developed in ANSYS Mechanical APDL 15.0 commercial software package to simulate the compressive loading condition for the unlipped channel column. The SHELL181 element was used to model the thin walls of the channel to incorporate out-of-plane deformations. To incorporate the inelastic strains that will be developed in the CFS sections, engineering stress (σ) and engineering strain (ε) were converted into corresponding true stress (σ_T) and true strain (ε_T) according to the following equations:

$$\sigma_T = \sigma(1 + \varepsilon) \tag{1}$$

$$\varepsilon_T = \ln(1 + \varepsilon) \tag{2}$$

The amplitude for geometric imperfection such as camber and sweep was taken as *L/1000* for length *L* of the column. The condition of fixed ends was simulated by restraining all six degrees of freedom at both ends except the translational degree of freedom at one end. The residual stresses were not incorporated while modeling since they are deemed negligible [13]. The effects of large deflections were accounted for by using NLGEOM, ON command. A static nonlinear analysis was carried out to obtain a solution with better accuracy. Size of mesh and distribution of finite elements throughout the body were decided based upon a rigorous mesh sensitivity analysis.

The axial force was applied exactly on the center of gravity (CG) of the cross section perpendicular to the plane of the cross section. The displacement control method was used for loading the model. Multi-point constraint (MPC) algorithm was used to assign the force at the CG points. Initially, CG point at each of the ends was defined as a reference point. Then, the nodes at the column ends were coupled to the respective reference points (Fig. 1).

By applying coupling constraints between the nodes at the column end and the corresponding reference point, the translational and rotational degrees of freedom of the column end were coupled to the corresponding reference point. For the fixed-end condition, displacement and rotation constraints ($U_x = U_y = 0$, $\theta_x = \theta_y = \theta_z = 0$) were applied at both ends, and additionally, the displacement constraint ($U_z = 0$) was applied at reference point *Y*. For each load step, the normal penalty stiffness
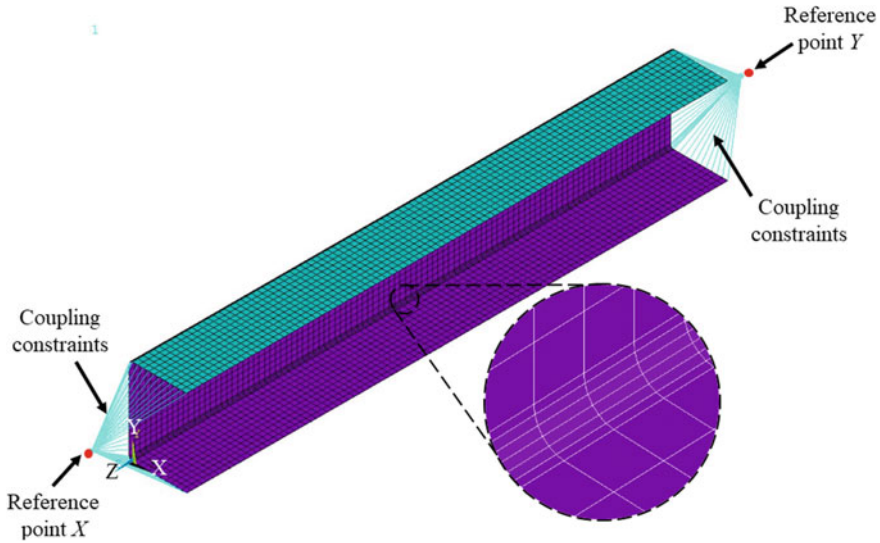
Fig. 1 Couplings, constraints, and mesh size in the FE model

factor was redefined to obtain more accurate results. The analysis was an iterative process which was terminated when the load value decreased for the increasing value of deflection.

3.3 Verification of Finite Element Model

The accuracy of the FE analysis was evaluated by comparing numerically derived load-carrying capacity and the mode of failure from FE analysis with the experimental test results. The developed FE model is validated with the results obtained from seven tests carried out by Young and Yan [7]. The tests were carried out at room temperature, and the validation is also performed at the same room temperature. Figure 2 shows the comparison of the buckled shape observed in the experimental test setup and FE analysis.

Table 2 shows the comparison of the values of the ultimate load-carrying capacity for the experimental test and FE analysis (FEA). The difference between the ultimate load-carrying capacity is found to be within acceptable limits with mean and coefficient of variation (CoV) of P_{exp}/P_{FEA} as 0.96 and 0.042, respectively. Hence, the model was used for further parametric analysis.

Difference in the failure modes observed in experiments and in simulations is attributed to the facts that the residual stresses are neglected while modeling the column, the amplitude of the geometric imperfections was assumed to be equal to
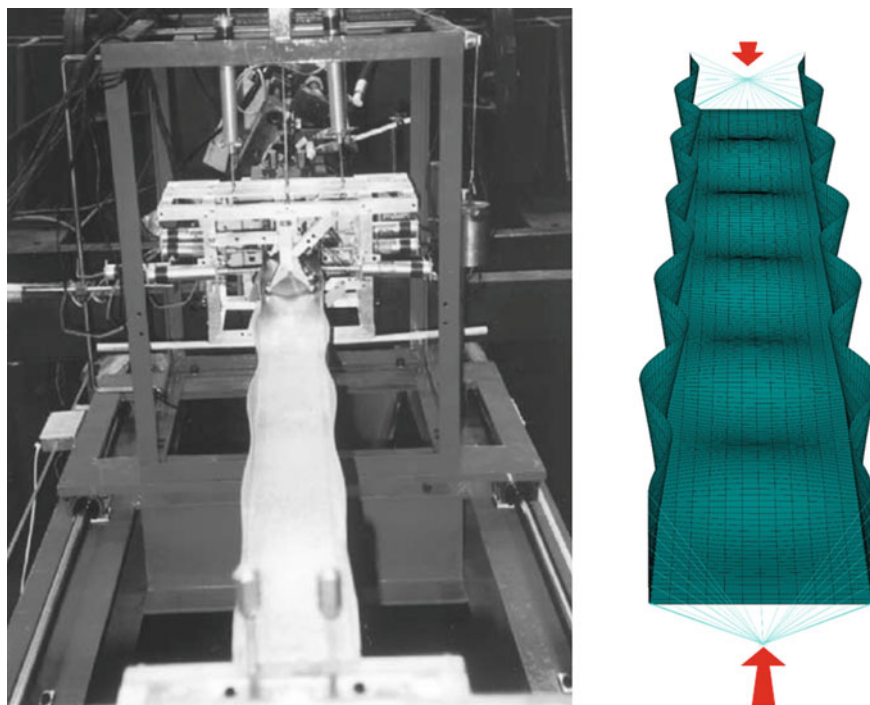
Fig. 2 Comparison of failure mode observed in experiment [7] and FE model

Table 2 Comparison of experimental and FEA results

Specimen	Experimental	FEA			Comparison
	P_{exp}	Failure	P_{FEA}	Failure	P_{exp}/P_{FEA}
P48F0300	66.0	L + F	69.3	L	0.95
P48F1000	62.7	L + F	61.3	L + F	1.02
P48F1500	55.5	L + F	59.6	L + F	0.93
P48F1850	47.2	L + F	49.0	L + F	0.96
P48F2100	43.6	L + F	47.5	L + F	0.92
P48F2500	38.5	L + F	41.4	L + F+FT	0.93
P48F3000	37.4	L + F+FT	36.9	L + F+FT	1.01
				Mean	0.96
				CoV	0.042

$L/$1000 for each length of beam, and the load was applied exactly at the CG point, which may not happen in practical situations.

3.4 Parametric Study

To understand the effect of different parameters on the load-carrying capacity of CFS channel column, the following parameters were considered for the numerical analysis:

1. The temperature of the specimen
2. Slenderness ratio of the specimen
3. The thickness of the CFS channel
4. Flange width.

The maximum and minimum temperatures of the specimen were considered to be −60 °C and 20 °C, respectively. Slenderness ratio of the specimen was varied by changing the length of the specimen from 250 to 3250 mm at an interval of 500 mm. The shortest length of the column was in accordance with the Structural Steel Research Council guidelines [14] for stub columns, whereas the longest length complies with the AS/NZS 4600 specifications [15] for slender columns. Flange width was varied as 30 and 50 mm. The thicknesses of 1 and 2 mm were considered. Larger thicknesses were not considered since plates thicker than 2.5 mm would produce cracks upon a 90° bend [16]. Ideal fixed support was considered as the end condition for the column.

3.5 Labeling of a Specimen

In the format for labeling, *P* represents pinned end. *W* and *L* denote the width of the flange and the unbraced length of the column, respectively. Figure 3 explains the labeling in general format.
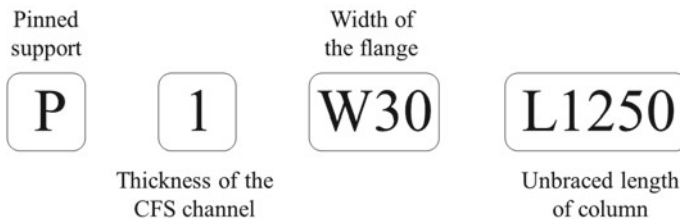

Fig. 3 Format for labeling the specimen

4 Design Rules and Comparison of Design Strengths

4.1 Direct Strength Method

The Direct Strength Method (DSM) as given in the supplement to the North American Specification [17] is used to determine the column strengths by substituting modified material properties at low temperature. The DSM developed by Schafer and Peköz [18] and Schafer [19] is used to predict the strength of CFS columns at low temperatures in this study.

The column design guidelines of DSM consider the local, distortional, and overall buckling. The unlipped channel sections do not fail in distortional buckling mode since they lack edge-stiffened flanges. Since the present study consists of only unlipped channel sections, distortional buckling is not considered while calculating the strength. The rules governing the design of columns are given in Eqs. (3)–(8). These equations take into account the effect of temperature while calculating the strength of the column.

$$P_{\mathrm{DSM}} = \min\left(P_{\mathrm{ne},T}, \ P_{\mathrm{nl},T}\right) \tag{3}$$

$$P_{\mathrm{ne},T} = \begin{cases} \left(0.658^{\lambda_{c,T}^2}\right) P_{y,T} & \text{for } \lambda_{c,T} \leq 1.5 \\ \left(\frac{0.877}{\lambda_{c,T}^2}\right) P_{y,T} & \text{for } \lambda_{c,T} > 1.5 \end{cases} \tag{4}$$

$$P_{\mathrm{nl},T} = \begin{cases} P_{\mathrm{ne},T} & \text{for } \lambda_{l,T} \leq 0.776 \\ \left[1 - 0.15\left(\frac{P_{\mathrm{crl},T}}{P_{\mathrm{ne},T}}\right)^{0.4}\right]\left(\frac{P_{\mathrm{crl},T}}{P_{\mathrm{ne},T}}\right)^{0.4} P_{\mathrm{ne},T} & \text{for } \lambda_{l,T} > 0.776 \end{cases} \tag{5}$$

$$\text{where} \quad P_{y,T} = A_g f_{y,T} \tag{6}$$

$$\lambda_{c,T} = \sqrt{P_{y,T}/P_{\mathrm{cre},T}} \tag{7}$$

$$\lambda_{l,T} = \sqrt{P_{\mathrm{ne},T}/P_{\mathrm{crl},T}} \tag{8}$$

In the above equations, A_g represents the gross cross-sectional area of the channel, and $f_{y,T}$ represents the yield strength of steel at temperature T. The nominal axial strength (P_{DSM}) is calculated for two cases. $P_{\mathrm{ne},T}$ represents nominal axial strength for flexural, torsional, and flexural–torsional buckling mode of failure at low temperatures. $P_{\mathrm{nl},T}$ represents nominal axial strength for local buckling as well as the interaction of local and global buckling at low temperatures. The critical elastic local buckling loads ($P_{\mathrm{crl},T}$) were determined in accordance with Appendix 2 of North American Specifications for CFS Structures. The nominal axial strength (P_{DSM}) is taken as the minimum of $P_{\mathrm{ne},T}$ and $P_{\mathrm{nl},T}$. The unfactored design column strengths (P_{DSM}) obtained are compared with the FE results in Table 3 for the series P-1-W30

Table 3 Comparison of DSM and FEA results

Specimen	DSM	FEA	Comparison
	P_{DSM}	P_{FEA}	P_{DSM}/P_{FEA}
P-1-W30-L0250	30,640	29,924	1.02
P-1-W30-L0750	25,506	25,400	1.00
P-1-W30-L1250	20,051	18,753	1.07
P-1-W30-L1750	17,783	16,777	1.06
P-1-W30-L2250	13,154	12,435	1.06
P-1-W30-L2750	9357	8828	1.06
P-1-W30-L3250	6621	6399	1.03
		Mean	1.07
		COV	0.02

at $-20\,°C$. From the table, it can be noted that, in general, DSM conservatively predicts the strength of CFS columns at low temperatures with a mean and coefficient of variation (CoV) of P_{DSM}/P_{FEA} as 1.07 and 0.02, respectively.

4.2 Results and Conclusion

Overestimated load capacities obtained from FE analysis may be attributed to the neglected residual stresses while modeling the column. Linear regression analysis is performed as shown in Fig. 4 by comparing the ultimate load-carrying capacity
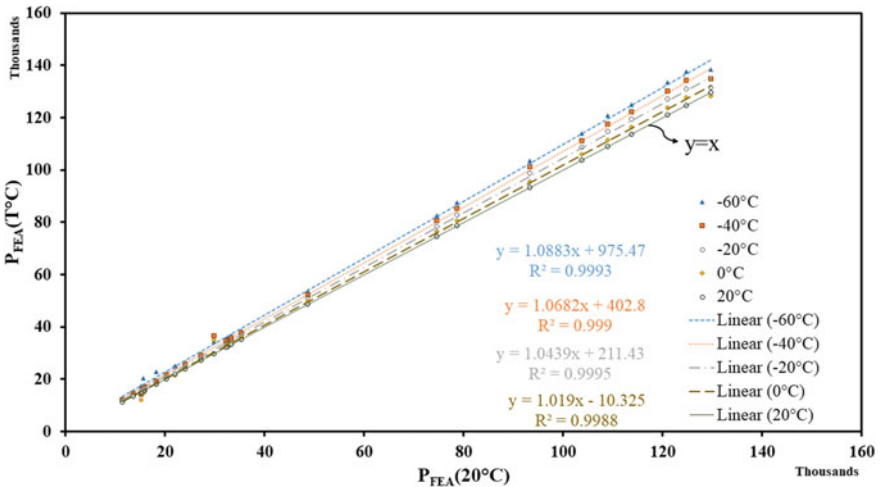

Fig. 4 Comparison between P_{FEA} (T) and P_{FEA} $(20\,°C)$ for fix-ended columns

at normal temperature (20 °C) and different low temperatures. The results indicate that on an average, the ultimate capacity of channel columns was approximately 1.9%, 4.4%, 6.8%, and 8.8% higher at temperatures 0 °C, −20 °C, −40 °C, and −60 °C, respectively, than at room temperature of 20 °C. Higher increment in the load-carrying capacity was observed at lower temperatures due to the improvisation of material properties at lower temperatures.

Stub columns were observed to fail in local buckling while slender columns were observed to fail primarily in flexural buckling. Intermediate columns failed in combined local and global buckling mode of failure.

5 Future Work

So far, the work is limited to the behavior of columns at low temperatures. To fully understand the performance, future study will be carried out on beams, frames, beam–columns, and connections to capture the modification in the load-carrying capacity and the failure modes. Design guidelines will be suggested for the design of such members at low temperatures.

References

1. Gautier, D. L., Bird, K. J., Charpentier, R. R., et al. (2009). Assessment of undiscovered oil and gas in the Arctic. *Science, 324*(5931), 1175–1179.
2. AISI (American Iron and Steel Institute). (2007). *Galvanized steel framing for residential buildings*. (Research Report RP06-1). Washington, DC: AISI.
3. Yu, W. W. (1982). *Cold-formed steel design*. N.Y.: Wiley Inc.
4. Gunalan, S., Kolarkar, P., & Mahendran, M. (2013). Experimental study of load bearing cold-formed steel wall systems under fire conditions. *Thin-Walled Structures, 65,* 72–92.
5. Laím, L., Rodrigues, J. P. C., & de Silva, L. S. (2014). Experimental analysis on cold-formed steel beams subjected to fire. *Thin-Walled Structures, 74,* 104–117.
6. Kankanamge, N. D., & Mahendran, M. (2011). Mechanical properties of cold-formed steels at elevated temperatures. *Thin-Walled Structures, 49,* 26–44.
7. Young, B., & Yan, J. (2002). Finite element analysis and design of fixed-ended plain channel columns. *Finite Elements in Analysis and Design, 38*(April), 549–566.
8. Huang, Z. F., & Tan, K. H. (2007). Structural response of restrained steel columns at elevated temperatures. Part 2: FE simulation with focus on experimental secondary effects. *Engineering Structures, 29*(September), 2036–2047.
9. Polyzois, D., Charnvarnichborikarn, P., Rizkalla, S. H., & Wong, C. K. (1990). Effect of temperature and galvanization on the compressive strength of cold-formed angles. *Canadian Journal of Civil Engineering, 17,* 440–451.
10. Abdel-Rahim, A. B., & Polyzois, D. (1996). Effect of temperature and galvanization on cold-formed steel. *Journal of Materials in Civil Engineering, 8*(3), 114–122.
11. Ritakallio, P., & Björk, T. (2014). Low-temperature ductility and structural behavior of cold-formed hollow section structures—Progress during the past two decades. *Steel Construction, 7,* 107–115.

12. Yan, J. B., Liew, J. R., Zhang, M. H., & Wang, J. Y. (2014). Mechanical properties of normal strength mild steel and high strength steel S690 in low temperature relevant to Arctic environment. *Materials and Design, 61*(September), 150–159.

13. Young, B., & Rasmussen, K. J. R. (1998). Test of fixed-ended plain channel columns. *Journal of Structural Engineering, 124*(2), 131–139.

14. Galambos, T. V. (Ed.). (1988). *Guide to stability design criteria for metal structures* (4th ed., pp. 708–710). New York: Wiley Inc.

15. Standards Australia. (2005). *Cold-formed steel structures*. AS/NZS 4600. Sydney, Australia: Standards Australia.

16. Hancock, G., Murray, T., & Ellifritt, D. (2001). *Cold-Formed steel structures to the AISI specification*. Boca Raton: CRC Press.

17. *Supplement to the North American specification for design of cold-formed steel structural members*. Washington (DC): American Iron and Steel Institute (2004).

18. Schafer, B. W., Peköz, T. (1998). Direct strength prediction of cold-formed steel members using numerical elastic buckling solutions. In *Proceedings of the 14th International Specialty Conference on Cold-Formed Steel Structures*. (pp 69–76) University of Missouri-Rolla.

19. Schafer, B. W. (2002). Local, distortional, and Euler buckling of thin-walled columns. *Journal of Structural Engineering, 128*(3), 289–299.

Experimental Investigation on Crack-Arresting Mechanism of Steel Fibre-Reinforced Concrete Prism Specimens Using DIC and AE Techniques

Chandrashekhar Lakavath, Aniket Bhosale, and S Suriya Prakash

1 Introduction

Steel fibres play an important role in improving the ductility of the concrete matrix which results in changing brittle failure mode to ductile failure mode. Many researchers [1–8] have observed that the steel fibre-reinforced concrete (SFRC) beams showcase increase in fracture energy with increase in fibre dosage. In addition to this, it is important to understand the crack-arresting mechanism in SFRC beams at different stages. Hence, to understand this behaviour, both digital image correlation (DIC) technique and acoustic emission (AE) technique are used. Surface strain quantities and crack propagation depths at different CMOD points were investigated using DIC. On the other hand, using the AE technique, internal crack formation mechanisms, such as concrete matrix rupture and fibre pull-out, were studied. The mechanism of each fracture point was classified based on AE parameters.

DIC is a non-contact full-field displacement measurement technique, which can be used to monitor the local surface displacement of the test specimen. In this technique, three basic stages need to be followed which are (i) pre-processing in which the specimen preparation and capturing of images were performed, (ii) correlation of images, which includes the analysis of all captured images by VIC-2D™ package and (iii) post-processing stage includes the extraction of strains, displacement and other

C. Lakavath · A. Bhosale (✉) · S. S. Prakash
Civil Engineering Department, Indian Institute of Technology Hyderabad (IITH), Hyderabad, Telangana 502285, India
e-mail: ce16mtech11027@iith.ac.in

C. Lakavath
e-mail: ce19resch11007@iith.ac.in

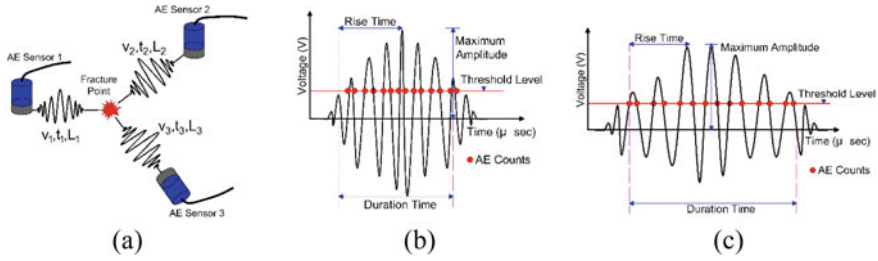S. S. Prakash
e-mail: suriyap@iith.ac.in

Fig. 1 3D damage source location in beams: **a** working principle of three sensors for identification of damage location; **b** tension crack identification; **c** shear crack identification

required data from analysed images. Acoustic emission (AE) is a widely used technique to monitor structural health performance. It works based on the phenomenon of detection of elastic waves in solids that occur when a material undergoes irreversible changes in its structure. In this experimental investigation, three wideband sensors of range 100–1000 kHz and three narrowband sensors of range 50–300 kHz were used for monitoring the damage in notched specimens. The 3D location of the fracture point is obtained based on the time difference in signals and respective velocities captured by sensors. In the AE system, an event generated once the same hit was captured by at least three sensors and it is identified as the source location.

Based on previous studies carried by Ohno [9, 10], the cracks were classified using elastic wave parameters such as duration, frequency, amplitude and rise time. The tensile fracture mode is having high frequency, low duration elastic waves and high amplitude. Whereas, the shear failure mode can be identified by its low frequency, high duration elastic waves and low amplitude as detailed in Fig. 1b, c.

Earlier studies [3, 6] have shown consistent results in locating the fracture process zone reinforced concrete prism specimens and quantifying AE energies. In this experimental study, a 3D source location was identified for the various damage mechanisms in the fracture process zone at different damage stages.

2 Research Significance

As a secondary reinforcement in the concrete matrix, the discrete hooked-end steel fibres were added. Due to which the variation in fracture energy, strain redistribution and crack propagation variations were investigated.

1. Variation in fracture energy with the addition of different volume fraction (V_f) of hooked-end steel fibres.
2. Role of steel fibres in strain redistribution and crack propagation across the depth of notched beams using DIC technique.
3. Identification of three-dimensional fracture location using AE sensors, which helps in indicating fracture points in FPZ.

3   Experimental Programme

The steel fibres of volume fraction (V_f) (0.0, 0.5, 0.75 and 1.0%) are the variables and other parameters such as concrete strength, dimensions of specimen, initial crack length and loading conditions were kept constant. The mix design details used in this experimental test programme is shown in Table 1. The hooked-end steel fibres of aspect ratio 50 were used in this test programme and other properties of the steel fibres are enlisted in Table 2.

3.1   Raw Materials

Concrete The concrete of compressive strength 60 MPa was prepared as per IS10262-2009 [11] used in this experimental programme. The details of concrete mix proportions of 60 MPa grade concrete is presented in Table 1. In the same concrete matrix, steel fibres with different volume fractions were added for steel fiber reinforced concrete mix.

Steel fibres To improve the post-peak response in plain concrete, hooked-end steel fibres were added to the concrete matrix. Based on the previous research [12–14], steel fibre was selected. The steel fibres of modulus of elasticity of 200 GPa with a diameter of 0.6 mm and length of 30 mm were used in Table 2.

Table 1   Mix design proportions of ingredients (kg/m³)

Ingredient	Cement	Fine aggregate	Coarse aggregate	Water	Steel fibres (0, 0.5, 0.75 and 1.0%)
Proportion	320	668	1062	144	0, 39.25, 58.875, 78.5

Table 2   Properties of fibres

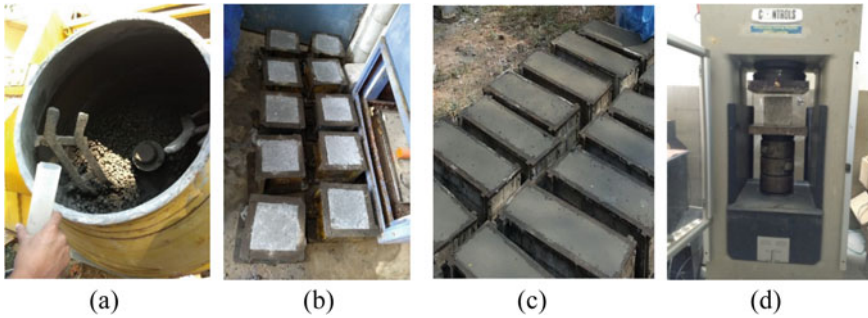| Specifications	Properties	Hooked-end fibre
Fibre type	Hooked-end steel	
Tensile strength (MPa)	1000	
Modulus of elasticity (GPa)	200	
Specific gravity	7.85	
Length (mm)	30	
Diameter (mm)	0.6	
Aspect ratio	50	
Density (kg/m³)	7850	

Fig. 2 Specimen preparation sequence: **a** mixing using drum-type mixture, **b** cubes after 24 h. of concreting, **c** prism specimens, **d** testing cube using compression testing machine

3.2 Casting and Testing Procedure

All raw materials were mixed by using drum-type mixture and steel fibres were spread by hand in the mixing process. The sequence of specimen preparation is depicted in Fig. 1. The concrete beams of size 150 mm × 150 mm × 500 mm were cast for each dosage in the same batch. Similarly, the concrete cubes were cast to examine the 28-day compressive strength of concrete.

The prism specimens were prepared as per EN14651-2005 [15] with a notch of 25 mm depth and 5 mm width at the middle of specimen perpendicular to the face of casting direction [16, 17]. The specimens were tested with a rate of 0.05 mm/min opening of CMOD by using a servo-controlled flexure testing machine as shown in Fig. 2. To evaluate the response of prism specimens, one LVDT at mid-span, CMOD gauge and CTOD gauge at notch location was used.

4 Experimental Results and Discussions

4.1 Compressive Strength of Concrete

In each mix, three numbers of cubes of size 150 mm × 150 mm × 150 mm were tested at a rate of 4120 N/s using compression testing machine as per IS456-2000 [18]. From test results, it is observed that there is not much improvement in compressive strength, the improvement in compressive strength is from 61.63 to 65.36 MPa (Table 3).

**Table 3** Concrete cubes of compressive strength (MPa)

Steel fibre dosage (V_f)	Compressive strength (MPa)	Standard deviation (MPa)
0.00% (Control)	61.63	1.97
0.50%	65.66	0.40
0.75%	63.09	1.83
1.00%	65.36	0.47

4.2 Residual Flexural Strength by RILEM Code and Fracture Energy by JCI Code

The test configuration of a Mode-I fracture test is shown in Fig. 3a. The response of load-CMOD curves represents that as increase in fibre volume fraction the ductility of fibres was increased (Fig. 3b). From this load-CMOD curves of Mode-I fracture test, the residual flexural tensile strengths ($f_{R,1}$, $f_{R,2}$, $f_{R,3}$ and $f_{R,4}$) are calculated based on RILEM [19] recommendations. The residual flexural strength calculated by Eq. (1) at 0.5 mm, 1.5 mm, 2.5 mm and 3.5 mm CMODs, respectively, to evaluate the fracture response through serviceability limit to the ultimate limit.

$$f_{R,i} = \frac{3F_{R,i}L}{2b'h_{sp}^2}(MPa) \tag{1}$$

As per Japanese concrete institute standards [16, 17], the fracture energy (G_F) of control beams (SF00) and steel fibre-reinforced concrete (SFRC) beams was calculated using Eqs. (2), (3) to evaluate and compare the effect of fibre addition on the fracture behaviour.

(a)   (b)
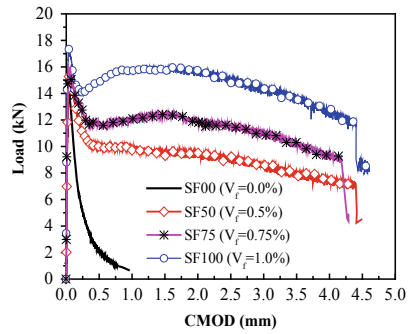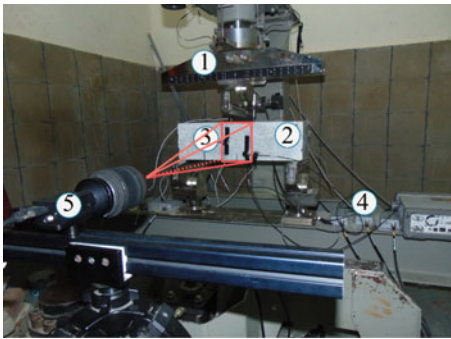
1. Loading Jig, 2. The notched specimen, 3. AE sensors, 4. Preamplifier, 5. DIC camera

Fig. 3 Fracture test of SFRC beams: **a** test set-up for Mode-I test, **b** load-CMOD response. 1 Loading Jig, 2 the notched specimen, 3 AE sensors, 4 preamplifier, 5 DIC camera

Table 4 Residual flexural SFRC prisms specimens

Beam ID	Residual flexural tensile strength (MPa)				Fracture energy (G_f) (N/mm)	Increment in fracture energy
	f_{R1} (CMOD = 0.5 mm)	f_{R2} (CMOD = 1.5 mm)	f_{R3} (CMOD = 2.5 mm)	f_{R4} (CMOD = 3.5 mm)	G_f ($\times 10^{-3}$)	$\Delta G_f = G_f/G_{fc}$
SF00	0.69	0.00	0.00	0.00	156.60	1.00
SF50	2.89	2.74	2.67	2.35	1656.8	10.58
SF75	3.36	3.57	3.34	2.97	1983.7	12.66
SF100	4.27	4.58	4.35	3.99	2697.9	17.23

$$G_F = \frac{0.75 W_0 + W_1}{A_{\text{lig}}} \tag{2}$$

$$W_1 = 0.75 \left(\frac{S}{L} m_1 + 2m_2 \right) g.\text{CMOD}_c \tag{3}$$

Fracture test results reveal that the fracture energy of steel fibre-reinforced concrete is improved to 10.6, 11.78 and 17.2 times in relation to control beams (SF00) for SF50, SF75 and SF100 beams (Table 4) [20]. The improvement in fracture energy is due to the steel fibres bridging action across the cracked plane. It has been observed at all the stages that the residual flexural strengths increased significantly as the V_f was increased. This improvement in residual strengths was more significant just after cracking resulting in improved stiffness of the beams.

From the load-CMOD response of SFRC notched beams, the improvement in post-cracking load distribution was increased. This is due to the steel fibres bridging action against the crack opening. The same mechanism was confirmed by observing the surface of tested specimens. It was observed that the few fibres along the depth of the beams were pulled out with some of the fibres hook ends were flattened; this confirms the perfect bond between the concrete and fibre, which leads to stress transformation. Due to this, the improvement in ductility is observed in steel fibre-reinforced concrete beams. As the volume fraction increases, the number of fibres along the depth of the beam was increased. Hence, the improvement in ductility is more in case of a higher dosage of fibres.

4.3 Monitoring of Crack-Arresting Mechanism by Using DIC Technique

In the pre-possessing stage, all the test prism specimens are painted using acrylic-based white paint for having good correlation over the speckled area. The equal

intensity of light on the test zone was ensured throughout the test to retain uniform illumination of the surface. Prior to the test starts, a calibration image (with scale) and a reference image (un-deformed shape) were captured. Digital images were captured at equal intervals throughout the test to capture deformed shapes. In post-processing, DIC works by pattern matching principle where the speckle patterns of the un-deformed and deformed images were correlated to obtain the corresponding displacement and strains. The subset size directly determines the area of the subset from the reference image to track in the target image. During analysis, the subset size of 35 × 35 pixels was used for correlation [3, 21–23].

To understand the crack-arresting mechanism of notched SFRC specimens, several CMOD points were considered throughout the test such as 0.5, 1.5, 2.5 and 3.5 mm. The surface strain redistribution across the crack was observed in SF75 and SF100 as shown in Fig. 4. As a result of more number of fibres bridging the crack, the strain localisation zone at 3.5 mm CMOD, which was observed at the tip of the crack in SF00 and SF50, was found to have distributed over the depth of beam in SF75 and SF100. This strain redistribution leads to absorb more energy and results
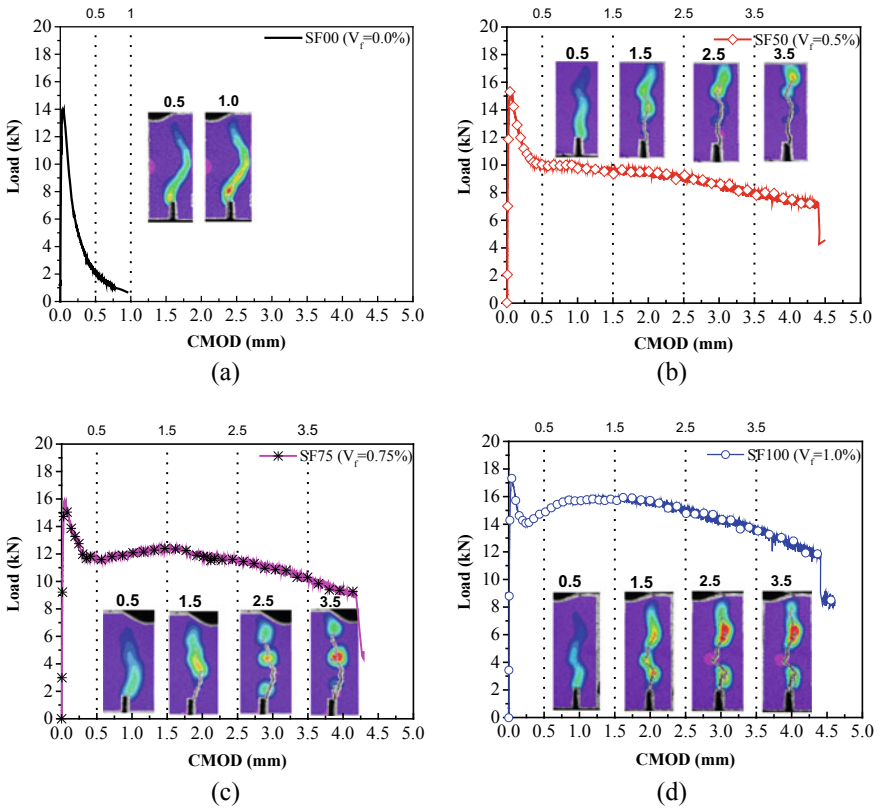

Fig. 4 Load versus CMOD of notched beams: **a** SF00, **b** SF50, **c** SF75, **d** SF100 specimen

Table 5 Crack length of steel fibre-reinforced notched beams at different CMOD points

Beam ID/CMOD	Crack length (mm)				
	0.2	0.5	1.5	2.5	3.5
SF00	56.9	87.7	96.85 (CMOD = 1 mm)	–	–
SF50	48.6	81.0	102.04	102.04	102.04
SF75	31.9	80.0	99.70	103.20	108
SF100	10.56	64.28	108.44	112.24	115.14

in efficient use of the cross section. The crack propagation path was also observed to be meandering as the fibre dosage was increased. It may be because of more fibres affecting the weak link path as shown in Fig. 4. Due to which the crack length at respective CMOD values were varied and same is presented in Table 5.

4.4 Monitoring of Crack Propagation Mechanism by Using Acoustic Emission Technique

A total of six acoustic emission sensors were attached on the specimen at the same coordinates of the beam as shown in Fig. 5. The sensors configuration was fixed to improve the accuracy of crack detection. Also, the proposed sensor configuration is required if the AE results are to be subjected to Simplified Green's functions for Moment Tensor Analysis (SiGMA).

Based on the distance between the sensors, the loss in the amplitude and scattering in capturing of signals was recorded. After conducting trial tests, the amplitude threshold was set to 40 dB to ignore the effect of environmental/electronic noise. In AE system, the preamplifier amplitude gain was set as 40 dB. Before the actual test starts, each AE sensor was calibrated by standard pencil lead test to ensure sensors
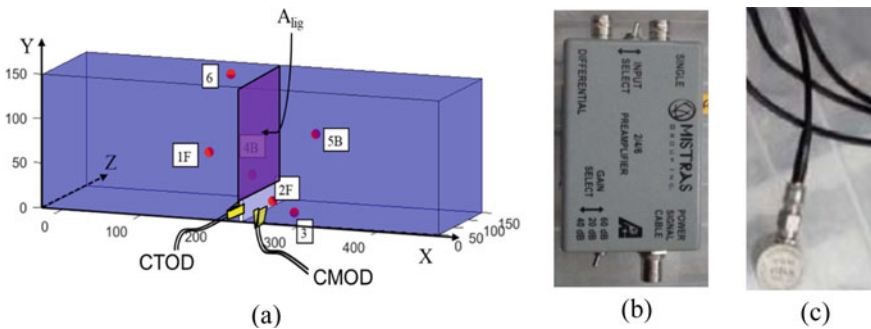

Fig. 5 Notched beam with AE sensors location: **a** position of AE sensors, **b** preamplifier, **c** AE sensor

attachment to the specimen surface. In this study, AE data acquisition (DAQ) system with eight channels was used for recording the signals at rate of 5 MHz.

As expected in fracture test, most of the fracture events captured by AE sensors were in tension mode. Since the test set-up (three-point bending) configuration causes the matrix to undergo Mode-I fracture. In case of control beams (SF00) at CMOD of 0.5 mm, the events were effectively distributed up to 100 mm height from the bottom-most fibre of the beam as shown in Fig. 6. The number of tension events was comparatively much higher than the number of shear events. The distribution of tension and shear events up to CMOD of 1 mm, as presented in Fig. 6b, represents the fracture process zone length.

In the case of 0.5% volume fraction (SF50) beams at CMOD of 0.5 mm, the AE activities clearly show the fracture process zone and nature of crack propagation. Inner progressive damage was fairly captured by AE sensors and surface crack propagation as well as strain redistribution was monitored by DIC. Figure 7a–d represents the detailed 3D locations of all the tension and shear events. As CMOD value was increased, the shift in FPZ was clearly showcased by the AE activities. The crack length is varying from 81 to 102 mm for CMOD of 0.5–3.5 mm.

Similarly, in the case of SF75 and SF100 specimens, the number of events increased with increase in respective CMOD values (Fig. 8 and Fig. 9). And, it was noticed that with an increase in fibre dosage, number of shear events also increased significantly. This may be due to the pull-out of steel fibres during the crack propagation. To understand the clear crack propagation mechanism in FPZ of SFRC specimens, further study is needed and a number of investigation points in load-CMOD curve have to be considered.

The width of FPZ is almost the same irrespective of fibre volume fraction; the 90% of events lie in the range of 160 mm along the length of the specimen as shown in Fig. 6 and Fig. 7. On contrary, the range of FPZ length along the crack propagation direction varies as fibre dosage was increased [3]. Since AE events depend on the number of fibres as well as the type of fibres added to the concrete matrix. To understand the effect of fibre volume fraction and types of fibres in FPZ, further study needs to be carried by using DIC and AE techniques.

5 Conclusions

To understand the influence of hooked-end steel fibres on crack propagation and fracture energy of the concrete matrix, notched beams and cube specimens were tested. The variable in this study is fibre volume fraction such as 0.0, 0.5, 0.75 and 1.0%. All experimental test specimens were monitored using acoustic emission (AE) and digital image correlation (DIC) techniques. From this test series, the following conclusions were observed,

1. With the addition of hooked-end steel fibres from 0.0 to 1.0% of volume fraction, there is not much improvement in compressive strength.

Fig. 6 Acoustic emission hits location and strain in longitudinal direction of SF00 beam: **a** events up to CMOD to CMOD of 0.5 mm, **b** strain at 0.5 mm of CMOD, **c** events up to CMOD of 1.0 mm, **d** strain at 1.0 mm of CMOD, **e** strain in *x*-direction

Fig. 7 Acoustic emission hits location and strain in longitudinal direction of SF50 beam: **a** events up to CMOD of 0.5 mm, **b** strain at 0.5 mm of CMOD, **c** events up to CMOD of 1.5 mm, **d** strain at 1.5 mm of CMOD, **e** events up to CMOD of 0.5 mm of CMOD, **f** strain at 0.5 mm of CMOD, **g** events up to CMOD of 0.5 mm, **h** strain at 0.5 mm of CMOD, **i** strain in x-direction

Fig. 8 Acoustic emission hits location and strain in longitudinal direction of SF75 beam: **a** events up to CMOD of 0.5 mm, **b** strain at 0.5 mm of CMOD, **c** events up to CMOD of 1.5 mm, **d** strain at 1.5 mm of CMOD, **e** events up to CMOD of 0.5 mm of CMOD, **f** strain at 0.5 mm of CMOD, **g** events up to CMOD of 0.5 mm, **h** strain at 0.5 mm of CMOD, **i** strain in x-direction
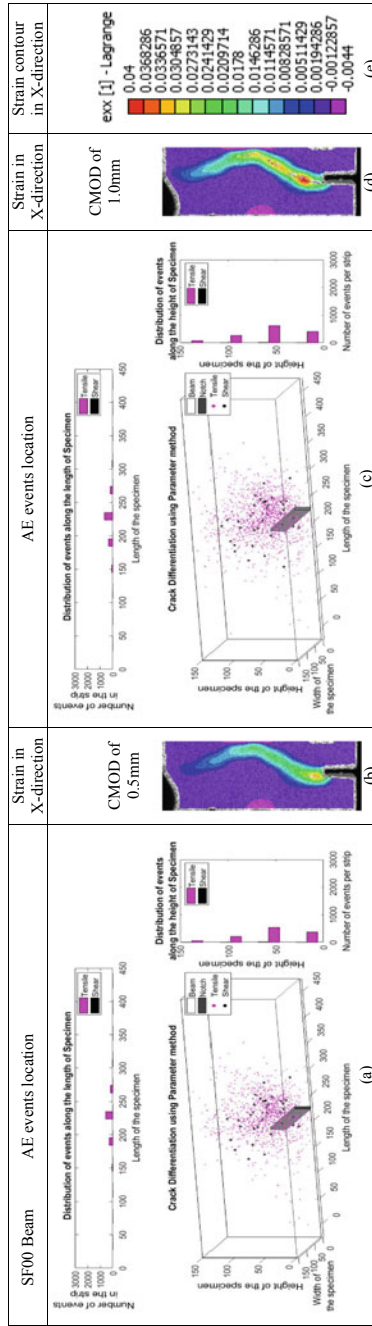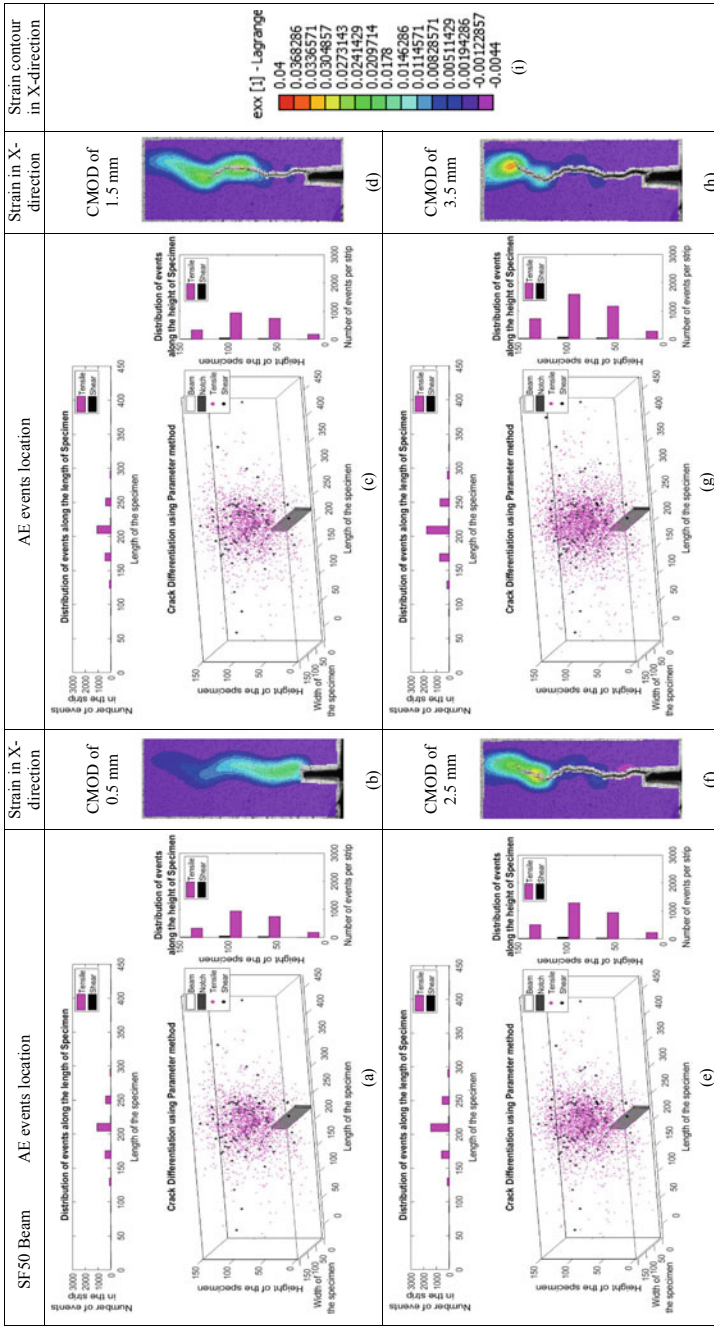
Fig. 9 Acoustic emission hits location and strain in longitudinal direction of SF100 beam: **a** events up to CMOD of 0.5 mm, **b** strain at 0.5 mm of CMOD, **c** events up to CMOD of 1.5 mm, **d** strain at 1.5 mm of CMOD, **e** events up to CMOD of 0.5 mm, **f** strain at 0.5 mm of CMOD, **g** events up to CMOD of 0.5 mm, **h** strain at 0.5 mm of CMOD, **i** strain in x-direction
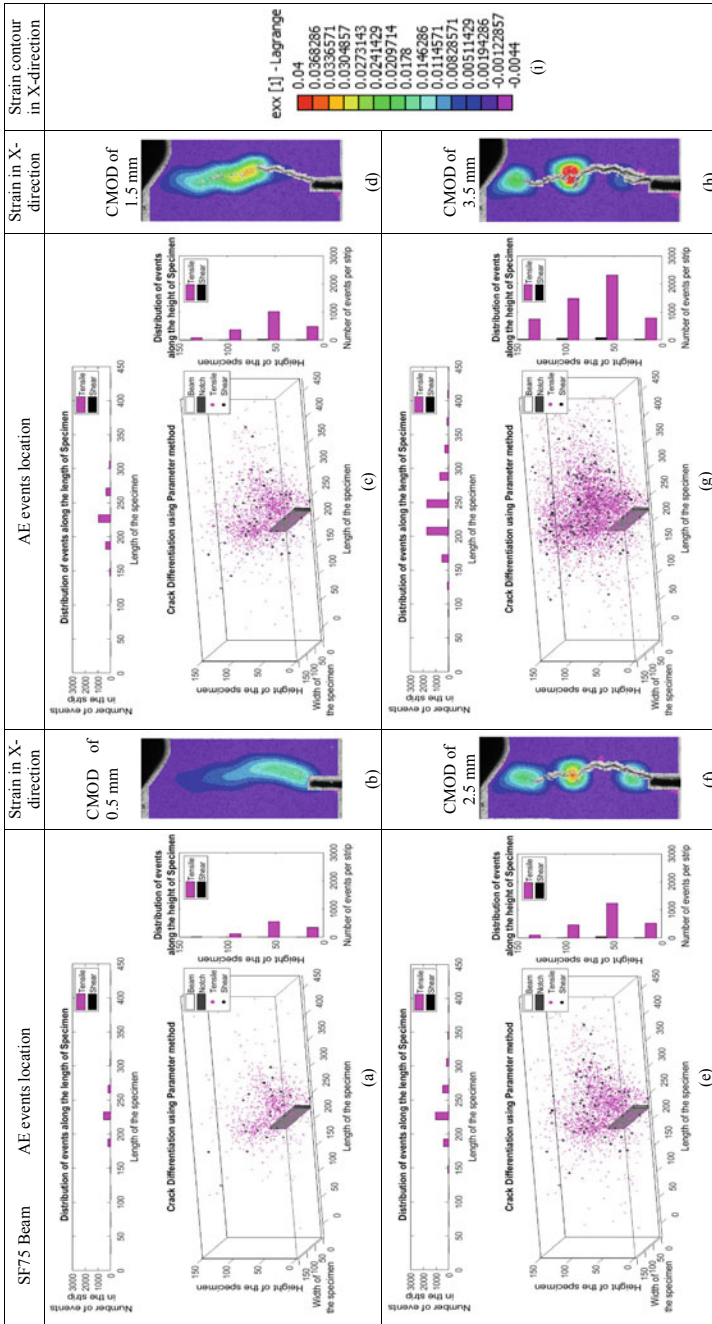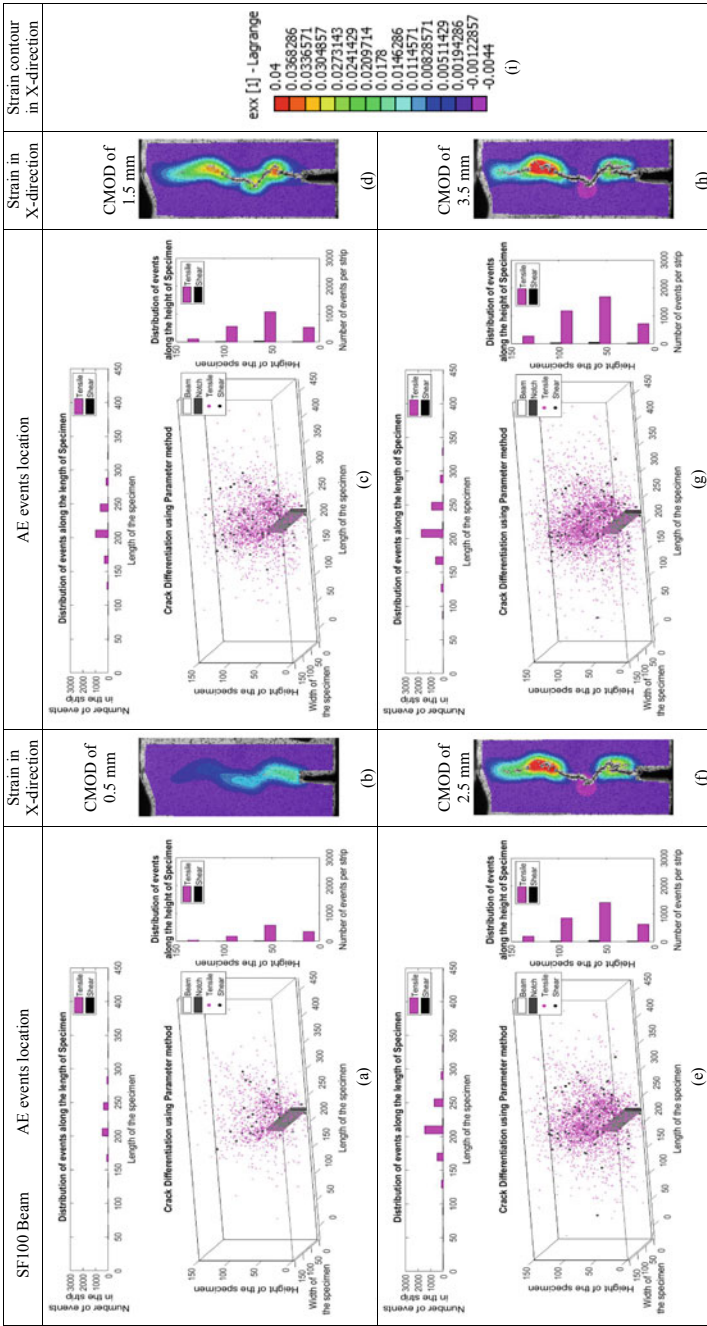
2. The three-point bending test reveals that the fracture energy is changing from 156.6×10^{-3} (N/mm) to 2697.9×10^{-3} (N/mm), i.e. energy absorption amount was increased to 17 times with the addition of fibres from 0.0 to 1.0% of volume fraction.
3. DIC investigation illustrates that the surface strain redistribution increased in the fracture process zone due to fibre bridging action, resulting in reduced crack length as well as crack width with an increase in fibre volume fraction.
4. The number of AE events increased with an increase in fibre dosage from 0.0 to 1.0%, which indicates a rise in the fibre pull-out activities in the fracture process zone.

References

1. Banthia, N., & Gupta, R. (2004). Hybrid fibre reinforced concrete (HyFRC): Fibre synergy in high strength matrices. *Materials and Structures, 37*(10), 707–716.
2. Majdzadeh, F., Soleimani, S. M., & Banthia, N. (2006). Shear strength of reinforced concrete beams with a fibre concrete matrix. *Canadian Journal of Civil Engineering, 33*(6), 726–734.
3. Bhosale, A., Rasheed, M. A., Prakash, S. S., & Raju, G. (2019). A study on the efficiency of steel vs. synthetic vs. hybrid fibres on fracture behavior of concrete in flexure using acoustic emission. *Construction and Building Materials, 199,* 256–268.
4. Das, S., Aguayo, M., Sant, G., Mobasher, B., & Neithalath, N. (2015). Fracture process zone and tensile behavior of blended binders containing limestone powder. *Cement and Concrete Research, 73,* 51–62.
5. Das, S., Aguayo, M., Dey, V., Kachala, R., Mobasher, B., Sant, G., et al. (2014). The fracture response of blended formulations containing limestone powder: Evaluations using two-parameter fracture model and digital image correlation. *Cement & Concrete Composites, 53,* 316–326.
6. Rasheed, M. A., Prakash, S. S., Raju, G., & Kawasaki, Y. (2018). Fracture studies on synthetic fibre reinforced cellular concrete using acoustic emission technique. *Construction and Building Materials, 169,* 100–112.
7. Lakavath, C., Pidapa, V., & Joshi, S. S. (2018). Shear behavior of steel fibre reinforced precast prestressed concrete beams. In *International Conference on Composite Materials and Structures*.
8. Lakavath, C., Allam, R., & Kondraivendhan, B. (2019). Experimental and numerical studies on the behaviour of broad-gauge railway sleepers in static bending condition. In *Sustainable construction and building materials* (pp. 781–792). Singapore: Springer.
9. Ohno, K., & Ohtsu, M. (2010). Crack classification in concrete based on acoustic emission. *Construction and Building Materials, 24*(12), 2339–2346.
10. Ohno, K., Shimozono, S., Sawada, Y., & Ohtsu, M. (2008). Mechanisms of diagonal-shear failure in reinforced concrete beams analyzed by AE-SiGMA. *Journal of Solid Mechanics and Materials Engineering, 2*(4), 462–472.
11. Indian standard concrete mix proportioning - Guidelines (First revision) IS 10262:2009, Bureau of India Standard, New Delhi, India.

12. Joo Kim, D., Naaman, A. E., & El-Tawil, S. (2008). Comparative flexural behavior of four fibre reinforced cementitious composites. *Cement & Concrete Composites, 30*(10), 917–928.
13. Lee, S. C., Oh, J. H., & Cho, J. Y. (2015). Compressive behavior of fibre-reinforced concrete with end-hooked steel fibres. *Materials, 8*(4), 1442–1458.
14. Hsu, L. S., & Hsu, C. T. (1994). Stress-strain behavior of steel-fibre high-strength concrete under compression. *Structural Journal, 91*(4), 448–457.
15. En, B. (2007). *14651, "Test method for metallic fibre concrete—Measuring the flexural tensile strength (Limit of proportionality (LOP), residual)*. London, UK: British Standards Institution.
16. JCI-S-002-2003. Method of test for load-displacement curve of fibre reinforced concrete by use of notched beam. 2003; (L):3–8.
17. JCI-S-001-2003. Method of test for fracture energy of concrete by use of notched beam. 2003; 2(2):1–14.
18. BIS: 456-2000 R 2005. Plain and reinforced concrete. Bur Indian Stand Dehli. 2005.
19. Vandewalle, L., Nemegeer, D., Balazs, L., Barr, B., Barros, J., Bartos, P., & Falkner, H. (2003). RILEM TC 162-TDF: Test and design methods for steel fibre reinforced concrete'-sigma-epsilon-design method-final recommendation. *Materials and Structures, 36*(262), 560–567.
20. Lakavath, C., Joshi, S. S., & Prakash, S. S. (2019). Investigation of the effect of steel fibres on the shear crack-opening and crack-slip behavior of prestressed concrete beams using digital image correlation. *Engineering Structures, 193,* 28–42. https://doi.org/10.1016/j.engstruct.2019.05.030.
21. Pan, B., Xie, H., Guo, Z., & Hua, T. (2007). Full-field strain measurement using a two-dimensional Savitzky-Golay digital differentiator in digital image correlation. *Optical Engineering, 46*(3), 033601.
22. Rajan, V. P., Rossol, M. N., & Zok, F. W. (2012). Optimization of digital image correlation for high-resolution strain mapping of ceramic composites. *Experimental Mechanics, 52*(9), 1407–1421.
23. Srikar, G., Anand, G., & Prakash, S. S. (2016). A study on residual compression behavior of structural fibre reinforced concrete exposed to moderate temperature using digital image correlation. *International Journal of Concrete Structures and Materials, 10*(1), 75–85.

Estimation of Fly Ash Reactivity and Dissolution Characteristics

G. V. P. Bhagath Singh [ORCID] **and K. V. L. Subramaniam**

1 Introduction

Fly ash is an industrial waste material produced by thermal power plants. In developing countries like India, there is an increasing gap between production and utilization of fly ash. Currently, 184 million tones of fly ash are available, but only 55% is being used for various applications [1]. Fly ash is rich in an aluminio-silicate source, and it is often used in the production of geopolymers and in binary fly ash cement system [2–5]. The alumina and silica in fly ash are present in both amorphous and crystalline phase [6]. Crystalline phases are indicative of the non-reactive portion, and it typically consists of quartz and mullite in predominant quantities [6]. The amorphous phase is representative of the glassy phase. The reactivity of fly ash depends on the glassy phase and release of reactive species into the solution.

Previous research has been shown; calcium and silicon were the first elements to dissolve followed by aluminium in a low alkaline environment [7]. The dissolution of aluminium and silicon was increased in the solution with an alkaline concentration and higher curing temperatures [8]. A study by Li et al. [9] reported that higher the molarity level, curing time and temperatures favour the dissolution of silicon and aluminium from the glassy phase. The lower reactive glassy content fly ashes are typically found in India, and large quantities of silica and alumina are present in crystalline portion [6]. Successful development of fly ash-based geopolymers requires an understanding of the dissolution characteristics of the reactive species from the glassy phase.

G. V. P. Bhagath Singh (✉)
Laboratory of Construction Materials, IMX, EPFL, 1015 Lausanne, Switzerland
e-mail: bhagath.gnagapatnam@epfl.ch

K. V. L. Subramaniam
Department of Civil Engineering, Indian Institute of Technology
Hyderabad (IITH), Hyderabad, Telangana 502285, India
e-mail: kvls@iith.ac.in

The current paper explores the estimation of reactivity and dissolution of silicon, and aluminium elements from low glassy content fly ash at various alkaline environments and at different curing temperatures are evaluated. The link between the dissolution of low reactive glass and releasing of elements into the solution is established.

2 Materials and Methods

Fly ashes used in this study are directly collected from power stations without any prior treatment and labelled as B and D. The chemical composition of fly ashes is listed in Table 1. Both the ashes are classified as siliceous fly ash as per BIS 3812 [10] and as per ASTM C 618 [11]. Due to the very low calcium content, further fly ashes are classified as low calcium siliceous fly ashes.

2.1 Dissolution Experiments

The dissolution mechanism of fly ash was analysed in two different alkaline environments and at two different curing temperatures. Sodium hydroxide (NaOH) was used as an alkaline activator. 1M and 6M NaOH alkaline solution and 25 and 60 °C temperatures were used. The experimental work is as follows: 1 gm of ash was added to 100 ml alkali solution in a 150 ml polypropylene container. Dissolution measurements were carried out at 3, 24 and 48 h. At a particular time, the solution was filtered through a Whatman filter paper. The solution was used for analyses purpose. In all the samples, Si and Al elements were evaluated, as these are the major elements for geopolymerization process as well as for pozzolanic reaction. The glassy content present in fly ashes was determined using two different techniques such as 1% HF acid dissolution [12] and Rietveld-based XRD method [13]. The dissolved elements

Table 1 Chemical composition of fly ashes (wt%)

Composition	Fly ash B	Fly ash D
SiO_2	55.42	55.57
Al_2O_3	27.10	29.01
Fe_2O_3	7.30	5.47
CaO	2.46	1.65
K_2O	2.55	2.12
TiO_2	1.91	2.28
MgO	1.20	0.63
SO_3	0.56	0.66
P_2O_5	0.54	0.78

present in the solution were determined using inductively coupled plasma optical emission spectrometry (ICP-OES).

D2 Phaser (Bruker) benchtop XRD was used to measure the intensity pattern of the samples. The readings were taken from 10° and 70° at a step size of 0.02° and 0.6 step per second, resulting in a total measurement time of 30 min per scan. Corundum was used as an external standard to determine various phases. The total glassy content present in the fly ash is determined by subtracting all the crystalline phases from unity [13]. The reactive Si and Al elemental contents present in the glassy phase were determined by subtracting the crystalline phases from the total Si and Al [9, 12, 13].

3 Results and Discussion

3.1 Identification of Glass Type

The XRD pattern of fly ash D is shown in Fig. 1. A wide hump is identified between 2θ angles equal to 15° and 30° along with various crystalline phases. The hump is the representation of the glassy phase present in fly ash. The crystalline phases primarily consist of quartz and mullite along with other minor phases. The XRD pattern of synthesized low and high calcium aluminosilicate glass is shown in Fig. 1b. By comparing the XRD pattern of fly ash amorphous portion with the synthesized glasses, the glass present in the fly ash is low calcium aluminosilicate glass, and it is centred at a lower 2θ angle approximately 22°.
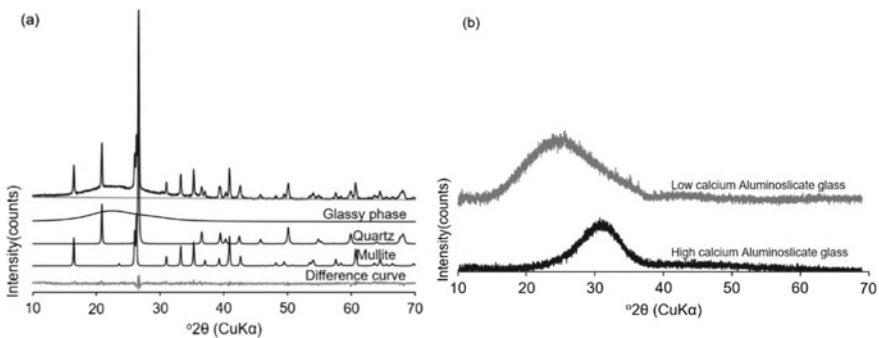

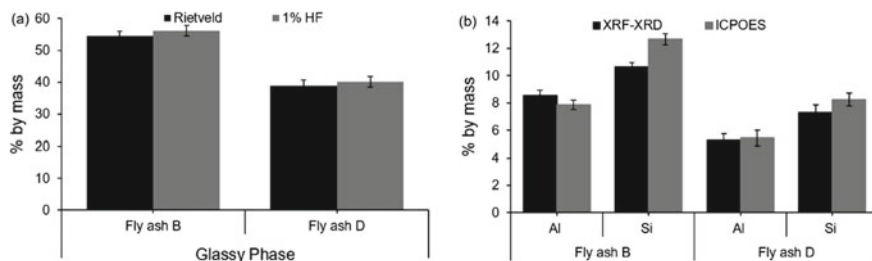Fig. 1 XRD pattern of **a** fly ash D and **b** synthesized glasses

Fig. 2 Comparison of **a** glassy content and **b** reactive Si and Al contents using both the methodologies

3.2 Comparison of Glassy Content and Reactive Species Using Different Methodologies

As shown in Fig. 2, both the methodologies are shown similar in values with a little difference. The glassy content obtained from the Rietveld refinement and elemental contents obtained from XRF-XRD methods are shown as lower values compared to 1% HF treatment method. The difference in the values is due to some of the crystalline phases sensitive to acid treatment, and few particles may be left on top of the filter paper.

3.3 Influence of Molarity and Temperature on Dissolution of Glassy Portion

The change in the XRD pattern of glassy portion in 6M alkaline solution at both the curing temperatures of fly ash B is shown in Fig. 3. It can be seen that the alkaline concentration clearly influences the dissolution process, and it enhanced with the curing temperature. During the dissolution process, crystalline phases remain inert in the system, and glass is completely depleted by 48 h at higher curing temperature.

3.4 Influence of Alkaline Concentration on Dissolution of Elements

The changes in the Si and Al elemental concentration at different molarities cured at 25 °C in both the fly ashes are shown in Fig. 4. Elemental concentration in the solution is increasing with time and molarities. At a given time, the elemental concentration in the solution is high at higher molarity. There is an increase in the elemental concentration from 1M to 6M. This is indicative of higher molarity that favours a more dissolution of the glassy phase. By comparing Fig. 2b, still Si and Al elements need to be dissolved, and it means that the dissolution process is still progressing in the system.
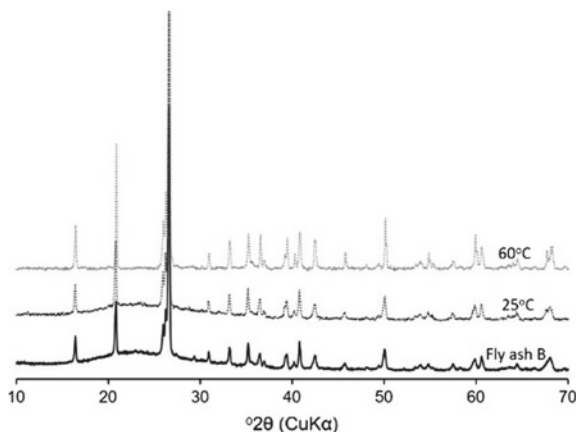
Fig. 3 XRD patterns of dissolved glassy content in 6M alkaline solution at 48 h
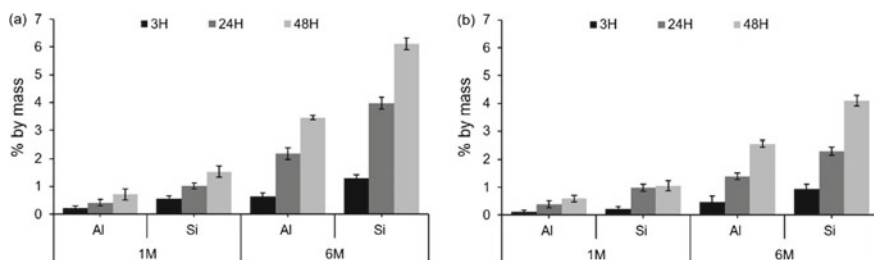
Fig. 4 Dissolved Al and Si elements with time at different molarities. **a** fly ash B and **b** fly ash D
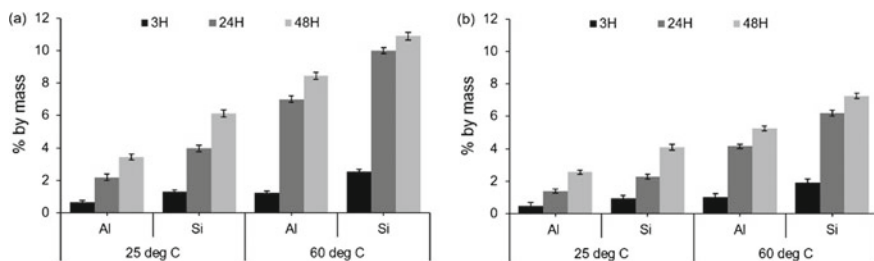
Fig. 5 Dissolved Al and Si elements at two different curing temperatures with time. **a** fly ash B, **b** fly ash D

3.5 Influence of Temperature on Dissolution of Elements

The changes in the elemental proportions in the 6M solutions at 25 and 60 °C for fly ashes B and D are shown in Fig. 5. As per the results, temperature clearly enhances

the elemental quantities in the solution at any particular time. Higher Si and Al elements were dissolved at 60 °C compared to 25 °C within 3 h. Samples cured at 60 °C, significant elemental quantities are observed at 48 h. By comparing Fig. 2b, Si and Al elements are completely dissolved at 60 °C by 48 h.

4   Conclusions

The dissolution behaviour of low glassy content siliceous fly ash system is evaluated. Dissolution process depends on the glassy content present in the fly ash. The experimental work shows that the dissolution of the glassy phase leads to releasing the reactive species into the solution, primarily Si and Al without affecting the crystalline phases. Molarity level and temperature enhance the rate of the dissolution process.

References

1. Central Electricity Authority. (2015). *Annual report on fly-ash utilization*. India.
2. Provis, L., & Van Deventer, J. S. J. (2009). *Geopolymers: Structure, processing, prosperities and industrial applications* (41p). Cambridge, UK: Woodhead Publishing Limited.
3. Davidovits, J. (1999). Geopolymers: Inorganic polymeric new materials. *Journal of Thermal Analysis, 37*(8), 1633–1656.
4. Palomo, A., Grutzeck, M., & Blanco, M. (1999). Alkali-activated fly ashes: A cement for the future. *Cement and Concrete Research, 29*(8), 1323–1329.
5. Bhagath Singh, G. V. P., & Subramaniam, K. V. L. (2014). Activation of siliceous fly ash at very high levels of cement replacement. *Indian Concrete Journal, 88*, 23–32.
6. Bhagath Singh, G. V. P., & Subramaniam, K. V. L. (2018). Characterization of Indian fly ashes using different experimental techniques. *Indian Concrete Journal, 92*, 10–23.
7. Lee, W. K. W., & van Deventer, J. S. J. (2002). Structural reorganization of class F fly ash in alkaline silicate solutions. *Colloids Surfaces A, 211*(1), 49–66.
8. Mikuni, A., Komatsu, R., & Ikeda, K. (2007). Dissolution properties of some fly ash fillers applying to geopolymeric materials in alkali solution. *Journal of Material Science, 42,* 2953–2957.
9. Li, C., Li, Y., Sun, H., & Li, L. (2011). The composition of fly ash glass phase and its dissolution properties applying to geopolymeric materials. *Journal of American Ceramic Society, 94*(6), 1773–1778.
10. BIS (Bureau of Indian Standards). (2003). *Pulverized fuel ash-specification. IS 3812-part 1*. New Delhi: Manak Bhavan.
11. ASTM C 618 Standard. (2015). Specification for fly ash and raw or calcined natural Pozzolan for use as a mineral admixture in Portland cement concrete.
12. Fernandez-Jimenez, A., De la Torre, A. G., Palomo, A., Lopez-Olmo, G., Alonso, M. M., & Aranda, M. A. G. (2006). Quantitative determination of phases in the alkali activation of fly ash. Part I. *Potential Ash Reactivity. Fuel, 85*(5), 625–634.
13. Bhagath Singh, G. V. P., & Subramaniam, K. V. L. (2016). Quantitative XRD analysis of binary blends of siliceous fly ash and hydrated cement. *Journal of Material in Civil Engineering (ASCE), 28*(8), 1–7 (04016042).

Numerical Modelling of Continuous Composite Beam Under Fire Loading

Priya S. Natesh and Anil Agarwal

1 Introduction

Composite beams consist of a steel beam and concrete slab connected through shear studs. The composite beam optimises the material by making use of concrete slab in the compression zone and structural steel beam in the tension zone of the member. A concrete slab can be of flat shape or trapezoidal metal deck in nature. Composite floor systems are gaining popularity in India as the need for rapid construction is increasing. Currently, there is a significant need to understand its behaviour, especially under various critical loading conditions such as earthquake, fire, and impact loading. When a composite beam subjected to fire loading, it leads to very complex behaviour. Usually, during a fire, the members will be subjected to service level gravity load along with the thermal loading associated with fire. The members are said to be healthy if they can resist the structural gravity load and thermal load without any overall collapse. Experimental investigation of structural members subjected to fire loading is very expensive and challenging. Experiments can be accompanied by numerical models to develop a deeper insight into the behaviour of structural members.

Wainman and Kirby [1] studied the functioning of the simply supported composite beam of effective span 4.58 m under fire loading. The specimens consisted of 254 × 146 × 43 UB steel beams that were connected to flat-reinforced concrete slabs using headed shear studs. The width and depth of the slab were 0.642 m and 0.130 m, respectively. 8 mm diameter reinforcement with 200 mm spacing in longitudinal

P. S. Natesh (✉)
Faculty of Science and Technology, ICFAI Foundation for Higher Education (Declared as Deemed to be University u/s 3 of the UGC Act 1956), Hyderabad 501203, India
e-mail: priyas@ifheindia.org

A. Agarwal
Indian Institute of Technology Hyderabad (IITH), Hyderabad, Telangana 502285, India
e-mail: anil@iith.ac.in

direction and 100 mm spacing in transverse direction is used in the concrete slab. Once the plastic moment capacity was reached at elevated temperature, the beam failed in flexure.

Zhao and Kruppa [2] performed an experimental investigation on 4.9 m long composite beam under fire loading. They investigated the effect of varying the concrete slab width and influence of protection for steel beam. IPE300 steel beams were connected to flat concrete slabs using 19 mm diameter headed shear studs. The slab widths considered were 1.20 m, 1.60 m, 0.80 m, and 1.20 m, respectively. Crushing of concrete leads to the failure of protected composite beams and plasticisation of the steel beam leads to the failure of unprotected beams.

Anil et al. [3–6] studied in detail the effect of various parameters including shear tab connection, in the stability of 10-storey office building subjected to a corner compartment fire. Wellman et al. [7] conducted an experimental investigation on the behaviour of lightweight composite floor assemblies subjected to fire loading. Selden et al. [8] investigated fire behaviour of composite beams and associated simple shear beam to column connections. A series of partial composite beams of span 3.65 m were tested. The authors observed that if the beams are overloaded, concrete compression failure is a potential failure mode for composite beams with flat slabs exposed to medium temperature levels. Prediction of behaviour of composite beams during the cooling phase makes it challenging, as the fracture of shear tab connection observed in the cooling period of loading. Fischer et al. [9–11] studied the behaviour of different types of the beam to column connections such as shear tab connection, single angle connection, and double angle connection under fire loading. Composite beams of span 3.81 m with thick lightweight concrete slab was considered for analysis. The authors observed that during the cooling phase of loading, in single angle and double angle connections, prying action develops which permits the contraction of steel beams, thereby avoiding the brittle failure.

Choe et al. [12] performed an experimental investigation on steel-concrete composite beam with double angle connections. The authors considered 12.3 m long-span beams (Test 2 and Test 3) subjected to combined structural and thermal loading. The effect of slab continuity was one of the parameters under consideration. Authors observed that local buckling of steel beam near the connection leads to an increase in tensile force demand in continuity bars of the concrete slab.

This paper presents 3D finite element-based modelling approach of composite beams. The model is validated against the fire tests on composite beams available in the literature, and the parametric study is conducted under various fire scenarios, continuity conditions, and amount of reinforcement provided.

2 Modelling Approach

Commercially available finite element-based computer programme ABAQUS [13] is used for simulating the behaviour of composite beams in fire conditions. The problem

is simplified into a sequentially coupled thermo-mechanical problem. The analysis was conducted in two parts as follows

1. Nonlinear heat transfer analysis performed independently to obtain nodal temperature histories.
2. Dynamic explicit stress analysis by incorporating nodal temperature histories from heat transfer analysis.

2.1 Heat Transfer Modelling

Since the thermal and structural models need to be compatible, the same mesh size is used for both models. The steel beam, concrete slab, insulation materials, rebars, shear studs, profiled steel deck, and connections were modelled using 8-node linear heat transfer elements (DC3D8), and a 3D heat transfer analysis is performed on the entire system. 30 mm mesh size was adopted after performing convergence analysis. The propagation of the heat along the member depends on thermal properties of various materials used such as specific heat, conductivity, and thermal expansion, which are the function of temperature and fire scenario. In all models, the fire scenario is adopted from literature. For heat transfer analysis, a user-defined subroutine developed by Cedeno et al. [14] used for finding the heat flux on various surfaces of the model. This subroutine integrates the conduction-based heat transfer within the solid elements with convection and radiation heat transfer on the surface.

2.2 Stress Analysis Modelling

3D structural modelling developed and 8-node linear brick elements with reduced integration and hourglass control (C3D8R) were used for the modelling the assembly. The coupled analysis conducted in two steps in ABAQUS. In the first step, the model loaded with gravity load, and in the second step, thermal loading is assigned to it. Time versus temperature response of each node obtained from the heat transfer analysis is incorporated in the second step as the thermal load. The predefined field option under loading module in ABAQUS was used for this purpose. Dynamic explicit analysis procedure chosen for second steps as the analysis is of time-dependent process and its ability to effectively handle severely nonlinear behaviour. Contact between surfaces such as steel-concrete, and connection-beam was modelled by using penalty contact with the coefficient of friction as 0.6 [15]. Shear stud—steel beam connection was developed by defining tie between the bottom of the stud and steel beam and connection between concrete and shear stud is developed by defining embedded constraint. Reinforcement bars and welded wire mesh were embedded in concrete. Welded connections of the angle with column were represented by giving
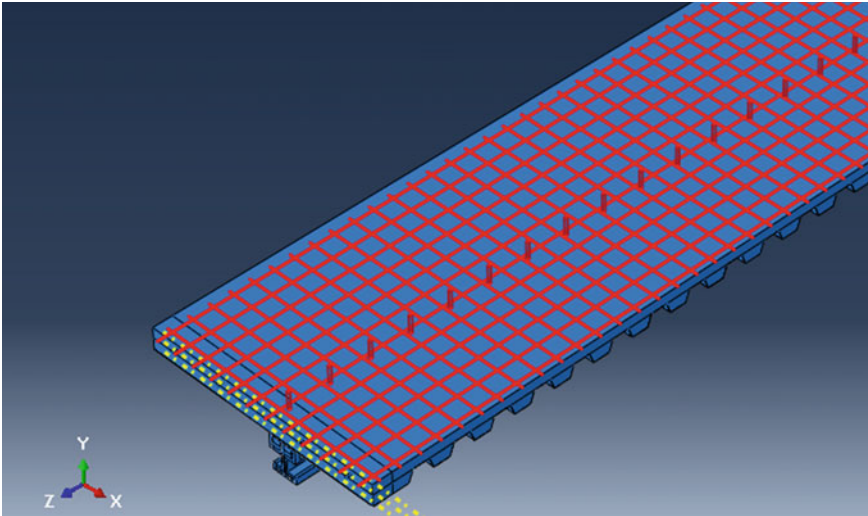
Fig. 1 Isometric view of the model (Choe_3)

displacement boundary conditions. Isometric view of the modelling the literature Choe et al. [12] with shear studs and wire mesh highlighted is shown in Fig. 1.

2.3 Material Properties

As the beam subjected to combined structural and thermal loading, temperature-dependent mechanical and thermal properties are adopted from Eurocode [16, 17]. Eurocode sketches various mechanical and thermal property models for structural steel, normal weight concrete, and lightweight concrete. For thermal property assignments, such as conductivity, specific heat, and thermal expansion the relationships defined by Eurocode were taken directly.

Steel For defining strength, stress-strain relationship and elasticity from Eurocode have been adopted. For both steel and concrete models, temperature-dependent strength reduction factors from the code taken care of reduction in strength at elevated temperature. From the published experimental works, the yield strength of steel taken as the inputs for Eurocode distinct relationships for mechanical properties. Ductile-damage model under plastic property, with damage strain 0.2 has been used for simulating damage in steel. Figures 2, 3, 4, and 5 show the typical Eurocode stress-strain curve for steel with yield strength 350 MPa, thermal conductivity, thermal expansion, and specific heat of steel as a function of temperature.

Concrete Figures 6, 7, 8, and 9 show the typical Eurocode stress-strain curve for concrete with characteristic compressive strength of 28 MPa, thermal conductivity,
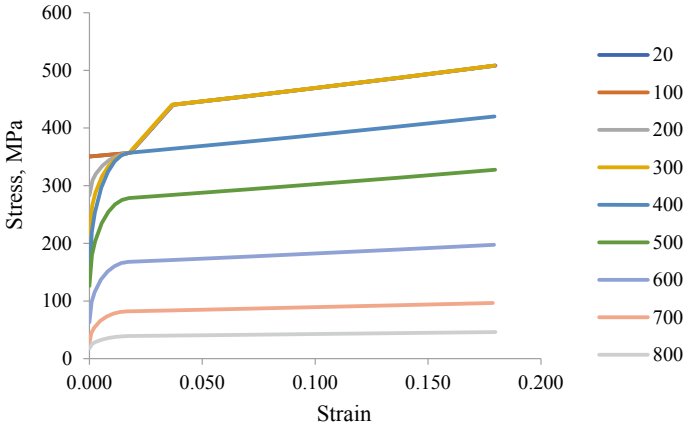
Fig. 2 Typical Eurocode stress-strain curve for steel with yield strength 350 MPa as a function of temperature
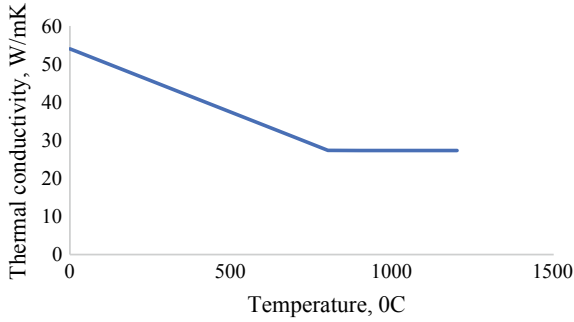
Fig. 3 Thermal conductivity of steel as a function of temperature
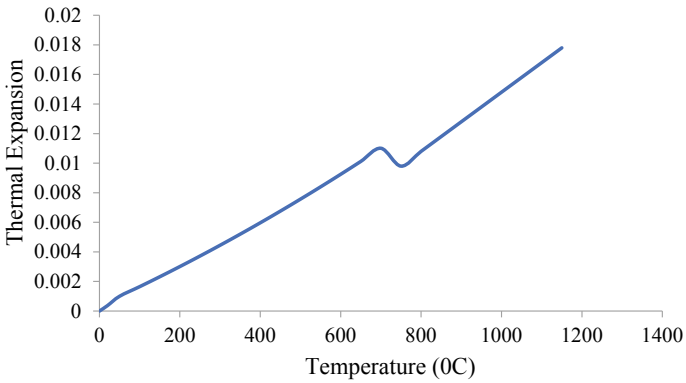
Fig. 4 Thermal expansion of steel as a function of temperature
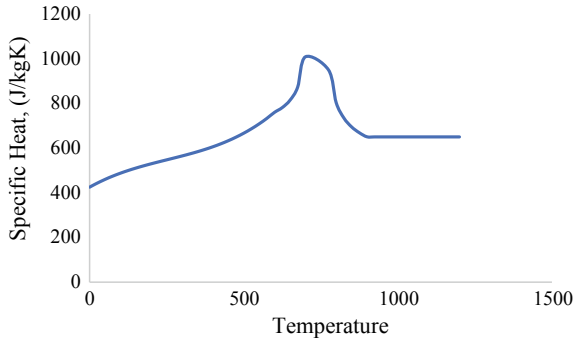
Fig. 5 Specific heat of steel as a function of temperature
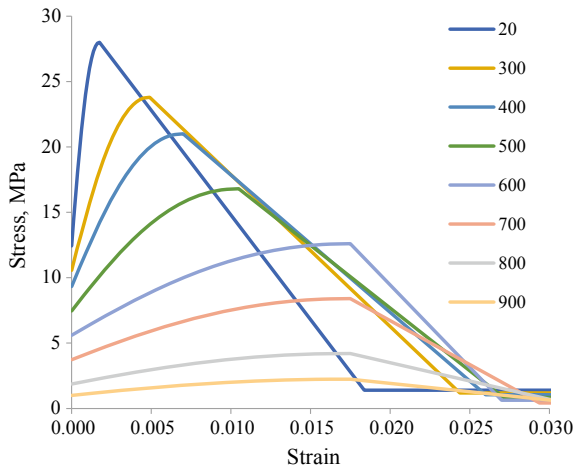
Fig. 6 Typical Eurocode stress-strain curve for concrete with characteristic compressive strength 28 MPa

thermal expansion, and specific heat as a function of temperature. Drucker–Prager plasticity model was used for simulating damage in concrete. Characteristic compressive strength of concrete for various models was taken from experimental data provided in the literature. Eurocode suggests upper and lower limits for thermal conductivity of concrete, as shown in Fig. 3b. For modelling purpose, the lower limits were adopted as it was showing better agreement with experimental results. Specific heat of concrete with 3% moisture content adopted for modelling purpose as shown in Fig. 3c.
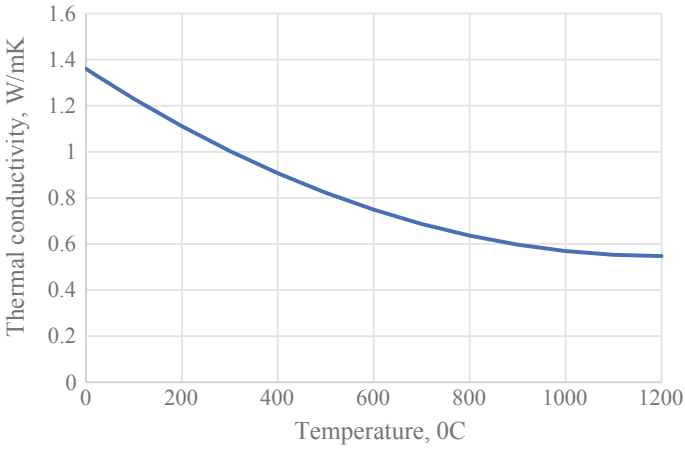
Fig. 7 Thermal conductivity of concrete as a function of temperature
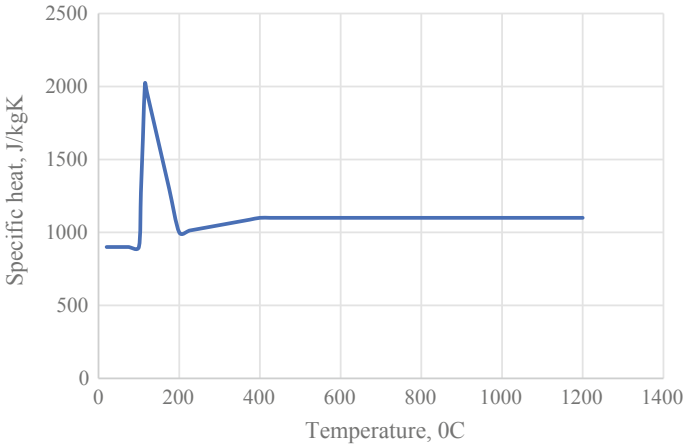
Fig. 8 Specific heat of steel as a function of temperature

3   Benchmarking of the Analysis Procedure

Both heat transfer and structural are benchmarked with experimental data available in the literature. Tests conducted by Wainman and Kirby [1], Zhao and Kruppa [2], and Choe [12] simulated the model parameters are calibrated accordingly.
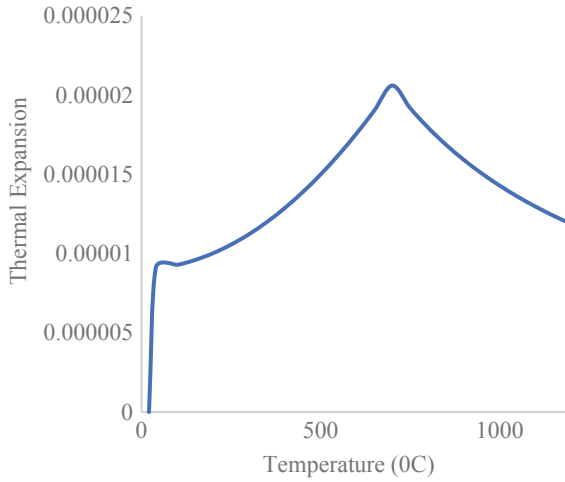
Fig. 9 Thermal expansion of concrete as a function of temperature

3.1 Wainman and Kirby [1]

Test 15 from Wainman and Kirby [1] has been taken and modelled in ABAQUS. Test 15 is a composite beam with a bare steel beam and flat concrete slab. Figure 10 shows the isometric view of model in ABAQUS. Furnace temperature reported by Wainman
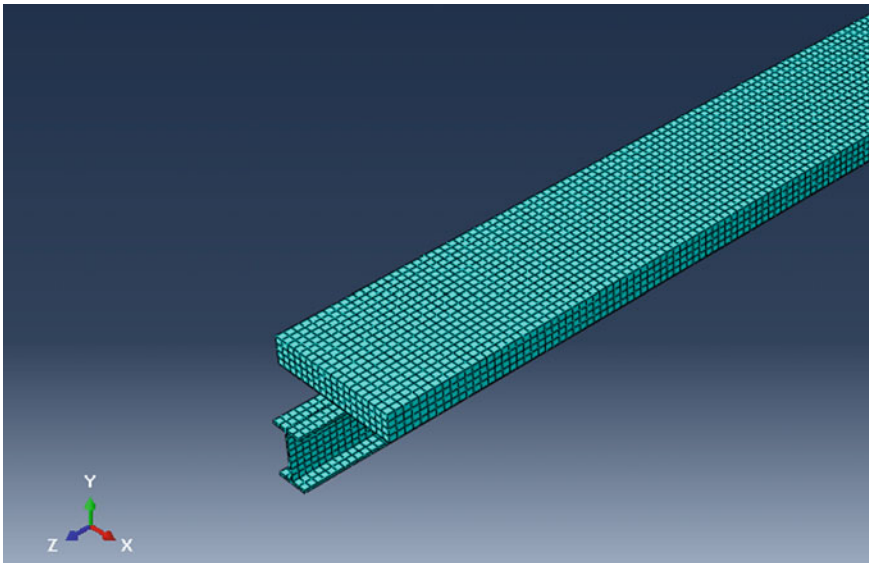
Fig. 10 Isometric view of the model (Wainman Test Specimen 15)

Fig. 11 Comparison of steel bottom flange temperature (Wainman Test 15)
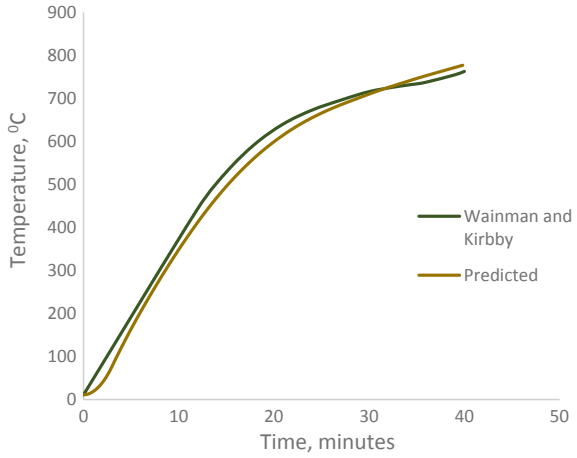
Fig. 12 Comparison of midspan deflection (Wainman Test 15)
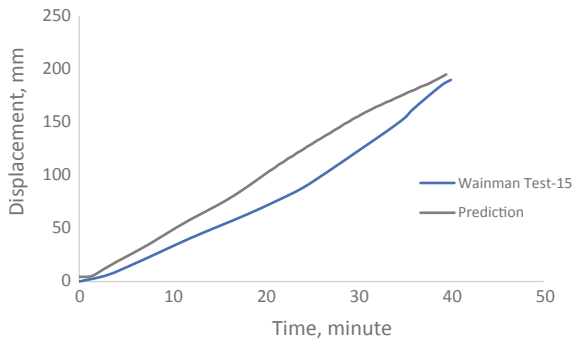
and Kirby [1] has been incorporated in the user subroutine to conduct the heat transfer analysis. The results from the heat transfer analysis are used as the thermal input for the structural analysis. Figure 11 shows the comparison of bottom flange temperature of the steel beam. In structural analysis, the mechanical loading applied at four points gradually and followed by the thermal load. The midspan displacement obtained from this procedure shown in Fig. 12 indicates good agreement with experimental results.

3.2   *Zhao and Kruppa [2]*

Test 1 from Zhao and Kruppa [2] is also simulated to validate the model. Test 1 was a composite beam with a protected steel beam and flat slab and is subjected to gravity load followed by fire. IPE 300 steel beam with 25 mm thick mineral wool used as fire protection. ISO fire curve was used as furnace temperature; the same is incorporated in the heat transfer analysis. Figure 13 shows the bottom flange

Fig. 13 Comparison of steel bottom flange temperature (Zhao Test 1)
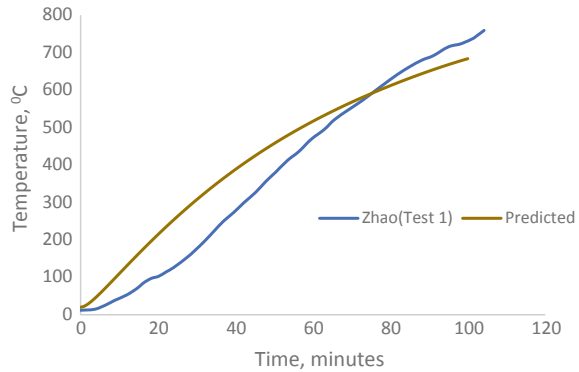
Fig. 14 Comparison of midspan deflection (Zhao Test 1)
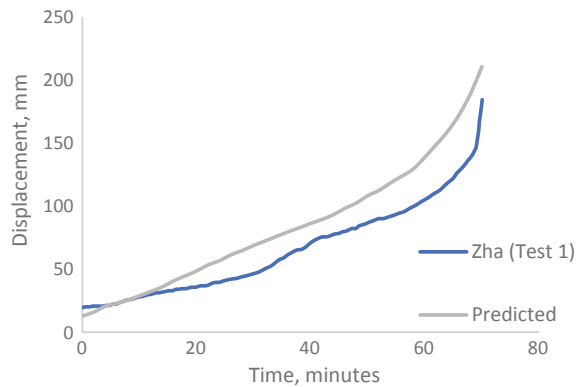
temperature distribution of the model compared with experimental data. A total load of 102.5 kN is applied as gravity load in the first step of structural analysis followed by thermal analysis. In thermal loading, nodal thermal histories of heat transfer analysis are used as input in the predefined field. Figure 14 shows the midspan deflection of the model, which shows a very good correlation with experimental values and Fig. 15 shows a comparison of the deflected shape of the experimental model and numerical model.

3.3 Choe et al. [12]

Test 3 from Choe et al. [12], Ramesh et al. [18] modelled. It is a 12.8 m long-span composite beam. W18x35 steel beam with 16 mm thick Southwest Type 5MD, a cementitious gypsum-based fire protection and 1.83 m wide profiled lightweight concrete slab with metal deck modelled. Four 12.7 mm diameter reinforced bars of yield strength 415 MPa used in hogging moment region to control crack width. The
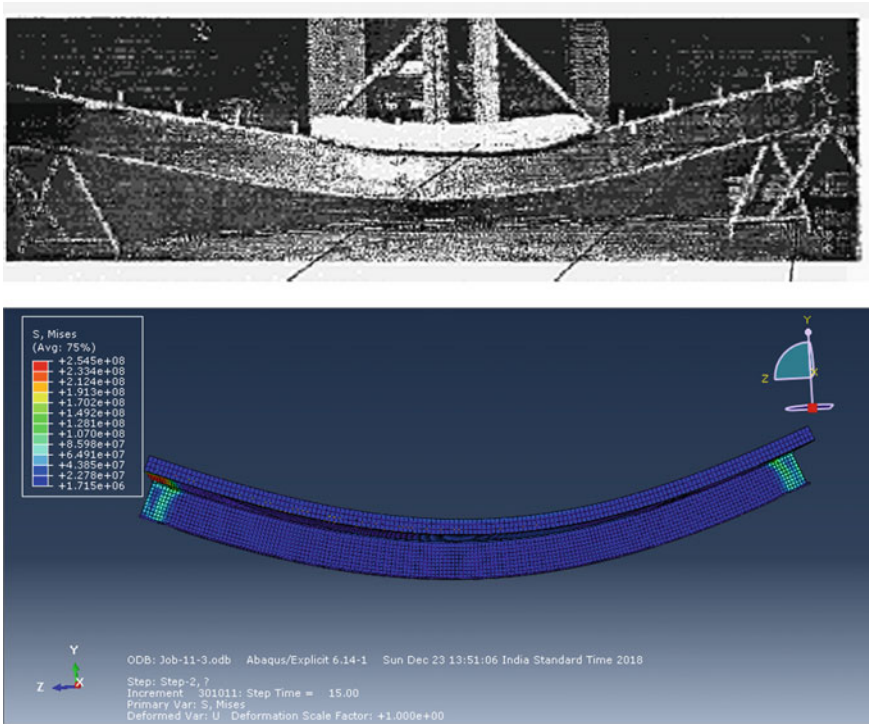
Fig. 15 Comparison of deflected shape of specimen in **a** experiment and **b** simulation

reinforcements were extended beyond the slab and tied to the support, to give continuity to the slab. Figure 16a, b shows the isometric view and cross-sectional view of the model. Furnace temperature distribution from the literature has been used in the subroutine to get nodal temperature history. Figure 17a–c shows the comparison of temperature distribution of steel beam and concrete slab of the model with experimental results. A total load of 106 kN at six equally distributed points have been applied gradually in the first step and step two, the thermal load applied. Around
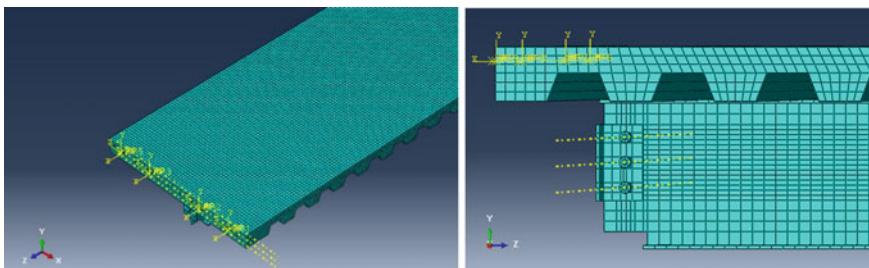
Fig. 16 **a** Isometric view of model, **b** cross-sectional view of the model (Choe Test 3)
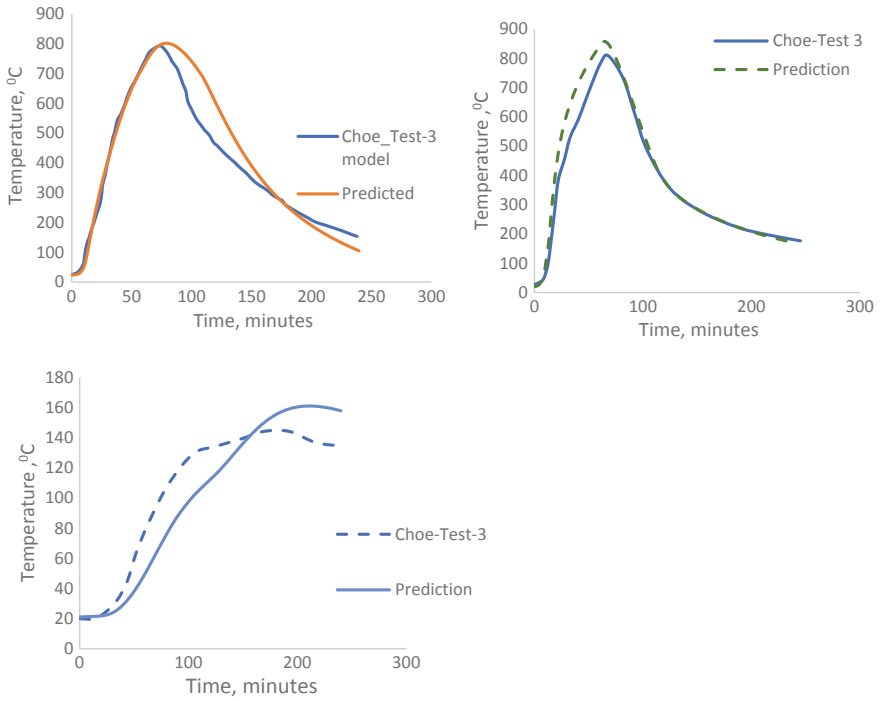
Fig. 17 a Comparison of bottom flange temperature distribution, **b** bottom concrete slab temperature distribution, and **c** top concrete slab temperature distribution (Choe Test 3)

30 min after commencing the experiment, local buckling of steel beam near to the connection leads to an increase in tensile force demand in continuity bars of the concrete slab. Figure 18 shows the comparison of the buckled shape of experimental test specimen and prediction. Similar behaviour has been observed in the analytical model also. The rebar was modelled using 3D brick element DC3D8, and slab continuity in the experiment was governed by anchoring the rebar to a hollow section
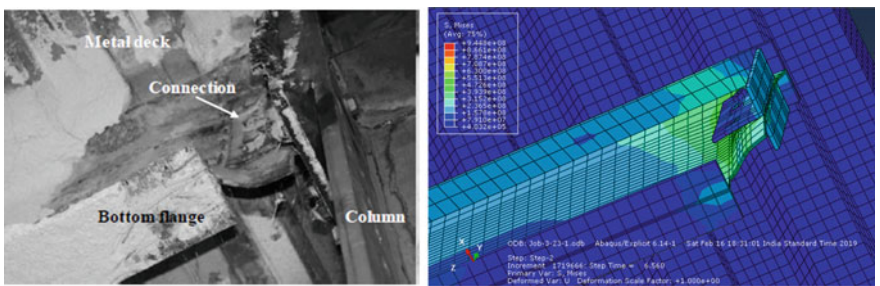
Fig. 18 Comparison of buckled shape of experimental test specimen and prediction (Choe Test 3)
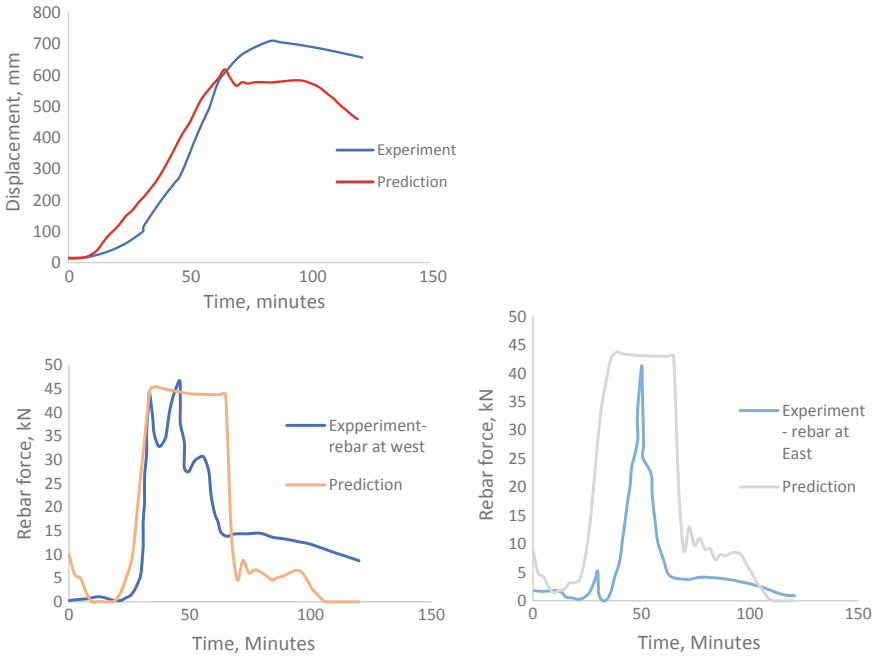
Fig. 19 Comparison of **a** midspan deflection versus time, **b** axial force versus time for rebar at west, and **c** rebar at east of experimental test specimen and prediction (Choe Test 3)

connected to supporting column. In the numerical model developed, continuity was modelled using connectors in interaction module of ABAQUS. Figure 19a–c shows the comparison of the prediction with the experimental results of bottom midspan deflection versus time and rebar force versus time. Gravity loading removed when the midspan deflection exceeds an allowable limit of 620 mm (L/20) at around 65 min.

4 Parametric Study

A parametric study has been conducted to understand the influence of continuity rebars in the global behaviour of the composite beams in fire conditions. The design principles of the model have been discussed in Ramesh et al. [18]. In the model, the rebar and welded wire mesh were designed primarily for crack control. For the present study, the number of bars provided and their diameters are the parameters considered. The number of bars, diameter of bars, and spacings considered in this parametric study were within the limit of codal provisions. The numerical models listed in Table 1 have been developed in ABAQUS to study the same. CB-1 has the same property as Choe-3 experimental model. The failure point is taken from the literature as when the midspan deflection reaches 620 mm (L/20). The midspan

Table 1 Model details used for parametric study

Model notation	Diameter of rebar (mm)	Number of rebars provided	Time at local buckling of steel beam web starts (min)	Midspan deflection at corresponding time (mm)	Failure time (min)	Maximum deflection under given fire scenario (mm)
CB-1	12.7	4	24	150	65	620
CB-2	8	4	24	148	56.3	743
CB-3	16	4	24	152	–	516
CB-4	12.7	2	24	154	57	715

deflection for all these models is shown in Fig. 12. Comparing CB-2 and CB-1, when the diameter of the bar is reduced from 12.7 to 8 mm, the failure occurs at 56 min (corresponding to the deflection of L/20), which is 9 min before the beams with rebar of diameter 12.7 mm. The maximum deflection observed is 743 mm. As the diameter of rebar is increased from 12.7 to 16 mm in CB-3, the maximum midspan deflection was 516 mm, which is significantly lower than the limiting value. Whereas in CB-4 with two number of 12.7 mm diameter rebars, the failure point occurs at around 57 min. And the maximum deflection observed under the given fire scenario is 713 mm.

Figure 20 shows the midspan deflection versus time for various models under consideration. In all four models, at around 24 min after starting the experiment, at 30 °C, when the vertical midspan deflection reaches around 150 mm, local buckling occurs in the web of steel beam near support and follows by a sudden increment in the axial tensile force in rebar have been observed. From Table 1, it is clear that the number of bars and its diameter affects the failure time and maximum deflection under the given fire scenario as the stiffness of rebars changes with diameter. The axial tensile force developed in west side and east side rebar located at 335 mm from

Fig. 20 Midspan deflection
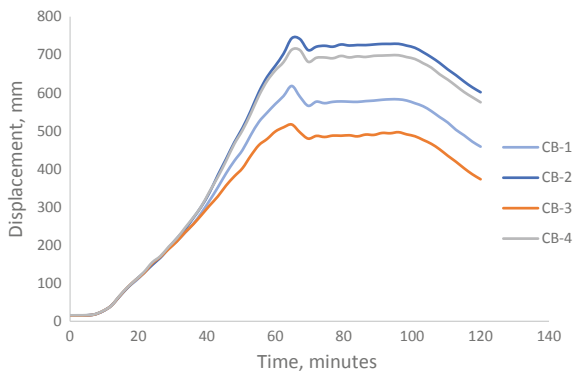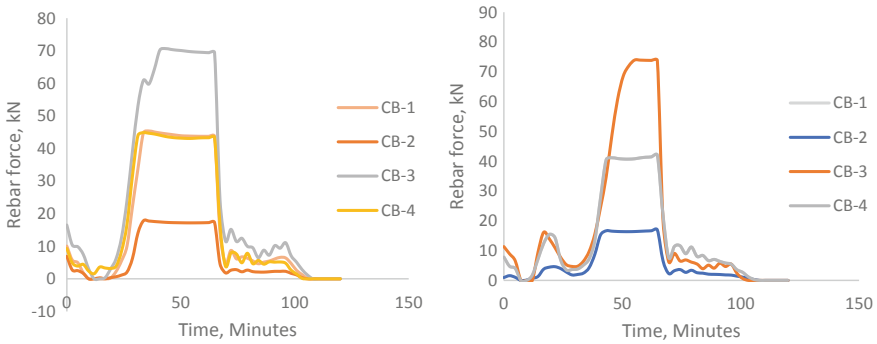
Fig. 21 Axial forces in continuity bars **a** west side, **b** east side

the central line of beam is shown in Figs. 21a and 15b. The presence of reinforcement bars does not have much influence in the beam until initial buckling happens, but it has a significant effect in maximum deflection value and thereby in failure time.

5 Conclusions

- Sequentially coupled two-step thermal-structural analysis procedure was developed using FEM tool ABAQUS for predicting the behaviour of steel-concrete composite beam under combined gravity and fire loading.
- The numerical procedure is validated with various experimental data available in the literature.
- A parametric study was conducted to understand the influence of continuity rebars in the behaviour of long-span continuous composite beams under fire.
- It was observed that until the initial local buckling of steel beam web, the rebar does not have a significant role in the overall fire behaviour of the beam. But it has a significant effect on the final maximum deflection value. By providing more quantity of rebar, we can increase the failure time of composite bars. Further study has to be performed to understand the detailed behaviour of the beam by increasing the variants.

References

1. Wainman, D. E., & Kirby, B. R. (1987). Compendium of UK standard fire test data, unprotected structural steel—1. Reference Number RS/RSC/S10328/1/98/B, British Steel Corporation (now Corus). Rotherham: Swinden Laboratories.
2. Zhao, B., & Kruppa, J. (1997). Fire resistance of composite slabs with profiled steel sheet and of composite steel concrete beams, Part 2: Composite beams. ECSC—agreement No. 7210 SA 509, CTICM, France.
3. Agarwal, A., Selden, K. L., & Varma, A. H. (2014). Stability behaviour of steel building structures in fire conditions: Role of composite floor system with shear-tab connections. *Journal of Structural Fire Engineering, 5*(2), 77–96. https://doi.org/10.1260/2040-2317.5.2.77.
4. Agarwal, A., & Varma, A. H. (2014). Fire induced progressive collapse of steel building structures: The role of interior gravity columns. *Engineering Structures, 58,* 129–140. https://doi.org/10.1016/j.engstruct.2013.09.020.
5. Agarwal, A. (2011). *Stability of steel building structures under fire loading* (Ph.D. dissertation). School of Civil Engineering, Purdue University.
6. Agarwal, A., & Varma, A. H. (2011). Design of steel columns at elevated temperatures due to fire: Effects of rotational restraints. Engineering Journal, AISC.
7. Wellman, E. I., Varma, A. H., Fike, R., & Kodur, V. (2011). Experimental evaluation of thin composite floor assemblies under fire loading. *Journal of Structural Engineering, 137*(9), 1002–1016.
8. Selden, K. L., Fischer, E. C., & Varma, A. H. (2015). Experimental investigation of composite beams with shear connections subjected to fire loading. *Journal of Structural Engineering, 142*(2), 04015118. https://doi.org/10.1061/(ASCE)ST.1943-541X.0001381.
9. Fischer, E. C., Selden, K. L., & Varma, A. H. (2017). Experimental evaluation of the fire performance of simple connections. *Journal of Structural Engineering, 143*(2), 04016181. https://doi.org/10.1061/(ASCE)ST.1943-541X.0001664.
10. Fischer, E. C., & Varma, A. H. (2016) Fire resilience of composite beams with simple connections: Parametric studies and design. Journal of Construction Steel Research, 119–135. doi: 10.1016/j.jcsr.2016.08.004.
11. Fischer, E. C., & Varma, A. H. (2015). Fire behaviour of composite beams with simple connections: Benchmarking of numerical models. *Journal of Constructional Steel Research, 111,* 112–125. https://doi.org/10.1016/j.jcsr.2015.03.013.
12. Choe, L., Ramesh, S., Seif, M., Hoehler, M., Grosshandler, W., Gross, J., & Bundy, M. (2018). Fire performance of long-span composite beams with gravity connections. In *Proceedings of the 10th International Conference on Structures in Fire FireSERT*, Ulster University, Belfast, UK, June 6–8, 2018.
13. ABAQUS. (2012). ABAQUS/Standard Version 6.12 User's Manuals, ABAQUS, Providence, RI.
14. Cedeno, G., Varma, A. H., & Agarwal, A. (2009). Behaviour of floor systems under realistic fire loading. In *Proceedings on CD-ROM of the ASCE Structures Congress* (pp. 1–10). Reston, VA: ASCE. https://doi.org/10.1061/41031(341)224.
15. Gorst, N. J. S., & Williamson, S. J. (2003). Friction in temporary works. HSE BOOKS. ISBN 0 7176 2613 X http://www.hse.gov.uk/research/rrpdf/rr071.pdf.
16. European Committee for Standardization (CEN). (2005). *Eurocode 4: Design of composite steel and concrete structures, Part 1-2: General rules—Structural fire design*. Brussels: European Committee for Standardization.
17. European Committee for Standardization (CEN). (2002). *Eurocode 1: Actions on structures, Part 1.2: General actions—Actions on structures exposed to fire*. European Committee for Standardization.
18. Ramesh, S., Choe, L., Hoehler, M., Grosshandler, W., & Gross, J. (2018). Design and construction of long-span composite beam specimens for large structural-fire tests. In *Proceedings of Structures Congress 2018*, Fort Worth, Texas, April 19–21, 2018.

Effect of Heating Rate on Bond Behavior Between Steel and Concrete at Elevated Temperatures

Ira Banoth and Anil Agarwal

1 Introduction

Bond behavior between steel and concrete at elevated temperatures is a very complex phenomenon. Bond is the transfer of force between steel and concrete at the interface. Bond strength is the main influencing parameter for the response of the structure in terms of loss of structural integrity. The influencing parameters for bond strength are concrete strength, concrete cover, aggregate type, rebar diameter, rebar size, surface of rebar, and heating rate.

In the past years, number of studies have been conducted for the bond strength between steel and concrete at ambient and after elevated temperature by varying different parameters (different concrete strengths, different types of concrete, different cooling regimes, different concrete cover, the different diameter of rebar). But the studies for the behavior of the bond during elevated temperatures are very less.

A. D. Edwards et al. studied the local bond stress-slip behavior under cyclic loading. In this study, the varying parameters were concrete cover (25 and 35 mm) and different load amplitudes (2, 3.9 and 5.6 MPa). The conclusions drawn from this study for the bond behavior between 16 mm diameter hot-rolled rebar and concrete of strength 43 MPa were (a) The destruction of bond strength was more with increasing load amplitude in the first cycle compared to the prospering cycles, and (b) The reduction of bond strength is more significant when the stress levels are well below the peak stress [1].

Morley and Royles studied the bond behavior between steel and concrete at elevated temperatures under different conditions: (a) Under constant stress and (b) Under

I. Banoth (✉) · A. Agarwal
Department of Civil Engineering, Indian Institute of Technology Hyderabad (IITH), Hyderabad, Telangana 502285, India
e-mail: ira.banoth@gmail.com

A. Agarwal
e-mail: anil@iith.ac.in

no stress, and he concluded that the bond strength was more in under constant stress condition than the unstressed condition [2].

Several studies have been carried out for the bond behavior between the steel and fiber-reinforced concrete after elevated temperatures. Fibers are used to reduce the crack width and spalling effect. Hadad et al. used different types of fibers hooked end steel, a mixture of hooked end steel and basalt coated steel, a mixture of hooked end steel and polypropylene and basalt coated steel. The inclusion of fibers prevents the spalling under the temperature of 600 °C and increased the ductility of bond behavior between the steel and concrete [3]. Eva Lubloy and Viktor Hlavicka have used hooked end steel fibers and polypropylene fibers with different types of aggregates (quartz gravel and expanded clay). The bond strength of concrete with quartz gravel and steel fibers gives more bond strength than followed by the sequence of quartz gravel, quartz gravel, and polypropylene fibers, expanded clay 2 and expanded clay 1. The reduction of bond strength was more significant in the range of temperature 400–500 °C for all the concrete, and this is due to the decomposition of Portlandite at the temperature of 450 °C [4].

Ferhat and Rustum gul have considered the parameters were concrete strength (20 and 35 MPa), embedment length (60, 100, and 120 mm), and cooling regimes (water and air cooling conditions). The conclusions drawn from this study were (a) The effect of cooling condition was not having a more significant effect for the embedment length of rebar is 60 mm and, (b) For 100 and 120 mm embedment lengths, water-cooled specimens were having more bond strength loss than air-cooled specimens, and this was more significant for the concrete of strength 20 MPa. The bond strength was increased with increasing concrete strength and embedment length [5].

Lee et al. studied the bond behavior between steel and concrete after the elevated temperature by considering different parameters like the heating rate, cooling conditions, and different types of rebar (epoxy coated and uncoated). Bond strength decreased with increasing of heating rate for both the cases (epoxy coated and uncoated rebar). The effect of the cooling condition has a less significant effect on the uncoated rebar [6].

The studies have been conducted for the bond behavior between steel and concrete subjected to elevated temperatures are very less. Some researchers have been studied; Schneider et al. studied the bond behavior of different types of rebars (plain (fresh as rolled, heavily rusted), cold deformed steel, and pre-stressing steel). They have concluded that the deformed steel was having more bond strength than the plain bar. The bond behavior of cold deformed steel and pre-stressing steel was almost similar because of both the bars having deformations [7]. Morley and Royles have studied the bond behavior between steel and concrete at elevated temperatures under different (stressed and unstressed) conditions, and the conclusions drawn were bond strength was more in stressed conditions than the bond strength in unstressed condition [2].

In the previous studies, the bond behavior between steel and concrete during elevated temperature is very limited. The effect of heating rate has a very significant effect on the bond behavior, but the consideration of this parameter is very less in literature and focuses only on elevated temperatures. So, in this present study,

Table 1 Concrete mix design details (kg/m^3)

Cement	Fine aggregate	Coarse aggregate	w/c ratio	Super plasticizer	Compressive stress (MPa)
369.7	828	1173	0.42	4.43	25

considering the heating rate is the main parameter, and how it affects the bond behavior at elevated temperatures.

There are no specific test methods for finding the bond behavior between steel and concrete. But according to prEN 10080, there are two types of test methods available; (a) Pullout test and (b) Beam test [8]. In this present study, pullout tests were conducted for studying the bond behavior between steel and concrete at room temperature and elevated temperatures.

2 Experimental Program

2.1 Material Properties

Concrete The compressive strength of concrete was 25 MPa calculated by the average of compressive strength of three cylindrical specimens of size (150 × 300 mm) tested in compression. Ordinary Portland cement of grade 53, fine aggregate (river sand), coarse aggregate (gravel of max size 20 mm), and admixture superplasticizers were used. The concrete mix was designed according to the code IS 10262:2009 [9]. Mix design details are given in Table 1. Concrete was mixed in a drum mixer of capacity 0.3 m^3. After mixing, concrete was casted in steel molds and left for 24 hours and then demolded and placed in water tank for curing. After 15 days of curing, specimens were allowed to dry for 15 days.

Steel Fe500 grade deformed steel of 12 mm and 20 mm diameter rebars were used.

2.2 Heating Procedure

The specimens were heated in an electrical furnace assembled by four heating panels of dimensions 350 mm wide and 480 mm long. The capacity of the furnace is 1100 °C. The specimens were heated up to the desired temperatures at the concrete–steel interface by following a heating rate of 2 °C/min and ISO 834 [10] standard fire curve. The temperature versus time plots for two different heating rates are shown in Fig. 1. Temperature versus time for different elevated temperatures by following different heating rates is presented in Fig. 2.
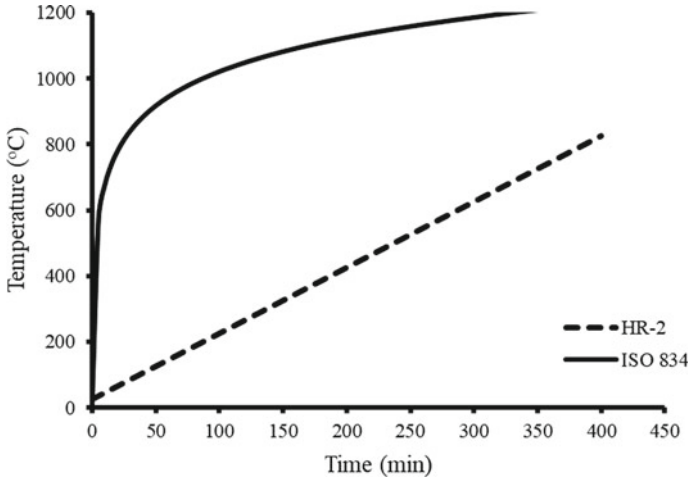
Fig. 1 Temperature versus time
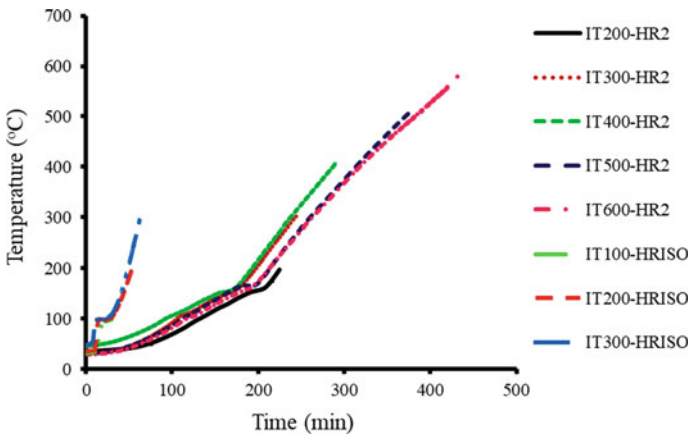
Fig. 2 Temperature versus time at different elevated temperatures

2.3 Pullout Testing

Pullout tests were carried out for finding the bond behavior between steel and concrete at ambient and elevated temperatures. Tested specimens were the cubical size of 200 × 200 × 200 mm with a central pullout rebar. The middle portion (4 d mm length) of the rebar was bonded, and the remaining length top and bottom portion of the rebar embedded in the concrete was un-bonded by PVC pipes (shown in Fig. 3a). Nine specimens of 12 mm diameter and twelve specimens of 20 mm diameter were tested. Three specimens of 12 mm diameter at ambient temperature and remaining
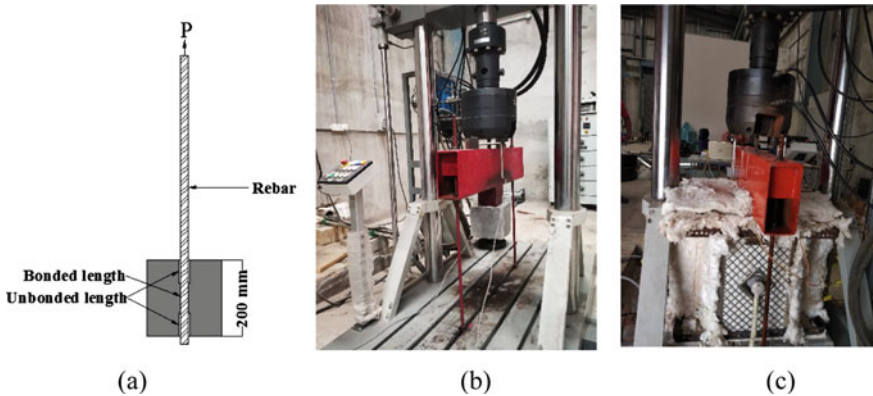
Fig. 3 Details of the test setup: **a** Geometric details of pullout specimen. **b** Test setup for ambient temperature and **c** Test setup for elevated temperatures

were tested at elevated temperatures. Four specimens of 20 mm diameter at ambient temperature and remaining at elevated temperatures were tested.

The load was applied after reaching a desired temperature at the steel–concrete interface by Fatigue Testing Machine of 500 kN capacity. LVDTs were placed on the concrete surface resting against the actuator as shown in Fig. 3b. Test setup at ambient and elevated temperatures are shown in Fig. 3b, c.

3 Test Results and Discussion

Figure 4 depicts the bond versus slip diagram for 12 mm diameter rebar at different elevated temperatures by different heating rates. Three tests were conducted at ambient temperature for checking the consistency. All the three specimens were failed by bond. The failure pattern is shown in Fig. 5a. The bond strength at ambient temperature was 20.4 MPa (average of 3 specimens) and at elevated temperatures of 200, 300, 400, and 500 °C were 8.1, 6.3, 3.1, and 3.9 MPa, respectively, by following the heating rate of 2 °C/min presented in Table 1. At all the temperature, the specimens were failed by bond. At 200 °C temperature, no cracks and at 300 °C small cracks appeared on the surface of the concrete. At 400 and 500 °C of temperature, more number of cracks appeared on the concrete surface. Failure patterns at different elevated temperature are shown in Fig. 5b.

The bond strength of rebar of 12 mm diameter at 100 and 200 °C was 8.7 and 2.1 MPa, respectively, by following heating rate according to ISO 834 standard fire curve presented in Table 1. At both the temperatures, specimens were failed by bond. After bond failure, there was a splitting failure formed in the form of longitudinal cracks along the length of the rebar. The failure patterns are shown in Fig. 5c. The bond strength decreased with increasing of the temperature by following the heating
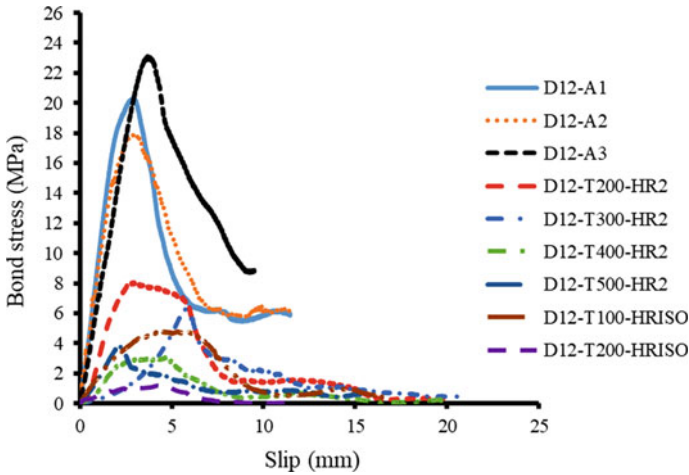
Fig. 4 Bond stress versus slip of 12 mm rebar at different elevated temperatures

Fig. 5 Failure patterns of 12 mm rebars: **a** At ambient temperature. **b** Heating rate of 2 °C/min and **c** Heating rate of ISO—834

rate of 2 °C/min and ISO standard fire curve, but in the case of ISO heating rate, the bond strength decreased very rapidly. The results are presented in the Table 2.

Specimen at ambient temperature: DX-AY; here X is diameter of rebar, Y is number of specimen.

Specimen at elevated temperatures DX-TY-HRZ; X is diameter of rebar, Y is desired temperature at the steel–concrete interface, and Z is the heating rate in °C/min.

The bond stress versus slip diagram of 20 mm diameter rebar at different elevated temperatures by different heating rates is presented in Fig. 6. Four specimens were tested at ambient temperature, and all the specimens were failed by bond, and strength was 13.6 (average of 4 specimens). The failure patterns are shown in Fig. 7a. The bond strengths of specimen at elevated temperatures of 200, 300, 400, 500, and 600 °C were 9.8, 6.1, 3.5, 3.2, and 2.1 MPa, respectively, by following heating rate of 2 °C/min. All the specimens were failed in bond followed by splitting cracks formed in the longitudinal direction of the rebar, and failure patterns are shown in Fig. 7b. With increasing temperature, bond strength was decreased, and a number of cracks were increased on the concrete surface. The specimens heated by following ISO curve also failed in bond followed by cracks formed in the longitudinal direction

Table 2 Test results of 12 mm rebar

| Specimen	Bond strength (MPa)	Slip at maximum load (mm)	RBS (% of 20 °C)	Type of failure
D12-A1	20.3	2.89	–	Bond
D12-A2	17.9	2.99	–	Bond
D12-A3	23.1	3.67	–	Bond
D12-A	20.4	–	100	–
D12-T200-HR2	8.1	3.11	39.6	Bond
D12-T300-HR2	6.3	5.73	30.8	Bond
D12-T400-HR2	3.1	4.65	15.2	Bond
D12-T500-HR2	3.9	2.22	19.1	Bond
D12-T100-HRISO	4.8	4.47	23.5	Bond
D12-T200-HRISO	1.2	4.20	5.9	Bond

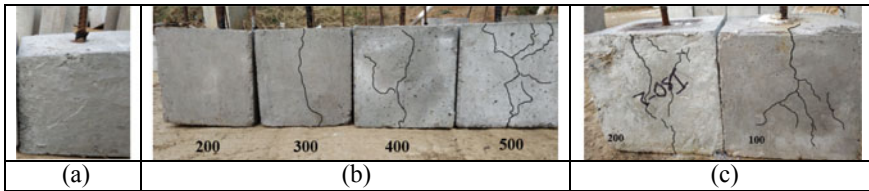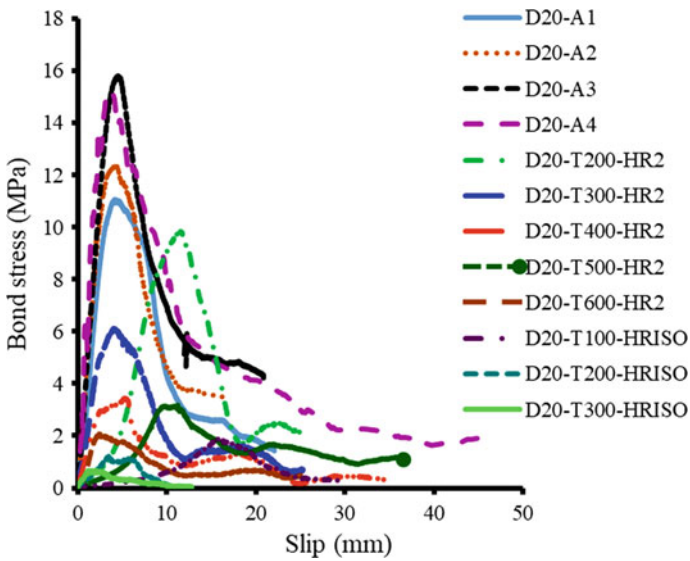**Fig. 6** Bond stress versus slip of 20 mm rebars at different elevated temperatures
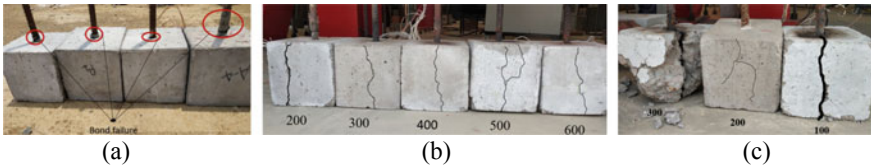
Fig. 7 Failure patterns of 20 mm rebars: **a** At ambient temperature. **b** Heating rate of 2 °C/min and **c** Heating rate of ISO—834

Table 3 Test results of 20 mm rebar

Specimen	Bond strength (MPa)	Slip at maximum load (mm)	RBS (% of 20 °C)	Type of failure
D20-A1	11.1	4.2	–	Bond
D20-A2	12.4	4.2	–	Bond
D20-A3	15.8	4.5	–	Bond
D20-A4	15.2	3.8	–	Bond
D20-A	13.6	–	100	–
D20-T200-HR2	9.8	11.5	59.4	Bond
D20-T300-HR2	6.1	4.0	44.8	Bond
D20-T400-HR2	3.5	5.3	25.7	Bond
D20-T500-HR2	3.2	11.2	23.5	Bond
D20-T600-HR2	2.1	2.4	15.4	Bond
D20-T100-HRISO	1.9	9.5	13.9	Bond
D20-T200-HRISO	1.3	3.5	9.5	Bond
D20-T300-HRISO	0.7	2.0	5.0	Bond

of the rebar. The bond strength at different elevated temperatures of 100, 200, and 300 °C was 1.9, 1.3, and 0.7 MPa, respectively as shown in Table 3. With increasing temperature, bond strength decreased, crack width increased, and number of cracks appeared on the concrete surface were more.

Specimen at ambient temperature: DX-AY; here X is diameter of rebar, Y is number of specimen.

Specimen at elevated temperatures DX-TY-HRZ; X is diameter of rebar, Y is desired temperature at the steel–concrete interface, and Z is the heating rate in °C/min.

3.1 Residual Bond Strength

Percentage of residual bond strength of rebar of different diameters with different heating rates is shown in Fig. 8. The residual bond strength of 12 mm rebar at different elevated temperatures of 200, 300, 400, and 500 °C by following heating rate of 2 °C/min was 39.6, 30.8, 15.2, and 19.1%, respectively. By following the heating rate of ISO curve, the bond strength at elevated temperatures of 100 and 200 °C was 23.5, and 5.9%, respectively. Residual bond strength of 20 mm diameter rebar when heated at 2 °C/min was 59.4, 44.8, 25.7, and 23.5% at the interface temperatures of 200, 300, 400, 500, and 600 °C, respectively. However, when the specimens were heated using the ISO standard fire curve, the measured residual bond strengths were 13.9, 9.5, and 5%, at the interface temperatures of 100, 200, and 300 °C, respectively. The loss in bond strength was more by ISO fire curve. Hence, the heating rate has a significant effect on the reduction of bond strength.
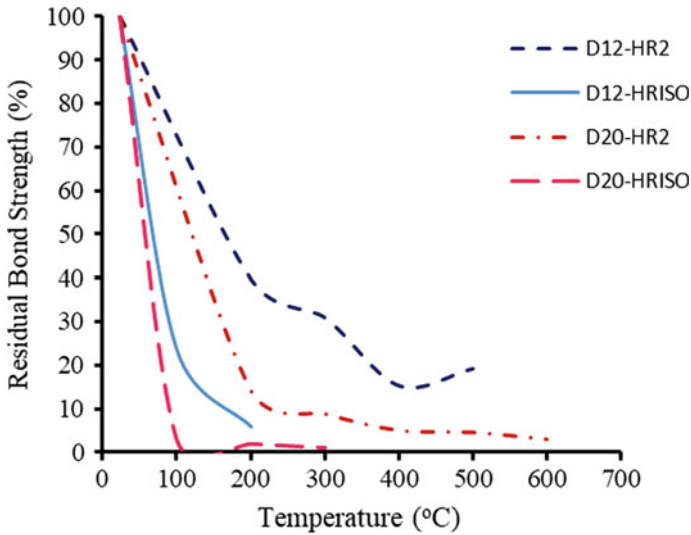
Fig. 8 Percentage residual bond strength of 12 and 20 mm rebar at different elevated temperatures by following different heating rates

4 Conclusions

- Pullout tests were carried out for studying the bond behavior between concrete and steel of different diameter of 12 mm and 20 mm at ambient and elevated temperatures by following heating rates of 2 °C/min and ISO-834 standard fire curve.
- Rate of heating has a very significant effect on the bond strength retention factors. Faster rate of heating leads to a more rapid decline in the bond strength.
- Larger diameter bars underwent a more rapid bond strength decrease with increasing temperature.
- The residual bond strength of 20 mm rebar was more than the residual bond strength of 12 mm rebar by following both the heating rates. The reduction of bond strength was very significant by following heating rate of ISO 834. So, bond strength decreased with faster heating rate. Hence, the heating rate has a significant effect on the reduction of bond strength.

References

1. Edwards, A. D., & Yannopoulos, P. J. (1978). Local bond-stress–slip relationships under repeated loading. *Journal Magazine Concrete Research, 30*(103), 62–72. https://doi.org/10.1680/macr.1978.30.103.62.
2. Royles, R., & Morley, P. D. (2009). Further responses of the bond in reinforced concrete to high temperatures. *Journal Magazine Concrete Research, 35*(124), 157–163. https://doi.org/10.1680/macr.1983.35.124.157.
3. Haddad, R. H., Al-Saleh, R. J., & Al-Akhras, N. M. (2008). Effect of elevated temperature on bond between steel reinforcement and fiber reinforced concrete. *Journal Fire Safety, 43*(5), 334–343. https://doi.org/10.1016/j.firesaf.2007.11.002.
4. Lubloy, É., & Hlavička, V. (2017). Bond after fire. *Journal of Construction and Building Materials, 132*, 210–218. doi:10.1016/j.conbuildmat.2016.11.131.
5. Bingöl, A. F., & Gül, R. (2009). Residual bond strength between steel bars and concrete after elevated temperatures. *Journal Fire Safety, 44*(6), 854–859. https://doi.org/10.1016/j.firesaf.2009.04.001.
6. Lee, J., Sheesley, E., JingY, Xi Y., & Willam, K. (2018). The effect of heating and cooling on the bond strength between concrete and steel reinforcement bars with and without epoxy coating. *Journal Construction Building Materials, 177,* 230–236. https://doi.org/10.1016/j.conbuildmat.2018.05.128.
7. Diederichs, U., & Schneider, U. (2009). Bond strength at high temperatures. *Journal Magazine Concrete Research, 33*(115), 75–84. https://doi.org/10.1680/macr.1981.33.115.75.
8. ENV 10080:1995, Steel for the reinforcement of concrete. Weldable reinforcing steel—General.
9. IS: 10262-2009, Concrete mix proportioning—Guidelines.
10. ISO: 834-11:2014, Fire resistance tests—Elements of building construction—Part 11: Specific requirements for assessment of fire protection to structural steel elements.

Idealised Bilinear Moment-Curvature Curves of Reinforced Masonry (RM) Walls

Jacob Alex Kollerathu

1 Introduction

Most houses in rural India are masonry houses built with either burnt clay brick or natural stone masonry. Technically, they are called **Unreinforced Masonry (URM) Houses**; as they have masonry walls with no steel reinforcement embedded in them to improve their behaviour during earthquakes. During an earthquake, unreinforced masonry (URM) walls are pushed sideways, along their length (in-plane) and thickness (out-of-plane) directions [8]. When shaken along their length, they develop diagonal cracks along their length and/or separate at wall junctions. When walls collapse, they bring down the roof along with them. This is the main reason for large loss of lives during earthquakes that have occurred in different regions of the country. The poor performance of URM structures even under low to moderate seismicity (Sikkim 2011 and Nepal 2015) has seen its use being banned in a few countries (New Zealand) through techno-legal regulations.

The other variant of masonry structures involves the introduction of both vertical and horizontal steel. The vertical steel is used to increase the flexural capacity of the wall, while the introduction of horizontal steel increases the shear capacity of the wall [1]. Nevertheless, Indian codes [2] have not formulated any design or detailing code for reinforced masonry possibly as the quality of bricks in our country, on an average, is not suitable for reinforced masonry. Bricks should be of high strength, dense and need to have low rate of moisture [3]. Reinforced masonry (RM) structural walls form the main lateral load resisting system in low- to mid-rise buildings, located in moderate/high seismic regions. Compared to unreinforced masonry walls, RM walls have higher flexural and shear strengths and are expected to efficiently resist earthquake shaking through inelastic actions. Proper design and detailing of

J. A. Kollerathu (✉)
Department of Civil Engineering, Faculty of Engineering, Christ (Deemed to Be University), Bengaluru, India
e-mail: jacob.alex@christuniversity.in
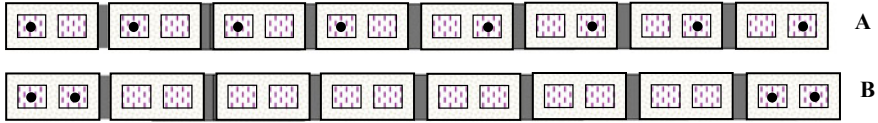
Fig. 1 Detailing of longitudinal steel in RM walls

longitudinal and transverse reinforcements helps in achieving the required strength and ductility. Two common ways of detailing longitudinal reinforcement in RC walls are:

(a) Uniform distribution of reinforcement along the length of the wall, and (b) reinforcement concentrated at the two ends of the wall (see Fig. 1a, b).

Although, in-plane flexural strength of walls with the two distributions is generally not too different for the same amount of total reinforcement, the former often results in enhanced shear strength and improved shear behaviour (displacement and ductility) as it resists the propagation of diagonal shear cracks in the wall [1]. The flexural strength and curvature ductility of RM walls sections can be determined from their axial load–moment interaction curves and nonlinear moment-curvature (M-Φ) curves. The M-Φ response curve must represent the effective (cracked) flexural rigidity, flexural strength and curvature ductility of the RM section. This paper proposes methods to arrive at idealised multi-linear M-Φ curves of RM wall sections with both uniformly distributed reinforcement along the length of the wall and reinforcement concentrated at the two ends of the wall, at different levels of axial stress.

2 Estimation of Axial Load, Flexural Capacity and Curvature

The axial load and the flexural strength of RM walls can be estimated from basic principles of mechanics considering equilibrium of forces, compatibility of strains and constitutive relations of materials, given in Eqs. (1)–(3):

$$\Sigma(f_{sci} - f_{msci})A_{sci} + f_{m,\text{avg}}tx_u - \Sigma f_{sti}A_{sti} = P \qquad (1)$$

$$\text{Compatibility conditions} \quad \frac{\varepsilon_{m1}}{x_u} = \frac{\varepsilon_{st4}}{L - x_u} \qquad (2)$$

The design flexural compressive σ-ε curve of masonry is parabolic up to an ultimate strain of 0.003 with maximum compressive stress f'_m. Also, strain limits ε_u of 0.003 used are from experimental observations [4]. The constitutive relation of masonry is defined by its design stress–strain curve given by:

$$f_m = 0.85 f'_m \left(2 \left(\frac{\varepsilon}{\varepsilon_u} \right) - \left(\frac{\varepsilon}{\varepsilon_u} \right)^2 \right) \tag{3}$$

where A_{sti} is the area of reinforcement bars in ith layer under tension,
A_{sci} is the area of reinforcement bars in ith layer under compression,
L' is the distance of the extreme layer of reinforcement from the extreme layer in compression, $f_{m,avg}$ is the average compressive stress in masonry,
f_{sti} is the stress in ith layer of reinforcement bars under tension,
f_{sci} is the stress in ith layer of reinforcement bars under compression (both estimated from stress–strain characteristics of reinforcement bar),
f_{msci} is the stress in masonry at the level of ith layer of reinforcement bars under compression,
x_u is the depth of neutral axis,
f'_m is the compressive strength of masonry,
ε_u is the compressive strain in masonry corresponding to f'_m,
and ε is the ultimate strain in masonry at highly compressed edge at peak stress (Fig. 2).

The limiting strain corresponding to yielding of reinforcement bars is given by:

$$\varepsilon_y = 0.002 + \left(\frac{0.87 f_y}{E_s} \right) \tag{4}$$

where

E_s: Youngs' modulus of reinforcing steel (200 GPa)
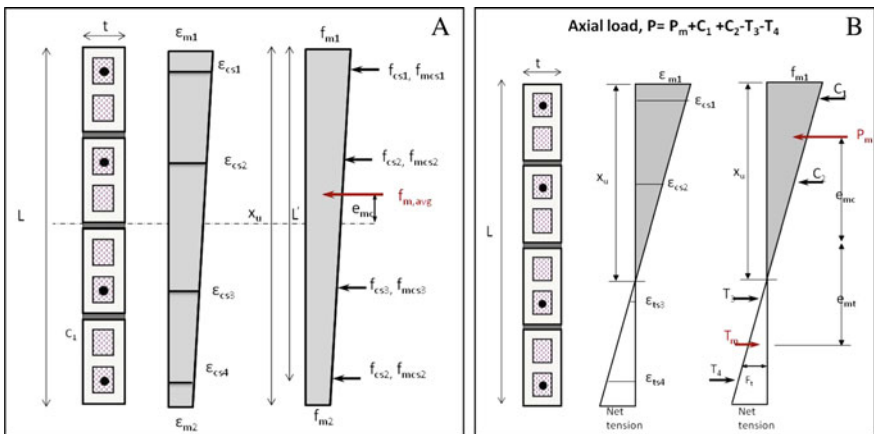
Fig. 2 Typical stress and strain distributions across rectangular RM walls. **a** Entire section under compression and **b** once tensile cracking commences

Once the stresses in the reinforcing steel and masonry are obtained, the axial load is calculated as in Eq. (1). The flexural strength of the RM wall is calculated by considering the moments of the tensile and compressive forces along the centroidal axis. Figure 4a shows a typical axial load–bending moment (P–M) interaction (normalised to their respective capacities) of RM walls. The failure of a RM wall is defined by values of the following limiting states of strains in masonry and the reinforcing steel.

- Tensile cracking of masonry
- Yielding of extreme of reinforcement on tension side
- Crushing of masonry

Based on the above-mentioned limit states, a P–M interaction envelope of RM sections has three distinct regions (see Figs. 3 and 4);

- Balance point: It is defined as the point on the P–M interaction at which the strains in concrete and steel reach corresponding limiting strains in crushing and tension simultaneously. The axial load at this point is denoted as balanced axial load P_{bal}.
- Compression failure region (above balanced point): Region on the P–M interaction where the failure is characterised by the strains in the extreme compressive fibre reaching the crushing strain of masonry (ε_u). The axial load in the region is greater than P_{bal}.
- Tensile failure region (below balance point): It is the region on the P–M interaction where the failure is due to the tensile strain in the extreme layer of reinforcement reaching its yield. The axial load in this region is lesser than the balanced axial load P_{bal}.

In the following paper, P–M interaction and nonlinear M-Φ curves are developed for two reinforced masonry walls (wall A with uniformly distributed steel and wall B with reinforced concentrated at the two ends of the walls). The curvature ductility of the walls has been examined at various levels of axial stress.
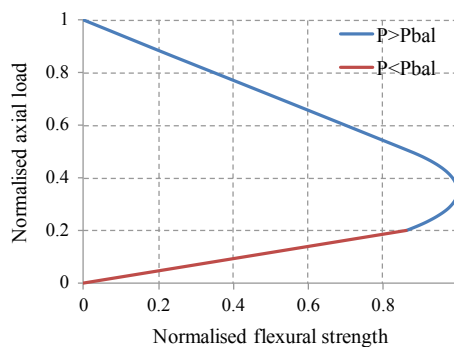
Fig. 3 Typical axial load–bending moment interaction of RM walls
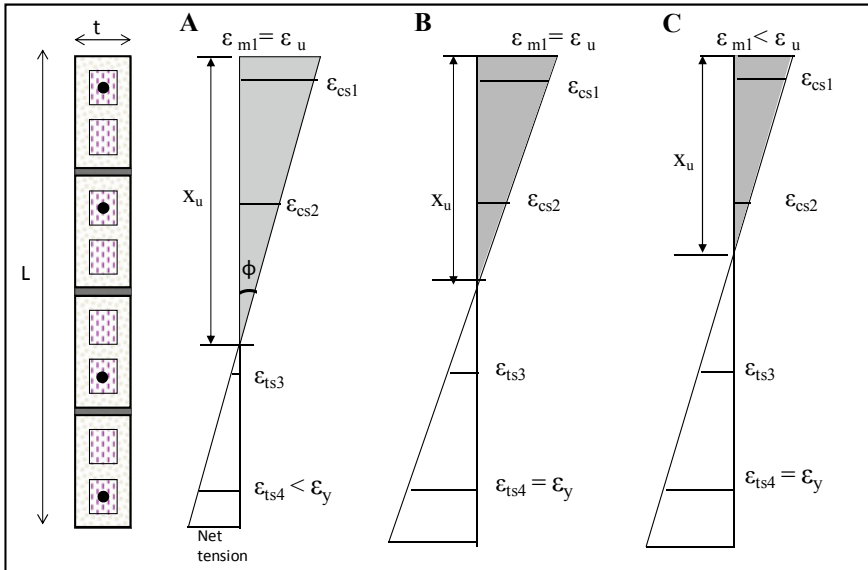
Fig. 4 Strain variations across RM sections under axial loads. **a** Above balance point, **b** at balance point, **c** below axial load

3 Axial Load–Flexural Capacity (*P*–*M*) Interaction and Moment-Curvature (*M*-Φ)

The *P*–*M* interaction and *M*-Φ curves of two reinforced masonry walls with reinforcing steel detailing as given in Fig. 1 is provided in these sections. The curves are determined from simple principle of mechanics considering equilibrium of forces, compatibility of strains and constitutive relations of materials. As per SP-7, the minimum reinforcement in each orthogonal should be at least 0.07% of the gross area of the wall. In this paper, the *P*–*M* interaction and *M*-Φ curves of a wall with dimensions of 3270 * 3000 * 200 mm (*l* * *h* * *t*) are examined. The reinforcing steel is detailed in two ways:

(a) Uniform distribution of reinforcement along the length of the wall (wall A), and
(b) Reinforcement concentrated at the two ends of the wall (wall B).

The *P*–*M* interaction of walls A and B is shown in Fig. 5. From Fig. 5 and Table 1, one observes that the detailing of the reinforcement does not have an effect on the axial load capacity of the wall. However, there is a 7.5% increase in the flexural strength of the wall with reinforcement concentrated at the corner. The *M*-Φ curve of walls A and B subject to different levels of axial stresses is also investigated. In this regard, *M*-Φ curves of the walls at an axial load of 0.21 P_u ($P = P_{bal}$), 0.4 P_u ($P > P_{bal}$) and 0.1 P_u ($P < P_{bal}$) are studied and reported in Fig. 6 and Table 2. The idealised bilinear curve is obtained by equating the energy dissipation capacity of
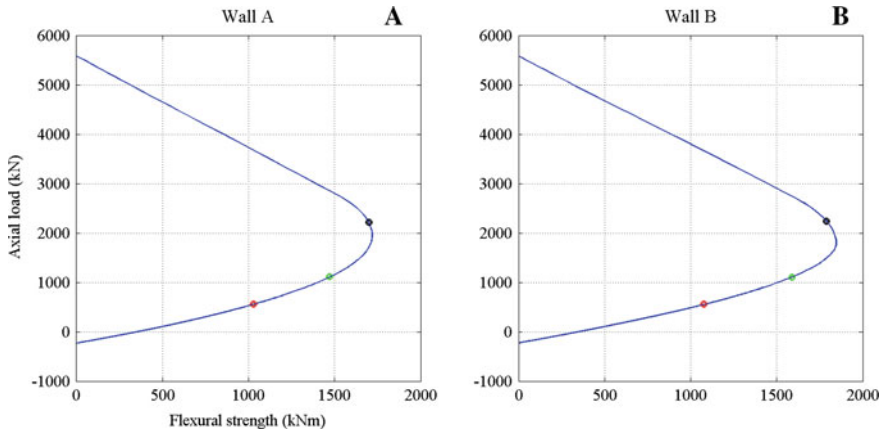
Fig. 5 Axial load–bending moment interaction diagram for the wall A and wall B

Table 1 Axial load and bending moment capacity of walls A and B

Wall #	Axial load capacity, P_u (kN)	Bending moment capacity, M_u (kN m)	Balanced axial load, P_{bal} (kN)
Wall A	5593	1717	1174
Wall B	5589	1845	1173
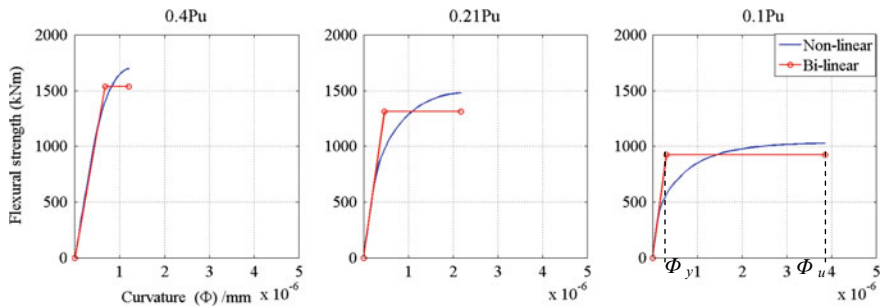
Fig. 6 Moment-curvature relationship of wall A

Table 2 Curvature ductility and effective flexural rigidity of walls A and B

Axial load demand	Curvature ductility, μ_Φ (wall A)	Curvature ductility, μ_Φ (wall B)	Effective flexural rigidity, EI_{eff} (wall A)	Effective flexural rigidity, EI_{eff} (wall B)
$0.4 P_u$	1.83	1.69	0.71	0.75
$0.21 P_u$	4.57	4.38	0.86	0.88
$0.1 P_u$	12.3	12.84	0.92	0.91
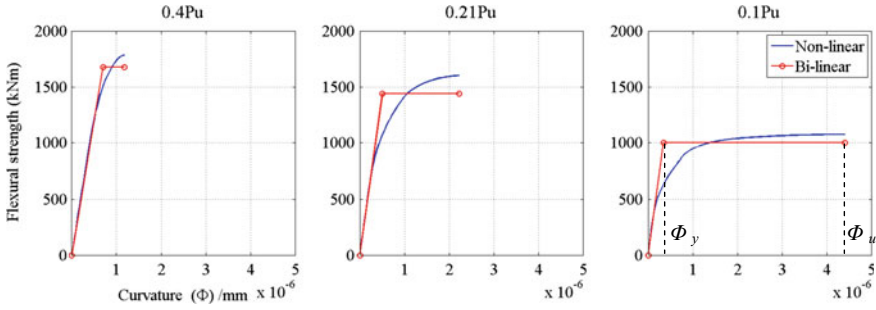
Fig. 7 Moment-curvature relationship of wall B

the nonlinear and idealised bilinear M-Φ curve. So the area below the nonlinear and idealised bilinear M-Φ curve must be the same. The moment capacity in the bilinear M-Φ curve does not imply the design value. An estimate of curvature ductility (μ_φ) and effective flexural rigidity (defined as the initial slope of the bilinear curve) of walls A and B are studied and reported in Table 2. The flexural rigidity is expressed as a function of the un-cracked flexural rigidity. The afore-mentioned parameters are estimated at axial load demands of 0.4 P_u, 0.21 P_u and 0.1 P_u. Results from Fig. 5, 6 and Table 2 indicate that

- Curvature ductility of walls A and B subject to high axial loads (>P_{bal}) is low since their failure is characterised by the compressive failure (crushing) of masonry rather than yielding of steel.
- A drop in the effective flexural rigidities is also observed at higher axial loads since the failure of walls at high axial is characterised by crushing of masonry rather than yielding of steel.
- Results also indicate that at medium to low axial loads, there is negligible effect of the reinforcement detailing on either the curvature ductility or the effective flexural rigidity (Fig. 7).

4   Idealised Moment-Curvature Curves

Analytical research by Sunitha et al. [5–7]) developed simple formulae based on limiting states of strain to obtain idealised bilinear M-Φ curve of RC sections. In this section, simple formulae are proposed to determine idealised multi-linear M-Φ curves. The points on the M-Φ curve are developed using point corresponding to limit states of strain in masonry and steel (as described in Sect. 2). Hence, simple formulae are proposed using the above limit states to develop idealised M-Φ curves of RM sections.

4.1 RM Walls with Axial Load, P < P$_{bal}$

The origin (0, 0) of the idealised bilinear M-Φ curve of RM section in the presence
of axial compressive load corresponds to the case of uniform strain variation across
depth ε_m of the section, at that level of axial load. Point 1 on the M-Φ curve away
from the origin is identified as the strain at which masonry cracks. Since masonry is
a material with negligible tensile strength, a small increment has to be provided at
the extreme compressed fibre to cause a strain gradient along the length of the wall.
In this study, 0.00005 is considered as the strain increment that gives a reasonably
accurate estimate of point 1 at all levels of axial loads. Strain at the opposite edge
is then estimated using principle of mechanics, discussed earlier. As described in
Fig. 8, point 2 corresponds to yielding of extreme layer of reinforcing steel in tension,
obtained only for axial loads $P \leq P_{bal}$. Point 3 corresponds to compression failure
limit state, while point 4 represents yield point of the M-Φ curve. The coordinates
of point 4 are determined as per Eqs. (5A)–(5C):

$$\phi_4 = \left[\frac{M_3 \phi_2 - M_2 \phi_3}{\phi_1 (M_3 - M_2) - M_1 (\Phi_3 - \phi_2)} \right] \phi_1 \tag{5A}$$

$$M_4 = M_1 \frac{\phi_4}{\phi_1} \tag{5B}$$
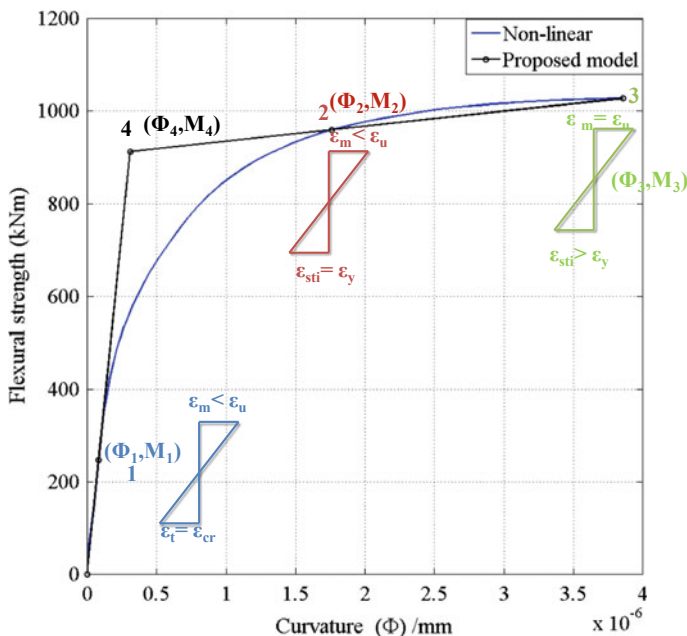
Fig. 8 Proposed multi-linear moment-curvature relationship of walls with low axial load

Table 3 Comparison of curvature ductility and effective flexural rigidity

Wall A			Wall B	
Parameter	Approach 1	Approach 2	Approach 1	Approach 2
Curvature ductility (μ_Φ)	12.47	12.31	12.84	12.84
Effective flexural rigidity	0.921	0.921	0.911	0.911
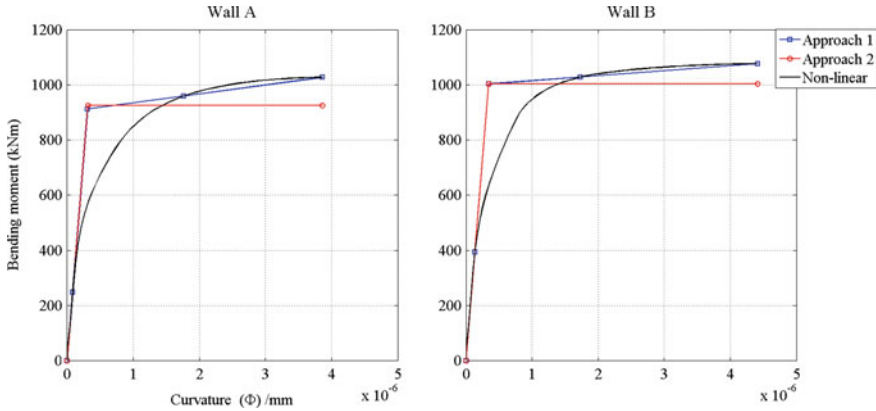
Fig. 9 Comparison of M-Φ curves ($P < P_{bal}$)

The curvature ductility is obtained as:

$$\mu_\varphi = \frac{\varphi_3}{\varphi_4} \tag{5C}$$

It is observed that the flexural strength of the RM wall obtained from the actual nonlinear M-Φ curve compares well with the flexural strength from Eqs. (5A) and (5B). The curvature ductility and effective flexural rigidities of walls A and B are compared with the respective values obtained in Sect. 3. Henceforth, the M-Φ curve obtained using the proposed method will be called **Approach 1** and the M-Φ curve obtained using equivalence of area will be called **Approach 2**. Idealised M-Φ curve obtained from Approach 1 and Approach 2 of wall A and wall B is compared with their respective nonlinear responses and is reported in Table 3 and Fig. 9. From the results obtained, it is observed that both curvature ductility and effective flexural rigidity obtained from Approach 1 compare very well with Approach 2.

4.2   RM Walls with Axial Load, $P = P_{bal}$

It is observed that in RM walls subject to an axial load that is equal to P_{bal} all the limit states in masonry and reinforcing steel are mobilised and results presented in Fig. 10 and Table 4 indicate that the equations prescribed in (5A) and (5B) hold good even for RM with an axial load $P = P_{bal}$.

Fig. 10 Comparison of M-Φ curves ($P = P_{\text{bal}}$)

Table 4 Comparison of curvature ductility and effective flexural rigidity

Wall A			Wall B	
Parameter	Approach 1	Approach 2	Approach 1	Approach 2
Curvature ductility (μ_Φ)	4.12	4.56	4.03	4.39
Effective flexural rigidity	0.863	0.863	0.884	0.884

4.3 RM Walls with Axial Load, $P > P_{bal}$

In RM walls subject to very high axial loads, all the limit states may not be mobilised (especially yielding of steel). So only three points are required to develop the idealised M-Φ curve that corresponds to limit states in masonry in cracking (point 1) and crushing (point 3). The coordinates of the yield point are obtained from the following formula:

$$\Phi_2 = \frac{M_3}{M_1}\Phi_1 \tag{6A}$$

$$M_2 = M_3 \tag{6B}$$

And curvature ductility is

$$\mu_\varphi = \frac{\varphi_3}{\varphi_2} \tag{6C}$$

If the limit state due to cracking of masonry is not mobilised (observed at axial loads close to and greater than 0.7 P_u), then point 1 is identified at a small strain increment $\Delta\varepsilon_m$ at the highly compressed edge. The authors would like to point out that Eqs. (6A) and (6B) are identical to proposed equations in Sunitha et al. [6, 7]. The idealised bilinear curve obtained from Eqs. (6A) and (6B) is compared to

the nonlinear response of wall (see Fig. 11). One observes that the proposed model gives a good estimate of the initial elastic behaviour and the flexural strength of the wall. The curvature ductility and flexural rigidity of wall A and wall B obtained from Eqs. (6A)–(6C) are compared with values obtained in Sect. 3, and results are reported in Fig. 12 and Table 5. From results obtained, it is observed that both the flexural rigidities and curvature ductility obtained from the proposed equation compare well with existing methods.
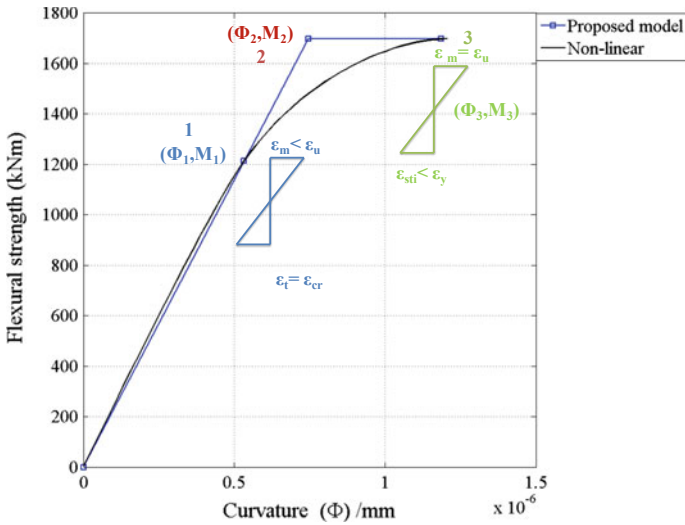
Fig. 11 Proposed multi-linear moment-curvature relationship of walls with high axial load
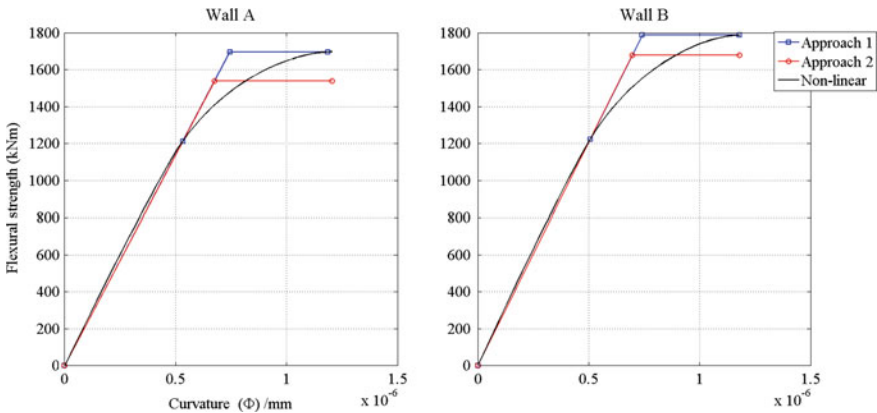
Fig. 12 Comparison of M-Φ curves ($P > P_{bal}$)

Table 5 Comparison of curvature ductility and effective flexural rigidity

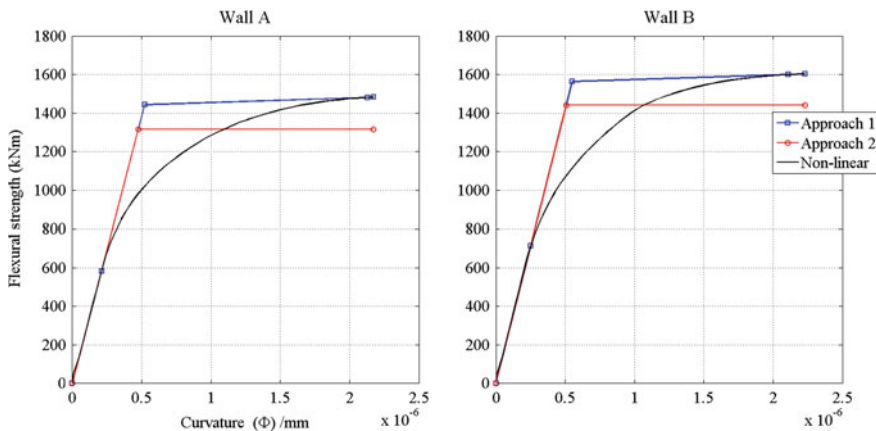| Wall A			Wall B	
Parameter	Approach 1	Approach 2	Approach 1	Approach 2
Curvature ductility (μ_Φ)	1.6	1.78	1.59	1.69
Effective flexural rigidity	0.710	0.710	0.756	0.756

5   Conclusions

The significant conclusions of this study are enumerated below:

- Simple hand-calculation-based multi-linear idealisation of actual nonlinear M-Φ curves proposed in this paper significantly reduces the computational time in determining the initial flexural rigidity, moment capacity and curvature ductility of RM sections subject to different levels of axial load without compromising on its accuracy. The equations proposed in this paper serve as a powerful yet simple to use tool to determine the multi-linear moment-curvature relation of reinforced masonry walls.
- Results from this paper indicate that the method of detailing of flexural reinforcement in a masonry wall affects neither the curvature ductility nor the initial flexural rigidity.

References

1. Gandhi, R., & Menon, A. (2014). Seismic performance of bed-joint reinforced solid brick masonry walls. In *Proceedings of the 9th International Masonry Conference, Guimaraes, Portugal.*
2. Indian Standard 1905 (1987), "Code of practice for structural use of unreinforced masonry", Bureau of Indian Standards, New Delhi.
3. Indian Standards-SP 7. (2016). *National building code, Part 6: structural design—Section 4: Masonry*. Bureau of Indian Standards.
4. Kaushik, H. B., Rai, D. C., Jain, S. K. (2007). Uniaxial compressive stress–strain model for clay brick masonry. *Current Science, 92*(4), 497–501.
5. Sunitha, P., Goswami, R., Murthy, C. V. R. (2015). Idealized bilinear moment-curvature curves of slender rectangular RC wall sections. *Journal of Seismology and Earthquake Engineering, 17*(3).
6. Sunitha, P., Goswami, R., Murthy, C. V. R. (2016). Seismic behaviour of RC moment resisting frame buildings designed and detailed as per first revision of IS 13920 draft provisions. *The Indian Concrete Journal, 90.*
7. Sunitha, P., Goswami, R., Murthy, C. V. R. (2016). Idealized moment-curvature curves of RC section for the pushover analysis of R.C. frame elements. *The Indian Concrete Journal, 90.*
8. Tomaževič, M. (1999). Earthquake-resistant design of masonry structures (pp. 159–173). Imperial College Press.

Performance of Self-flowing Concrete Incorporated with Alumina Silicates Subjected to Elevated Temperature

Manish S. Dharek, Prashant Sunagar, K. Harish, K. S. Sreekeshava, S. U. Naveen, and Bhanutej

1 Introduction

Concrete is one of the major building materials. With the accumulative need for housing both in rural and urban areas, the demand for building resources has been endlessly growing. The construction materials are produced by using natural wealth thus affects the surroundings by exhausting natural properties, using energy, and discharging toxins to the land and water. So in order to overcome from these problems, the alternative building materials for conventional concrete are used incorporating mineral admixtures, alumina silicates, etc.

Davidotis [1] in the year 1978 came up with a construction material as an green alternative for cement which was innovative and ecofriendly material which is sometimes referred as "geo-polymer." This was made by blending primarily silicon and aluminum materials such as fly ash, silica fume, rice husk ash. This process was carried under high alkaline conditions on Si-Al minerals, yielding polymeric Si-O-Al-O bonds in amorphous form.

The fire-resisting performance of concrete when compared to other structural materials such as wood and steel is by far superior. The main reason for the concrete to be fire resistant is due to non-combustibility and its capacity to withstand higher

M. S. Dharek (✉) · S. U. Naveen · Bhanutej
Department of Civil Engineering, BMS Institute of Technology and Management, Bengaluru, India
e-mail: manish.shashikant@gmail.com

P. Sunagar
Department of Civil Engineering, Ramaiah Institute of Technology, Bengaluru, India

K. Harish
Arvind Infrastructures Ltd., Bengaluru, India

K. S. Sreekeshava
Department of Civil Engineering, Jyothy Institute of Technology, Bengaluru, India

temperature gradients. It has been observed that the properties of concrete do not get affected when the temperature is less than 100 °C. However, when the temperature gradually goes on increasing beyond 100 °C, slight changes tend to occur inside the concrete. When the temperature exceeds more than 300 °C, contraction of cement paste and reduction in its compressive strength are observed. When the temperature exceeds 500 °C, the bond between the cement paste and the aggregate tends to get weaker in addition to rapid contraction of cement paste due to rapid loss of water from the concrete resulting in expansion of concrete and strength degradation

Abdullah [2] studied the impact of molarities of NaOH solutions on the compressive strength of fly ash-based geo-polymer paste. The samples which were calcined at high temperature showed improved mechanical properties, low porosity, higher density, low water absorption when compared to samples that were calcined at low temperatures. Dharek et al. [3] studied the impact of varying molarity of NaOH solution on the workability and mechanical properties of self-flowing concrete incorporating alumina silicates. It was concluded that chemical admixtures such as high range water reducers and viscosity-modifying admixtures played a vital role in improving workability and the compressive strength also improved with increase in molarity of NaOH solution. Mathew et al. [4] reported increase in compressive strength of geo-polymer concrete samples which were oven cured at a temperature of 100 °C and the compressive strength of the samples reduced when the temperature levels were increased beyond 100 °C. The total aggregate content played a vital role in increase of tensile strength of geo-polymer concrete. Ushaa et al. [5] studied the impact of various mineral admixtures by varying the molarity of NaOH solution in geo-polymer concrete. The GGBS-based geo-polymer mixes showed better workability properties when compared to mixes made with other mineral admixtures. The mixes containing silica fume showed superior mechanical properties when compared to mixes containing other mineral admixtures.

2 Materials and Methods

The program consisted of casting, curing and testing concrete cubes for compressive strength subjected to elevated temperature. (200, 400, 600 °C) by varying the molarity (6, 8, 10 M) maintained for a period of 60 min and air-cooled. The materials used for investigation included GGBS, fly ash, alkaline liquids, manufactured sand. The trial mix design for four proportions (fly ash: GGBS)—0:100, 10:90, 20:80, 30:70—was carried out. The mix design was carried out as per the method proposed by Rangan and Lloyd [6]. Since there was workability-related issues with 20:80 (fly ash: GGBS) proportion, to arrive at the optimum dosage of superplasticizer, Marsh cone test was carried out for the 30:70 proportion of fly ash to GGBS ratio. The details of the same are shown in Fig. 1a, b. The superplasticizer dosage of 0.4% was chosen based on trials from Marsh cone test. Initially, trials were conducted for 30:70 proportion with superplasticizer and later to obtain a mixing trials were conducted using Viscosity modifying agents. The mix proportion (30:70) with admixture dosage
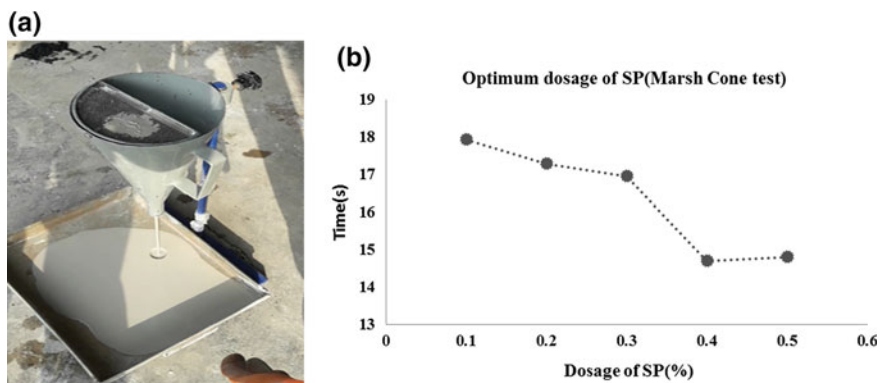
Fig. 1 **a** Marsh cone test. **b** Variation of SP dosage (percentage) versus time (seconds)

of superplasticizer weight of cementitious material (0.4%) and viscosity-modifying agent (0.1%) was chosen as it satisfied the workability criteria required for self-flowing concrete. The mix proportion details are shown in Table 1. The materials used in the present study were acquired locally from in and around Bengaluru except coarse aggregate which was procured from Bijapur, India, and the engineering properties were studied as per pertinent Indian Standards. The details of the same are given below

Table 1 Details of the mix proportion adopted

Sl. no.	Materials	Quantity
1	Coarse aggregate—10 mm downsize	$840/m^3$
2	M-Sand	$840/m^3$
3	Na_2SiO_3	$160/m^3$
4	NaOH	$64 g/m^3$
5	GGBS	$348/m^3$
6	Fly ash	$149/m^3$
7	Water	$125 kg/m^3$ (25% of cementitious materials)
8	Superplasticizer—PCE based	0.4% of cementitious material (GGBS + fly ash)
9	Viscosity-modifying agent	0.1% of cementitious material (GGBS + fly ash)

2.1 Fly Ash

Fly ash was obtained from RTPC, Raichur, for the present study. The fly ash obtained belonged to low calcium F-grade conforming to IS 3812-1981 requirements [7].

2.2 GGBS

This was acquired from JSW Steel Plant Bellary, India, conforming to IS 16714-2018 requirements [8].

The color was found to be whitish.

2.3 Fine Aggregate

M-Sand was used as a fine aggregate obtained from an M-Sand plant in Chikkaballapur, India. The M-Sand was found to be clean and dust-free conforming to IS 383-2016 [9] requirements. The specific gravity and fineness modulus were found to be 2.52 and 3.15, respectively. The M-Sand conformed to Zone II.

2.4 Coarse Aggregate

Coarse aggregate used for the present study was crushed basalt stone obtained from Bijapur, India. The coarse aggregate was conforming to IS 383-2016 [9] requirements. The specific gravity and fineness modulus were found to be 2.83 and 7.4, respectively.

2.5 Alkaline Liquids

Alkaline liquids used in the present study comprised of combination of sodium hydroxide (NaOH) and sodium silicates (Na_2SiO_3). The NaOH solution was prepared for different molarities of 6, 8, 10 M. The solution was prepared by dissolving the pellets in calculated amount of water. The sodium silicate solution was obtained from a local authorized manufacturer in Bengaluru. Sodium silicate was available in semisolid form.

2.6 Water

Water for the present study used was potable type conforming to requirements specified in IS-456-2000 [13].

2.7 Chemical Admixtures

In the present study, since high workability was the requirement, poly carboxylic ether based new age super plasticizer (PCE) was used. The dosage of the same was arrived by conducting trials using Marsh cone test as shown in Fig. 1b.

Since self-compaction was the requirement as part of the study, in addition to superplasticizer, viscosity-modifying agents were also used to modify the viscosity of concrete incorporating alumina silicates and to reduce the segregation. The chemical admixtures conformed to IS 9103-1999 [10].

3 Details of Casting and Experimentation

Sodium hydroxide solution was prepared 24 h before casting. The fine aggregates, coarse aggregates, fly ash and GGBS were weighed as per the proportions obtained through the mix proportion as per Rangan and Lloyd [6] given in Table 1. The workability tests were conducted as shown in Table 2. The cube specimens were kept in hot air oven at 60 °C for duration of 24 h. The specimens were taken out of the oven after 24 h and demoulded. The specimen was then kept for air curing for 28 days.

Table 2 Results of workability tests for varying molarity of self-compacted geo-polymer concrete

Sl. no.	Molarity (M)	Slump flow (mm)	V-funnel test (s)	L-box test
1	6	600	10.31	0.81
2	8	640	9.85	0.83
3	10	650	9.92	0.82
Range as per EFNARC specifications [12]		>600 mm	8–12 s	>0.8

Fig. 2 Details of slump flow, V-funnel and L-box test

3.1 Workability Tests

Tests such as slump flow, L-box, V-funnel test [12] were conducted for the samples by varying the molarities of NaOH, viz. 6, 8, 10 M with 30:70 proportion The details of the same are in Table 2 and Fig. 2.

3.2 Self-flowing Concrete Incorporating Alumina Silicates Subjected to Elevated Temperature

The cubes were air-cured for duration of 28 days under ambient temperature. Later, the cubes tested in a heavy-duty oven as shown in Fig. 3 for different temperature ranges (200, 400, 600 °C) for a duration of 1 h after the temperature levels of 200, 400, 600 °C as retention period were obtained. After the retention period, the specimens were removed and kept for air cooling to be brought to ambient temperature before the samples were kept inside the heavy-duty oven as shown in Fig. 3, and the mass of the cubes was noted down. After bringing the cubes to ambient temperature, again the

Fig. 3 Heavy-duty ovens used for subjecting the cubes to elevated temperature

mass of the cubes was noted down to get the percentage loss in mass after subjecting the self-compacted geo-polymer concrete cubes to elevated temperature.

4 Results and Discussion

The percentage weight loss and compressive strength of cubes oven cured for 24 h and subsequently air-cured subjected to elevated temperature ranges for a retention period of 1 h after the temperature levels of 200, 400, 600 °C is shown in Tables 3, 4 and 5, respectively, for variation of molarity (6, 8, 10 M). Figure 4 shows the cube samples after subjected to elevated temperature, respectively.

The percentage mass loss increases with increase in temperature which can be clearly seen in Fig. 5. This value is higher for samples subjected to temperature of 400, 600 °C when compared to samples subjected to temperature of 200 °C. An

Table 3 Mass loss and compressive strength of self-flowing concrete incorporating alumina silicates subjected to 200 °C temperature

Sl. no.	Molarity (M)	Specimen no.	1	2	3	Average
1	6	Mass loss (kg)	0.03	0.04	0.03	0.03
		Compressive strength (MPa)	50.0	39.6	49.6	46.4
2	8	Mass loss (kg)	0.02	0.03	0.03	0.04
		Compressive strength (MPa)	51.1	50.6	50.5	50.7
3	10	Mass loss (kg)	0.02	0.03	0.02	0.03
		Compressive strength (MPa)	54.4	59.3	59.8	57.8

Table 4 Mass loss and compressive strength of concrete incorporating alumina silicates subjected to 400 °C temperature self-flowing

Sl. no.	Molarity (M)	Specimen no.	1	2	3	Average
1	6	Mass loss (kg)	0.18	0.21	0.15	0.18
		Compressive strength (MPa)	59.0	47.7	60.6	55.7
2	8	Mass loss (kg)	0.24	0.21	0.21	0.22
		Compressive strength (MPa)	64.3	62.6	59.9	62.3
3	10	Mass loss (kg)	0.21	0.21	0.23	0.21
		Compressive strength (MPa)	64.5	70.8	60.3	65.2

Table 5 Mass loss and compressive strength of self-flowing concrete incorporating alumina silicates subjected to 600 °C

Sl. no.	Molarity (M)	Specimen no.	1	2	3	Average
1	6	Mass Loss (kg)	0.22	0.38	0.39	0.33
		Compressive Strength (MPa)	62.0	58.5	57.6	59.3
2	8	Mass Loss (kg)	0.24	0.25	0.27	0.25
		Compressive Strength (MPa)	66.3	64.8	63.5	64.8
3	10	Mass Loss (kg)	0.23	0.27	0.29	0.26
		Compressive Strength (MPa)	67.5	68.4	66.3	67.4

Fig. 4 Concrete incorporated with alumina silicates samples subjected to elevated temperature

increase in average compressive strength can also be observed with the increase in molarity as shown in Fig. 6.

5 Conclusions

The following conclusions are drawn based on the experimental investigations on self-flowing concrete incorporated with alumina silicates.

- The percentage mass loss in samples increased with increase in temperature. The reason attributed to this can be due to evaporations of calcium alumina silicate gel and sodium aluminosilicate hydrate as noticed by Rao et al. [11]. This is shown in Fig. 5. The percentage mass loss is more in the case of samples with 10 M.
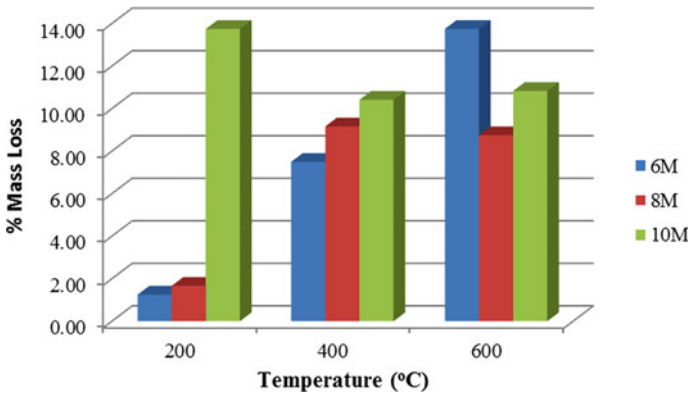
Fig. 5 Variation of percentage mass loss of specimens subjected to elevated temperature
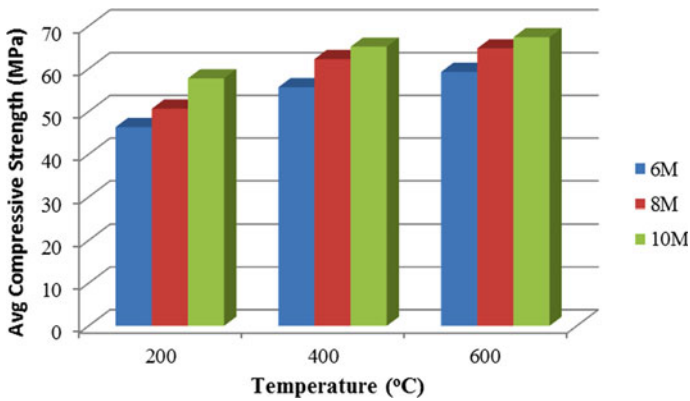
Fig. 6 Variation of compressive strength of specimens subjected to elevated temperature

- The increase in concentration of NaOH leads to an increase in compressive strength of samples subjected to higher temperature indicating the importance of molarity.

References

1. Davidovits, J. (2013). Geopolymer cement a review. In *Geopolymer science and technics*. Saint-Quentin, France: Technical Paper #21, Geopolymer Institute Library.
2. Abdullah, L., Al Bakri, A. M. M., Kamarudin, H., Ruzaidi, C. M., Yahya, Z., Salleh, M. A. A., et al. (2014). Compressive strength and morphology of fly ash based geopolymer as artificial aggregate with different curing temperature. *Key Engineering Materials*, *594–595*, 151–155.

3. Dharek, M. S., Sunagar, P., Bhanu Tej, K. V., & Naveen, S. U. (2019). Fresh and hardened properties of self-consolidating concrete incorporating alumina silicates. In B. Das & Neithalath N (Eds.), *Sustainable construction and building materials. Lecture notes in civil engineering* (Vol 25). Singapore: Springer.
4. Mathew, B. J., Sudhakar, M., & Natarajan C. (2013). Strength, economic and sustainability characteristics of Coal ash-GGBS based geopolymer concrete. *International Journal of Computational Engineering Research, 3*(1).
5. Ushaa, T. G., Anuradha, R., & Venkatasubramani, G. S. (2015). Performance of self-compacting geopolymer concrete containing different mineral admixtures. *Indian Journal of Engineering & Materials Sciences, 22,* 473–481.
6. Rangan, B. V., & Lloyd, N. A. (2010). Geopolymer concrete with fly ash. In *Second International Conference on Sustainable Construction Materials and Technologies*, Italy.
7. IS 3812-1981. *Specification for fly ash for use as pozzolana and admixture*. New Delhi: Bureau of Indian Standards.
8. IS 16714-2018. *GGBS for use in cement, mortar and concrete-specifications*. New Delhi: Bureau of Indian Standards.
9. IS 383-2016. *Coarse and fine aggregate for concrete—code of practice*. New Delhi: Bureau of Indian Standards.
10. IS 9103-1999. *Concrete admixtures-specification*s. New Delhi: Bureau of Indian Standards.
11. Mallikarjuna Rao, G., Gunneswara Rao, T. D., Siva Nagi Reddy, M., & Rama Seshu, D. (2019). A study on the strength and performance of geopolymer concrete subjected to elevated temperatures. In A. Rao, & K. Ramanjaneyulu (Eds.), *Recent advances in structural engineering, Volume 1. Lecture notes in civil engineering* (Vol. 11). Singapore: Springer.
12. EFNARC. (2005). *The European guidelines for self compacting concrete, specification, production and use.*
13. IS 456-2000. *Plain and reinforced concrete—Code of practice*. New Delhi: Bureau of Indian Standards.

Response of RC Short Column Under Combined Fire and Axial Loading

Chinthapalli Hemanth Kumar, B. Subash, and Anil Agarwal

1 Introduction

Columns are the main structural members that transfer loads of superstructure to the foundation. RC structures are one of the majorly adopted construction practices. Numerous characteristics of an RC column affect the overall strength of the members: volume of longitudinal and confining reinforcement, length, load eccentricity, cross-section area, end connections, type of concrete, and strength of the steel.

Mander et al. [1] studied the behavior of RC columns of different cross-section like rectangular, square, and circular. For all section types, the most important parameter influencing the stress–strain curve of confined concrete was the volume of confining reinforcement. Confining reinforcement for square or rectangular columns may be in the form of rectangular hoops or cross ties, spirals for circular columns. The volumetric ratio of confining reinforcement increases the strength and decreases (flattened) the slope of the falling branch. The circular, spiral-confined columns performed better than rectangular or square columns. This results in both the strength and the ultimate compression strain enhancement for a given volumetric confinement ratio.

Cusson and Paultre [2] studied the behavior of high-strength-concrete (HSC) columns confined by rectangular ties under axial loading. The lateral reinforcement ratio increases from 2.0 to 2.8% showing 10% increase in the strength. Larger confining pressure due to smaller tie spacing results in better confinement efficiency on the concrete core. An increase in the strength of the confining reinforcement results

C. Hemanth Kumar (✉) · A. Agarwal
Department of Civil Engineering, Indian Institute of Technology Hyderabad, Hyderabad, India
e-mail: ce15resch11006@iith.ac.in

B. Subash
Department of Civil Engineering, SASTRA Deemed to be University, Thanjavur, India

increase in strength and toughness only for well-confined specimens with a large volume of confining reinforcement ratios. Some interactions between other variables were noticed. Therefore, when evaluating the influence of an individual variable on confined concrete behavior, this should be viewed as only a partial effect. Jun-Ichi et al. [3] also observed that the columns with a high amount of lateral ties perform better than the columns with a small number of lateral ties at ambient temperature. Different parameters like column length, cross-section, longitudinal reinforcement that influence the fire performance of RC Columns are studied by several researchers [4–11].

The behavior of RC columns under fire conditions are different from ambient conditions which result in thermal stresses and spalling of the concrete. Few researchers such as Kodur et al. [10, 12] made comparitive study of the fire resistance performance of high-strength-concrete (HSC) columns with that of normal-strength-concrete (NSC) and fiber-reinforced HSC columns. The observations are different type of fibers prevent the cracking implies an increase in the tensile strength and spalling of the concrete, results in fire endurance of HSC concrete. The columns with stirrups bent at 135° bend at ends performed better than the columns with stirrups at 90° bend at ends. The confining pressure from stirrups does play a role in fire endurance of the RC columns. The current design specifications such as Eurocode-2 and IS:1642 provide design guidelines for fire safety of concrete structures and strength calculation methods based on the amount of longitudinal reinforcement, temperature contour of the section, the percentage of design load acting on the column, and clear cover.

The main focus is to study the confining reinforcement spacing on the fire behavior of the RC column capacity by keeping all other parameters same, i.e., using the same concrete mix, volume of longitudinal reinforcement, shear reinforcement, and the same moisture content in all the specimens. To achieve this, the specimens with the same volume of lateral reinforcement with different spacing (by changing the diameter of the stirrup) are heated for the required duration and tested for mechanical loads to quantify the load carrying capacity of the RC columns.

1.1 Experimental program

1.1.1 Test Setup and Instrumentation

The concrete column tests were conducted at Indian Institute of Technology, Hyderabad, for exploitation; Fig. 1a shows the experimental test setup and loading mechanism and Fig. 1b shows the thermocouple locations along the cross-section at mid height of the column. This heating test setup was designed to fix in the desired configuration as a rectangular, square or heating wall in loading frames available at Indian Institute of Technology, Hyderabad. The radiant heating panels can heat the assembled chamber up to 1000 °C. The test set up consists of four radiant heating panels; every heater is with 305 mm × 450 mm heating area with a PID controller. A data acquisition system with two modules having 16-thermocouple channels for
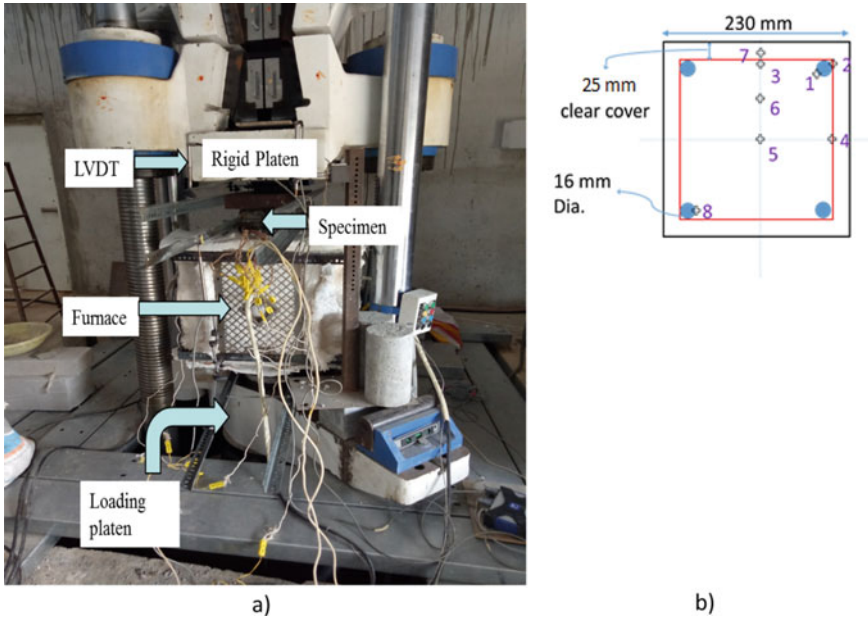
Fig. 1 **a** Test setup with loading frame **b** thermocouple locations in the specimen at mid height

each module is used to acquire temperature data from the specimen and chamber cavity at desired intervals. The sample rate at which each module can acquire data is 75 S/s at high speed and 1 S/s at high resolution.

A set of four heaters are arranged as a rectangular tube of internal size approximately 420 mm × 420 mm, around the column. These heaters are placed such that all the four sides of the column are parallel and at equal distance from the face of each radiant heater, i.e., the internal face of the rectangular tube chamber. To prevent the electrocute and damage of the heater surface due to direct contact of the spalled concrete portions, a clear space of 90 mm was ensured on each face of the specimen and furnace internal heating surface. It should be noted that the full length of the column was not subjected to heating, the specimen ends were not heated because of their proximity to the hydraulic system and column supports on rigid platens. To prevent the escape of the heat from the rectangular tube, ceramic glass wool fiber blanket of density 128 kg/m³ is filled at the ends of furnace and opening which can resist temperature up to 1260 °C. It was observed that the maximum temperatures did not exceed 50 °C at the column ends during the experiment. Four linear variable differential transformers (LVDTs) are used to measure the axial deformations at the end of the column to trace the deformation at the center of the column. The test results shown in this paper include axial loads, concrete and reinforcing steel temperatures in the column and the furnace chamber temperatures for each specimen.

Table 1 Specimen heating duration and failure load

S. No.	ID of the specimen	Spacing of stirrups (mm)	Dia. of stirrups (mm)	Heating duration min (Hrs)	$f'c$ (MPa)	Failure loads (in kN)
1	S75H2	75	6	120(2)	30	830
2	S130H2	130	8	120(2)	30	908
3	S200H2	200	10	120(2)	30	800
4	S75H3	75	6	180(3)	30	724
5	S130H3	130	8	180(3)	30	729
6	S200H3	200	10	180(3)	30	664

1.1.2 Testing Procedure

The column specimens were tested as follows: (1) The column was centered in the loading frame to prevent the load eccentricity and heaters are assembled around the column with clear distance of minimum 90 mm from the face of the column as discussed in test setup and instrumentation section. The specimen is heated for specified duration mentioned in Table 1 to achieve desired ISO fire curve in the furnace chamber. For the safety of the instrument and its limitations, after the one-hour duration, the average temperature in the furnace chamber was maintained constant at 950 °C till the desired time duration. During the heating process, the columns are allowed to expand freely, i.e., no axial restraints. (2) Axial load was increased monotonically up to the failure of the column. The columns are deemed to fail when the load falls by 20 percent of the peak load.

1.1.3 Test Matrix

Test matrix of the column tests, including the details of the lateral reinforcement bar diameter, duration of heating are presented in Table 1. The test matrix includes six reinforced concrete columns out of which all have the same amount of lateral and longitudinal reinforcements.

The dimensional details of the column are 860 mm long, 230 mm × 230 mm^2 cross-section and the column slenderness ratio (*L/D*) was approximately equal to 3.73. All the specimens are reinforced with the same volume of longitudinal reinforcement four numbers-16 diameter bars, i.e., 804.2 mm^2 of grade Fe500.

The concrete mix proportion is designed as per IS 10262:2009 to achieve cylindrical strength of 30 MPa. The average ($f'c$) strength is 31.76 N/mm^2. The concrete mix proportion is presented in Table 2.

Table 2 Mix proportions

Grade of concrete	W/C ratio	Cement	Sand	Coarse aggregate
M30	0.4	1	1.92	3.6
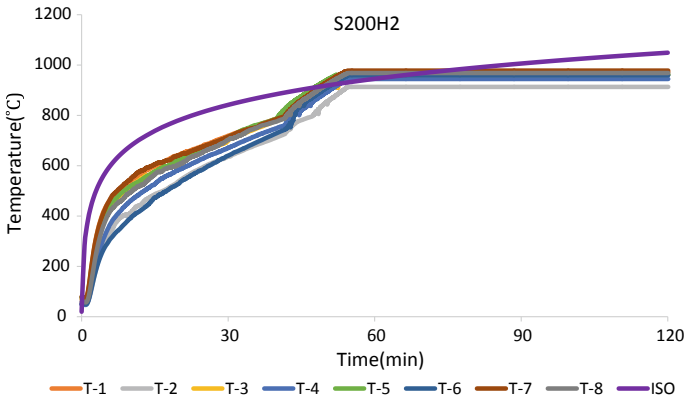
Fig. 2 Chamber time–temperature curves of cavity

1.1.4 Time–Temperature Responses in Furnace Chamber

Figure 2 shows the average temperature–time $(T - t)$ responses measured in the cavity. Minimum eight thermocouples are placed inside the cavity to measure the average temperature in the furnace as per the requirements mentioned in ASCE-E119 and IS: 3809-2000 for column tests apart from the PID-thermocouple and limit thermocouple to control the furnace temperature. The location of the furnace thermocouples is shown in Fig. 4.

The temperature is measured during the experiment from the eight chambers thermocouple; we have shown in Fig. 2 for one of the specimens (S200H2). The average furnace temperature from all the thermocouples for six specimens is shown in Fig. 3 (Fig. 4).

1.1.5 Temperature–Time Responses of Specimens

The temperature–time $(T - t)$ response measured from the specimens in reinforcement and core of the concrete. The location of the thermocouples in the cross-section for all the specimens is same, which is presented in Fig. 1b. The temperature–time curves in the specimens S200H2 and S200H3 are presented in Fig. 5. It was observed that the temperatures in all the section at a given location is almost same for all the samples for a given furnace temperature–time curve, the slight variation of the temperature profiles are due to the small difference in the average furnace cavity temperature–time curves which were presented in Fig. 3.
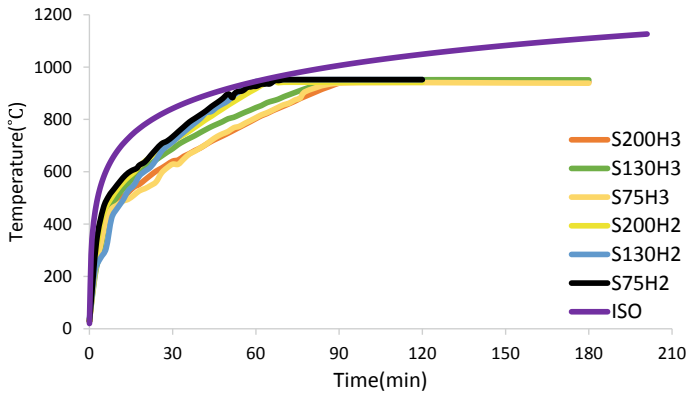
Fig. 3 Average cavity temperatures in the furnace

(a) Plan   (b) Elevation
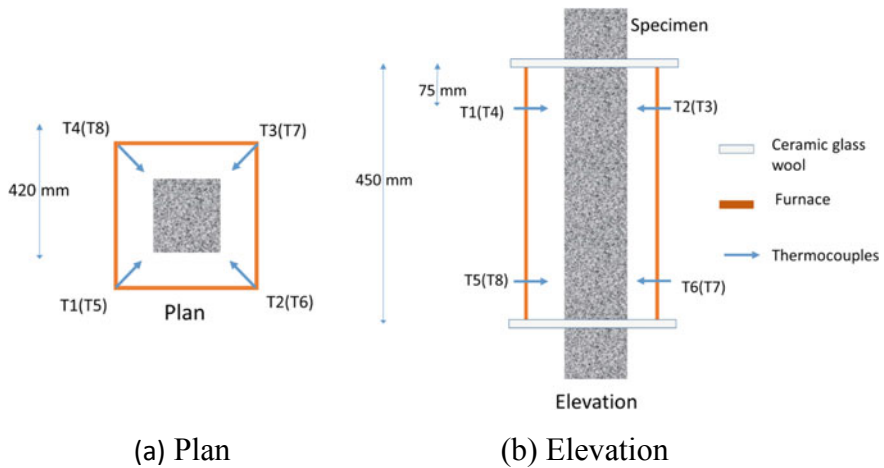
Fig. 4 Schematic of the furnace showing the location of the chamber thermocouples
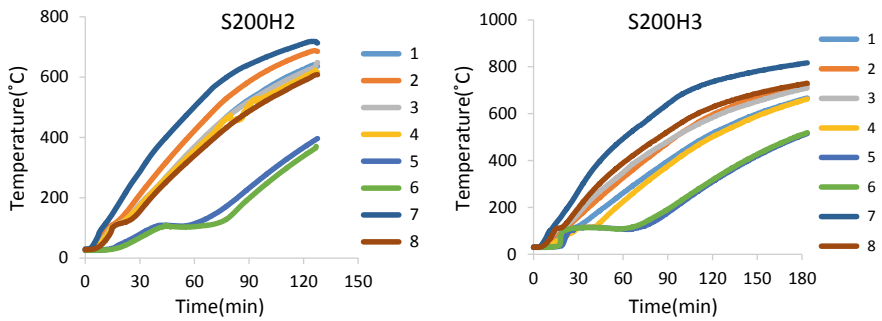
Fig. 5 Temperature–time curve of specimens

2 Test Results

In the present study, the volumetric ratio of transverse reinforcement is kept the same in all the test specimens irrespective of the diameters of stirrups used (6, 8 and 10 mm). It was observed that the columns with 8 mm dia. stirrups at 130 mm spacing having a high load carrying capacity 907 kN for 120 min and 728 kN for 180 min duration of heating under ISO fire curve, respectively. Whereas the column with 6 mm stirrups at 75 mm spacing having a maximum load bearing capacity of 829 kN and 724 kN for 120 min and 180 min duration of heating under ISO fire curve, respectively. Similarly, 10 mm stirrups at 200 mm spacing having maximum load bearing capacity of 800 kN and 664 kN for 120 min and 180 in duration of heating under ISO fire curve. The load–deformation curve is presented in Fig. 6; we can clearly observe that stiffness and strength of specimens with 8 mm stirrups are more than specimens with 6 and 10 mm stirrups.

From the failure loads, it is observed that 8 mm stirrup gave higher load capacity at elevated temperature, which creates a mismatch with the ambient temperature behavior. It was observed from the graph that the stiffness of the columns with 8 mm dia. stirrup columns gave higher performance when compared with 6 and 10 mm stirrup columns. The ductility of the columns with 6 mm dia. stirrups are executing more than the other two columns.

As per the literature available on the RC columns at ambient temperatures, the load bearing capacity of the column increases with decrease in spacing between the stirrups, this may be due to increase in spacing between the stirrups, the effective confining zone decrease, which cannot prevent the lateral bulging of the column results in failure. Whereas in case of columns with closer spacing of stirrups, the effective confined area by the lateral reinforcement is effected by the closer stirrups and results in constant load bearing capacity after certain closer spacing. The hypothesis that
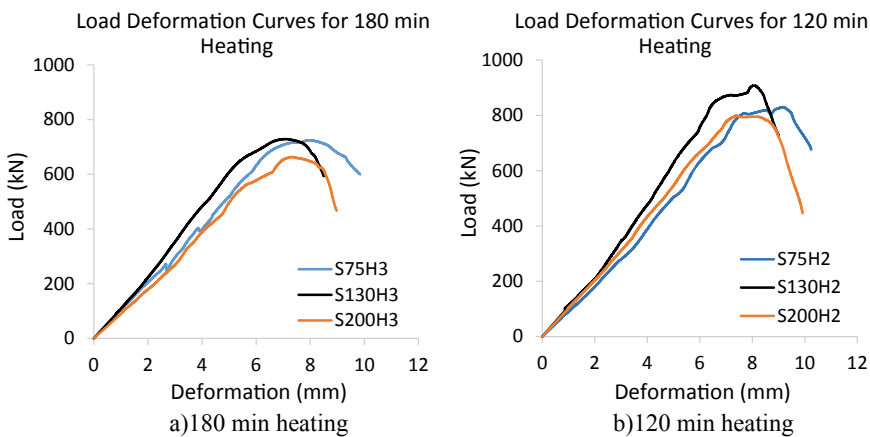
Fig. 6 Load–deflection response; **a** 180 min **b** 120 min duration of heating

the authors made here to explain the decrease in load carrying capacity with lesser spacing between the stirrups is: due to overlapping of the confining zone or region by a stirrup the effective confining pressure on concrete between the stirrups is limited. Which may results in constant load bearing capacity, after certain decrease of spacing between the stirrups. But when the confining reinforcement strength decreases at high temperature due to material property degradation, the effective confining pressure at higher temperatures on the same zone increases results in higher load carrying capacity, which was observed in case of columns heated for 180 min duration under ISO fire curve.

In Fig. 7, the peak loads are compared between different spacing of reinforcement at 120 min and 180 min duration of heating. In the case of 180 min duration of heating, the peak loads for specimens S75H3 and S130H3 are almost same but whereas for specimen S200H3, the spacing of shear reinforcement affected the load carrying capacity of the columns with increase in spacing of stirrups the loading capacity decreases. This is true in case of S130H2 and S200H2, the increase in spacing of stirrups from 130 to 200 mm spacing with same volumetric ratio.

This hypothesis made by the authors is also validated with the numerical analysis developed by the authors to simulate the RC columns under fire conditions [13, 14]. To get understanding and insight into this problem, authors are conducting few more experiments with wide range of parameters. The hidden parameter, the effective cover, may play a role in better performance of the column in case of larger diameter stirrups as the clear cover kept same to all the stirrups. This will be addressed by studying a detailed parametric study using numerical model developed by the authors [13, 14].
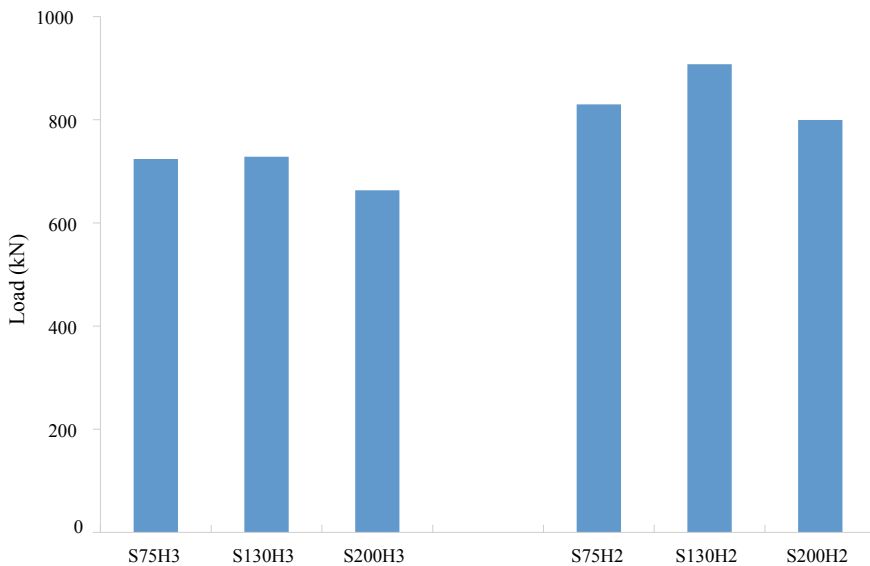
Fig. 7 Peak load comparison of specimens with different volume of stirrups

3   Conclusions

The photographs of damaged specimens after the test were presented in Fig. 8; it was observed that the columns failed in pure compression at the center of the heating portion. The columns with 8 mm diameter stirrup at 130 mm spacing performed better than the columns with 6 mm and 10 mm stirrups at 75 and 200 mm spacing, respectively.

The behavior observed in the tests leads to the following conclusions:

1. The moisture in the concrete evaporates at an initial 60 min duration of heating. During the initial 60 min, the test zone reaches about 130 °C. The change in concrete temperatures is very small in between 90 and 130 °C. In the outer periphery of the column, the moisture effect on temperatures is not high due to the escape of hot vapor from the periphery of the column.
2. All the columns failed in a compression mode at the mid height of the heating zone.
3. The columns with 8 mm diameter stirrups at 130 mm spacing gave approximately 10% higher load capacity than 10 mm dia. stirrups at 200 mm spacing for 120 min duration under ISO fire curve.
4. The columns with 6 mm and 8 mm dia. stirrups at 75 mm and 130 mm spacing, respectively, carried 8% higher load compared to columns with 10 mm dia. stirrups at 200 mm spacing for 180 min duration under ISO fire curve.

A more detailed experimental program (12 more columns) is planned by the authors with a wide range of variables to get insight into the effect of spacing on the fire behavior keeping the total volume of confining reinforcement constant.
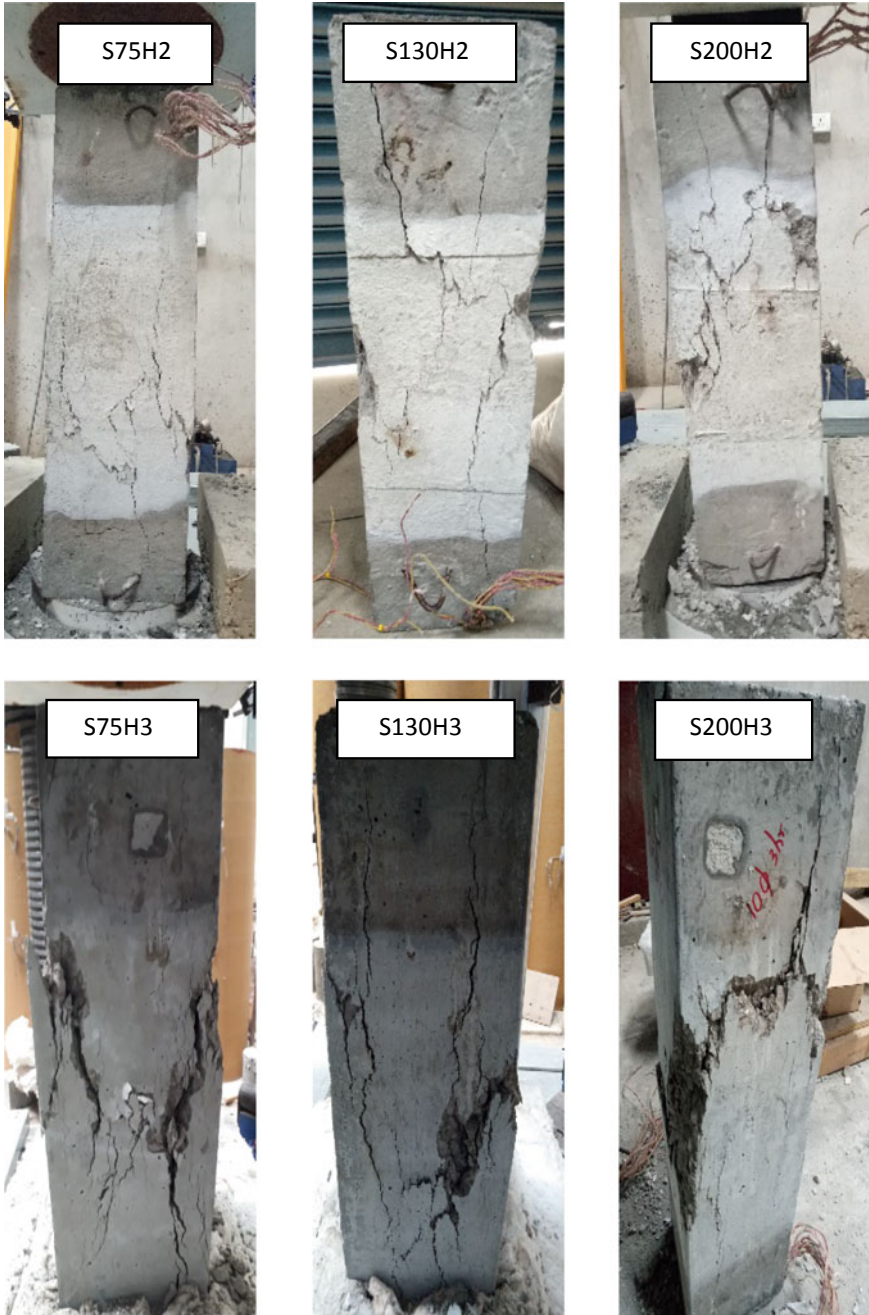
Fig. 8 Photographs of the specimen after test for 120 and 180 min of heating

References

1. Mander, J. B., Priestley, M. J. N., & Park, R. (1988). Observed stress-strain behavior of confined concrete. *Journal of Structural Engineering, 114*(8), 1827–1849.
2. Cusson, D., & Paultre, P. (1994). High strength concrete column confined by Rectangular ties. *Journal of Structural Engineering, 120*(3), 783–804.
3. Hoshikuma, J., Kazuhiko, K., Kazuhiko, N., & Taylor, A. W.(1996) A model of confinement effect on stress-strain relation of reinforced concrete columns for seismic design.
4. Kodur, V., Cheng, F.-P., Wang, T.-C., & Sultan, M. (2003). Effect of strength and fiber reinforcement on fire resistance of high-strength concrete columns. *Journal of Structural Engineering, 129*(2), 253–259.
5. Wu, H., & Lie, T. T. (1992). Fire resistance of reinforced concrete columns: experimental studies. *NRC Publications Record*, No. 632.
6. Lie, T., & Woollerton, J. (1988). *Fire resistance of reinforced concrete columns: Test results, national research council of Canada* (Internal Report 569). Institute for Research in Construction.
7. Lie, T. T. (1989). Fire resistance of reinforced concrete columns: A parametric study. *Journal of Fire Protection Engineering, 1*(4), 121–129.
8. Dotreppe, J.-C., Franssen, J.-M., Bruls, A., Baus, R., Vandevelde, P., Minne, R., et al. (1997). Experimental research on the determination of the main parameters affecting the behaviour of reinforced concrete columns under fire conditions. *Magazine of Concrete Research, 49*(179), 117–127.
9. Kodur, V., & Phan, L. (2007). Critical factors governing the fire performance of high strength 456 concrete systems. *Fire Safety Journal, 42*(6), 482–488.
10. Kodur, V., Cheng, F., Wang, T., Latour, J., & Leroux, P. (2001). Fire resistance of high performance concrete columns. *NRC Publications Record* (I R C - I R - 8 3 4).
11. Kodur, V., McGrath, R., Leroux, P., & Latour, J. (2005). Experimental studies for evaluating the fire endurance of high-strength concrete columns.
12. Kodur, V., & Mcgrath, R. (2003). Fire endurance of high strength concrete columns. *Fire Technology, 39*(1), 73–87.
13. Chinthapalli, H. K., & Agarwal, A. (2018). Role of confinement on fire resistance capacity of RC columns. In *3rd R. N. Raikar Memorial International Conference and Gettu-Kodur International Symposium on Advances in Science and Technology of Concrete, Mumbai*.
14. Chinthapalli, H. K., & Agarwal, A. (2019). Effect of confining reinforcement on fire behavior of reinforced concrete columns–An experimental and numerical study. *Journal of Structural Engineering, ASCE*.

Numerical Analysis of Post-earthquake Fire Resistance of Concrete-Filled Tubular Steel Columns

Smita Singh and Anil Agarwal

1 Introduction

Earthquakes are one of the most devastating forms of natural hazard, which can have a severely debilitating effect on structures. But if an earthquake event is followed by fire, it may cause even more damage than the earthquake. In the past several cases of fire following the earthquake, a large amount of damage has been documented. In the early twentieth century, devastating fire following the San Francisco, California earthquake in 1906 and Tokyo earthquake in 1923 caused significant damage to both the cities [1]. Although large-scale post-earthquake fires have not been reported recently, there are numerous incidents of isolated post-earthquake fires causing significant damages [2]. Hundreds of fires were reported after the 1994 Northridge, 1995 Kobe and 1989 Loma Prieta earthquakes. Recently, Davidson [3] reported several conflagrations after Japan earthquake of 2011.

After a major earthquake, the ability of the structure to resist fire drastically reduces. Also, the risk of fire after an earthquake increases significantly. Although the fire following an earthquake has a devastating effect, the subject has not received enough attention. There is a need to investigate the resistance capacity of structures under the combined effect of earthquake and fire. Until now, several researchers have studied the behaviour of CFST columns at fire and earthquake separately, but none have studied the behaviour of CFST column under the effect of both incidents.

Several researchers have worked on the seismic behaviour of CFST columns and indicated the desirable seismic performance of CFSTs. In the interest of brevity, only one example is being presented here. Han and Yang [4] experimentally investigated

S. Singh (✉) · A. Agarwal
Department of Civil Engineering, Indian Institute of Technology Hyderabad, Hyderabad, India
e-mail: ce17resch11007@iith.ac.in

A. Agarwal
e-mail: anil@iith.ac.in

the seismic behaviour of eight circular CFST columns. Specimens were tested under constant axial load and cyclically increasing flexural loading. They also performed the nonlinear full range analysis of these composite columns for simulating the test results and did the parametric study. They analysed the influence of several parameters on the behaviour of the moment versus curvature response and the lateral load versus lateral displacement relationships for the composite columns.

A number of other studies have exhibited the superior fire resistance properties of CFSTs in comparison with steel members [5, 6]. Hong and Varma [5] analytically studied the behaviour of loaded CFT columns under standard fire. The sequentially coupled thermal stress analysis was used to predict the behaviour of the CFT columns subjected to standard fire loading. They conducted a detailed sensitivity analysis to determine relevant input parameters for the analytical models. Consequently, they used Poh 2001 σ–ε–T model for modelling steel tube and Lie and Irwin 1995 σ–ε–T model for the concrete infill [7]. They used linear thermal expansion models for steel and concrete materials and recommended full composite action with no local buckling to model the CFT column specimens.

Very few researchers [8–11] have studied the post-earthquake fire behaviour of different structural systems. Yassin et al. [8] conducted an analytical study on the performance of moment-resisting steel frames in the post-earthquake fire. They found that the performance of the structure highly depends upon the residual lateral deformations present in structure caused by the earthquake. Fire induces asymmetrical deformations due to uneven heating. This amplifies the previously present residual deformations in the structure and significantly reduces the fire resistance of the structure, while the frames with no residue displacement from a prior seismic loading exhibit better fire resistance properties.

Imani et al. [9, 10] demonstrated through both experimental and numerical studies effect of post-earthquake fire resistance of concrete-filled double-skin tube (CFDST) columns. After an initial simulation of lateral loading, they observed that concrete damage plasticity (CDP) model for concrete failed to capture the pinching phenomena of the hysteresis behaviour. Considering the shortcoming of the CDP model, they modified the model by inserting the horizontal discrete crack [12] at the location of maximum tensile stress. The numerical predictions of failure time-matched preferably with the experimental results.

Talebi et al. [11] developed and validated a nonlinear three-dimensional finite element model for investigating the behaviour of CFST columns subjected to post-earthquake fire. They reported that CFT columns use benefits of the composite action between the steel tube and in-filled concrete and could behave in a ductile manner.

Concrete-filled steel tube (CFST) column has shown good resistance under cyclic as well as fire loading conditions. This study expands on these previous studies by investigating the behaviour of CFSTs numerically when exposed to fire after an earthquake. In this paper, a three-dimensional finite element model was developed in ABAQUS [13]. The various key variable also included in modelling like material degradation properties at elevated temperature, contact between steel tube and concrete core, initial imperfection. The steps involved in numerical modelling were cyclic, heat transfer and structural analysis. First effect of earthquake loading was

simulated by cyclic loading of the specimen, and then, the outcome of the cyclic loading in terms of residual deformation was applied as an initial condition to the sequentially coupled thermal stress analysis. Results of the finite element model were compared with the experimental results of cyclic loading test [4] and fire loading test [14] separately to check the accuracy of the numerical model. Finally, validated numerical model was used to study the behaviour of CFST column under cyclic and fire loading as multi-hazard event.

2   Numerical Model Under Cyclic Loading

Effect of earthquake loading was studied by subjecting the CFST column under cyclic loading. A three-dimensional finite element model was modelled in ABAQUS. The validity of the numerical model was verified by the results of the experiment on CFST columns conducted by Han and Yang [4]. They have experimentally studied the behaviour of eight CFST column under cyclic loading, and columns labelled as SC2-3 and SC2-4 modelled in this study for verification purpose. Details of the specimens are enlisted in Table 1 where N_o is the axial load applied on the composite specimen, f_c is the compressive strength of concrete; f_y is the yield strength of steel, E_s is the modulus of elasticity of steel.

2.1   Loading, Boundary Condition, Contact at the Steel Tube–Concrete Core Interface and Initial Imperfection

Two rigid steel plates of 16 mm thick were modelled at the columns endings to apply the boundary condition and axial loading. Pinned-pinned boundary conditions were modelled at both the endings, and one end was free to move longitudinally for application of axial load. To apply the cyclic loading, a rigid steel stub of 150 mm length was modelled at the centre of the CFST column to exactly replicate the experimental setup. Loading was applied stepwise. First, the axial load was applied and kept constant throughout the analysis, and then, cyclic loading is applied according to ATC-24 [15] loading protocol to simulate the seismic behaviour. Cycles were imposed in levels of Δy, 1.5 Δy, 2 Δy, 3 Δy, 5 Δy, 7 Δy, 8 Δy, where Δy was the yield displacement of the column and Δy were used as obtained in the test [13]. Specimens are generally not straight due to the manufacturing process and consist of some initial geometric

Table 1   Detail of the CFST columns for cyclic analysis

Column	L (mm)	$D \times t$ (mm)	f_c (MPa)	f_y (MPa)	E_s (GPa)	N_o (KN)
SC2-3	1500	114 × 3	38.9	308	200	286
SC2-4	1500	114 × 3	38.9	308	200	429

imperfection. So, to account for initial geometric imperfection, eigenvalue buckling analysis was conducted in ABAQUS [13]. Then, first mode shape was multiplied by an amplification factor of L/1000 was used as an initial imperfection. L is the length of the column. Boundary conditions were chosen such that they could replicate the experimental condition. To model, the interface between the steel tube and concrete core normal behaviour and tangential behaviour were used. A "hard contact" definition was used to simulate the normal behaviour. Coulomb friction model with a constant coefficient value of 0.2 used to simulate the tangential behaviour.

2.2 Material Model

For modelling the steel material properties, a bilinear material model consisting of a linear elastic phase and post-yield linear hardening phase was used. The elastic response of steel was modelled using elastic modulus as 200 GPa and Poisson's ratio as 0.3. Plastic behaviour of the structural steel was modelled by kinematic hardening model. The behaviour of concrete in tension and compression was done according to EN 1992 1-1. Initial elastic modulus of concrete was calculated according to EN 1992 1-1, and Poisson's ratio was taken as 0.2. To model, the plastic behaviour of concrete damage plasticity model [11, 13, 16] implemented in ABAQUS was used.

2.3 Element Model

The 3D solid element is used to model the concrete core, steel tube and steel plate because it can capture large deformation and plastic strains. Because of the high computational time of 20 node elements during analysis, a three-dimensional eight-node solid elements with reduced integration are used to model in the present study to decrease the computational time during analysis. Figure 1 shows the whole finite element model of column.
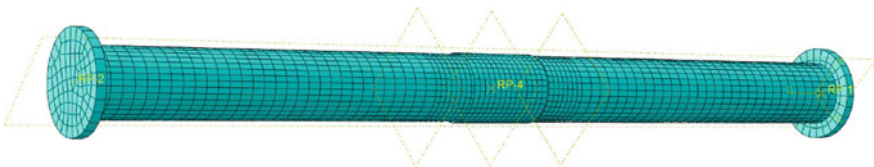
Fig. 1 Whole FE model

2.4 Validation of Numerical Model Under Cyclic Loading

The cyclic performance of the columns is represented in terms of lateral load versus mid-span deflection. Figures 2 and 3 show a comparison between the results of the finite element model and experiment. Comparison of the hysteresis curve from the numerical model and experiments shows the comparable results. Results also show that by increasing axial load, lateral ductility and bearing also decrease.

3 Numerical Model Under Fire Loading

A three-step sequentially coupled thermal stress analysis approach was used for modelling the fire resistance of the CFST column. The validity of the numerical model was verified by the results of the experiment of CFST columns conducted by Lie and Chabot [14]. They have experimentally investigated the behaviour of 44 CFST columns, and among them, the columns labelled as C-26 and C-23 were selected
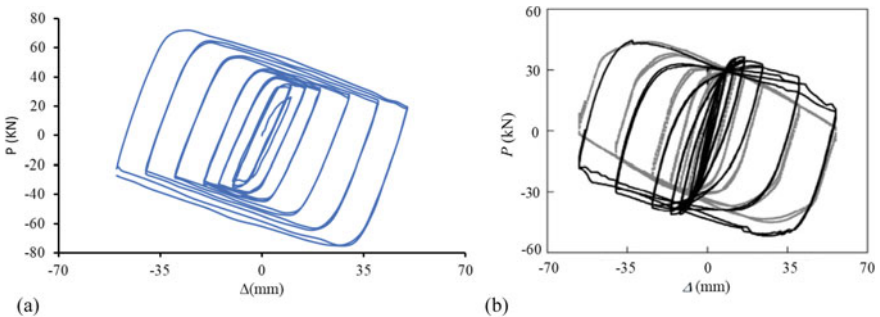
Fig. 2 Lateral deflection versus lateral load for column SC2-3 in **a** numerical model **b** experiments
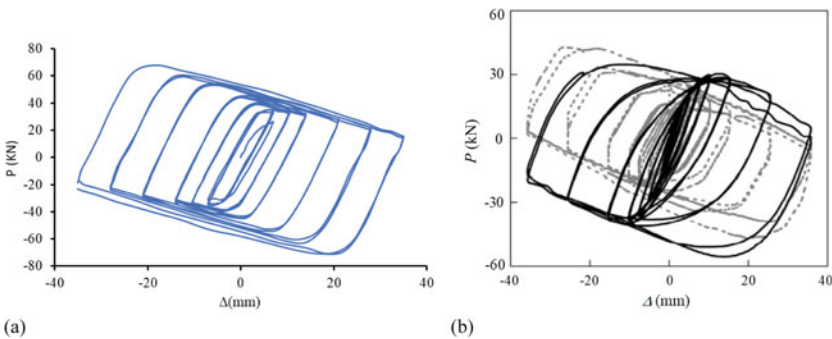
Fig. 3 Lateral deflection versus lateral load for column SC2-4 in **a** numerical model **b** experiments

Table 2 Detail of the CFST columns for fire analysis

Column	L (mm)	$D \times t$ (mm)	f_c (MPa)	f_y (MPa)	E_s (GPa)	N_o (KN)
C-26	3810	323.9×6.35	24.3	350	200	1050
C-23	3810	273.1×12.7	27.4	350	200	525

to validate the numerical model. Length of the column was 3810 mm including the endplate, but only middle 3048 mm length of column was exposed to fire. The thickness of the endplates for columns C-26 and c-23 was 38 mm and 25 mm, respectively. Details of the selected CFST column are described in Table 2.

3.1 Heat Transfer Analysis

A transient heat transfer analysis was conducted on the selected CFST columns to simulate the effects of the standard ASTM E119 1-1 Fire curve [17]. First, the recorded time–temperature history obtained from heat transfer analysis is applied at the outer surface of the steel tube by setting the boundary condition. Two heat transfer mechanisms conduction and radiation were defined for steel tube and concrete core interface. In the heat transfer analysis, the model was meshed using three-dimensional eight-node solid elements (DC3D8) for the steel tube and the in-filled concrete. The results of heat transfer analysis consist of the nodal time–temperature history, which was stored as an output data.

3.2 Stress/Deformation Analysis

In the stress analysis, three-dimensional eight-node solid elements with reduced integration (C3D8R) were used for meshing both the steel tube and the concrete core. Two steel end plates were designed at the columns ending to apply the boundary condition and axial loading. Loading was applied sequentially. First, axial loading was applied at the top plate and kept constant throughout the analysis. In the second step, fire loading was applied in terms of the nodal time–temperature curve a predefined field, which was obtained from the heat transfer analysis.

3.3 Material Properties at Elevated Temperature

The thermal properties of concrete at an elevated temperature were taken as per EN 1992-1-2 [18]. For structural steel, thermal properties recommended by EN 1993-1-2
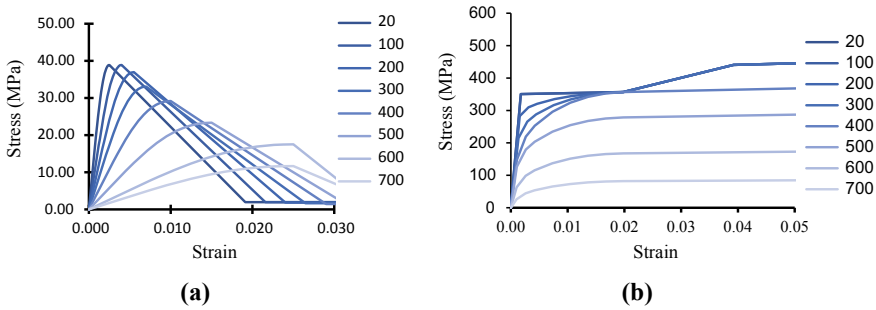
Fig. 4 Stress–strain curve at an elevated temperature **a** concrete **b** steel

[19] were adopted. The value of thermal expansion coefficient and thermal conductivity of steel and concrete were adopted from EN 1994 1-2 [20]. A classic metal plasticity material model implemented in ABAQUS was used for modelling the plastic behaviour of steel which follows von Mises yield and associated plastic flow. Elastic behaviour of concrete was modelled by modulus of elasticity and Poisson's ratio (μ = 0.3). The nonlinear response of the concrete was modelled using Drucker–Prager yield criteria available in ABAQUS. Figure 4 shows the stress–strain relationship for concrete and steel at elevated temperatures.

3.4 Initial Geometric Imperfection of the Column

Specimens are generally not straight due to the manufacturing process and consist of some initial geometric imperfection. So, to account for initial geometric imperfection, eigenvalue buckling analysis was conducted in ABAQUS. Then, first mode shape was multiplied by an amplification factor of L/1000 was used as an initial imperfection.

3.5 Loading, Boundary Condition and Contact at the Steel Tube–Concrete Core Interface

Figure 5 shows the standard ASTM E119 [17] fire curve for thermal loading as the same was used in the experiments. To exactly replicate the experimental condition, a fixed–fixed boundary condition was used for both the selected CFST columns. The modelling of steel tube and concrete core interface in the thermal stress analysis is similar to that of cyclic loading case in Sect. 2.3. Friction coefficient value of the Coulomb friction model is independent of thermal loading.
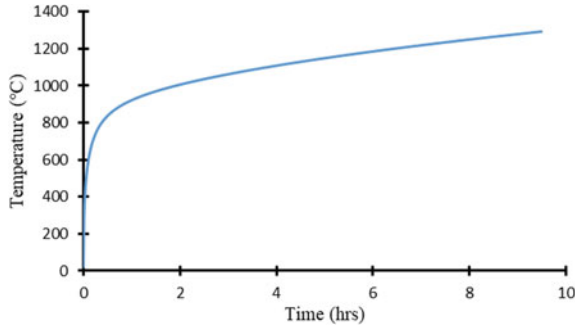
Fig. 5 Standard ASTM E119 fire curve

3.6 Validation of Numerical Model Under Fire Loading

The numerical model showed good agreement with the tests, as can be seen in Fig. 6. Maximum fire resistance time and maximum axial displacement for the simulated column C-23 were 163 min and 36 mm, respectively. The experimental graph shows the comparable values as 143 min and 36 mm. Column C-23 experienced the maximum fire resistance time and maximum axial displacement as 102 min and 15.23 mm, respectively. The corresponding experimental values were 93 min and 15.7 mm.

4 Numerical Model Under Post-earthquake Fire Scenario

The numerical models, thus calibrated, will be used to study the behaviour of the CFST column subjected to post-earthquake fire loading. Detail of the CFST column is presented in Table 3. The column selected for post-earthquake fire case is stocky. For predicting the behaviour of the column under post-earthquake fire case, two
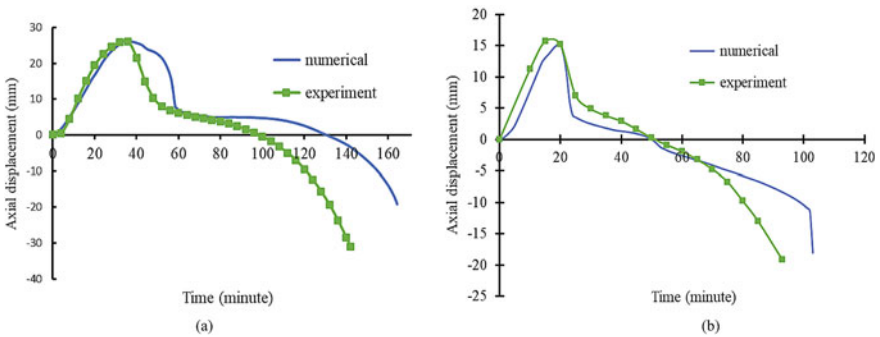
Fig. 6 Comparison of the axial displacement versus time curve for **a** C-23 **b** C-26

Table 3 Detail of the CFST column for post-earthquake fire analysis

Column	L (mm)	$D \times t$ (mm)	f_c (MPa)	f_y (MPa)	E_s (GPa)	N_o (KN)
C-26	3810	323.9 × 6.35	24.3	350	200	1050

analysis steps are required, namely cyclic analysis and sequentially coupled thermal stress analysis. Boundary condition and loading were applied through the end plates.

4.1 Stepwise Analysis Procedure

To simulate the behaviour of the CFST column under post-earthquake fire scenario, the analysis was performed stepwise as follows. First, a cyclic analysis was conducted to simulate the seismic behaviour of the column. Analysis procedure and modelling parameters are the same as mentioned in Sect. 2. Two damage levels in terms of drift ratio were considered for this study. After the cyclic analysis, residual deformations generated were used as an input for the thermal stress analysis. In the cyclic analysis, seismic damage level was chosen such that there will not be any fracture on the steel tube. In the next step, sequentially coupled thermal stress analysis was conducted to simulate the fire loading. Thermal stress analysis process follows the techniques defined in Sect. 3.

4.2 Result and Discussion

From Fig. 7, it can be seen that as the drift ratio increases even by small quantity, the fire resistance time for column decreases. This can be attributed due to the residual displacement of the column after cyclic loading and also because of the material capacity being reached due to the axial loading. The column is also stocky in nature. Fire resistance time after fire loading for the case of (a) without drift is 45 min, (b) 0.5% drift is 33 min and (c) 2% drift is 24 min.

5 Conclusions

Further numerical and experimental investigations on slender and stocky CFST columns are required to understand the influence of the fire loading after an earthquake. Numerical study on one column cannot give a clear picture of the post-earthquake fire behaviour. Thermal and general structures material properties taken from the Eurocode were accurate enough to model the behaviour of the CFST columns under cyclic loading and post-earthquake fire loading.
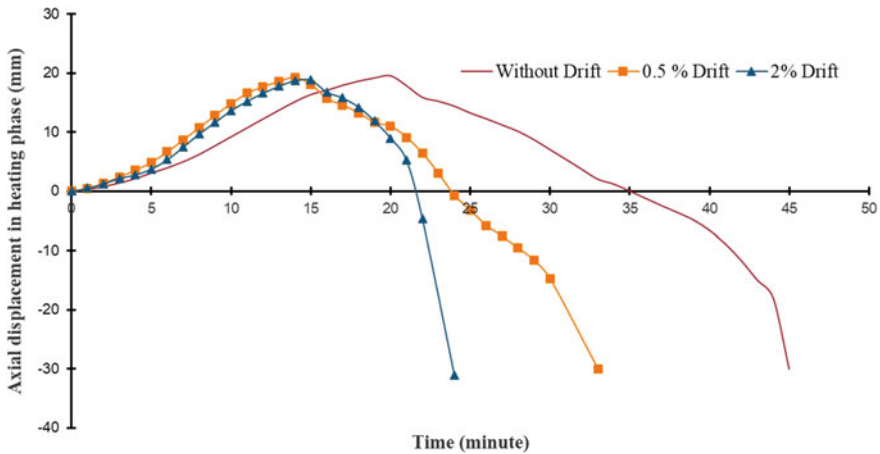
Fig. 7 Axial displacement vs time for column C-26 at different damage levels

References

1. Scawthorn, C., Eidinger, J. M., & Schiff, A. J. (2005). *Fire following earthquake*. American Society of Civil Engineers.
2. Scawthorn, C. R. (2008). *Fire following earthquake—The shake out scenario report*. (SPA Technical Report}. Berkeley, CA: SPA Risk, LLC.
3. Davidson, R. (2012). Post-earthquake fires in the March 2011 Japan earthquake and tsunami. In *Proceedings of 2012 Japan and New Zealand RAPID and Research Needs Workshop*, Arlington, VA: NSF, February 9–10.
4. Han, L. H., & Yang, Y. F. (2005). Cyclic performance of concrete-filled steel CHS columns under flexural loading. *Journal of Constructional Steel Research, 61*(4), 423–452. https://doi.org/10.1016/j.jcsr.2004.10.004.
5. Hong, S., & Varma, A. H. (2009). Analytical modelling of the standard fire behaviour of loaded CFT columns. *Journal of Constructional Steel Research, 65*(1), 54–69. https://doi.org/10.1016/j.jcsr.2008.04.008.
6. Kodur, V. K. R. (1998). Performance of high strength concrete-filled steel columns exposed to fire. *Canadian Journal of Civil Engineering, 25*(6), 975–981.
7. Poh, K. W. (2001). Stress-strain–temperature relationships for structural steel. *Journal of Materials in Civil Engineering, 13*(5), 371–379. https://doi.org/10.1061/(ASCE)0899-1561(2001)13:5(371).
8. Yassin, H., Iqbal, F., Bagchi, A., & Kodur V. K. R. (2008). Assessment of post-earthquake fire performance of steel-frame buildings. In *The 14th World Conference on Earthquake Engineering, 2008* (pp. 12–17). Beijing, China.
9. Imani, R., Mosqueda, G., & Bruneau, M. (2014). Experimental study on post-earthquake fire resistance of ductile concrete-filled double-skin tube columns. *Journal of Structural Engineering, 141*(8), 04015055. https://doi.org/10.1061/(ASCE)ST.1943-541X.0001168.
10. Imani, R., Mosqueda, G., & Bruneau, M. (2015). Finite element simulation of concrete-filled double-skin tube columns subjected to post earthquake fires. *Journal of Structural Engineering, 141*(12), 04015055. https://doi.org/10.1061/(ASCE)ST.1943-541X.0001301.
11. Talebi, E., Korzen, M., & Hothan, S. (2018). The performance of concrete-filled steel tube columns under post-earthquake fires. *Journal of Constructional Steel Research, 150*(1), 115–128. https://doi.org/10.1016/j.jcsr.2018.07.013.

12. Chen, W. F. (2007). *Plasticity in reinforced concrete* (Vol. 474), J. Ross Publishing: Plantation, FL.
13. ABAQUS Standard User's Manual. (2013). *The Abaqus Software is a product of Dassault Systèmes Simulia Corp., Providence*, RI, USA Dassault Systèmes, Version 6.14.1, USA.
14. Lie, T. T., & Chabot, M. (1992). *Experimental studies on the fire resistance of hollow steel columns filled with plain concrete* (Internal Report No. 611). Ottawa (Canada): Institute for Research in Construction, National Research Council of Canada NRCC.
15. ATC-24. (1992). *Guidelines for cyclic seismic testing of components of steel structures*. Redwood City (CA): Applied Technology Council.
16. Lakavath, C., Allam, R., & Kondraivendhan, B. (2019). Experimental and numerical studies on the behaviour of broad-gauge railway sleepers in static bending condition. In *Sustainable construction and building materials* (pp. 781–792). Singapore: Springer. https://doi.org/10.1007/978-981-13-3317-0_70.
17. ASTM. (1990). *Standard ASTM E119–88: Standard Methods of Fire Test of Building Construction and Materials*, Philadelphia (PA), American Society for Testing and Materials.
18. EC2. (2004). EN 1992-1-1, *Eurocode 2: Design of concrete structures—Part 1–1: General rules and rules for buildings, European Committee for Standardization*, Brussels (Belgium).
19. EC3. (2005). EN 1993-1-2, *Eurocode 3: Design of steel structures—Part 1–2: General rules—Structural fire design, European Committee for Standardization*, Brussels (Belgium).
20. EC4. (2005). EN 1994-1-2, *Eurocode 4: Design of composite steel and concrete structures—Part 1–2: General rules-Structural fire design, European Committee for Standardization*, Brussels (Belgium).

Mathematical Model for Prediction of Compressive Strength of Normal, Standard and High Strength SCC with RCA

Srinivas Vasam, K. Jaganadha Rao, and M. V. Seshagiri Rao

1 Introduction

Concrete is the most widely used man-made material and its consumption is now next to water. Concrete has become popular because of its mouldability into any complex shape, abundant availability of its ingredients, relative economy and high compressive strength. Concrete is no mere a mixture of cement, coarse aggregates, fine aggregates and water. The development of new admixtures has completely changed the definition of concrete. Though there is a considerable research in the last few decades on concrete-making materials and technologies, concrete has certain drawbacks like the presence of voids due to improper mixing/compaction which affects strength and durability. Self-compacting concrete (SCC) is one of the solutions to minimize such voids in concrete. Self-compacting concrete finds several applications in the construction field due to its multiple advantages like ease of placement, reduced noise pollution, less concreting time, etc. A lot of research is being carried out in the last few decades on SCC with the use of different combinations of mineral and chemical admixtures.

The focus on recycled aggregate concrete is gaining importance to address the problems of depletion of natural resources and disposal of construction and demolition waste to some extent. The use of recycled concrete aggregate (RCA) in SCC

S. Vasam (✉)
Department of Civil Engineering, Siddhartha Institute of Technology & Sciences, Korremula, Hyderabad 501301, India
e-mail: nivas_vasam@yahoo.com

K. Jaganadha Rao
Department of Civil Engineering, Chaitanya Bharathi Institute of Technology, Gandipet, Hyderabad 500075, India

M. V. Seshagiri Rao
Department of Civil Engineering, Jawaharlal Nehru Technological University, Hyderabad 500085, India
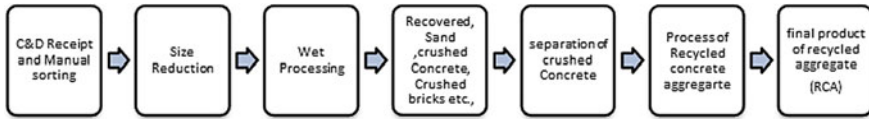
Fig. 1 Flow chart showing conversion of recycled concrete aggregate to a useful product

combines the advantages of both SCC and RCA. In general, the design of concrete mix is a trial and error procedure and more so when new materials like RCA are used. In the current paper, an empirical model is developed to predict the compressive strength and other mechanical properties of SCC with RCA by carrying out the multiple regression analysis on the test data obtained by carrying out extensive laboratory investigations. The variables considered in the model are the grade of concrete and percentage of RCA. The empirical equation developed is found to predict the compressive strength of SCC with RCA to an accuracy of about 90%. Thus, a lot of effort, time and material can be saved by using the developed strength prediction equation due to the reduced trial mixes. The following sections present the methodology followed, results obtained, discussions and conclusions

1.1 C&D Waste Minimization

Minimization of C&D waste should commence from day one of the project. This includes better planning, use of precast construction, reuse and recycling of C&D waste materials on site with minimal import and export (Fig. 1).

1.2 Objective

The objective of the present work is to develop mathematical model to predict the compressive strength of recycled aggregate self-compacting concrete (RASCC), enabling the minimization of laboratory trial mixes for finalization of mix proportion.

1.3 Scope of the Work

The scope of the work is limited to the use of data pertaining to compressive strength values with variables of study as grade of concrete (M20 to M70—normal to high grades), percentage of RCA replacement ratio (0–100%). The data consist of 28 days compressive strengths of 6 Grade of concrete with 5 Percentage replacement of RCA as given in Table 6. NCSS and MATLAB software are used for modelling purpose.

The self-compatibility of the mixes is ensured by conducting various tests specified by EFFNARC [1], viz., T50 Slump flow, L-Box, U-Box and V-funnel tests. Su et al. [2] conducted research on the mix design for Self Compacting Concrete and arrived at a simple mix design procedure. As this method is simple and already established, the same method is adopted for SCC with recycled aggregate and suitable modification factors are suggested. The model is expected to predict the compressive strength of RAC. The study also aims at validating the model and estimating the percentage error between theoretical (predicted) results and experimental results.

2 Experimental Programme

2.1 Materials

2.1.1 Cement

Ordinary Portland cement of Grade 53 confirming to IS: 12269 [3] with specific gravity 3.15 was used in this investigation. The chemical composition of cement is given in Table 1a.

Table 1 **a** Chemical composition of cement (as per manufacturers' test report). **b** Chemical composition of fly ash

Chemical property	Limits (as per IS)	Results
(a)		
Lime saturation factor (%)	0.66–1.02 (max.)	0.82
Alumina iron ratio	Min. 0.665%	1.2%
Insoluble residue	Max. 2%	0.95%
Magnesia (%)	Max. 6	2.4
Sulphuric anhydride	2.5–35%	1.1%
Loss on ignition	Max. 5%	2.2%
Chemical property	Result (% mass)	
(b)		
Loss on ignition	0.43	
Alumina (as Al_2O_3)	16.31	
Silica (as Sio_2)	60.82	
Iron (as Fe_2O_3)	17.17	
Calcium (as CaO)	4.64	
Magnesium (MgO)	Not found	
Sodium(as Na_2O)	0.34	
Potassium (as K_2O)	0.08	

Table 2 Properties of sand, natural coarse aggregate and recycled concrete aggregate

Property	Sand	NCA	RCA
Specific gravity	2.59	2.81	2.35
Total water absorption (%)	1.0	0.3	2.40
Moisture content (%)	0.15	0.8	0.45
Bulk density (Loose) (kg/m^3)	1567	1380	1355
Bulk density (Compacted) (kg/m^3)	1713	1530	1590
Fineness modulus	2.39 (Zone III)	6.36	6.35
Elongation index (%)	–	7.10	15.5
Flakiness index (%)	–	6.15	5.8

2.1.2 Mineral Admixtures

Fly ash conforming to IS 3812 (Part-1): 2003 [4] was used. The chemical composition of fly ash is given in Table 1b.

2.1.3 Fine and Coarse Aggregates

The physical properties of sand, NCA and RCA used in the present experimental investigations are tabulated in Table 2. The maximum size of coarse aggregate was 12.5 mm.

2.1.4 Chemical Admixtures

Chemical Admixtures were used in this investigation. Super plasticizer (polycarboxylate ether based) with specific gravity 1.01 and pH: 8 and viscosity modifying admixture (Glenium B233 stream 2) with specific gravity 1.1 and pH: 6 were used in this work.

2.1.5 Water

Locally available potable water was used for mixing and curing (Figs. 2, 3, 4 and 5; Tables 3, 4 and 5).

Fig. 2 Sustainable concrete approach

Fig. 3 Demolished concrete material

3   Development of Model

Multi-linear regressions determine the relationship between two or more independent variables and a dependent variable by fitting a linear equation to the observed data. Every value of the independent variable is associated with a value of the dependent variable as represented in the equation as per the general form of the multiple linear regressions as below:

$$y = a_0 + a_1x_1 + a_2x_2 + a_3x_3 + a_4x_4$$
$$\ldots \text{(multi linear regression quation)}$$

Here, 'y' is dependent variable; X_1, X_2, X_3 and X_4 are independent variables representing various parameters. We measure a quantity y for several values of parameters X_1, X_2, X_3 and X_4.

Fig. 4 LAB tests

Fig. 5 Concrete testing
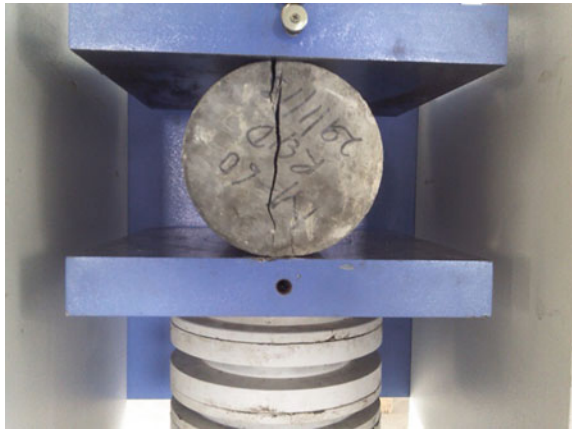
The compressive strength of concrete after 28 days of curing depends upon the grade of concrete. It also varies with varying the percentage of recycling aggregate mixed in the concrete

Considering the grade of concrete and percentage of recycling aggregates as independent variables and compressive strength of concrete after 28 days of curing as dependant variable, the following formula was arrived at:

$$f_{cke} = 17.04 + 0.85 \times g_c - 0.05 \times p_{ra}$$

Table 3 Mix proportions and quantities of different grades of SCC

Mix prop. of concrete grade	Cement	Fly ash	CA—12.5 mm (NA)	CA—12.5 mm (RA)	River sand	Admixture (SP)	VMA	Water	W/P
NASCC-M20-0%	1.000	0.647	2.179	0.000	2.317	0.020	0.002	0.644	0.39
NASCC-M30-0%	1.000	0.394	1.812	0.000	1.927	0.017	0.002	0.521	0.37
NASCC-M40-0%	1.000	0.322	1.655	0.000	1.760	0.016	0.002	0.458	0.35
NASCC-M50-0%	1.000	0.226	1.508	0.000	1.603	0.015	0.001	0.407	0.33
NASCC-M60-0%	1.000	0.105	1.294	0.000	1.376	0.013	0.001	0.328	0.30
NASCC-M70-0%	1.000	0.057	1.039	0.000	1.105	0.013	0.001	0.261	0.25

Table 4 Acceptance criteria for self-compacting concrete

S. No.	Testing method	Typical range of values as per EFNARC		Property	Unit	Range of values obtained as per experiment	
		Min.	Max.			Min.	Max.
1	Slump flow by abrams cone	650	800	Filling ability	mm	658	800
2	T50 cm slump flow	2	5	Filling ability	s	2	6.5
4	V-funnel	6	12	Filling ability	s	6.5	9.5
5	V-funnel at T5 min	0	+3	Segregation resistance	s	9.5	12.5
6	L-box	0.8	1.0	Passing ability	($h2/h1$)	0.82	0.98
7	U-box	0	30	Passing ability	($h2 - h1$) mm	20	28

Table 5 Input–output data for the mathematical model to predict the compressive strength of SCC

Input/Output data	Range
Grade of concrete (g_c—Input data)	M20 to M70 (with an increment of 10)
Percentage of replacement ratio (P_{ra}—Input data)	(0–100%) (with an increment of 25%)
Compressive strength, MPa (f_{cke}—Output data)	29.483–76.625 Mpa

where 'f_{cke}' is the estimated compressive strength of SCC after 28 days of curing, in N/mm^2

g_c—The grade of concrete in N/mm^2 (it is found to be suitable for ordinary, medium and high strength SCC).

p_{ra}—The percentage of recycling aggregate mixed in the concrete (percentage of recycled aggregate content varying from 0 to 100% in the increment of 25%).

Table 6 shows the compressive strength of concrete in N/mm^2 after 28 days of curing, computed as per the authors' formula and the actual value obtained by experimental investigation.

Independent variable	Regression coefficient $b(i)$	Standard error $Sb(i)$	Lower 95% conf. limit of $\beta(i)$	Upper 95% conf. limit of $\beta(i)$
Regression coefficients confidence intervals				
Intercept	17.03507	1.214267	14.5436	19.52654

(continued)

(continued)

Independent variable	Regression coefficient $b(i)$	Standard error $Sb(i)$	Lower 95% conf. limit of $\beta(i)$	Upper 95% conf. limit of $\beta(i)$
C2	0.85128	0.02254838	0.8050146	0.8975455
C3	−0.04577333	0.0108919	−0.06812167	−0.023425

Figures 6, 7 and 8 give the comparison between the actual value obtained by experimental investigation and the predicted values from the above equation for normal, standard and high strength RASCC and NASCC after 28 days in N/mm^2 with different percentages of replacement of NA by RCA.

4 Results and Discussions

The fresh state properties of concrete are shown in Table 4. The values of different workability tests are within the acceptable limits as given by EFNARC. For normal and medium strength self-compacting concrete, i.e. M20 to M50, it was observed that 50% replacement of NA with recycled aggregate gives the design strength at 28 days. For high strength self-compacting concrete, i.e. M60 to M70, 25% replacement is observed as optimum replacement value.

There is not much change in the compressive strengths of SCC with and without RCA for M20 and M30 grade at three days and seven days for all percentages of RCA replacements. However, at the ages of 28 days and beyond, loss of strength of about 14% is observed for RCA 75 and 100%. For design mix M20 to M50 grade concrete, all the replacements with RCA gained early strength and required strength of 72% at 14 days age. The regression equation was developed for prediction of compressive strength

$$\text{Compressive strength } (f_{\text{cke}}) = 17.04 + 0.85 \times g_{\text{c}} - 0.05 \times p_{\text{ra}}$$

The R^2 value obtained in the regression analysis was 0.98, indicating a good correlation between the experimental and theoretical compressive strengths. The regression equation can predict the compressive strength values with a maximum error of 10.9% for different mixes.

5 Conclusions

Based on the results and discussions presented above, the following conclusions are drawn:

Table 6 Multiple linear regression equation values for the compressive strength of concrete for normal, medium and high strength RASCC and NASCC after 28 days in N/mm^2 with different percentage of replacement of NA by RCA

S. No.	Grade of concrete (M)	RCA replacement ratio	Compressive strength (Mpa)		Percentage error with respect to theoretical value
			Experimental	Theoretical model predicted value	
1	20	0	34.25	34.061	−1
2	20	25	33.85	32.916	−3
3	20	50	32.93	31.772	−4
4	20	75	32.15	30.628	−5
5	20	100	31.45	29.483	−7
6	30	0	41.36	42.573	+3
7	30	25	39.77	41.429	+4
8	30	50	37.80	40.285	+6
9	30	75	35.30	39.140	+10
10	30	100	35.03	37.996	+8
11	40	0	53.60	51.086	−5
12	40	25	51.18	49.942	−2
13	40	50	50.30	48.798	−3
14	40	75	48.85	47.653	−3
15	40	100	48.55	46.509	−4
16	50	0	58.45	59.599	+2
17	50	25	56.50	58.455	+3
18	50	50	55.25	57.310	+4
19	50	75	54.10	56.166	+4
20	50	100	52.85	55.022	+4
21	60	0	70.25	68.112	−3
22	60	25	69.85	66.968	−4
23	60	50	68.10	65.823	−3
24	60	75	67.35	64.679	−4
25	60	100	66.70	63.535	−5
26	70	0	75.45	76.625	+2
27	70	25	73.55	75.480	+3
28	70	50	72.85	74.336	+2
29	70	75	72.15	73.192	+1
30	70	100	71.85	72.047	0

+ Indicate higher theoretical (predicted) values and
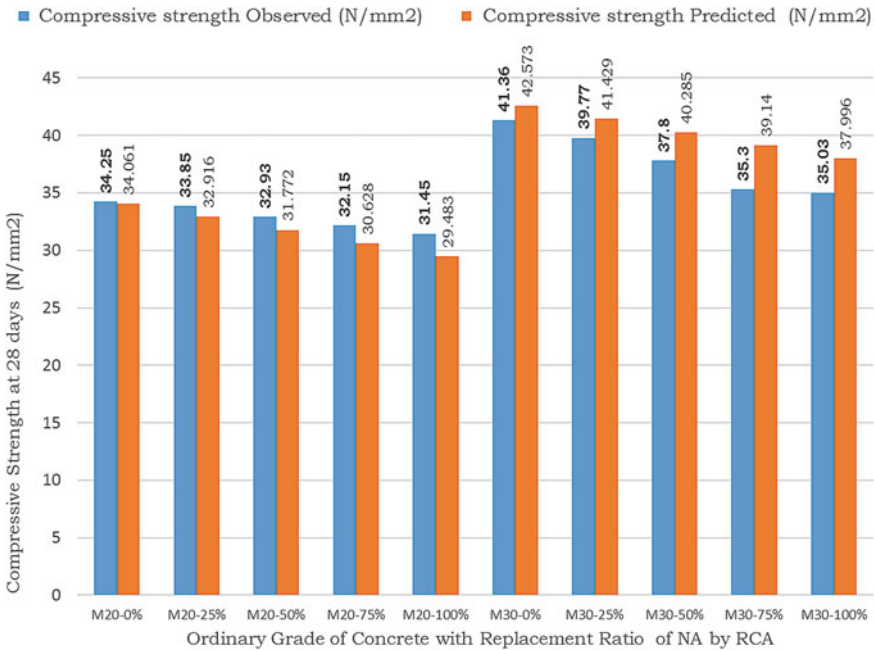− Indicate lower theoretical (predicted) values

Fig. 6 Experimental and predicted value of compressive strength of normal grade (M20 and M30) SCC with different RCA content

- Utilization of recycled concrete aggregate as natural aggregate replacement avoids the environmental and ecological damages caused by quarrying and exploitation of raw materials like coarse aggregate for making concrete. The substitution of RCA will help to conserve the valuable natural resources.
- The developed mathematical model (by using multiple regression analysis) was found to predict compressive strength of NASCC and RASCC in terms of grade of concrete and percentage of recycled aggregate.
- A very good correlation is obtained between the experimental and theoretical (predicted) compressive strength values with correlation coefficient (R^2) value of 0.98.
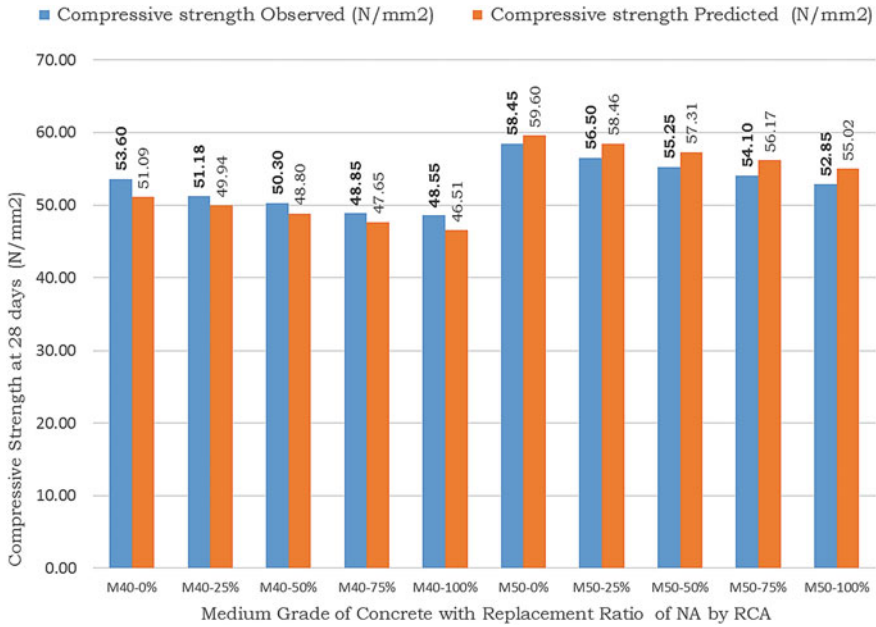
Fig. 7 Experimental and predicted value of compressive strength of medium grade (M40 and M50) SCC with different RCA content
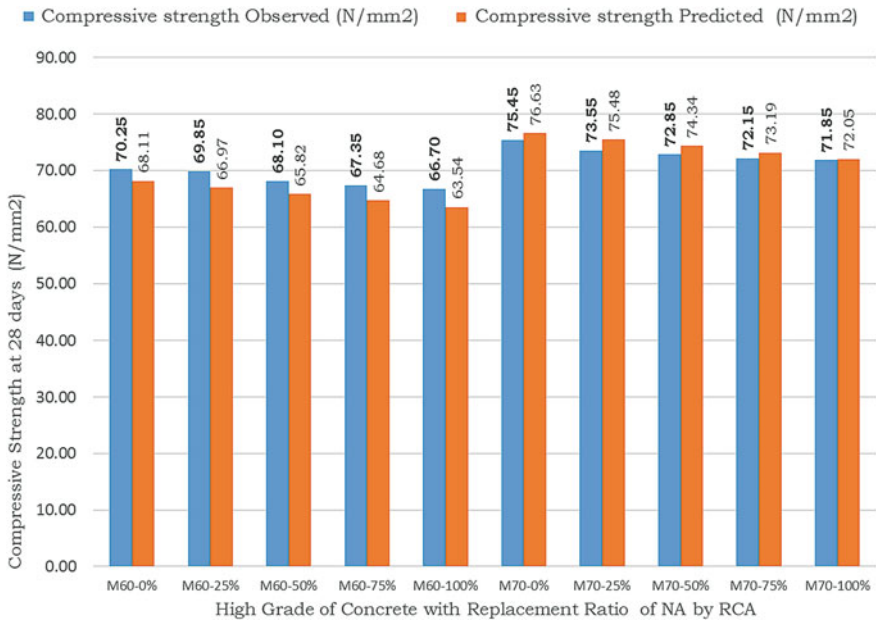

Fig. 8 Experimental and predicted value of compressive strength of higher grade (M60 and M70) SCC with different RCA content

References

1. *Specifications and guidelines for self compacting concrete*. 99 West Street, Farnham, UK: EFNARC, Association House, February 2002.
2. Su, N., & Hsu, K. C. (2001). A simple mix design method for self-compacting concrete. *Cement and Concrete Research*, 1799–1807.
3. *Indian Standard Code IS: 12269, Specifications for 53 grade ordinary Portland cement*.
4. Indian Standard Code 3812-2003 (Part-1), Indian standard pulverized fuel ash specification Part-1; for use as pozzolana in cement, cement mortar and concrete.
5. Brouwers, H. J. H., & Radix, H. J. (2005). Self-compacting concrete: Theoretical and experimental study. *Cement and Concrete Research, 35,* 2116–2136.
6. Jayaram M. A., et al. (2010). A fuzzy-neuro approach for design of light weight concrete mixes. *Journal of Computing in Civil Engineering*.
7. Nashat, M., et al. (2012). Comparative study on fuzzy ınference systems for prediction of concrete compressive strength. *International Journal of the Physical Sciences*.
8. Stremberk, P., et al. (2010). Fuzzy logic model of fibre concrete with effect of age. In *10th International Conference on Modern Building Materials, Structures and Techniques,* Luthiana.
9. Rasheeduzzafar, A. K., et al. (1984). Recycled concrete—A source of new concrete. *Cement, concrete and aggregates* (Vol. 6, No.1, pp. 17–27). ASTM.
10. Ray, S. P., et al. (1991). Recycled aggregate concrete. *Journal of Structural Engineering, 18*(2), 67–75.
11. Vasam, S., Jagannadha Rao K, & Vasu K. (2012). Study on self compacting concrete (SCC) and recycled coarse aggregates (RCA) in the present construction ındustry. In *National Conference on Advances in Civil Engineering* (ACE-2012), May 2012.
12. Vasam, S., & Jagannadha Rao, K. (2013). Use of SCC and RCA for sustainable construction—An overview. *IJRET, 02*(11), 629–633.eISSN 2319-1163, ISSN 2321-7308.

Seismic Response of UHPC Strengthened Reinforced Concrete Frame Using Concrete Damaged Plasticity Model

Nidhi Sannametla and **Jyosyula Sri Kalyana Rama**

1 Introduction

Numerical analysis is the study of algorithms which use numerical approximation instead of symbolic manipulation to solve engineering problems. Finite element analysis (FEA) is a numerical method typically used in structural engineering to solve problems whose analytical solutions require solving for boundary values of partial differential equations. It yields approximations for values of unknown components at discrete points over the domain by dividing a large problem into small, simple elements. Concrete is a highly heterogeneous, quasi-brittle material that shows nonlinear mechanical behavior (post elastic limits). The major modes of failure of concrete are tension cracking and compression crushing. Tension and low/unconfined compression cause failure processes that result in irreversible deformations and degradation of the material stiffness called strain softening. However, a high confined compression is described by a ductile hardening response.

N. Sannametla · J. Sri Kalyana Rama (✉)
Birla Institute of Technology and Science, Pilani, Hyderabad, India
e-mail: kalyan@hyderabad.bits-pilani.ac.in

N. Sannametla
e-mail: f20150603@hyderabad.bits-pilani.ac.in

J. Sri Kalyana Rama
Vignana Bharathi Institute of Technology, Hyderabad, India

1.1 Concrete Damaged Plasticity Model (CDPM)

The typical behavior of concrete can be determined using the concrete damage plasticity (CDP) model which is available in ABAQUS, a FEA software. CDP is a constitutive continuum-based model that combines plasticity and damage mechanics. It is a modified form of the Drucker–Prager strength hypothesis in which the failure of a material is determined by the non-dilatational strain energy, and the failure surface is assumed to be of conical shape with circular cross section (not completely consistent with the real behavior of concrete). In CDP, various parameters (scalar damage variables) are used to describe the behavior of concrete in terms of yield surface and flow.

1. Dilation/dilatancy angle (β or ψ): 36°–40°
2. Flow potential eccentricity (ϵ): Ratio of tensile to compressive strength. (~0.1)
3. fb_0/fc_0: Ratio of biaxial to uniaxial compressive yield stress (~1.16)
4. K_c: Ratio of 2nd stress-invariant on tensile to compressive meridian (~2/3).
5. Viscosity parameter (υ or μ): 0.

The above five parameters along with stress–strain behavior of concrete in tension and compression are the input parameters for CDPM in ABAQUS. Besides this, compression damage (d_c) and tension damage (d_t) input are also to be defined (yield stress vs. inelastic and cracking strain). Figures 1 and 2 depict the constitutive stress–strain relationships of concrete used to describe the numerical structural response.
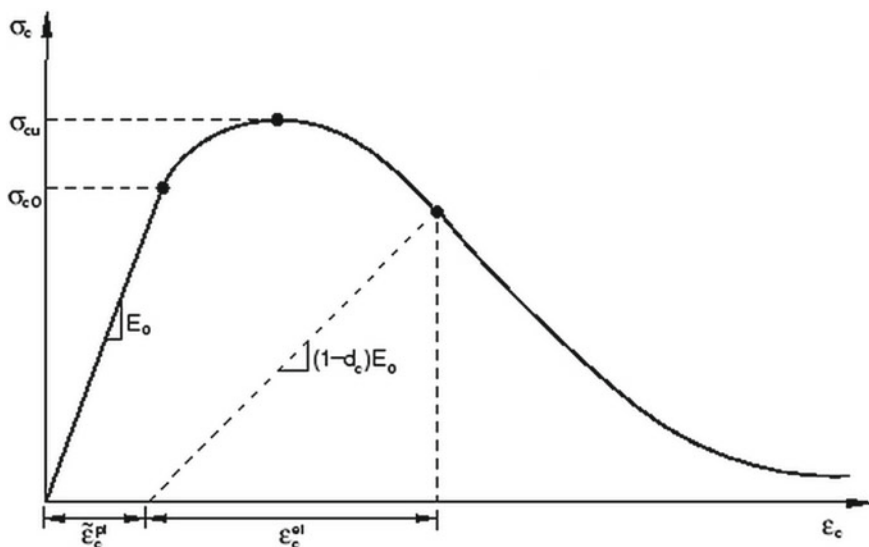

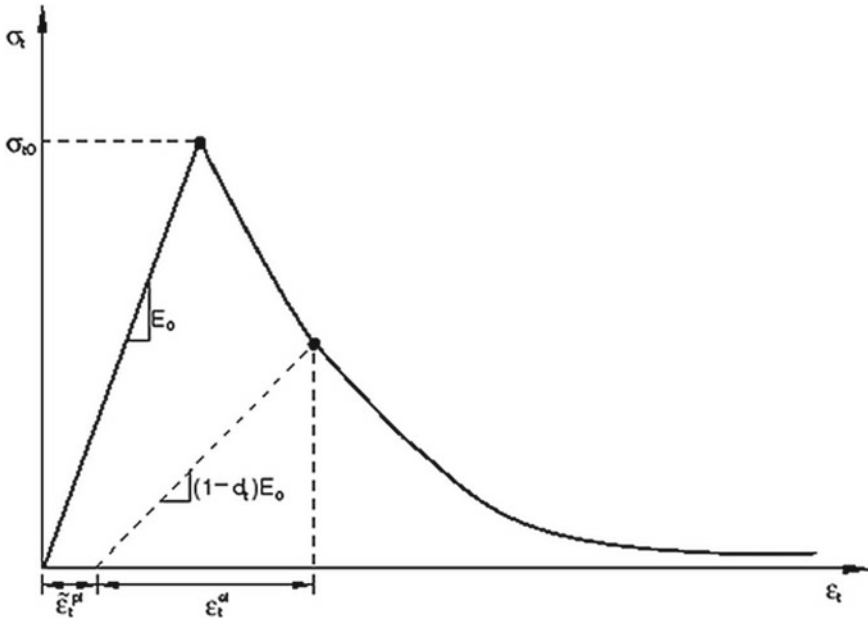**Fig. 1** Response of concrete to uniaxial compression loading

Fig. 2 Response of concrete to uniaxial tension loading. Dassault Systèmes Simulia Corp. ABAQUS/CAE Documentation. Version 6.8–3. Providence, RI, USA (www.simulia.com); 2008

This paper aims to explore the dynamic response of a CDP model of an RC frame with and without slab subjected to real-time earthquake load through numerical FEA using ABAQUS 6.14-5.

1.2 Literature Review

One of the most essential facets of analyzing failure of concrete structures is the modeling of crack commencement and proliferation caused by continuous creation and connection of several micro-cracks [1]. This may cause stiffness degradation in case of dynamic loading which is hard to represent using classical plasticity. Hence, CDP is adopted instead, which is a fracture energy-based model, predominantly developed through constitutive modeling based on internal variable formulation of plasticity theory for nonlinear analysis of concrete [2].

In order to develop the model further, identification of parameters of the concrete damage plasticity (CDP) model was done [3]. Additionally, an equation for damage parameters to capture damage behavior of concrete was suggested [4].

CDPM was used to assess the damage of various structures. Application and calibration of the CDPM parameters for assessing the damage in an RC frame were

done [5]. Simulation and analysis of the responses of five concrete slabs, using CDP model with material parameter calibration, through ABAQUS were done [6].

CDPM was also used to study the effects of structural response under various loading conditions. The effect of quasi-static cyclic lateral load on the behavior and failure mode of a conventional RC beam–column joint was investigated [7]. Numerous approaches to elucidate the performance of these masonry infill walls subjected to dynamic loads have been presented [8]. Mechanical properties of concrete depend significantly on the loading rate (dynamic, i.e., time-varying load). A rate-dependent continuum model (based on visco-elastic constitutive relationships) is presented for concrete modeling when subjected to dynamic load. Stefan effect (tensile strength increasing with loading rate) and additional rate effect due to micro-inertia are explained. The capabilities of the damage plasticity model in visualizing localization, energy dissipation and hysteresis are described by Pedersen et al. [9].

CDPM was used to study the seismic response of various structures such as dams and bridges. The seismic response of a bridge in Poland subjected to an earthquake of moderate intensity was considered while using the CDP model to characterize the inelastic behavior of concrete [10]. A 3-D analysis based on a continuous approach was used to study the dynamic response of a suspended bridge which was subjected to earthquake and moving vehicular loads both separately and simultaneously [11]. A novel CDP model for the analysis of earthquake load on concrete dams through the response of Koyna dam during 1967 earthquake was presented [12]. The same was also investigated through a 2-D analysis [13]. A plastic damage model was used to investigate the damage response of concrete gravity dams using various damping mechanisms [14]. The damage of a concrete gravity dam subjected to hydrostatic, gravity and earthquake loading was studied [15]. A micro-plane model to describe the dynamic behavior of a concrete gravity dam was formulated and implemented [16]. Push-over analysis was used to study the vulnerability of RC structures to earthquake loading owing to irregularities in plan and elevation [17]. The behavior of beam–column joint retrofitted with FRP wrapping under seismic loading was investigated [18]. The seismic response of RC columns retrofitted with concrete jacketing, steel jacketing, CFRP wrapping, etc., was studied [19]. A novel methodology was proposed to evaluate the fracture properties of concrete using concrete damage plasticity model in tandem with stress-strain model. Results indicated that the proposed model is in good agreement with experimental values of size independent fracture energy [20].

In this paper, novel CDP data is acquired from stress–strain curves, which are derived from on-field destructive tests. These are then used as material properties for concrete.

2 Methodology

The following steps were followed while modeling an RC frame subjected to real-time earthquake loading in ABAQUS software. Dimensions (in mm) adopted are as
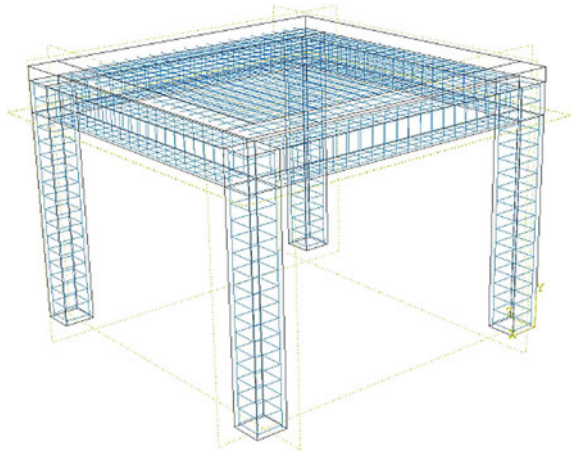
follows: Beam of 4000 × 450 × 450, Column of 3500 × 450 × 450 and Slab of 4000 × 4000 × 450. Reinforcement is provided as shown in Fig. 3.

UHPC casing of 20 mm thickness was provided throughout the length of the column. Ultra-high performance concrete (UHPC) is a cementitious material with a minimum compressive strength of 120 MPa to over an excess of 200 MPa. It is formulated by a combination of Portland cement, supplementary materials, limestone/quartz powder, reactive powders, high range water reducers/plasticizers, fine sand and water. Fine materials in the matrix lead to a dense and smooth surface. In combination with metallic fibers, it can provide a tensile strength of 48 MPa, hence sometimes eliminating the need for reinforcement in its applications, thus simplifying construction. M40 concrete of density 25 kN/m^3, with Young's modulus of 31,623 N/mm^2 and Poisson's ratio of 0.2, varying Ψ's of 13, 25, 35, 40, ϵ of 0.1, fb_0/fc_0 of 1.16, K_c of 0.667 and μ of 0, was adopted. These specific dilation angles were chosen based on the following rationale. These four dilation angle values were found to be critical values or points of trend change in previously conducted studies [18]. Fe 415 steel of density 78.5 kN/m^3 with Young's modulus of 200,000 N/mm^2 and Poisson's ratio of 0.3 was adopted. All the boundary conditions and constraints (detailed later) are set in this step and remain constant throughout the analysis, i.e., they are extended to further steps. The linear perturbation step is carried out to obtain the natural frequencies of the first six modes of vibration of the structure. Then, the dynamic implicit step is used for analysis of real-time earthquake data (Elcentro earthquake, May 18, 1940) for a period of 31.18 s is specified in a tabular form; the data gives acceleration of the ground. Reinforcement is embedded into concrete; rebars are tied to each other and so are any connecting faces of members. The column bases are fixed, except Z-translation, to permit definition of earthquake load.

In order to obtain a relatively medium-sized mesh, a 250 cm seed interval was adopted for the entire model and all the individual elements. However, it was observed that mesh sizing did not have a significant effect on the analysis, when comparing 100, 250 and 500 cm seed intervals. The slab is designated as an independent part
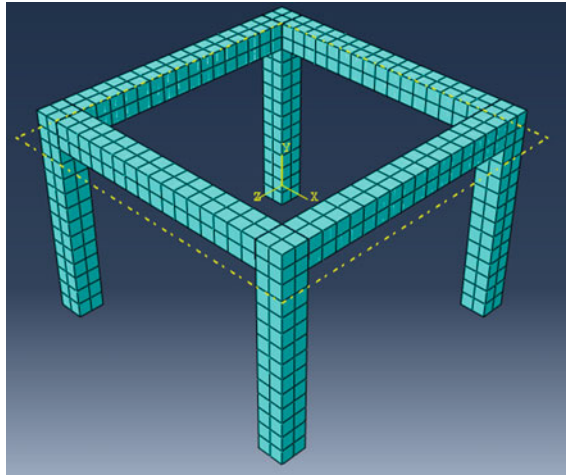
Fig. 4 Mesh in space frame

Table 1 Number of nodes and element details

Type/nodes	Shape	Order	Without slab	With slab
C3D8R	hexahedral	linear	480	880
T3D2	line	linear	8064	9280

(in assembly), and the rest of the instances are designated as dependent instances (to be meshed part by part). Figure 4 depicts the mesh adopted in the FEA software. Table 1 gives element details.

2.1 Element for Concrete Modeling

The concrete is modeled with the brick elements for uniform stress distribution. Cube Three Dimensional eight node Reduced integration (C3D8R) elements are utilized as shown in Fig. 5. C3D8R uses linear interpolation in all directions, and hence, it is called linear element of first order. They only have three degrees of freedom and are

Fig. 5 Concrete element (C3D8R)

Fig. 6 Truss element
(T3D2)

stress-displacement elements. The convergence rate of quadrilaterals is better than that of triangles and tetrahedrons; however, sensitivity of displacement calculations to mesh orientation in regular meshes is higher.
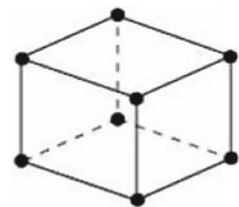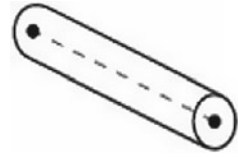
2.2 Element for Rebar Modeling

Reinforcement or steel rebars are modeled as three-dimensional truss elements (T3D2) as shown in Fig. 6. It is a two-node straight truss element that uses linear interpolation for position displacements, with stress being a constant throughout. The cross-sectional area of the truss element is detailed as part of the section definition. When the displacements are large, the updated cross-sectional area is calculated by assuming that the material is incompressible, regardless of the actual material definition.

The concrete-rebar interface was modeled through ABAQUS by using the embedded slave–master setting.

3 Results and Observations

3.1 With UHPC Improvement

The values of displacement and reactions observed were at the points where these quantities attained their maximum values. These points are close to the base, for columns, and close to the mid-span, for beams.

From Fig. 7, it is observed that there is a substantial increase in load-carrying capacity with the increase in dilation angle. The increase from 25 to 35° is more predominant. From Fig. 8, it is observed that there is a marginal decrease in the displacement with the increase in the dilation angle.

From Fig. 7, it is observed that load-carrying capacity of space frame with slab is slightly higher than space frame without slab. From Fig. 8, it is observed that displacement in space frame with slab is slightly lower than space frame without slab. From Table 2, the natural frequencies of space frame with and without slab for the first five modes are in between the range of 0.08–0.32 Hz. The natural frequencies of space frame with slab are almost comparable to those of space frame without slab.

Fig. 7 Reaction in kN versus dilation angle in degrees
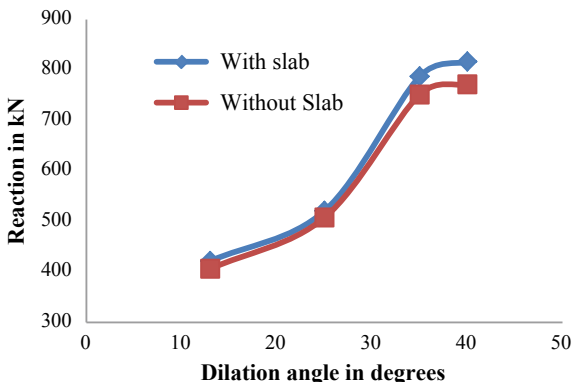
Fig. 8 Displacement in mm versus dilation angle in degrees
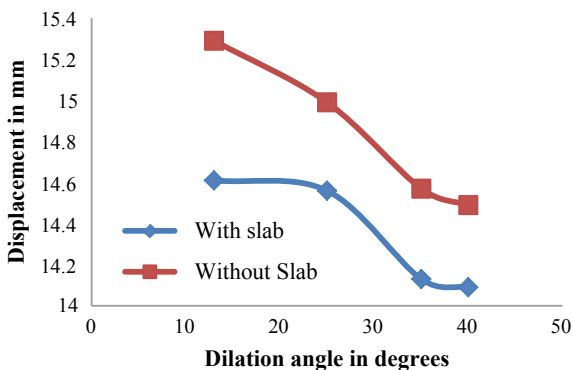
Table 2 Natural frequencies of space frame with slab

Mode	Frequency (Hz, cycles/time)	
	With slab	Without slab
1	0.1	0.084
2	0.107	0.136
3	0.126	0.195
4	0.245	0.213
5	0.259	0.224
6	0.2633	0.314

From Fig. 9, correlating observed failure to modes of vibration, it is seen that the first mode contributes the most to the response of the space frame justifying the failure of column first. The damage then propagates to beam, as is visible in the second. The later modes correspond to twisting of members. From Fig. 10: For space frame with slab, it is observed that the first cracking load of concrete is increasing with decreasing dilation angle, due to higher ductility. For space frame without slab, it is
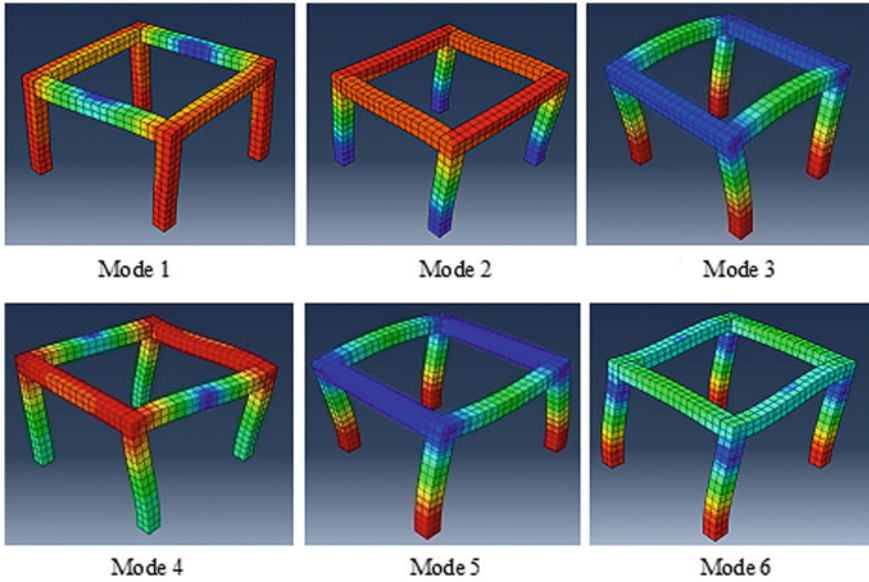
Fig. 9 First six modes of vibration of space frame

Fig. 10 Concrete first crack load in kN versus dilation angle in degrees
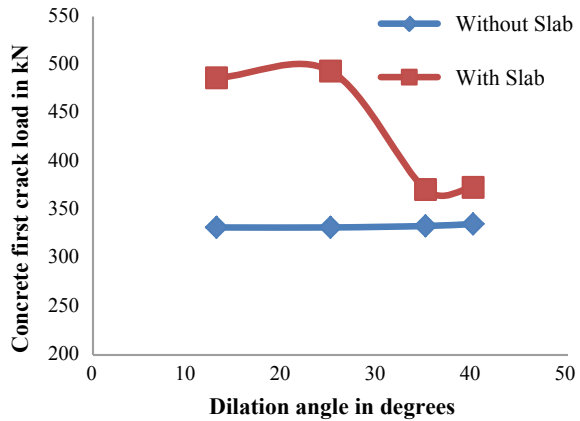
observed that the first cracking load of concrete has negligible change with dilation angle. From Figs. 11 and 12, for space frame with and without slab, it is observed that the first yielding loads of column and beam reinforcement increase with increasing dilation angle, due to higher stiffness. For space frame with slab, it is observed that the cracking of concrete is delayed at lower dilation angles. A delayed cracking signifies that the concrete was able to sustain more deformation. This is a result of decreased stiffness and improved ductility at lower dilation angles. From Table 3, it is observed that, with UHPC improvement, the first cracking/yielding loads of concrete,
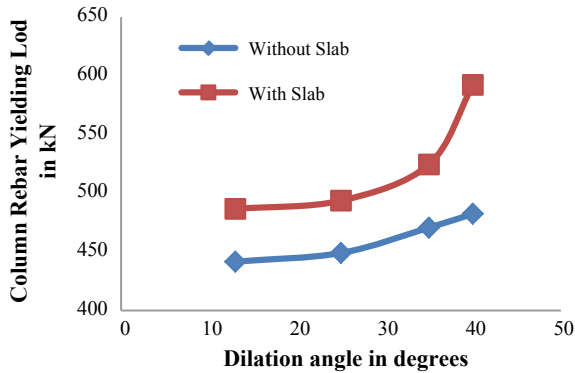
Fig. 11 Column rebar yielding load in kN versus dilation angle in degrees
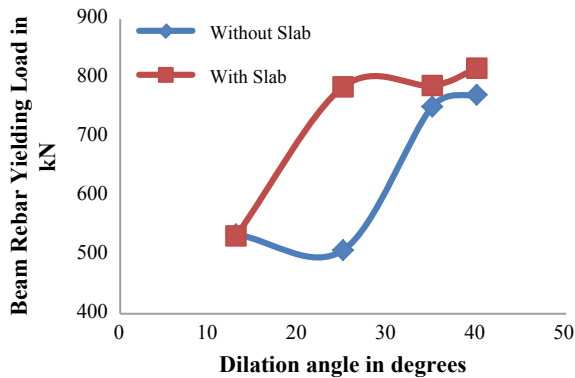
Fig. 12 Beam reinforcement yielding load in kN versus dilation angle

Table 3 First cracking/yielding loads in kN and displacement in mm with and without UHPC for space frame with slab at dilation angle 40

Case	Concrete crack load	Colum rebar yielding load	Beam rebar yielding load	Displacement
No UHPC, dilation angle 40	373.3	592.3	816.8	14.09
With UHPC, dilation angle 40	558.7	887.9	927.6	14.23

column reinforcement and beam reinforcement are substantially increased, with a negligible increase in displacement. From Figs. 13 and 14, it is observed that the extent of damage is greatly reduced by UHPC casing. In general, the space frame with slab has higher first cracking loads and thus a higher resistance to failure than space frame without slab. In general, it is seen that the reaction developed at higher

Fig. 13 Damage in tension without UHPC
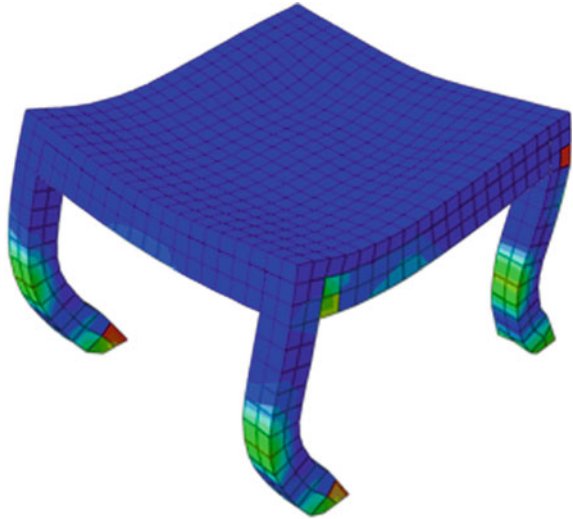
Fig. 14 Damage in tension with UHPC
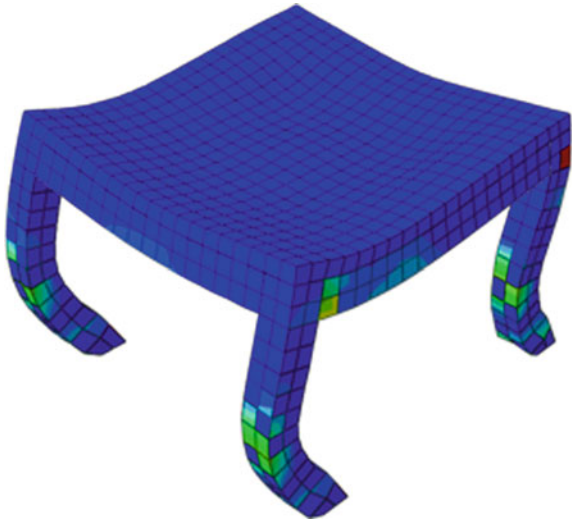
dilation angles is higher in comparison with that of lower dilation angles, with the exception of lateral reaction in *X*-direction, which reaches a peak at dilation angle 25° and then decreases, the displacement variation displaying no apparent pattern.

4 Conclusions

The natural frequencies of modes of vibration are similar in both space frames with and without slab. The modes successfully describe the failure behavior of the structure. Dynamic (seismic) analysis with parametric variation of dilation angle was successfully performed on space frames with and without slab. Higher dilation angles are superior to lower dilation angles, due to higher load-carrying capacity as well as lower displacements attributed to higher stiffness. Space frame with slab is superior to space frame without slab, due to higher load-carrying capacity as well as lower displacements attributed to higher stiffness. At lower dilation angles, due to higher ductility, resistance of concrete increases, and failure of concrete is delayed. This advantage is only seen in space frame with slab. At higher dilation angles, due to higher stiffness, the resistance to failure of reinforcement increases. This is the case, in both space frames with and without slab. Earthquake being a displacement loading, it is desirable to have deformability over strength, and sufficient warning before failure is an important factor. The space frame without slab deforms more and at an earlier time step without sufficient warning. Since the space frame with slab (concrete and reinforcement) has a higher resistance to failure and delayed failure than space frame without slab, providing ample warning, it is suggested to adopt space frame with slab. UHPC column casing improvement greatly increases the load-carrying capacity of the structure and reduces extent of damage, as computed using the CDPM. As per the above conclusions, it is suggested to adopt space frame with slab of concrete with higher dilation angles due to provision of ample warning, with UHPC improvement due to reduction in extent of damage, applicable for construction of structures resistant to seismic loads, or retrofitting of existing structures near seismically active zones.

References

1. Lee, J., & Fenves, G. (1998). A plastic damage model for cyclic loading of concrete structures. *Engineering Mechanics, 124*(8), 892–900.
2. Lubliner, J., Onate, E., Oller, S., & Oliver, J. (1989). A constitutive model for cracking of concrete based on the incremental theory of plasticity. *Engineering Computations, 5*(4), 309–319.
3. Jankowiak, T., & Łodygowski, T. (2005). Identification of parameters of concrete damage plasticity constitutive model. *Foundations of civil and environmental engineering, 6*(1), 53–69.
4. Sümer, Y., & Aktaş, M. (2015). Defining parameters for concrete damage plasticity model. *Challenge, 1*(3), 149–155.
5. Michal, S., & Winnicki, A. (2015). Numerical simulations of corners in RC frames using Strut-and-Tie method and CDP model. In *XIII International Conference on Computational Plasticity: Fundamentals and Applications* (pp. 608–619). Barcelona: CIMNE ed.

6. Genikomsou, S., & Polak, M. (2015). Finite element analysis of punching shear of concrete slabs using damaged plasticity model in ABAQUS. *Engineering Structures, 98,* 38–48.
7. Fadwa, I., Ali, T. A., Nazih, E., & Sara, M. (2014). Reinforced concrete wide and conventional beam–column connections subjected to lateral load. *Engineering Structures, 76,* 34–48.
8. Ali Shah, S. A., Shahzads, K., Afzal, S., Shabab, M. E., & Khattak, N. (2013). Behaviour of infill walls under lateral loads in reinforced concrete frames—A review. *International Journal of Advanced Structures and Geotechnical Engineering, 2*(3), 106–109.
9. Pedersen, R., Simone, A., & Sluys, L. (2008). An analysis of dynamic fracture in concrete with a continuum visco-elastic visco-plastic damage model. *Engineering Fracture Mechanics, 75,* 3782–3805.
10. Dulinska, J. M., & Szczerba, R. (2013). Simulation of dynamic behaviour of rc bridge with steel-laminated elastomeric bearings under high-energy mining tremors. *Key Engineering Materials, 531–532,* 662–667.
11. Konstantakopoulos, T. G., Raftoyiannis, I. G., & Michaltsos, G. T. (2012). Suspended bridges subjected to earthquake and moving loads. *Engineering Structures, 45,* 223–237.
12. Lee, J., & Fenves, G. (1998). A plastic-damage concrete model for earthquake analysis of dams. *Earthquake Engineering and Structural Dynamics, 27,* 937–956.
13. Calayir, Y., & Karaton, M. (2005). Seismic fracture analysis of concrete gravity dams including dam–reservoir interaction. *Computers & Structures, 83*(19–20), 1595–1606.
14. Omidi, O., & Vi, Lofti. (2012). Dynamic analysis of the Koyna Dam using three-dimensional plastic-damage modelling. *Dam Engineering, 22*(3), 197.
15. Zappitelli, M. P., Villa, E. I., Fernández-Sáez, J., & Rocco, C. (2014). Cracking development prediction in concrete. *Mecánica Computacional*, *XXXIII*, 23–26.
16. Indriyantho, B. R., Zreid, I., & Kaliske, M. (2017). Modeling of a concrete dam under earthquake loading by a nonlocal microplane approach. *Procedia Engineering, 171,* 1010–1018.
17. Ravikumar, C. M., KS, B. N., Sujith, B. V., & Reddy, V. (2012). Effect of irregular configurations on seismic vulnerability of RC buildings. *Architecture Research, 2*(3), 20–26.
18. Ashish, U. K., & Harshalata, R. (2014). Investigation on behaviour of reinforced concrete beam column joints retrofitted with FRP wrapping. *International Journal of Civil Engineering Research*, 2278–3652.
19. Truong, G. T., Kim, J. C., & Choi, K. K. (2017). Seismic performance of reinforced concrete columns retrofitted by various methods. *Engineering Structures, 134,* 217–235.
20. Kalyana Rama, J. S., Chauhan, D. R., Sivakumar, M. V., Vasan, A., & Murthy, A. R. (2017). Fracture properties of concrete using damaged plasticity model-A parametric study. *Structural Engineering and Mechanics, 64*(1), 59–69.

Mix Design Methodology for Fly Ash and GGBS-Based Geopolymer Concrete

G. Mallikarjuna Rao and M. Venu

1 Introduction

With the continuous increase in human population, the housing sector and construction industry have gained boom to meet the current demand. The increased usage and demand for cement production day by day lead to huge depletion of natural resources which ultimately results in environmental issues. To overcome these problems, there is a need to focus on new emerging binding materials such as industrial by-products, which will reduce the environmental pollution. Emerging technology aids for the utilization of industrial by-products into useful materials such as fly ash, GGBS, metakolin and rice husk ash. The development of alkali-activated binders with superior engineering properties as well as longer durability has emerged as an alternative to ordinary Portland cement (OPC). Geopolymer (inorganic polymer concrete) is an emerging class of cementitious material and could be the next-generation concrete for civil infrastructure applications. This innovative technology provides a new platform for the sustainable growth of our urban society in the coming decades and helps in building durable structures. These materials can be used as a replacement to the binder in concrete as a major construction material.

Davidovits, 1970, reported the use of waste materials like fly ash and GGBS as high alkaline solution activators to form geopolymer. The constituents of the commonly used alkaline solution are sodium hydroxide (NaOH) and sodium silicate (Na_2SiO_3). The alkaline solution helps to bind the loose aggregates in mixture to form geopolymer concrete (GPC) which has high strength, durability and low creep [1]. The alkaline solution activates silica and alumina to form aluminosilicate hydrate in fly ash and forms calcium silicate hydrate (C–S–H) by reacting with calcium in GGBS. The curing conditions, especially temperature, play a significant impact on the polymerization process [2]. Researchers have [3] concluded that a combination

G. Mallikarjuna Rao (✉) · M. Venu
Department of Civil Engineering, Vardhaman College of Engineering, Hyderabad, India
e-mail: gmyadav25@gmail.com

of sodium hydroxide and sodium silicate solutions can be a good application for activators. High concentration of sodium hydroxide solution and curing temperature enable the concrete compressive strength to be higher. Various authors have studied the importance of molar ratio of Na_2SiO_3/NaOH and suggested that to achieve maximum compressive strength the binder content to be constant. The reported constant binder content value is 2.5 [4]. Rangan [5] proposed a mix design methodology for geopolymer concrete with fly ash and [6] suggested modifications in Indian Standard code for suitability of GPC. Black [7] carried out research on fly ash-based geopolymer concrete by considering different mix proportions and developed a mix design process by varying the water to geopolymer solids ratio with two different molarities of NaOH, i.e. 8M and 12M. The research concluded that the flash set was a significant problem for GPC mixes.

In the present study, a mix design procedure was developed for both normal- and standard-grade geopolymer concrete by varying the ingredients. The ingredients varied for all the mixes are quantity of fly ash, quantity of water, grading of fine aggregate, fine aggregate-to-total aggregate ratio by maintaining sodium silicate-to-sodium hydroxide ratio as 1 and sodium hydroxide molarity. Based on the past work done on GPC, the present research work is planned by considering the parameters, viz. type of binder, binder content, alkaline/binder ratio. The ratio of sodium silicate to sodium hydroxide is kept at 2.5 with molarity of NaOH as 8M. This investigation aims to study the influence of the above-considered parameters on strength and durability of geopolymer concrete.

2   Research Significance

From the literature survey, to the best of authors' knowledge, there is no proper mix design for fly ash and GGBS-based geopolymer concrete till date, and it shows that the study needs to focus on mix design aspects for geopolymer concrete. This will help the structural engineers in design aspects to implement the same for the field application. The present investigation aims a proper mix design methodology for fly ash and GGBS-based GPC.

3   Materials

3.1   Fly Ash and GGBS

Materials used in this research are GGBS obtained from Andhra Cements, Vishakhapatnam, India, and fly ash from Ramagundam Thermal Power Plant, India, with a specific gravity of 2.90 and 2.17, respectively. The chemical compositions of GGBS and fly ash were presented in Table 1.

Table 1 Chemical composition of both fly ash and GGBS (% by mass)

Chemical composition	Fly ash	GGBS
SiO_2	60.10	34.02
Al_2O_3	26.50	20.00
Fe_2O_3	4.20	0.81
SO_3	0.33	0.93
CaO	4.00	32.65
MgO	1.21	7.86
Na_2O	0.20	NIL
LOI	0.85	NIL

3.1.1 SEM and XRD for Fly Ash and GGBS

Scanning electron microscopy (SEM) is performed to study the microstructure of fly ash and GGBS. The scanned images of fly ash and GGBS are shown in Figs. 1 and 2. Scanning electron microscopy image gives an approximate idea about the shape, angularity, size and surface texture of fly ash and GGBS. The GGBS particles appear
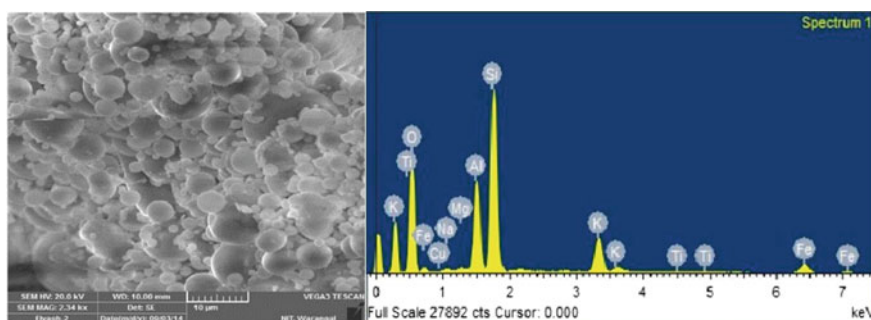
Fig. 1 Scanning electron microscope of fly ash and EDXA of fly ash
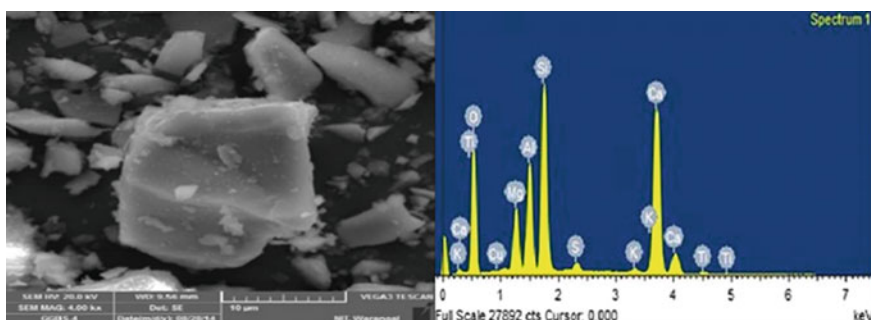
Fig. 2 Scanning electron microscope of GGBS and EDXA of GGBS
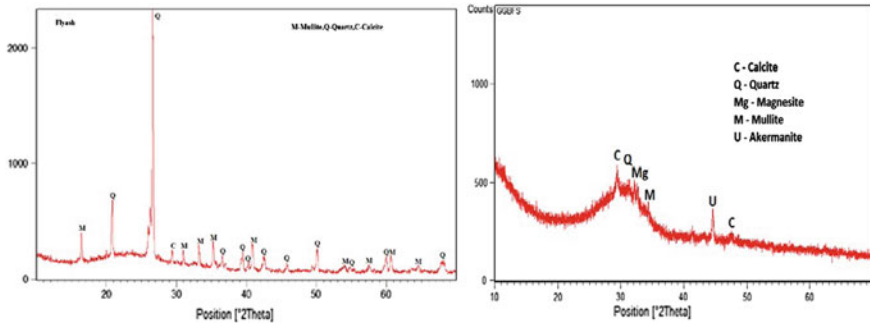
Fig. 3 XRD analysis for fly ash and GGBS

to have straight, flaky-elongated shape with sharp-edged angularity, rough surface texture and large variation in size (1–10 µm). The fly ash particles appear to have spherical shape with smooth surface in a broad range of sizes (with the lower limit being approximately 1/10 the maximum fly ash particle size, i.e. 1–10 µm in size). The energy-dispersive X-ray spectroscopy of fly ash and GGBS is also shown in Figs. 1 and 2. From the energy-dispersive X-ray spectroscopy, it is seen that GGBS is enriched with more silica percent than other elements. Fly ash particles contain more percent of silica and alumina (Fig. 3).

3.2 Alkaline Liquid

The alkaline solution is the combination of sodium hydroxide and sodium silicate solutions. Sodium hydroxide is used in the present study because it is less expensive than potassium hydroxide and widely available. Sodium hydroxide of 98% purity available in pellets form is used in the investigation. These sodium hydroxide pellets were dissolved in potable water and prepared the solution of required molarity. Sodium hydroxide solution of required molarity and sodium silicate in liquid form and the chemical composition of the sodium silicate is Na_2O—7.5–8.5%, SiO_2—26.5% and remaining is H2O content are mixed and stored at room temperature for 24 h before its use (Fig. 4).

3.3 Fine Aggregate

A locally available river sand is used as a fine aggregate, and it conforms to Zone-2 according to IS: 383 [8]. The specific gravity and bulk density are 2.62 and 2.59, respectively.

Fig. 4 Sodium hydroxide and sodium silicate solution

3.4 Coarse Aggregate

A locally available crushed rock maximum size of 20 mm is used as a coarse aggregate, and it is according to IS: 383 [8].

3.5 Water

Potable water was used for entire research work to prepare NaOH solution.

3.6 Preparation of Concrete

The fly ash and GGBS are mixed well until once it reaches homogeneity, and thereafter, fine and coarse aggregate is added, and these are allowed to mix for 2 min in Hobart electric mixer. For instance, the prepared alkaline activator is added to the prepared mix which is a combination of fly ash, GGBS, fine aggregate, and it is mixed well for another 3 or 4 min in Hobart electric mixer. The prepared fresh mixes are cohesive and resistant to segregation. Afterward, GPC is poured into the molds of size 100 mm × 100 mm × 100 mm by three layers consecutively with compaction and vibration to avoid air bubbles in concrete. After 24 h of casting, the specimens were demolded, and these were cured under ambient temperature until the age of testing.

3.7 Experimental Program

An experimental program consisting of five mixes, in each mix fly ash—GGBS proportion varied between 75FA:25GGBS, 50FA:50GGBS, 25FA:75GGBS and 0FA:100 GGBS for the binder. For the corresponding mixes, alkaline liquid-to-binder ratios were selected as 0.45, 0.5, 0.55 and 0.6, respectively. Geopolymer concrete density was noted, and it varied from 2200 to 2400 kg/m^3. Once the density of concrete is known, then the total amount of binder and alkaline solution can be calculated easily. The ratio of sodium silicate to sodium hydroxide solution is kept constant as 2.5 for the total experimental program.

4 Results and Discussions

The density of the fly ash and GGBS based geopolymer concrete specimens are shown in Fig. 5. With increase in density, there is an increase in the alkaline/binder ratio, and the maximum density was observed for the mix of 0% FA+100% GGBS. Maximum density was observed at alkaline/binder ratio 0.6 for all the combinations. Geopolymer concrete is a new concrete, and the density of the geopolymer was quite similar to that of the conventional concrete. The density of the geopolymer concrete depends on the binder content, alkaline/binder ratio and method of compaction. The density range observed for geopolymer concrete was 2300–2500 kg/m^3.

The UPV test is a measure to presence of voids and the consistency of concrete. The 7 days UPV for different combinations of the fly ash and GGBS mix was found to be 3.26–4.5 km/s for outdoor-cured specimens for different combinations, whereas
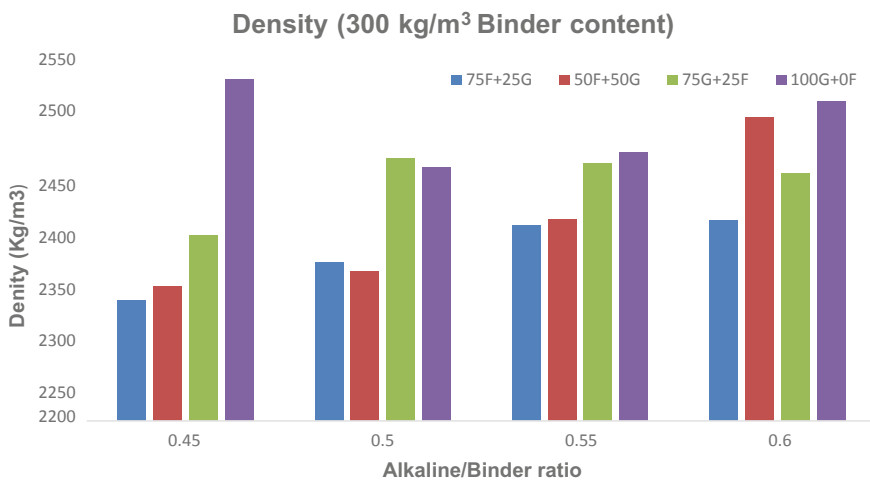

Fig. 5 Density for fly ash and GGBS-based geopolymer concrete (300 binder content)

for higher GGBS content mixes, there is a little rise in the values compared to that of lower GGBS content. **Whitehurst** classified fly ash-based geopolymer concrete as excellent, good, doubtful, poor and very poor for UPV values of 4.5 km/s and above, 3.5–4.5, 3.0–3.5, 2.0–3.0 km/s and below 2.0 km/s, respectively. Generally, high-pulse velocity reading in concrete is indicative of concrete of good quality. The presence of voids has been recognized to have an influence on the UPV transmission. The measured 28-day UPV values for all geopolymer concrete specimens are presented in Fig. 6. In geopolymer concrete, for the attainment of strength, polymerization process plays an important role. The quality of the concrete mainly depends on the internal microstructure formed.

Figure 7 shows the compressive strength of different alkaline to binder ratios with binder content 300 kg/m^3. In the present study, effect of fly ash and GGBS concrete under outdoor curing was studied. The compressive strength of GPC cured under outdoor curing (0% FA+100% GGBS) combination shows the higher strength than the mixes prepared with the other combinations of GGBS. In order to eliminate the oven curing, the specimens were casted with the fly ash and GGBS combination. For many practical applications, it is very important that the concrete should be cast and cured under normal temperatures. The maximum compressive strength of 45 MPa is attained at 100% GGBS even under outdoor curing. This concludes that combination of fly ash and GGBS can produce satisfactory results even with 8M NaOH. Hence, the obtained results proved that oven curing can be eliminated for producing GPC, where there is difficulty in providing oven curing. At 7 days age of curing, 100% GGBS achieved the maximum compressive strength. In the case of 75% FA-25%, GGBS proportion indicates the lesser compressive strength. The
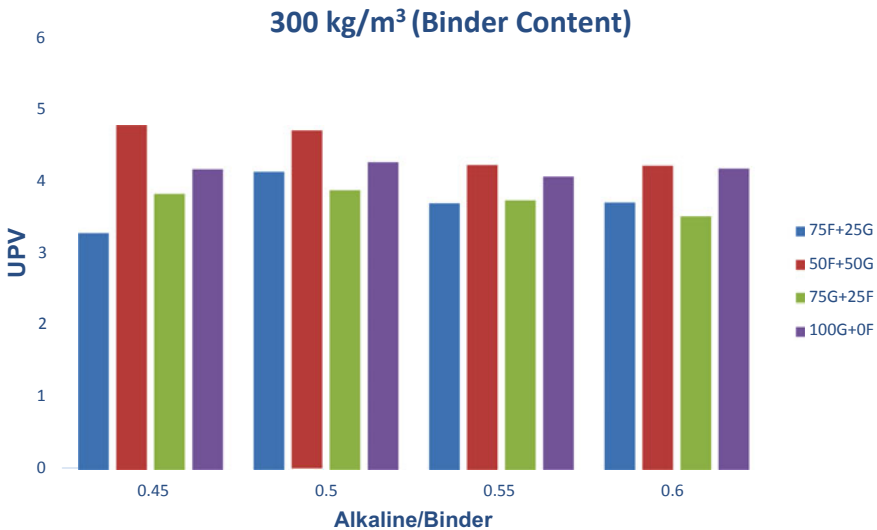
Fig. 6 UPV for fly ash and GGBS-based geopolymer concrete (300 binder content)
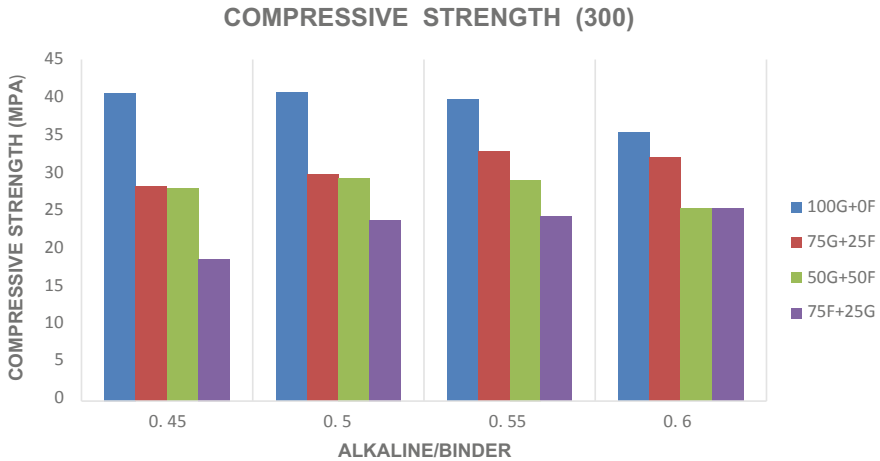
Fig. 7 Compressive strength for fly ash and GGBS-based geopolymer concrete (300 binder content)

increase in compressive strength is mainly due to high amount of calcium present in GGBS. The improvement of strength of fly ash and GGBS-based GPC is due to increased calcium content present in GGBS which significantly accelerates the polymerization process to improve strength.

5 Conclusions

- The percentage increase of GGBS in binder content shows the increase in compressive strength of geopolymer mortar.
- The combination of fly ash and GGBS is a possible solution for producing GPC even under outdoor curing condition.
- The geopolymer concrete dry density varied from 2400 to 2500 kg/m^3 for (100% GGBS+0% fly ash) binder proportion, and for remaining proportions, it varied from 2300 to 2400 kg/m^3 which is likely to be conventional concrete.
- For higher density samples show the higher in the compressive strength when the age of 7 days for all mixes.
- The significant increase in compressive strength was observed at alkaline/binder ratio of 0.55 for a binder content of 300 kg/m^3.
- UPV performance is good for GPC at the age of 7 days, and it shows the similar trend to that of conventional concrete noticed, i.e. 3.5–4.5 km/s. This range shows the good sign of concrete quality and homogeneity.

References

1. Wang, S. D., Pu, X. C., Scrivener, K. L., & Pratt, P. L. (1995). Alkali-activated slag cement and concrete: A review of properties and problems. *Advances Cement Research, 27,* 93–102.
2. Glukhovsky, V. D. (1959). Soil silicates. Gosstroiizdat, Kiev, (in Russian 1959).
3. Hardjito, D., Wallah, S. E., Sumajouw, D. M. J., & Rangan, B. V. (2004). On the development of fly ash-based geopolymer concrete. *ACI Materials Journal, 101*(6), 467–472.
4. Pinto, A. (2004). *Alkali-activated metakaolin based binders* (PhD thesis). University of Minho.
5. Rangan, B. V. (2008). Mix design and production of fly ash based geopolymer concrete. *Indian Concrete Journal, 82*, 7–15.
6. Anuradha, R., Sreevidya, V., Venkatasubramani, R., & Rangan, B. V. (2012). Modified guidelines for geopolymer concrete mix design using Indian standard. *Asian Journal Civil Engineering (Build Hous),13*(3), 353–364.
7. Black, J. R. (2012). *Mix design process for alkaline-activated class f fly ash geopolymer concrete*. University of New South Wales at the Australian Defence Force Academy.
8. IS-383-1970, Specification for coarse and fine aggregates from natural sources for concrete.

Experimental and Analytical Behavior of Recycled Aggregate Concrete Using ANN

B. Suguna Rao, Vithal Joshi, and Srikanth M. Naik

1 Introduction

Concrete is being one of the most consumed material in the area of infrastructure. Among the various ingredients present in the concrete, aggregates play an important role. Aggregates play a vital role in concrete by providing volume stability to the concrete. The increase in population and rapid urbanization has increased the demand for increased infrastructure development. The construction activity is being majorly using concrete as a material of construction. For satisfying the demand of the increased construction activity, there is a huge requirement of aggregates. Availability of aggregates in large scale and at the time of need has become scarce and is also causing environmental impacts. In order to facilitate the need of aggregates, an effort has been made to utilize construction and demolition waste as aggregates in concrete. A large quantity of C & D waste is being generated yearly and the quantity measured is around 14.5 million tons as per the reports of Central Pollution Control Board (CPCB), Delhi. The quantity of waste being utilized in a useful way is only around 3% and the rest of the waste goes into landfill areas. Increased population explosion has also reduced the land availability. Utilizing C & D waste is one of the solutions for environmental sustainability and economical benefit. C & D waste being concrete waste has properties of concrete finding its suitability in concrete production. According to the literature, recycled aggregates have specific gravity lesser than natural aggregates and have higher water absorption than natural

B. Suguna Rao (✉)
Department of Civil Engineering, M.S. Ramaiah Institute of Technology, Visvesvaraya Technological University, Bangalore, Karnataka, India
e-mail: suguna_rao@msrit.edu

V. Joshi · S. M. Naik
Department of Civil Engineering, M.S. Ramaiah Institute of Technology, Bangalore, Karnataka, India
e-mail: srikanth_naik@yahoo.com

aggregates which may be due to adhered mortar to RAC. While utilizing recycled aggregates for structural concrete, the characterization of the material properties is required to understand the water absorption and specific gravity of recycled aggregate concrete. The compressive strength of concrete made from recycled aggregate concrete with respect to controlled mix with same water–cement ratio was studied and variations are observed with respect to elastic modulus, shrinkage and creep [1]. Hence, an effort is made to understand recycled aggregate concrete by characterizing them initially and checking the fresh properties to be suitable for hardened concrete. Concrete made from recycled aggregates are tested for their strength and results are utilized for predicting their behavior using artificial neural networks (ANN). ANN is a powerful modeling tool specially useful tool when high reliable results are expected from varying variables [2]. ANN develops a multilayer perceptron made up of several neurons grouped in three layers such as input layer, hidden layer and output layer imitating the functioning of biological brain being utilized in wide range of application from structural concrete to timber panels [3]. This study aims at understanding the behavior of recycled aggregate concrete by conducting various experiments and validating it through ANN.

2   Materials and Methodology

2.1   Materials

The materials used to carry out the experimental investigation of recycled aggregate concrete are as follows:

1. Cement: Cement used here is OPC of 43 grades.
2. Fine Aggregate: Manufactured sand.
3. Coarse Aggregate:

    (1) Natural aggregate of size 20 mm downsize for M40 grade of concrete and 12.5 mm downsize for M60 grade of concrete.
    (2) Recycled aggregates are procured from rock well crystal recycling plant of size 20 mm downsize for M40 grade and 12.5 mm downsize for M60 grade.

4. Admixtures:

    (1) Mineral admixture: 10% silica fume and 10% fly ash.
    (2) Chemical admixture: Superplasticizer Aura mix 400 as per workability requirement.

5. Water: Portable water.

2.2 Characterization of Materials

Initially, the basic characterization of the material used is carried out and is as shown in Table 1 for cement and Table 2 for fine aggregate and Table 3 for coarse aggregate. Results of the characterization of materials were within the acceptable limits of codes. These materials are considered for preparing the mix design of recycled aggregate concrete.

Table 1 Properties of cement

Properties of cement	Test results
Specific gravity	3.05
Setting time	Initial setting time 40 min Final setting time 345 min
Fineness (%)	6
Standard consistency (%)	33

Table 2 Properties of fine aggregate

Properties	Fine aggregate
Specific gravity	2.48
Fineness modulus	3.943
Moisture content (%)	4

Table 3 Properties of natural and recycled coarse aggregates

Properties	Natural coarse aggregate		Recycled coarse aggregate	
	12.5 mm downsize	20 mm downsize	12.5 mm downsize	20 mm downsize
Water absorption	1.3%	1.8%	3.2%	3.4%
Crushing value	23.67%	15.69%	32.39%	20.94%
Abrasion value	–	26.75%	–	30.72%
Impact value	25.49%	–	34.39%	–
Specific gravity	2.56	2.61	2.30	2.34
Fineness modulus	8.182	6.716	8.298	6.752

Table 4 Mix proportion used for M40 and M60 grade of concrete

Materials	M40-per cubic meter (Kg/m^3)	M60-per cubic meter (Kg/m^3)
Cement	414.766	444.4
Water	139.984	150
FA	603.309	551.4
NA	1136.468	1000
RCA	–	–
SP	3.111	3.333
SF	51.846	55.56
FA	51.846	55.56

2.3 Mix Design and Testing

After testing the basic characterization of the materials, mix design procedure proposed by Perumal [4] for high strength concrete is being adopted for M60 grade of concrete and IS 10262:2000 is adopted for M40 grade of concrete. Fresh properties tests were conducted to fix the dosage of superplasticizer by considering 100% replacement ratio as the worst combination of mix. Table 4 shows the mix design proportions adopted for M60 and M40 grade of concrete for normal aggregate concrete. The mix design is adopted to achieve M60 and M40 grade of concrete for replacement ratio of 0, 50 and 100% for W/B (water–binder) ratio of 0.27 and 0.36.

2.4 Experiment

Concrete cubes of sizes 150 mm × 150 mm × 150 mm were casted for *W/B* (water–binder) ratio of 0.27 and 0.36 for M40 and M60 grade of concrete. The concrete cubes were tested for 1, 3, 7, 14 and 28 days strength. Three specimens were casted for each of the mix proportion and for each testing day considered. Compressive strength of 180 specimens was observed. The achieved 28 day compressive strength is plotted as shown in Figs. 1 and 2.

From the above experimental analysis, we can say that for replacement ratio of 50% there is a reduction in compressive strength by 15–25% and for 100% replacement ratio of recycled aggregate the compressive strength reduces by 28–38%. When compared with the grade of concrete, high strength concrete performed better than concrete of grade M40 for *W/B* ratio of 0.27 than for 0.36. One of the reasons for the variation in the strength of the concrete may be due to the sizes of the aggregates of M40 and M60 grade of concrete.
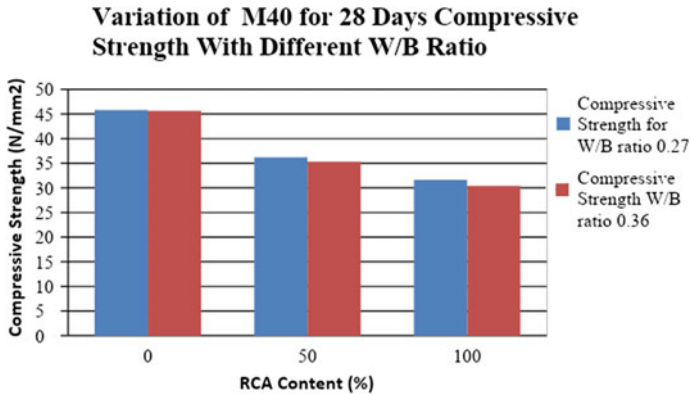
Fig. 1 Compressive strength of M40 grade of concrete for different W/B ratio
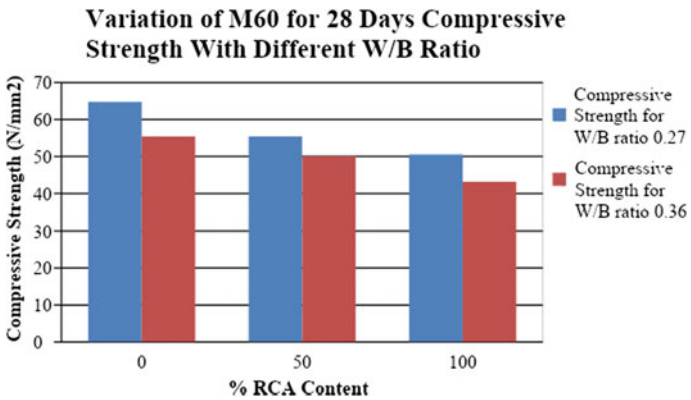
Fig. 2 Compressive strength of M60 grade of concrete for different W/B ratio

3 Predictive Analysis Using ANN

The need of the hour is to develop sustainable concrete by utilizing the C & D waste as aggregates. Several constrains exist while using secondary products like recycled aggregates. The major concern is quality and consistency of the products. The challenge in using recycled aggregates dependents on source, age of old concrete, crushing technology adopted, etc. Hence, to understand the strength parameter of recycled aggregate concrete, a powerful tool like ANN is used where the aggregates used are consisting of varying properties and source. This varying property leads to variation in the result of concrete. Predicting the compressive strength of concrete with its constituents is a nonlinear function [5–11]. The strength parameter of concrete not only depends upon water-to-cement ratio, but also depends upon the additive constituents. The lack of empirical relationships to judge the compressive

strength of concrete has created the need for using soft computing tools by various researchers. Soft computing tool uses the optimization tools for learning and predicting and creating new patterns based on the previous data. ANN consists of networks of simple nonlinear computing elements called neurons. ANN is a useful tool used for processing the data through training, testing and arriving at suitable results for a specific nature of problem and is easily transportable between the computing systems. The capability of ANN to arrive at a model in which relationship between dependent variable and independent variable is popular machine learning method. This unconventional method of arriving at a solution has created an immense interest in the field of neural networks. ANN has the capability of constructing a relationship between the data provided for training. While using ANN, there is no need to provide any functional relationship among the variables. ANNs modeling ability to derive meaning from unknown and nonlinear interrelationships among variables have been harnessed to aid the prediction of behavior of engineering and natural systems. Compressive strength of concrete is unstructured in nature and involves a high nonlinear relationship among its constituents. Therefore, an attempt is made to predict the compressive strength of concrete considering 14 input parameters and compressive strength as output parameter. Using machine learning technique like ANN, to predict the compressive strength of concrete significantly reduces the time and money for the industry.

3.1   Experiment Design was Designed Using ANN

A total of 14 input parameters were chosen to design the model to give one output value which is compressive strength of concrete at 28 days.

Selection of Input Parameters Factors affecting the strength of concrete are considered as input parameters. Concrete constituents: Quantity of cement, water, sand, natural aggregates and recycled aggregate are the most important factors affecting the strength of concrete. While understanding the nature of aggregates influencing the compressive strength of concrete fineness modulus of sand is overlooked in many studies, which influences the workability, permeability and strength of concrete. The properties of coarse aggregates like maximum particle size, SSD specific gravity and water absorption are some of the factors that affect the strength greatly [12]. The data collected for the study varied from low to high strength as the variation in strength also depends upon crushing process involved, source of these aggregates and age of the aggregates. Source of the aggregates is an important factor that needs to be considered while proposing the concrete for structural purpose [13]. Table 5 shows the list of input parameter used in this study.

Selection of Output Parameter The 28 days compressive strength of concrete was the output parameter considered in this study.

Table 5 List of input parameters

Parameter	Min.	Max.
Cement (kg/m^3)	220	450
Mineral admixture (kg/m^3)	0	102.5
Water (kg/m^3)	120	271
Sand (kg/m^3)	540	1020
N.A. (kg/m^3)	0	1186.18
R.A. (kg/m^3)	0	1070.9
W/B	0.3	0.76
F.M.	2.11	3.88
Max. size of CA (mm)	12.5	25
Water absorption (%)	2.24	10.6
SSD specific gravity	2.27	2.76
Rv (%)	0	100
Chemical admixture (%)	0	3
Impurity (%)	0	5
Compressive strength MPa	17	85

Data Collection A total of 136 sets of experimental data from different literature sources were collected to train and check the reliability of the strength model [14–32]. The available data is divided into three parts consisting of training set which consists of 75% of the data, and the second part is 12.5% of data utilized in validation while the remaining data is used for testing, to test the accuracy of the prediction.

3.2 Construction of ANN Model

Feed-forward back-propagation network was used in this study with 14 input variables and one unit in output. The network parameter included three hidden layer = 0, 1 and 2; and number of hidden neurons = 2–50; learning rate varied 0.1 variation up to 2.0; the momentum factor used are 0, 0.3, 0.5, 0.7, 0.9 and 1; the variation of learning cycle = 500, 1000, 5000, 10,000, 20,000 and 50,000. These momentum factors cover the entire database available for training.

Functions used as solver are Quasi-Newton, Levenberg–Marquardt and conjugate gradient decent. Activation functions used here are hyperbolic tangent, logistic and linear. To maximize the R^2 value and to ascertain the error of integral testing set after conducting a series of trials, the best network architecture and parameters were used. From the 14 input parameter included for the study, the best network architecture was developed for 30 hidden units within one hidden layer and one output layer. The rate of momentum is 0.1 with 1000 learning cycle. Quasi-Newton was the solver function that resulted in hyperbolic tangent as activation function.

Table 6 Performance of network

	Test set	Training set	All sets
R^2	0.95	0.94	0.94
MAE	2.19	2.36	2.47
Correlation	0.98	0.97	0.97

3.3 Analysis Results and Discussion

The performance of the network is judged based on R^2 (coefficient of determination), mean absolute error (MAE) and correlation coefficient values. Table 6 shows the results for the best network model.

Coefficient of determination value was 0.95 for test set and 0.94 for training set and for all sets considered together. MAE value was 2.19 for test set, 2.36 for training set and 2.94 for all sets. Correlation value of 0.98 was obtained for testing set and the ANN model provided with 28 day compressive strength closer to the experimental determined values.

The performance of ANN predicted a relationship between different input parameters and output parameter. The prediction is depicted in Figs. 3, 4 and 5. The results arrived from ANN are listed in Table 7.

From Table 7, we can observe that maximum and minimum absolute errors in the testing sets were 5.78 MPa and 0.02 MPa, respectively. The range of errors is from 0.06 to 11.35%. The relative error was about 5.07% which is considered good and acceptable. Predicted values of 28 day compressive strength matched very well for target strength of concrete.

The ANN model predicted good performance of compressive strength which is closer to the target strength. Some of the test data did not fit very well, and this might be due to several reasons including:

Fig. 3 Training set
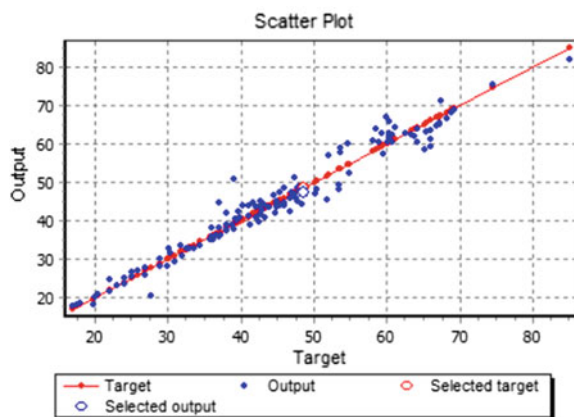
Fig. 4 Testing set used in ANN
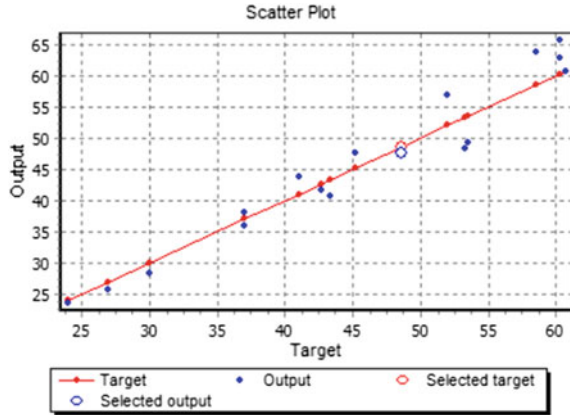
Fig. 5 Validation of ANN model using 28 days compressive strength data from literature
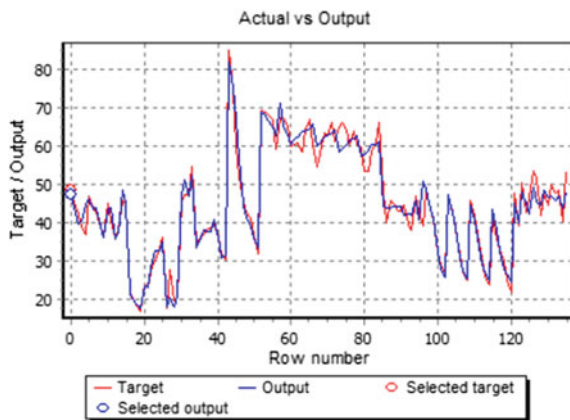
(1) Conversion of cylindrical strength to cube strength of concrete leads to error due to approximation of strength data.

(2) The missing information in various literatures regarding type of cement is one of the setbacks to streamline the results.

(3) The processing method adopted to procure recycled aggregates, source of recycled aggregate and strength index is not mentioned in many literatures which will help to improve the accuracy of prediction.

Test results showed that the constructed ANN model was able to predict the compressive strength values of RAC accurately. When using ANN to predict the compressive strength value of RAC, the maximum particle size of aggregate, water absorption and SSD specific density can generally reflect the properties of RA, however, the performance of ANN model can still be improved if more parameters can be considered, such as cement type and quality of the recycled aggregate.

Table 7 Comparison of actual and predicted values

Sr. No.	Actual value	Predicted value	Absolute error	Absolute relative error (%)
1	43.8	43.45	0.35	0.79
2	38.9	41.2	2.3	5.91
3	20	22.27	2.27	11.35
4	36.16	33.94	2.22	6.13
5	35.8	32.78	3.02	8.43
6	32.04	32.06	0.02	0.06
7	68.82	69.85	1.03	1.49
8	60.72	60.91	0.19	0.31
9	64.2	61.34	2.86	4.45
10	65.12	59.34	5.78	8.87
11	60.72	58.58	2.14	3.52
12	44.9	43.01	1.89	4.20
13	44	43.08	0.92	2.09
14	43	39.36	3.64	8.46
15	36	39.84	3.84	10.66
16	50.41	46.14	4.27	8.47
17	53.34	53.88	0.54	1.01

4 Conclusion

In this paper, an effort is made to understand the basic characteristics of recycled aggregate concrete with the inclusion of various ingredients. The parameters studied were within the acceptable limits of the codes. The experimental analysis conducted to study compressive strength of concrete gave us an infer that high strength concrete performed better than normal strength concrete and at lower W/B ratio of 0.27. The ANN model created, predicted the compressive strength of concrete with minimal error. The model can be further improved by considering parameters like source of recycled aggregate and method of processing. Along with compressive strength, properties of concrete such as creep, shrinkage, modulus of elasticity and durability can be studied using ANN.

References

1. Sabaa, B., & Ravindrarajah, R. S. (1997). *Engineering properties of lightweight concrete containing crushed expanded polystyrene waste*. Sydney, Australia: Faculty of Engineering, University of Technology.
2. De Veaux, R. D., & Ungar, L. G. (1996). *A brief introduction to neural networks*. http://www.cis.upenn.edu/Datamining/publications/nnet-intro.pdf. Last accessed 26 May 2014.

3. Yeh, I. C. (1998). Modelling of strength of high-performance concrete using artificial neural networks. *Cement and Concrete research, 28*(1), 797–808.

4. Perumal, K., & Sundararajan, R. (2004). Effect of partial replacement of cement with silica fume on the strength and durability characteristics of high performance concrete. In *29th conference on our world in concrete and structures*, 25–26 Aug 2004. Singapore.

5. Duan, Z. H., Kou, S. C., & Poon, C. S. (2013). Prediction of compressive strength of recycled aggregate concrete using artificial neural networks. *Construction and Building Materials, 40*, 1200–1206.

6. Chopra, P., Sharma, R. K., & Kumar, M. (2015). Artificial neural networks for the prediction of compressive strength of concrete. *International Journal of Applied Science and Engineering, 13*(3), 187–204.

7. Shao, J., Ji, X., & Li, R. (2015). Application of BP neural network model in the recycled concrete performance prediction. In *International Conference on Advances in Energy, Environment and Chemical Engineering (AEECE)*.

8. Chandwani, V., Agrawal, V., & Nagar, R. (2014). Applications of artificial neural networks in modeling compressive strength of concrete: a state of the art review. *International Journal of Current Engineering and Technology*, E-ISSN 2277–4106, P-ISSN 2347–5161, ©2014 INPRESSCO®. http://inpressco.com/category/ijcet.

9. Yousif, S. T., & Abdullah, S. M. (2009). Artificial neural network model for predicting compressive strength of concrete. *Tikrit Journal of Engineering Sciences*, *16*(3), 55–66.

10. Chopra, P., Sharma, R. K., & Kumar, M. (2016). Prediction of compressive strength of concrete using artificial neural network and genetic programming, Hindawi Publishing Corporation. *Advances in Materials Science and Engineering, 2016*(Article ID 7648467), 10. http://dx.doi.org/10.1155/2016/7648467.

11. Nikoo, M., Torabian Moghadam, F., & Sadowski, A. (2015). Prediction of concrete compressive strength by evolutionary artificial neural networks, Hindawi Publishing Corporation. *Advances in Materials Science and Engineering, 2015*(Article ID 849126), 8. http://dx.doi.org/10.1155/2015/849126.

12. Malesev, M., Radonjanin, V., & Marinkovic, S. (2010). Recycled concrete as aggregate for structural concrete production. *Sustainability, 2*, 1204–1225. https://doi.org/10.3390/su2051204. http://www.mdpi.com/journal/sustainability.

13. Mirza, F. A., & Saif, M. A. (2010). Mechanical properties of recycled aggregate concrete incorporating silica fume. In *Second International Conference on Sustainable Construction materials and Technology*. http://www.claisse.info/Proceedings.htm.

14. Vyas, C. M., & Bhatt, D. R. (2013). Destructive strength properties of recycled coarse aggregate. *International Journal of Innovative Technology and Exploring Engineering, 2*(3).

15. James, M. N., Choi, W., & Abu-Lebdeh, T. (2011). Use of recycled aggregate and fly ash in concrete pavement. *American Journal of Engineering and Applied Sciences, 4*(2), 201–208. Department of Civil, Architecture and Environmental Engineering, North Carolina A and T State University, USA.

16. Sivakumar, N., Muthukumar, S., Sivakumar, V., Gowtham, D., & Muthuraj, V. (2014). Experimental studies on high strength concrete by using recycled coarse aggregate. *Research Inventy: International Journal of Engineering and Science, 4*(01), 27–36. Department of Civil Engineering, Jay Shriram Group of Institutions, Tirupur, Tamil Nadu, India.

17. Sonawane, T. R., & Pimplikar, S. S. (2013). Use of recycled aggregate concrete. *IOSR, Journal of Mechanical and Civil Engineering (IOSR-JMCE)*, 52–59, ISSN: 2278–1684. www.iosrjournals.org.

18. Parekh, D. N., & Modhera, C. D. (2011). Assessment of recycled aggregate concrete. *Journal of Engineering Research and Studies, JERS, II*(I), 1–9. Applied Mechanics Department; Sardar Vallbhbhai National Institute of Technology; Surat; Gujarat.

19. Kou, S. C., & Poon, C. S. (2012). Enhancing the durability properties of concrete prepared with coarse recycled aggregate. *Construction and Building Materials, 35,* 69–76.

20. Kou, S., Poon, C., & Agrela, F. (2011). Comparisons of natural and recycled aggregate concretes prepared with the addition of different mineral admixtures. *Cement and Concrete Composites, 33,* 788–795.

21. Babu, V. S., Mullick, A. K., Jain, K. K., & Singh, P. K. (2013). Mechanical properties of high strength concrete with recycled aggregate-influence of processing. *The Indian Concrete Journal, 88,* 10–26.

22. Qasrawi, H. (2014). The use of steel slag aggregate to enhance the mechanical properties of recycled aggregate concrete and retain the environment. *Construction and Building Materials, 54,* 298–304.

23. Mukharjee, B. B., & Barai, S. V. (2014). Influence of nano-silica on the properties of recycled aggregate concrete. *Construction and Building Materials, 55,* 29–37.

24. Yadav, S. R., & Pathak, S. R. (2009). Use of recycled concrete aggregate in making concrete-an overview. In *34th Conference, Our World In Concrete and Structures*, 16–18 Aug 2009. Singapore.

25. Kalpavalli, A., & Naik, S. M. (2015). Use of demolished concrete wastes as coarse aggregates in high strength concrete production. *International Journal of Engineering Research and Technology (IJERT), 4*(7), ISSN: 0181–2278, IJERTV4IS070935. www.ijert.org.

26. Poon, C. S., Shui, Z. H., Lam, L., Fok, H., & Kou, S. C. (2004). Influence of moisture states of natural and recycled aggregates on the slump and compressive strength of concrete. *Cement and concrete research, 34*(1), 31–36.

27. Poon, C. S., Kou, S. C., & Lam, L. (2007). Influence of recycled aggregate on slump and bleeding of fresh concrete. *Materials and Structures, 40*(9), 981–988.

28. Suguna Rao, B., Suresh, A., & Naik, S. M. (2019). Shrinkage behaviour of high strength concrete using recycled concrete aggregate. *As proceeding of ICSCBM*, pp 829–837. Springer book chapter https://doi.org/10.1007/978-981-13-3317-0_74.

29. Yong, H. L., Yaw, T. Y., Ta, C. P., & Ching, Y. C. (2004). An assessment of optimal mixture for concrete made with recycled concrete aggregates. *Cement Concrete Research, 34*(8), 1373–1380.

30. Cabo, A. D., Lázaro, C., Gayarre, F. L., López, M. A. S., Serna, P., & Tabares, J. O. C. (2009). Creep and shrinkage of recycled aggregate concrete. *Construction Building Material, 23*(7), 2545–2553.

31. Kou, S., & Poon, C. (2012). Effect of quality of parent concrete on the mechanical properties of high performance recycled aggregate concrete. In *Submitted to the 9th symposium on high performance concrete design, verification and utilization*, 9–11 Aug 2011. Christchurch, New Zealand.

32. Mill Valley. (1989). CA: University Science.

Effect of Vehicle Impact on Reinforced Concrete Structures

Mohammed Mujeeb, Venkata Dilip Kumar Pasupuleti, and Archanaa Dongre

1 Introduction

There are number of reasons for the increase of vehicular density on city roads, one being comfortable travel from home to any other place in city or outside the city. Second reason would be traveling at any time with capacity of four or more. Third reason is population density of the considered city. Over and above one of the major factor is limited availability of public transportation. These reasons have led huge traffic in cities. With improper planning of urban development or lack of vision in expansion of cities, construction of apartments, flyovers have led to sharp turns, columns of houses on roads. These abrupt structures are leading to the fatal accidents. Even though these kinds of studies are not new to American and European researchers, very less research has been done for Indian roads.

Studies have proven that most of these accidents have occurred during the night. Similar kinds of accidents have also been reported on the Indian roads. And if proper care is not taken in coming years, these types of accidents would be more, as many abrupt structures have been spotted by the authors in the existing city, Hyderabad, as shown in Fig. 1.

This study mainly concentrates in building the methodology to understand the structural behavior due to vehicular impact. It is assumed that masonry structures would most probably have minor to major damage based on vehicle weight and

M. Mujeeb (✉) · A. Dongre
The Northcap University, Gurgaon, Haryana, India
e-mail: mohammed18cvd001@ncuindia.edu

A. Dongre
e-mail: archanaadongre@ncuindia.edu

V. D. K. Pasupuleti
Mahindra Ecole Centrale, Hyderabad, Telangana, India
e-mail: venkata.pasupuleti@mechyd.ac.in

Fig. 1 Probable locations of vehicle and structural impact

speed of collision. As framed structures are more resistant towards sudden impacts by vehicles, the same has been dealt in brief. Apart from on road collision; there are situations where vehicles have ramped into columns while they are being parked or while moving out of the structure. So, based on the previous cases, case studies have been formed.

2 Literature Review

The ever-increasing speed of vehicles and the growing infrastructure has led to the collision of vehicles with structures, apart from terrorist attacks. Cormic and coauthors have raised the point of terrorists attacks were changed from static blasting to dynamic blasting, also said to be transformed from parking to hitting of critical elements of structure. In this regard, it is necessary to understand the structural collapse behavior under such vehicle-structure collisions [1]. Tay et al. [2] carried out vehicular crash test of a security bollard, and compared the results with those of numerical simulations using two different loading approaches in LS-DYNA [2]. Sharma et al. [3] developed a basic framework for the estimation of dynamic shear force capacity of an RC column subject to vehicle impact [3].

Kang et al. [4] have developed numerical simulations for vehicular crash with two dimensional frames for different speeds of vehicle; results obtained from their research has been shown in Fig. 2 [4]. Apart from the above studies there have been some of the experimental studies for understanding the crash of vehicle. But there has been very less research on experimental for structural behavior due to its setup and costly process. That is one major reason for the development of analytical models for understanding the structural behavior due to vehicular impact.
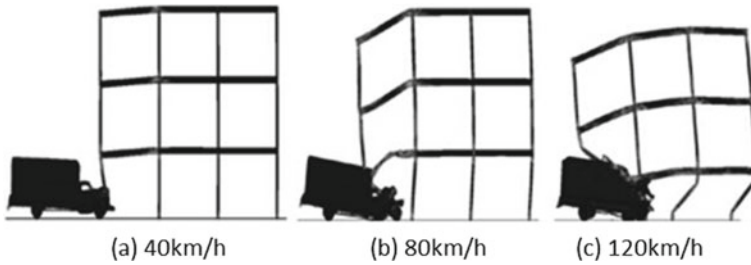
Fig. 2 Two-dimensional frame impact solutions for 40, 80 and 120 km/hr [4]

3 Vehicle Impact Load

Several codes have demonstrated the impact load calculations apart from fundamental mechanics. For this study, calculations have been taken from both Euro code and fundamental mechanics. But as the study is more focused on behavior, an approximate load of 150 kN is considered for all cases.

3.1 Formulation of Impact Load

In Annex B of Eurocode EN1991-1-1:2002 [5, 6], which is related to the vehicle barriers and parapets for car parks, the horizontal force of vehicle impact, in kN, normal and equally distributed at any length of 1.5 m car park barrier, is given by the expression:

$$F = \frac{0.5 \ mv^2}{\delta_c + \delta_b} \tag{1}$$

where: m is the gross mass of the vehicle in (kg); v is the velocity of the vehicle (m/s), normal to the barrier; δ_c—deformation of the vehicle (mm); δ_b—deformation of the barrier (mm). Equivalent static force of 150 kN is applied for a vehicle mass less than 2500 kg and velocity at impact upto 16.2 km/h as given in Table 1.

3.2 Application of Impact Load

The impact load is applied using time history as shown in the Fig. 3.

Table 1 Values of equivalent static load obtained by different codes [7]

Source	Expression	Vehicle mass (kg)	Impact velocity (km/h)	Equivalent static load (kN)
CTE (Spanish Code [7])	…	3000	No shown	50
EUROCODE 1 PART 1.1 ANNEX B	$F = 0.5 \, \text{mv}^2/(\delta_c + \delta_b)$	<2500	16.2	150
		3000	20	308
EUROCODE 1 PART 1.7	…	No shown	<20	50–100
EUROCODE 1 PART 1.7 ANNEX C	$F = v_r \cdot \sqrt{k \cdot m}$	1500	10	59
		3000	20	166
		3000	10	83
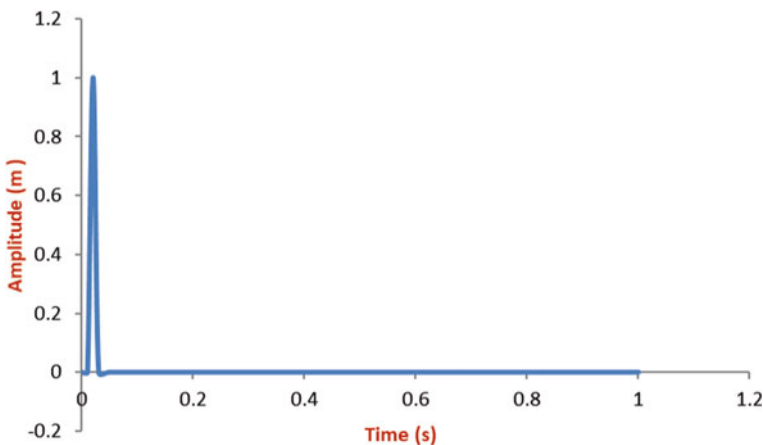
Fig. 3 Impact load time history applied at the various heights of the building in Sap2000

4 Case Studies

In this study, four cases have been considered. Case (i) simple 2D reinforced concrete frame with single bay, case (ii) 2D two bay by two bay reinforced concrete frame structure, case (iii) 3D two bays by two bays with single storey structure, case (iv) actual existing 3D reinforced concrete structure. All the developed numerical models have been assumed with basic dimensions and their designs have been checked according to IS 456 Indian standard code. For all the numerical models, dead loads and live loads are considered to be same and mentioned briefly at the respective sections. As impact its self is dynamic in behavior, linear dynamic analysis is carried out for all the case studies. The duration of impact is assumed to be 0.02 s as shown in the Fig. 3.

4.1 Case Study: 2D Single Frame Structure

The dimensions of two columns and beam are considered to be 230 mm × 230 mm. Grade of the concrete for beam is taken as M25 and for the column is considered to be M30. Grade of the steel used for rebar is taken as Fe415.

Figure 4a shows the Schematic diagram of two-dimensional frame and column considered for the application of impact load. Figure 4b shows locations where impact loads are applied on column 'C1'. The combination of dead load and live load applied on to the frame is equal to 6.35 kN/m and are calculated using IS 875 Indian standard code.

The linear dynamic results obtained for case-(i) are presented in the Fig. 4. For an impact load of 150 kN acting at 0.25 h, maximum displacement is observed to be 4.94 mm as shown in Fig. 5. Similarly, for 0.5 and 1 h, the maximum displacement are observed to be 16.28 mm, 29.16 mm and 38.71 mm respectively. It is also observed
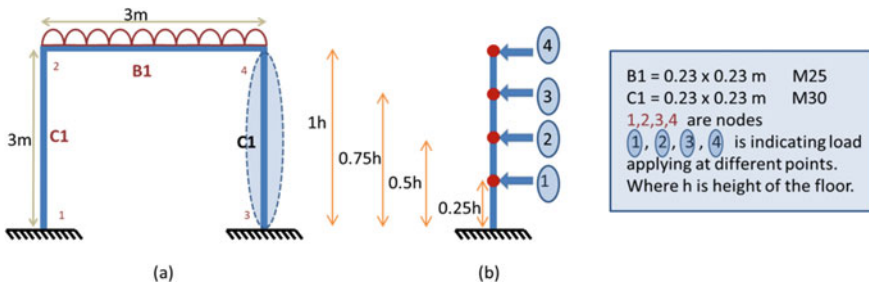

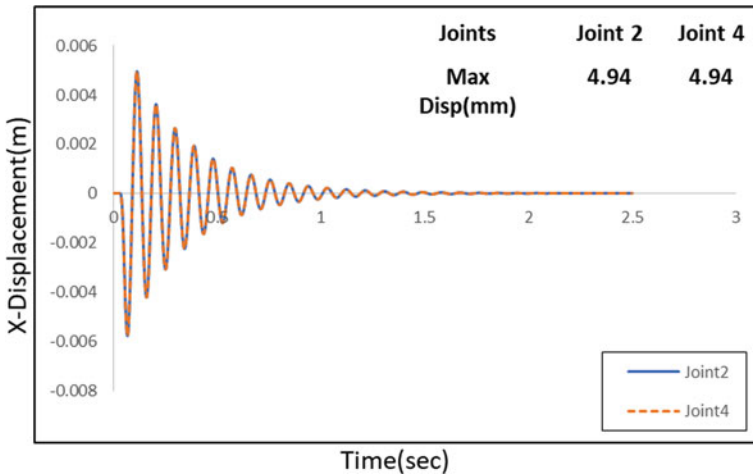**Fig. 4** Two-dimensional frame and locations of impact load applied

Fig. 5 Time history response for impact

the maximum displacement at joint 2 and joint 4 are same for all the cases. This clearly indicates, as the location of impact height increases, damage to the structure would be more. Impact load considered for this study is 150 kN. And related to the vibrations, all the sub cases have shown similar behavior. There is an increment of 0.93 mm horizontal displacement between 0.25 and 0.5 h, where as for other two subcases the increment of displacement is 0.65 and 0.62 mm. This shows as the height of the impact increases there would be increase in maximum deflection, but comparatively the difference amount of horizontal displacement remains almost same. For this sub case and all other subcases, only horizontal displacements are considered.

4.2   Case Study: 2D Two Bay by Two Bay Frame Structure

Similar study has been done for two storey with two bays to understand the same phenomenon of impact effect for a horizontal load of 150 kN, applied suddenly at the locations shown in the Fig. 6. Geometry of all the columns are taken as 0.3 m × 0.3 m with a grade of M30 and all the beam of 0.23 m × 0.23 m with a grade of M25 are considered. Dead load and live load acting on the structure are calculated to be 6.35 kN/m and the same has been applied on the beam as shown in the Fig. 7. Complete structure is assumed to be fixed at the bottom. Column and beam numbers are given based on the material and geometrical properties. Length of each bay is considered to be 3 m and height of each floor is considered to be 3 m.

The results obtained for case-(ii) are showed in the Fig. 7. This study shows the effect of impact on internal column and on external column also to observe the difference in behavior if the impact occurs at two different floors. In this study, it is assumed their impact would happen at only one place at any given time. Obtained results indicate there is a minute difference if the impact has occurred in the ground
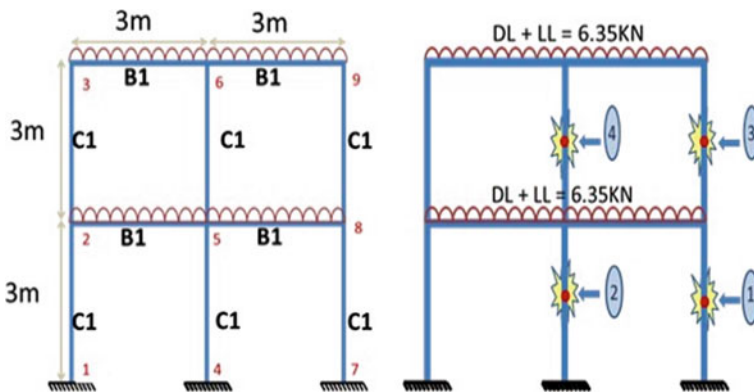

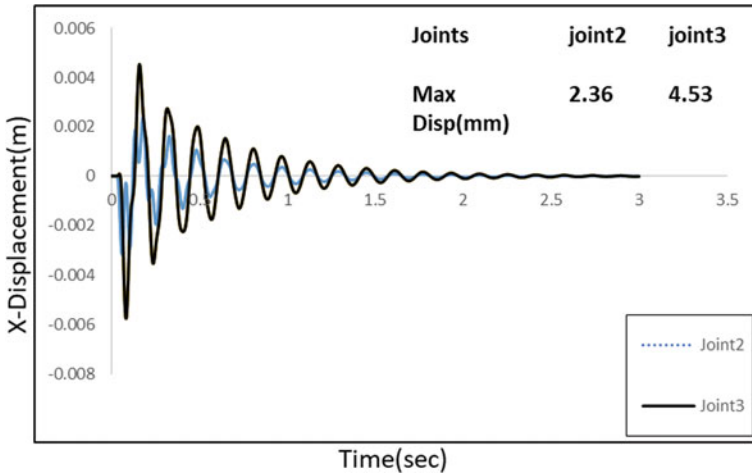**Fig. 6** Two-dimensional frame and considered locations for impact load

Fig. 7 Time history response for impact

floor at location one and at location two. And horizontal deflections are more for the impact occurred at location two. Which indicates impact at the internal column would be more dangerous than external column. But for the same column impact on the first floor have shown the different behavior, that is for external column and internal column, the displacements are same. Which means as the impact occurs on the top floors; mostly the behavior of the structure would remain constant.

And for all the impacts, it has been seen there is almost negligible effect on the deformation of the beams. Figure 7 shows the displacement obtained for number of steps, instead of time. Joints 3, 6 and 9 have shown same displacement profile and joints 2, 5 and 8 have shown same displacements profiles. As they are in the same floors, and two crystal curves can be seen, that is between first floor and second floor. Damping of the structure is assumed to be 5%, same is seen for all the results. Consistent logarithmic decrement of the displacement along the steps considered.

4.3 Case Study: 3D Two Bay by Two Bay Single Story Structure

After analyzing two 2D frames, three-dimensional frame is also considered to understand the effect of the third dimension as shown in Fig. 8. And effect of third dimension is only seen when structure is unsymmetrical or the load applied is unsymmetrical. As for the subcase considered, the load acting on the structure is unsymmetrical and displacements profiles obtained are not similar to the subcase-1. Geometry and material properties are similar to case study-2 and thickness of slab is considered to be 0.12 m. Results for both the cases have been found to be same and this is due to
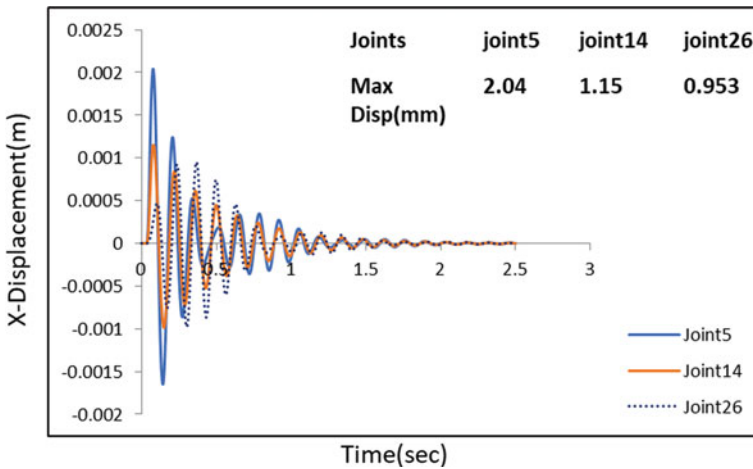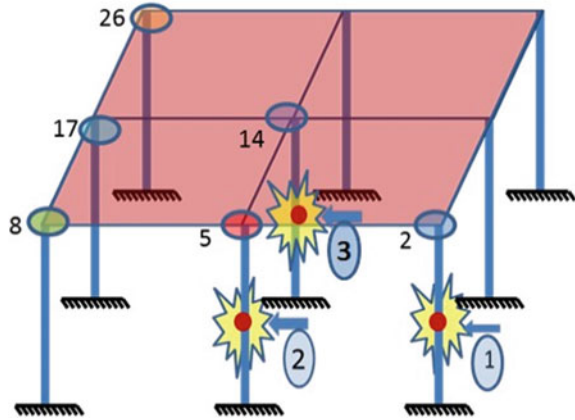
Fig. 9 Time history response for impact

rotational behavior. Detailed time history response for given impact load is seen in
Fig. 9.

4.4 Case Study: 3D Two Story Existing Structure

Existing structure G + 2 has been considered to understand its response due to vehicle
impact loads. Plan of the considered structure and developed 3D numerical modal
are shown in Fig. 10. Three-dimensional existing structure with different column
sizes of grade M30 and different beam sizes with a grade of M25 along with slab of
0.12 m thick have been considered. Similar to earlier cases a load of 3 kN is assumed

(a) Plan of the building.   (b) 3D model of the building.
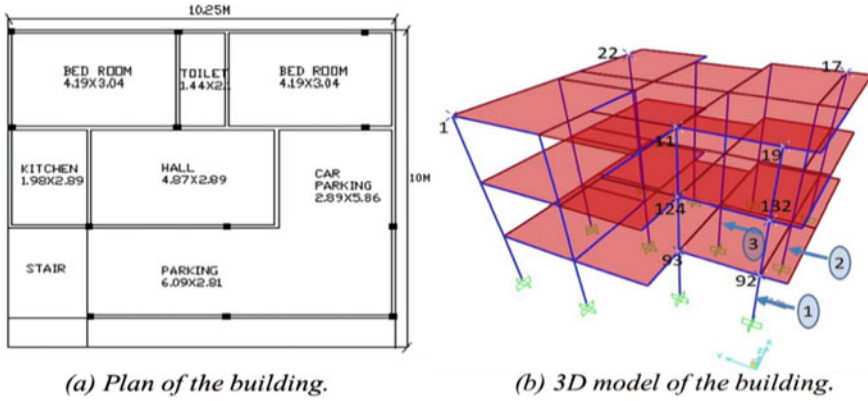
Fig. 10 G + 2 structure and locations of impact load applied

to be acting on the slab. Results obtained are shown in the Fig. 11, unlike previous cases, the displacements response obtained varied at different levels as the structure is unsymmetrical.

Fig. 11 Time history response for impact at the relative height of 0.5 h at locations 1(**a**) 2(**b**) and 3(**c**)

5   Conclusions

Structures are prone to vehicular impacts for various reasons be at a soft storey, structure on mid of a road, sudden diversions, temporary constructions, poor banking or over speeds, whatever the reason, impacts are increasing and structures are undergoing minor to major damage. In this work, a fundamental study is carried out to understand the structural behavior to vehicular impacts at the different heights of the structure. And to understand more clearly on the g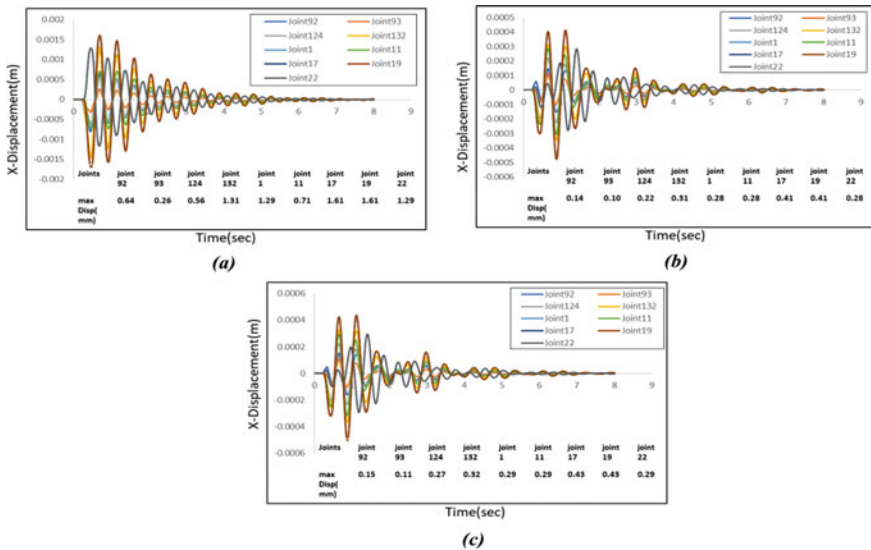eometry of the structure, four cases have been considered and linear dynamic analysis are presented. Numerical models developed indicate maximum response is seen if the impact is occurred at the top of the column. As slabs are considered as rigid diaphragm, internal and external impact have led to similar results for symmetric structures. If structure is asymmetric, then there is large difference in structure behavior and corner column impact would lead to higher displacements.

References

1. Cormie, D., Mays, G., & Smith, P. (2009). Vehicle-borne threats and the principles of hostile vehicle mitigation. In *Blast effects on buildings* (2nd ed.). Thomas Telford.
2. Tay, S. K., Lim, B., & Ng, S. H. (2012). Crash impact modelling of security bollard. In *12th International LS-DYNA Users Conference*, vol. 13, pp. 1–10, Detroit.
3. Sharma, H., Hurlebaus, S., & Gardoni, P. (2012). Performance-based response evaluation of reinforced concrete columns subject to vehicle impact. *International Journal of Impact Engineering, 43*(5), 52–62.
4. Kang, H., Shin, J., & Kim, J. (2013). Analysis of steel moment frames subjected to vehicle impact. APCOM and ISCM, 11–14 Dec (2013).
5. European Standard. (1998). Road restraint systems, EN 1317. London: British Standards Institution.
6. Eurocode 1: Action on structures—part 1–1: general actions—Densities, self-weight, imposed loads for buildings, Final draft prEN 1991-1-1, comite europeo denormalization, julio (2001).
7. Ferrer, B., Ivorra, S., Segovia, E., Irles, R. (2009) Impact load in parking steel column: code review and numerical approach. In *ECCOMAS Thematic Conference on Computational Methods in Structural Dynamics and Earthquake Engineering*, 22–24 June 2009. Rhodes, Greece.

Seismic Behaviour of G+7 RC Open Ground Storey Buildings with Fluid Viscous Dampers

Shaik Shayza and Bodige Narender

1 Introduction

Earthquakes lead to ground shaking due to the sudden slip on a fault. From past many decades, earthquakes have been occurring all over the world in a large number. The damage severity depends on the intensity of the earthquake. Some severe earthquakes cause death and also destroy the basic livelihood of many people. Almost all the earthquakes directly damage the structures built leading to the loss of life and property. In the case of developing countries, the constructions can be seen almost everywhere. Nowadays, as the population is increasing, the need for construction is going high with limited availability of land. Many structures are being built without following proper guidelines and safety measures. Many high-rise buildings are built with lot of investments. In order to protect the structures from devastating earthquakes, the structures need to be earthquake-resistant. In many metropolitan areas, multi-storey buildings such as office buildings and residential apartment buildings are designed to have a parking facility in the bottom storey. Due to the lack of masonry infill walls in the bottom storey, it has very low strength and stiffness compared to the above storeys. Such stories are called "Soft Storeys" which are more prone to damage and collapse during strong ground motions. Many researchers have tried and implemented many techniques to reduce the severity caused by an earthquake. Over the past decades, many research studies were carried out for seismic protection of structures. The studies concentrated on traditional techniques such as increasing stiffness of structures, post tensioning methods and enlarging the sectional dimensions which resulted in high construction costs. Later, civil engineering structures

S. Shayza (✉) · B. Narender
Department of Civil Engineering, Anurag Group of Institutions, Ghatkesar, Telangana, India
e-mail: shayzashaik444@gmail.com

B. Narender
e-mail: drnbodigece@cvsr.ac.in

are upgraded with modern seismic reduction methodologies for better performance during seismic events. Damping comes into this category which helps in designing earthquake-resistant structures in earthquake-prone areas. This can be achieved by implementing different techniques in structures such as base isolation, shear walls, bracings and dampers. These methods can be applied to both newly constructed as well as existing structures. Fluid viscous dampers (FVD) are passive energy dissipating devices widely applied to many civil engineering structures in recent times to minimize the structural responses caused during an earthquake or wind. They are known for easy installation, low construction cost and zero maintenance. They dissipate energy via orifices. In the year (2008), Hwang and Huang [1] had modified the existing design formulas of supplemental FVDs in different configurations which were provided by FEMA 273 [2]. In the year (2014), Bisht and Setia [3] explained the seismic behaviour of soft storey building with and without viscous dampers. In the year (2018), Maurya and Singh [4] analysed a multi-storeyed RC building by adding FVDs at corner and middle positions and compared the building responses. The main objective of the present study is to analyse the behaviour of G+7 reinforced (RC) open ground storey buildings using fluid viscous dampers placed in different positions. The responses of open ground storey buildings without FVDs are compared with responses of open ground storey buildings with FVDs placed at the corner, middle and periphery. The responses are compared in seismic zones IV and V. From the results, it is concluded that FVDs achieved a great attention in recent times by offering massive benefits in the field of earthquake engineering.

1.1 Fluid Viscous Dampers

FVD consists of a piston rod made up of stainless steel with a bronze orifice head and an accumulator. It consists of a cylinder filled with highly viscous fluid usually silicon oil which is inert, non-toxic, non-flammable, non-ageing and thermally stable. A piston head with orifices separates the cylinder into chamber 1 and chamber 2. FVD works mainly on the principle of fluid flow via orifices. When the structure is subjected to external ground motions due to the earthquake, the piston inside the cylinder moves and pushes the viscous fluid via orifices, and the fluid passes from chamber 2 to chamber 1 with large velocity and gets transferred into kinetic energy. Later when the fluid movement slows down, the kinetic energy is lost due to the turbulences. The pressure differences between two chambers result in generating a large force known as the viscous force which provides resistance against structural movements. FVDs can be operated on temperatures ranging from -40 to $+70$ °C. Equation (1) shows the damping force of a FVD which is given by [5].

$$F = C \cdot V^{\alpha} \tag{1}$$
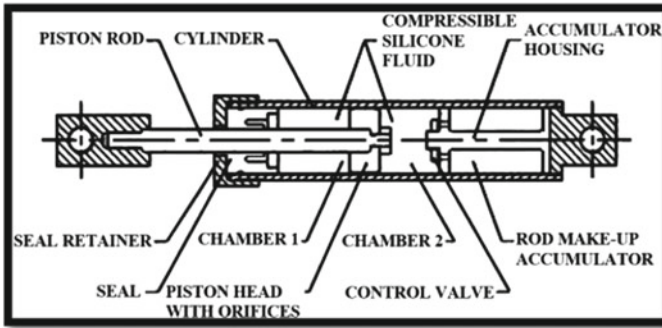
Fig. 1 Typical FVD manufactured by Taylor Devices, Inc.

where,

F is the damping force, C is the damping coefficient, V is the velocity of the piston relative to the cylinder, and α is the damping exponent. The typical FVD manufactured by Taylor Devices, Inc., is shown in Fig. 1 [6].

2 Methodology

In this paper, linear dynamic analysis (response spectrum analysis) is performed using ETABS software. This analysis considers dynamic forces which are applied to the structures as per code-based design spectrum. It helps to determine the effect of the higher modes of vibration and distribution of forces. In response spectrum analysis, multiple mode shapes are taken into consideration. Depending upon the modal mass and modal frequency, a response is read from the design spectrum for each mode. Later, these responses are combined to determine the total response of the structure by modal combination methods. This method is performed for the structures whose modes, except the fundamental one, influence the response of a structure. Response spectrum is the estimation of maximum response such as maximum absolute acceleration, maximum relative velocity and displacement of single degree of freedom system for different values of damping for a particular ground motion.

Fig. 2 Plan of the building
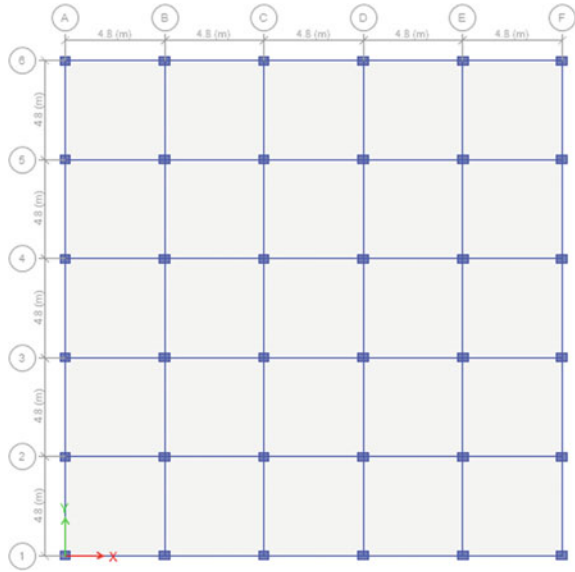
3   Modelling Details

3.1   Basic Building Details

In this study, G+7 RC buildings are modelled using ETABS software. The plan of the building is symmetric with dimensions 24 m × 24 m. The building has total five numbers of bays in both *x*- and *y*-directions, with each bay having a width of 4.8 m. Total height of the building is 24 m with each storey height of 3 m. Figure 2 shows the plan view of the building. Beams with 300 mm × 400 mm and columns with 400 mm × 500 mm dimensions are considered. Thickness of slab is 150 mm; thickness of exterior and interior walls is taken as 230 mm and 155 mm, respectively. Materials used are of M25 grade concrete and Fe415 rebar. Loads and load combinations are considered based on IS 456-2000 [7] and IS 875-1987 [8] codes. Earthquake loads are taken as per IS 1893-2002, clause 7.3 [9]. In this work, live load is taken as 2 kN/m^2, floor finish is taken as 1 kN/m^2, and wall load is calculated and taken as 13.66 kN/m.

3.2   Fluid Viscous Damper Details

FVDs considered in the present study are manufactured by Taylor Devices. The link property data is taken from the standard dimensions given by the Taylor Devices, Inc., 1956. In this study, FVDs of 250 kN force are considered. In link property data, enter link type as damper, and total mass and weight are taken as 44 kg and

250 kN, respectively. In directional properties, U_1 direction is selected with fixed end properties, and the rotating inertia R_1, R_2, R_3 are considered to be zero. After defining the link properties, the links defined are drawn in the building models in diagonal configuration using draw links icon in ETABS software.

3.3 Structural Modal Details

In this work, five buildings are modelled in zone IV and zone V to understand the seismic behaviour of buildings individually in different zones. The FVDs are added to the building models in different positions in the bottom storey. The following are the building models considered in the present study:

Model 1: Bare frame building (BF).
Model 2: Bare frame building with infill walls in all storeys except the bottom storey (BFI).
Model 3: Bare frame building with infill walls in all storeys except the bottom storey and fluid viscous dampers in all exterior corners bays of bottom storey (BFIFDC).
Model 4: Bare frame building with infill walls in all storeys except the bottom storey and fluid viscous dampers in all exterior middle bays of bottom storey (BFIFDM).
Model 5: Bare frame building with infill walls in all storeys except the bottom storey and fluid viscous dampers in all exterior bays (corner and middle) of bottom storey (BFIFDP).
The elevation view of the building models is shown in Fig. 3.

4 Results and Discussions

In this study, G+7 RC buildings are modelled and analysed by response spectrum analysis using ETABS software. The buildings are modelled in seismic zones IV and V. The parameters considered in the response spectrum method are base shears, storey displacements, storey drifts, storey shears and storey stiffness. To study the seismic responses after using FVDs at particular zone, the results are compared with respect to zone IV and zone V. In order to find out the best position for placing the FVDs in the buildings, the dampers are placed at corners bays, middle bays and periphery of bottom storey, and the building responses are compared.

From modal analysis, the mode shapes, time periods and frequencies for all the building models are obtained. Mode shapes present the configurations into which the building will naturally displace. They help us to identify the point where the building will amplify the effect of a load. For the building models considered in this study, i.e. bare frame (BF), bare frame with infill walls (BFI), bare frame with infill
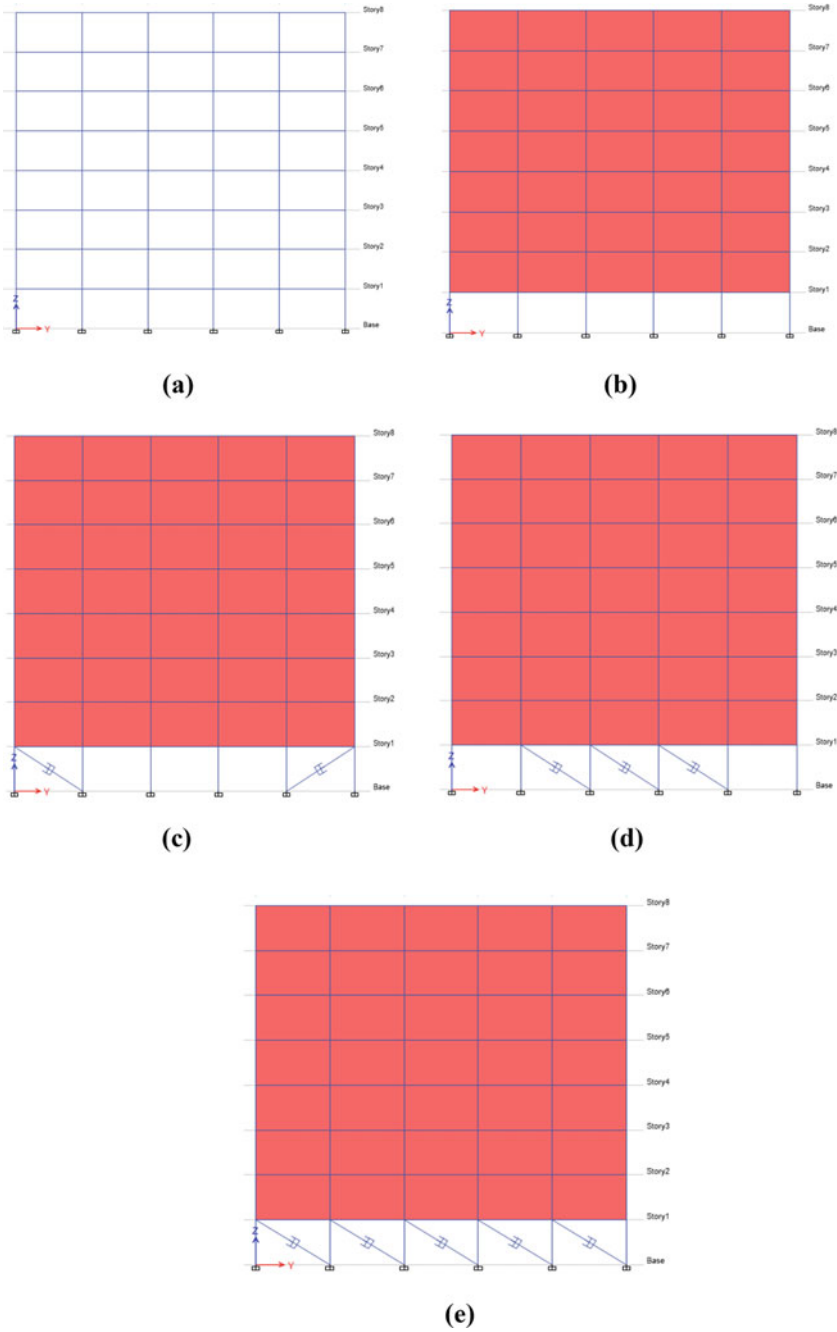
Fig. 3   Elevation views of (a) BF, (b) BFI, (c) BFIFDC, (d) BFIFDM, (e) BFIFDP
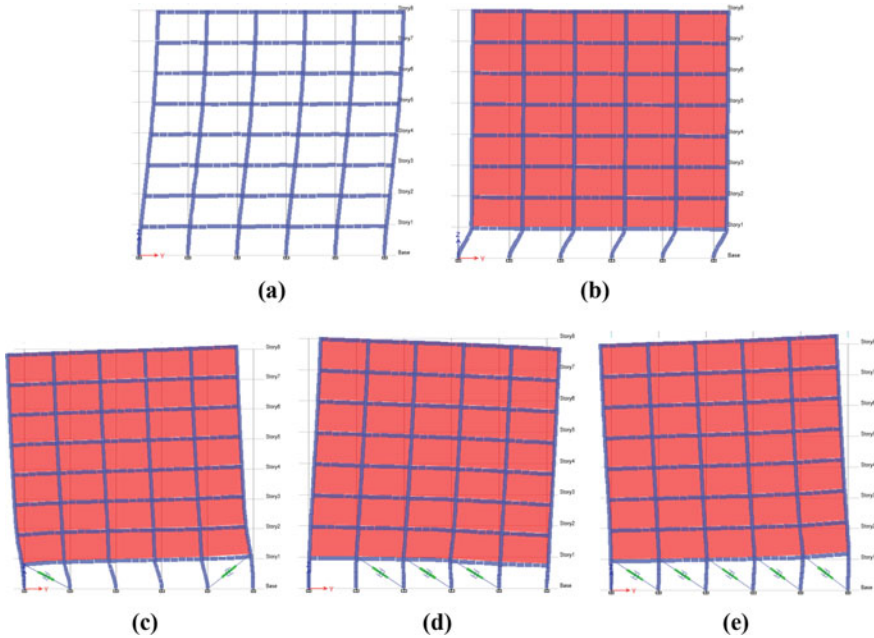
Fig. 4 First mode shapes of: (**a**) BF, (**b**) BFI, (**c**) BFIFDC, (**d**) BFIFDM, (**e**) BFIFDP

walls and FVDs at corner bays (BFIFDC), bare frame with infill walls and FVDs at middle bays (BFIFDM) and bare frame with infill walls and FVDs at periphery (BFIFDP), 12 modes are showing 90% of total mass participation. The BF model has shown four mode shapes; BFI, BFIFDC and BFIFDM models have shown three mode shapes; BFIFDP model has shown only two mode shapes. The first mode shapes of all five building models considered in the study are shown in Fig. 4. From Fig. 4, it can be observed that the modal deformations are reducing in the buildings modelled with FVDs, i.e. BFIFDC, BFIFDM and BFIFDP. The positions where the FVDs are added had shown rigid action unlike the positions without FVDs in the building and because of this reason the deformations reduced in buildings modelled with FVDs. On comparing the three FVDs positions, BFIFDP model has shown very less deformations.

Table 1, shows the time periods and frequencies for 12 numbers of modes for all five building models. As the stiffness of the structure increases, the time period decreases. Time period is inversely proportional to frequency so as the time period increases, the frequency decreases. From Table 1, it can be observed that the modal time periods using FVDs decreased up to 58%, 67.35% and 69.6% in BFIFDC, BFIFDM and BFIFDP models, respectively, when compared with BFI model. This shows the buildings modelled with FVDs have lesser time periods than the buildings modelled without FVDs.

Table 1 Time periods and frequencies for all five building models

| Mode	BF		BFI		BFIFDC		BFIFDM		BFIFDP	
	Period (s)	Freq (Hz)	Period (s)	Freq (Hz)	Period (s)	Freq (Hz)	Period (s)	Freq (Hz)	Period (s)	Freq (Hz)
1	1.205	0.83	0.487	2.054	0.201	4.977	0.159	6.297	0.148	6.751
2	1.131	0.884	0.403	2.479	0.198	5.04	0.157	6.374	0.144	6.946
3	1.042	0.959	0.403	2.481	0.1	9.975	0.085	11.757	0.08	12.564
4	0.388	2.578	0.069	14.518	0.052	19.252	0.049	20.613	0.047	21.324
5	0.358	2.791	0.068	14.724	0.052	19.391	0.047	21.27	0.044	22.487
6	0.334	2.998	0.038	26.417	0.033	29.87	0.033	30.175	0.033	30.414
7	0.219	4.571	0.034	29.498	0.032	30.89	0.029	33.917	0.028	35.83
8	0.197	5.07	0.03	33.56	0.027	37.069	0.027	36.783	0.027	37.378
9	0.187	5.359	0.028	35.93	0.027	37.195	0.027	37.511	0.026	37.857
10	0.146	6.865	0.028	35.946	0.027	37.206	0.026	38.432	0.025	39.432
11	0.128	7.822	0.024	41.663	0.024	42.26	0.024	42.319	0.023	42.637
12	0.123	8.143	0.024	41.765	0.024	42.359	0.024	42.413	0.023	42.759
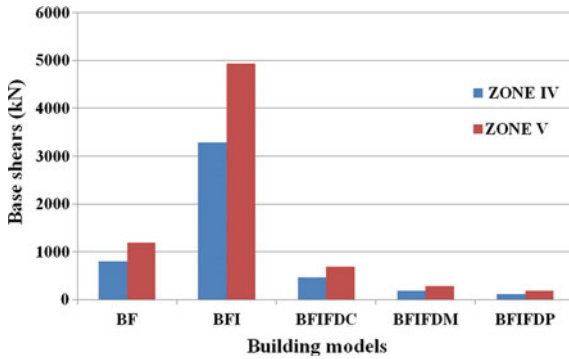
Fig. 5 Time periods for different building models

Figure 5 shows the base shear values of different building models in seismic zones IV and V. The buildings modelled with FVDs have lesser base shear values when compared to models without FVDs in both the zones. The base shear values in BFIFDC, BFIFDM and BFIFDP models decreased up to 85.91%, 94.28% and 96.31%, respectively, when compared with BFI model in zone IV whereas in zone V the base shears reduced to 85.96%, 94.28% and 96% in BFIFDC, BFIFDM and BFIFDP models compared to BFI model. Figure 6(a & b) shows the storey displacements for different building models, i.e. bare frame building (BF), bare frame building with infill walls in all storeys except the bottom storey (BFI), bare frame building with infill walls in all storeys except the bottom storey and FVDs in all exterior corners bays of bottom storey (BFIFDC), bare frame building with infill walls in all storeys except the bottom storey and FVDs in all exterior middle bays of bottom storey (BFIFDM) and bare frame building with infill walls in all storeys except the bottom storey and FVDs in all exterior bays (corner and middle) of bottom storey (BFIFDP) in seismic zones IV and V. The maximum storey displacements in bottom storey after using FVDs decreased up to 84.21%, 89.47% and 94.73% in BFIFDC, BFIFDM and BFIFDP models, respectively, when compared to BFI model in zone IV and decreased up to 82.14%, 92% and 92.85% in BFIFDC, BFIFDM and BFIFDP
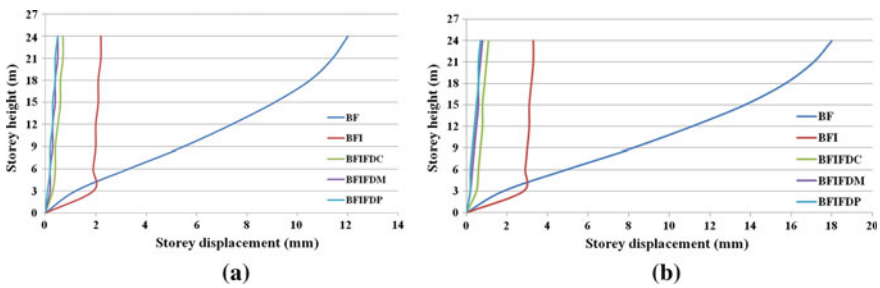
Fig. 6 Storey displacements for different building models **a** zone IV, **b** zone V
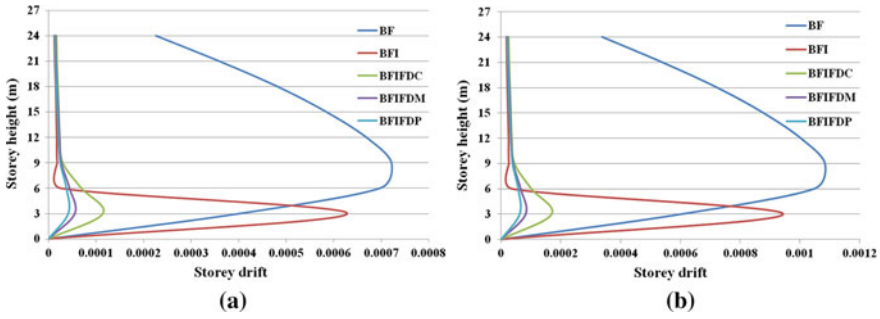
Fig. 7 Storey drifts for different building models **a** zone IV, **b** zone V
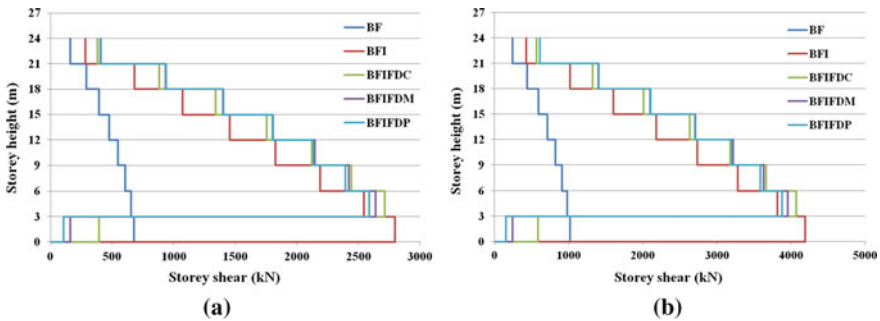
Fig. 8 Storey shears for different building models **a** zone IV, **b** zone V

models compared to BFI model in zone V. Figure 7(a & b) shows the storey drifts for all five building models in zones IV and V. The maximum storey drifts in BFIFDC, BFIFDM and BFIFDP models decreased up to 81.87%, 86.8% and 90.14%, respectively, in zone IV and 81.97%, 91.19% and 93.42%, respectively, in zone V when compared to BFI model in bottom storey. Figure 8(a & b) shows the storey shears for all five building models in zones IV and V. The maximum storey shears in BFIFDC, BFIFDM and BFIFDP models decreased up to 85%, 94.2% and 96.3%, respectively, in zone IV and 86%, 94.27% and 96.3%, respectively, in zone V when compared to BFI model in bottom storey. It can be observed that the damper force is resisting the earthquake forces and significantly reducing the storey shears. Figure 9(a & b) shows the storey stiffness for all five building models in zone IV and V. The storey stiffness in BFIFDC, BFIFDM and BFIFDP models approximately increased up to 17%, 12.8% and 2.4%, respectively, in both the zones when compared to BFI model in bottom storey.
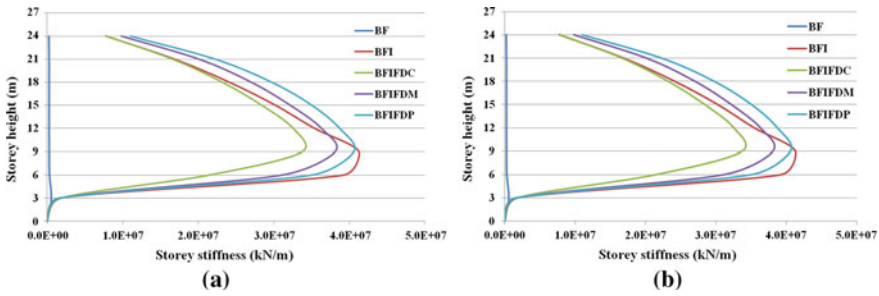
Fig. 9 Storey stiffness for different building models **a** zone IV, **b** zone V

5 Conclusions

In this paper, the study on seismic behaviour of G+7 RC open ground storey buildings located in seismic zones IV and V is carried out using ETABS software. The open ground storey buildings with and without fluid viscous dampers in the bottom storey are compared. Following are the conclusions of present work:

- The time periods in open ground storey buildings with FVDs decreased up to 65% when compared to the open ground storey buildings without FVDs.
- The values of base shears, storey displacements, storey drifts and storey shears in buildings with FVDs reduced up to 90% when compared to the buildings without FVDs in both seismic zones IV and V which shows the reduction of structural responses to a great extent.
- The storey stiffness increased significantly in bottom storey after using FVDs in the open ground storey buildings, which are said to have very low stiffness due to the absence of infill walls in the bottom storey. Increase of stiffness adds strength to the building to withstand the vibrations during earthquakes.
- From the results, it can be observed that the building responses in seismic zone V are higher when compared to seismic zone IV, and the application of fluid viscous dampers in the buildings reduced the responses in both the zones effectively by dissipating the energy during an earthquake.
- From the observations, out of all the positions compared, FVDs placed in all exterior bays (BFIFDP) have shown better and effective results due to more number of dampers and more amount of energy dissipation.
- Thus, it can be concluded that the addition of fluid viscous dampers to the buildings reduces the structural responses which helps in minimizing the damage occurred during an earthquake and allowing faster reoccupation after an earthquake.

References

1. Hwang, J.-S., & Huang, Y.-N. (2008). Design formulations for supplemental viscous dampers to building structures. *Journal of Structural Engineering, 134*(1), 22–31. https://doi.org/10.1061/(ASCE)0733-9445(2008)134:1(22).
2. FEMA 273/274—Federal Emergency Management Agency. (1997). *NEHRP guidelines for the seismic rehabilitation of buildings* (Report No. 273/274). Washington, D.C.: Building Seismic Safety Council.
3. Bisht, Y., & Setia, S. (2014). Seismic behaviour of a soft storey building with & without viscous dampers. *International Journal of Engineering Research and Applications (IJERA)*, 10–15 ISSN: 2248-9622.
4. Maurya, A. K., & Singh, V. K. (2018). Analysis of building using viscous dampers in seismic zone-V. *International Journal of Advances in Mechanical and Civil Engineering, 5*(3). ISSN: 2394-2827.
5. Mathew, L., & Prabha, C. (2014). Effect of fluid viscous dampers in multistoried buildings. *International Journal of Research in Engineering & Technology, 2*(9), 59–64. ISSN(E): 2321-8843; ISSN(P): 2347-4599.
6. Taylor Devices Company. (1956). North Tonawanda, NY, US, Site: http://taylordevices.com/.
7. IS 456:2000, Code of practice for plain and reinforced concrete (fourth revision).
8. IS 875-1987, Code of practice for design loads (other than earthquake) for buildings and structures.
9. IS 1893 (Part 1). (2002). *Criteria for earthquake resistant design of structures Part 1 General provisions and buildings* (Fifth Revision). New Delhi: Bureau of Indian Standards.

Mathematical Model for the Compressive Strength and Elastic Properties of Triple-Blended Steel Fiber Self-Compacting Concrete Based on the Experimental Investigation

S. Vijaya Kumar, B. Dean Kumar, and B. L. P. Swami

1 Introduction

The present study clearly indicates that the self-compacting concrete is essential in the concrete field to prevent external compaction. It can be filled under its own weight at all the corners of the formwork and get completely compacted even in dense steel. SCC is homogeneous and dense and has similar structural parameters of the vibrated cement concrete (VCC). Investigations for required design and self-compatibility methods have been carried out to make it as standard concrete. SCC can cast in a way that there is no additional vibration needed.

1.1 Need for Design Mix

For obtaining SCC, the main criterion involves in design of a mix is the determination of the physical properties of the concrete. The fresh SCC shows better fluidity, self-compacting and resistance against segregation. These contribute to reduce the problem of honeycombing in the concrete. Hence, SCC can significantly raise reliability along with durability. SCC shows better contribution in axial compressive strength test and can satisfy the requirements.

S. Vijaya Kumar (✉)
Department of Civil Engineering, Vasavi College of Engineering, Hyderabad 500031, India
e-mail: s.vijayakumar@staff.vce.ac.in

B. Dean Kumar
Department of Civil Engineering, Jawaharlal Nehru Technological University Hyderabad, Hyderabad, Telangana 500085, India

B. L. P. Swami
Department of Civil Engineering, MCET, Hyderabad, India

The materials for SCC are same as vibrated cement concrete. It has cement, fine aggregate, coarse aggregate and water along with admixtures. Presently, to the best of authors' knowledge, there is no standard approach for determining mix proportions for SCC. Some more modifications will be required to gain strength and other rheological properties like flow requirements. The fine aggregate content will balance other constituents by volume for this type of special concrete.

1.2   Applications of SCC

Applications of SCC are minimization in manpower, more comfortable while placing, smooth finishing, low sound level which are some of the benefits of this type of concrete. SCC usually reaches the slump flow value of more than 600 mm without segregation. SCC shall remain flowable and self-compacting for 540 s. This special SCC is able to withstand a slope 3° in case of a free horizontal surface.

1.3   Objectives of the Current Study

The objective of this experimentis to study the presence of steel fiber percentage and aspect ratio on the strength and elastic properties of the triple-blended self-compacting concrete. The M40 grade is considered as base concrete. The base mix is as per the IS 10262 specification; then, these material proportions are rearranged in such a way that fine aggregate to total aggregate is around 0.58–0.64 to get the requirements of SCC as per provisions. The triple blending includes the replacement of cement with fly ash at 15% and condensed silica fume at 10% in each mix by the weight of cement. The superplasticizer and viscosity-modifying agent are used for good rheological properties. The workability tests like slump flow, V-funnel and L-box tests are performed as per the directions of EFNARC-2005 [1] to fulfill the SCC requirements. In this work, the percentage of steel fiber is varied from 0.20 to 0.80, and aspect ratios of 20, 30 and 40 were adopted for each percentage of steel fiber. A comparison is extracted for the results of the compressive strength along the Young's modulus and Poisson's ratio. These properties are evaluated, and the necessary conclusions are extracted.

2   Literature Review

The ideology of self-compacting concrete was developed in the late 90s by Professor Hajime Okamura. The prototype beams were examined in Japan by Professor Ozawa in Tokyo University. The self-compacting concrete was designed at that time for better strength and durability of concrete structural elements without the need of

external compaction. Researchers have been carried out in this special concrete by incorporating supplementary cementitious materials (SCM).

Professor Okamura [2] developed mix design method for SCC, and the main intention was to do the test on paste and mortar to examine the compatibility and properties of the superplasticizer (SP). Su et al. [3] reported a mix design procedure for SCC, and the main intention in doing so was to fill gaps in unstructured aggregates with paste that was a binder in nature.

Okamura and Ouchi [4] investigated the current and future use of the SCC and developed design mix approach by rearranging the fine aggregate-to-total aggregate ratio, until flowability, passing ability and resistance against the segregation were achieved.

Petersson et al. [5] did the experimental study to develop guidelines for self-compacting concrete and discussed various methods for the workability of concrete.

Pajak et al. [6] reported the flexural variation of SCC by using straight, hooked-end steel fibers at various percentages of 0.5, 1.0 and 1.5; conclusions were drawn with vibrated cement concrete (VCC).

Corinaldesi et al. [7] organized self-compacting concrete mixes which use three varied fibers consisting of steel, polyvinyl alcohol (PVA), polypropylene along with different types of minerals (limestone and recycled concrete generated powder). The results showed that the utilization of recycled concrete powder is better than limestone powder for producing SCC.

Iyer et al. [8], fiber-reinforced concrete (FRC) is used in different elements such as concrete pavements, floors and airport runways. The basalt chopped fibers in filament shape are used to develop basalt fiber-reinforced concrete (BFRC). They studied the possible enhancemnet in the compressive strength along with the modulus of rupture.

Sahmaran et al. [9] investigated on straight- and hooked-end steel fibers in fresh and hardened state of the concrete. The authors reported that it is possible to attain self-compaction up to 60 kg/m^3 of fiber content.

Cunha et al. [10] reported the influence of steel fiber percentage on concrete for compressive behavior of SCC. The compressive strength and modulus of elasticity increased with age but decreased when steel fiber increased from 30 to 45 kg/m^3.

Kosmatka et al. [11], reported that SCMs (supplementary cement materials) generally enhance the workability of concrete. The fly ash cement and slag cement have frequently been reported to enhance concrete rheological properties.

SCC have been developed by Vijaya et al. [12] to get strength and durability in structures. The reference mix proportion of SCC was arrived from the NAN SU method of mix for M40 grade plastic fiber-reinforced self-compacting concrete (PFRSCC). It was developed by varying percentages of fibers from 0.0, 0.25, 0.5, 0.75, 1.00, 1.1, 1.2, 1.3 and 1.4%. EFNARC [1] gave some guidelines for mix design for SCC. The specifications about the original compositions, the volume of paste, fine particles, the dosage of superplasticizers and viscosity-modifying agents had been given. Details of various workability tests along with the limiting values are presented.

Ganeshan et al. [13] examined, the influence of the steel fiber on the structural behaviour of fiber reinforced self compacting concrete (FRSCC) subjected to flexure. In this investigation, optimum volume portion of fibers was observed as 0.5%, from the experimental work considering 0,0.25,0.5 and 0.75% of steel fiber with the variable aspect ratio 15, 25 and 35.

3   Materials Used

3.1   Cement 53 Grades

53 Grade cement was adopted for this experiment confirming to the Indian Standard code IS: 10269-1987 [14].

3.2   Fine Aggregate (FA)

In this experimentation, river sand was used as fine aggregate. The physical tests on the fine aggregates like specific gravity, gradation curve, bulk density, and fineness modulus were conducted as per IS-2386 [15]. Here, 30% of FA was replaced by artificial sand (Robo sand).

3.3   Coarse Aggregate (CA)

The coarse aggregate of size 10–16 mm was acquired from aggregate crushing unit. The physical properties of aggregate specify its specific gravity, gradation curve, bulk density and fineness modulus which were examined as per the code provisions of IS-2386 [15]. The coarse aggregate was chosen by shape as per IS 2386 (Part I).

3.4   Fly ash

Fly ash of F type was used as one of the substitution materials for cement. It was collected from thermal power plant in Telangana State. The specific surface area of fly ash is found as 4750 cm^2/g by Blaine's permeability apparatus.

3.5   Condensed Silica Fume (CSF)

CSF was collected from VBC. Ferro Alloys Ltd. (VBCFAL), Rudraram in Hyderabad. Its fineness was found to be greater than 10,000 cm^2/g.

3.6 Superplasticizer

Superplasticizer used in this experimentation is B233 (M/S BASF INDIA LTD).

3.7 Viscosity Modifying Agent (VMA)

VMA ensuring the consistency and minimize the fluid mix segregation, in this work Glenium2 is used as VMA, this is brought from M/S BASF INDIA LTD, the Performance variations are due to different in the material quality and the moisture in the aggregate were adjusted for an effective quality control.

3.8 Steel Fibers

Mild steel fibers of 1 mm diameter was used at various aspect ratios of 20, 30 and 40. Fiber is varied from 0.2 to 0.8% in four stages.

3.9 Water

Water is the most important for concrete; for good concrete, it should be free from impurities such as oil, alkali and acidic.

4 Concrete Mix Design and Testing the Specimens

The mix design for M40 grade of concrete as per specifications of IS 10262-2009 [16] by utilizing the materials selected. The details of the reference mix mentioned in Table 1 and the design mix for SCC employed in this work are given in Table 2.

Table 1 Concrete mix proportions for M40 (VCC)[a]

Sl. no.	Grade of concrete	Cement	Fine aggregate	Coarse aggregate	Water/cement ratio
1	M40	1	1.38	2.4	0.45

[a]*VCC* Vibrated cement concrete

Table 2 Concrete mix proportions for M40 (SCC)[a]

Sl. no.	Grade of concrete	Cement	Fine aggregate	Coarse aggregate	Water/cement ratio
1	M40	1	2.33	1.37	0.45

[a]*SCC* Self-compacting concrete

Table 3 Quantities of materials required with mineral admixtures (20% fly ash and 10% CSF)

Sl. no.	Materials required	Quantities in kg. per m^3 for M40
1	Cement	350
2	Fly ash	70
3	CSF	35
4	Fine aggregate	745
5	Robo sand	320
5	Coarse aggregate	624
6	Water	205

The mineral admixtures of fly ash and CSF were used as a replacement to OPC at optimum percentages of 15 and 10 to achieve triple blending. The water/cement ratio is to be maintained at 0.45. The quantity of materials used is given in Table 3.

4.1 Optimum Dosages of Chemical Admixtures Used

By gradually increasing the dosages of superplasticizer and VMA by trial, the final dosages of 1.0 and 0.15% were arrived to achieve the requirements for the percentage of steel fibers up to 0.4; later, for percentage of steel fibers of 0.6 and 0.8, the superplasticizer is 1.2 and VMA 0.2 percentage which is used to fulfill the requirements of SCC.

4.2 Workability Tests

Workability tests as per EFNARC-2015 [1] specifications consisting of slump flow, L-box, V-funnel tests were examined; the results of different trials are presented in Table 4.

Table 4 Trial tests for workability

Sl. no	Method	Units	Trial mix1	Trial mix2	Trial mix3	Acceptance criteria
1	Slump flow	mm	460	550	680	650–800
2	T50 cm slump flow	s	–	7	4	2–5
3	V-funnel	s	52	22	8	6–12
4	V-funnel at T5 min	s	63	26	10	6–15
5	L-box test	H_2/H_1	2.2	0.8	0.95	0.8–1

Fig. 1 Arrangement of the dial gauges for the elastic properties of SFSCC and testing setup

4.3 Tests on Hardened Concrete (Fibrous Triple-Blended SCC)

4.3.1 Number of Mixes

A total of 13 mixes were tried in this experimental investigation. The steel fiber percentages of 0.2, 0.4, 0.6 and 0.8 by volume of the concrete and three aspect ratios of 20, 30 and 40 were adopted (Fig. 1).

5 Results

5.1 Compressive Strength

Three cube specimens of size $150 \times 150 \times 150$ mm were casted for each combination; a total of 39 samples $(36 + 3)$ for three combinations for aspect ratio and four combinations of each percentage of steel fibers were casted. The normal cured approach is adopted and tested at the age of 28 days for compressive strength. The values are presented in Table 5. Its variation is plotted in Fig. 2. The compressive strength of the reference concrete which did not include the blending of admixtures and steel fibers is greater than 40 N/mm². This fulfills the requirements; SCC mix with triple blending (fly ash 20% and CSF 10%) and without fibers indicated strength that was moderately higher than the reference mix. The mineral admixtures consisting of fly ash and CSF were added to increase the strength besides giving more workability properties. It clearly indicates from Table 5, the compressive strength of

Table 5 Compressive strength of the SFSCC

Sl. no.	Code no.	Steel fiber percentage	Aspect ratio	Average cube strength (N/mm^2)
1	M0	0	–	44.50
2	M1	0.20	20	47.25
3	M2	0.20	30	48.15
4	M3	0.20	40	49.82
5	M4	0.40	20	48.25
6	M5	0.40	30	51.25
7	M6	0.40	40	54.15
8	M7	0.60	20	53.25
9	M8	0.60	30	58.30
10	M9	0.60	40	60.74
11	M10	0.80	20	59.90
12	M11	0.80	30	63.72
13	M12	0.80	40	68.50

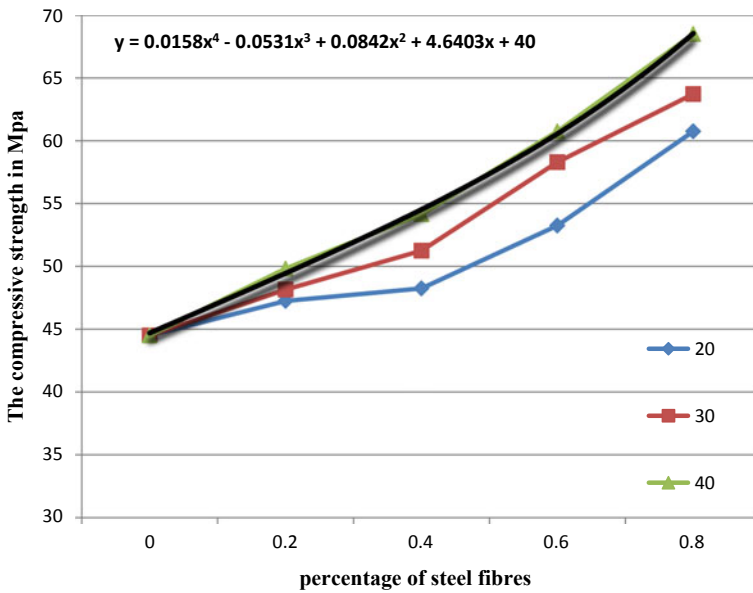$$y = 0.0158x^4 - 0.0531x^3 + 0.0842x^2 + 4.6403x + 40$$

Fig. 2 Variation of the compressive strength for steel fiber triple-blended SCC

SCC of M40 grade is increasing with an increase in steel fiber percentages. There is a significant increase in the compressive strength due to fibers and its aspect ratio. In the present investigation, the maximum percentage of fiber is kept at 0.8 and the maximum aspect ratio is 40. The strength is higher with an aspect ratio of 40. Hence, it is clear that up to a specific favorable percentage and a significantly proportionate aspect ratio, steel fibers played a part in increasing the strength. Further increase in the fiber percentage or aspect ratio may interfere with the flow of SCC. The mathematical models for the compressive strength of steel fiber for different percentages of steel fiber are given by most fit fourth-degree polynomial equation for typical aspect ratio of 40.

$$y = 0.0158x^4 - 0.0531x^3 + 0.0842x^2 + 4.6403x + 40$$

y is the compressive strength in MPa, and
x indicates the percentage of fiber.

The above equations can be derived for other aspect ratios also. The addition of steel fibers makes concrete more and more compact and denser. The enhancement in aspect ratio (up to optimum value) contributes toward better strength as it makes concrete become stiffer.

5.2 Modulus of Elasticity

For the Young's Modulus and Poisson's ratio, total of 39 numbers of standard cylinders of size 150 mm diameter and 300 mm height were tested. The Young's modulus is determined on cylinder specimen by direct compression and measuring the strains using dial gauges in two orthogonal directions. The Young's modulus of concrete depends upon the modulus of elasticity of the aggregates, cement and their relative proportions. Average Young's modulus is computed from the measurements in the elastic range following the code procedure IS: 516 [17]. In the present study, the Young's modulus is increasing with increase in fiber percentage. Table 6 shows the Young's modulus values. SFSCC combines with triple mixing of fly ash 20% and CSF 10% with fiber 0.8% showing the highest value which is about 35% more compared to the base mix. The Young's modulus of triple-blended fibrous SCC of M40 grade enhanced while increasing fiber percentage and the aspect ratio. The mathematical equation for the Young's modulus of the triple-blended steel fiber self-compacting concrete had been drawn as exponential which is the fitting curve for the experimental values for typical aspect ratio of 40. The arrangement of the dial gauges for experimental setup is shown in Fig. 1. And variation of the Young's modulus is shown in Fig. 3. Equations can be derived for other aspect ratios. The strength increase with the introduction of fiber causes higher stress and lowers the strain; hence, Young modulus increases with higher percentage of fibers.

Table 6 Elastic properties of SFSCC

| Sl. no.	Code no.	Steel fiber percentage	Aspect ratio	Young' modulus MPa	Poison's ratio
1	M0	0	0	32,669.00	0.152
2	M1	0.2	20	34,618.25	0.150
3	M2	0.2	30	34,930.50	0.142
4	M3	0.2	40	35,500.00	0.133
5	M4	0.4	20	36,000.00	0.147
6	M5	0.4	30	36,800.75	0.135
7	M6	0.4	40	37,200.50	0.130
8	M7	0.6	20	39,250.00	0.129
9	M8	0.6	30	40,010.25	0.128
10	M9	0.6	40	42,030.00	0.117
11	M10	0.8	20	43,900.25	0.124
12	M11	0.8	30	44,000.50	0.110
13	M12	0.8	40	34,931.12	0.107
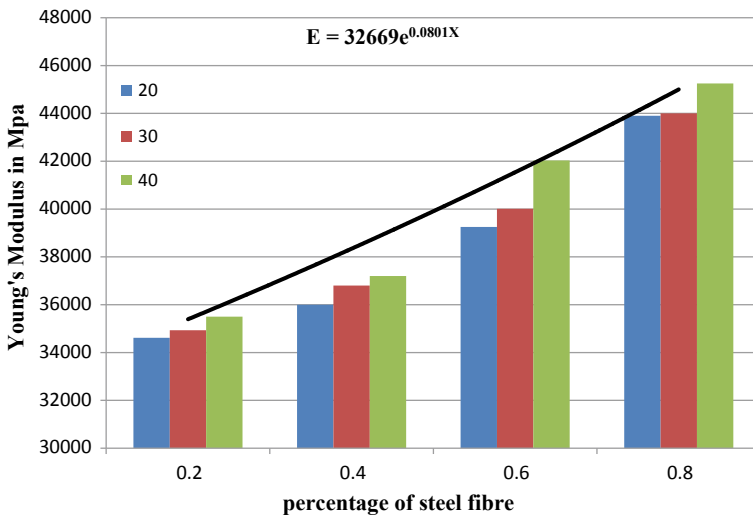
Fig. 3 Variation of the Young's modulus for steel fiber triple-blended SCC

$$E = 32669e^{0.0801(X)}$$

E is the Young's modulus in MPa, and
x indicates the percentage of fibers.

5.3 Poisson's Ratio

In the present study, Poisson's ratio is decreasing while increasing steel fiber percentage. Table 6 shows Poisson's ratio values. The concrete mix with triple blending and with steel fiber shows lower value than the reference mix. It is noted that Poisson's ratio of triple-blended fibrous SCC of M40 grade of the concrete reduces with enhancing fiber percentage and aspect ratio. The variation of Poisson's ratio with respect to steel fiber percentage in this triple-blended steel fiber self-compacting concrete is observed as linear. For aspect ratio of 40, best-fitted curves are shown in Fig. 4. It is recorded that Poisson's ratio for the optimum dosage of steel fiber and maximum aspect ratio is 30% lesser than the reference mix. An increase in the fiber percentage causes higher stress capacity resulting in lower strain; hence, the Poisson's ratio gets reduced with higher percentage of fibers.

$$y = -0.0116x + 0.152$$

- y is the Poison's ratio, and
- x indicates the percentage of fibers

As regression analysis was conducted for best fitting curves; hence, separate statistical distribution was not required.
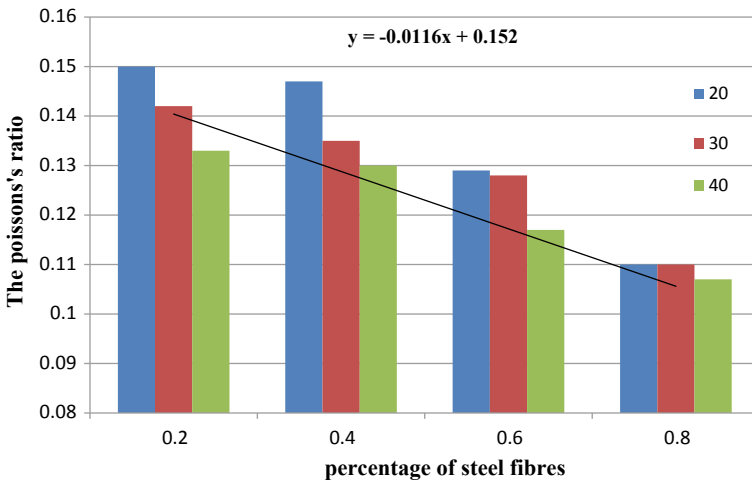

Fig. 4 Variation of the Poisson's ratio for steel fiber triple-blended SCC

5.4   Influence of the Aspect Ratio

As the aspect ratio of the fiber increases, there is an increase in strength, as the aspect ratio is high; it will interfere with the flow of concrete because of its weight. With higher aspect ratio, there may be balling effect also.

5.5   Use of Triple Blending

The triple blending of cement using admixtures like fly ash and condensed silica fume renders the concrete mix to flow smoothly and contributes better strength. The use of the mineral admixtures in specified percentages in the concrete matrix will imporove the strength and durability properties. In this investigation, M40 concrete mix was adopted as the reference mix, and triple blending was carried out with fly ash and silica fume at percentages of 20 and 10, respectively. In this case, the benefit received out of triple blending may be marginal in strength, but it has more contributed to better workability. Hence, for today's concrete constructions in which SCC is used, a triple-blended cement with mineral admixtures has advantageous for strength, durability along with the rheological requirements.

6   Conclusions

The following are some of the conclusions which were noted in the experimental investigation.

1. The optimum percentage and aspect ratio are found to be 0.8% and 40, respectively, for steel fiber self-compacting concrete for fulfilling the requirements of the SCC.
2. The compressive strength of fibrous SCC increases with fiber percentage and aspect ratio; hence, the concrete becomes stiffer because of steel fibers.
3. It is nearly 15% increase in the compressive strength with an aspect ratio of 40 compared to 20 for all the steel percentages except 0.2%, and lower percentage of steel fibers will not contribute much on the strength parameter.
4. The Young's modulus of triple-blended fibrous SCC of M40 grade was enhanced with increase in steel fiber percentage and also with aspect ratio; there is nearly 35% enhanced in the value of the Young's modulus with 0.8% of steel fiber at an aspect ratio of 40 compared to the basic mix, it clearly indicates due to steel fibers in the SCC cause higher stress capacity and lower the strain.
5. The Poisson's ratio of triple-blended fibrous SCC of M40 grade is reducing with increase in fiber percentage and the increase in aspect ratio. It is noted that the Poisson's ratio for optimum dosage of steel fiber and aspect ratio has 30% lesser than the reference mix, due to longitudinal strain more than the lateral strain in this case.

6. By triple blending SCC with 20% fly ash and 10% condensed silica fume (CSF), strength increase is marginal; due to these mineral admixtures, flowability of the mix has increased.
7. For the compressive strength and elastic properties for the triple-blended steel fiber self-compacting concrete, the mathematical models are developed and the equations are almost agreeing with the experimental values.

References

1. EFNARC. (2005). Specifications and guidelines for self-consolidating concrete.
2. Okamura, H. (1997). Self compacting high-performance concrete. In *Concrete international* (pp. 50–54).
3. Su, N. (2003). A new method for the mix design of medium strength flowing concrete with low cement content. *Cement & Concrete Composites, 25*, 215–222.
4. Okamura, H., & Ouchi, M. Self compacting concrete development, present use, and future. In *1st International RILEM Symposia on Self Compacting Concrete.*
5. Petersson, O, Billiberg, P., et al. (1996). A model for self-compacting concrete. In P. J. M. Bartos, D. L. Marrs & D. J. Cleand (Eds.), *Production methods & workability of concrete*. Londres: E&FN Spon.
6. Pajak, M., & Ponikiewski, T. (2013). The flexural behavior of self-compacting concrete reinforced with different types of steel fibres. *Construction and Building Materials, 47*, 397–408.
7. Corinaldesi, V., & Moriconi, G. (2011). Characterisation of self-compacting concrete prepared with different fibers along with mineral additions. *Cement & Concrete Composites, 33,* 596–601.
8. Iyer, P., Kenno, S. Y., & Das, S. (2015). Mechanical properties of fiber-reinforced concrete made with basalt filament fibers. *Journal of Materials for Civil Engineering.*
9. Sahmaran, M., Yutseven, A., et al. (2005). Workability of hybrid fiber reinforced self-compacting concrete. *Building and Environment, 40*(12), 1672–1677.
10. Cunha, V. M. C. F, J. A. O. Barros, et al. (2006). Compression behavior of steel fiber reinforced self-compacting concrete: age influence and modeling.
11. Kosmatka, S. H., & Wilson, M. L. (2011). *Design and control of concrete mixtures, engineering bulletin 001*, 15th ed. Skokie, IL: Portland Cement Association.
12. Vijaya, G., Vaishali, V, et al. (2011). The behavior of self-compacting concrete with waste plastic fibers when subjected to acid attack. ISSN:0975-4024.
13. Ganeshan, N. (2005), Strength behavior of steel fiber reinforced self-compacting concrete in flexure. In *International Conference on Advances in Concrete composites and Structures*, 2005 (pp. 2691–2698).
14. IS-10269- Specification of ordinary Portland cement properties.
15. IS-2386-Method of testing the aggregate for concrete.
16. IS 10262-2009—Guidelines for design mix for the concrete.
17. IS-516 reaffirmed 2004-Methods of testing for strength concrete.

Prediction of Concrete Compressive Strength Using Fuzzy Logic and Model Tree

Vardhan Nagarkar, Preeti Kulkarni, and Shreenivas Londhe

1 Introduction

Concrete is an essential material in Civil Engineering field. Ascertaining the compressive strength of concrete has great importance as it offers an option to do the essential modification on the mix proportion to avoid circumstances where concrete does not attain the design strength and also for more economic use of raw material and fewer construction failures, hence reducing construction cost. The property of concrete strength differs depending on the factors like proportion of its constituents, the construction methods, the loading and environmental conditions, etc. Traditionally, ascertaining the strength of concrete includes actual testing which demands material and time (minimum 28 days) [1]. Moreover, concrete compressive strength is a nonlinear problem for Construction Engineering field. It is difficult to predict the concrete strength due to its nonlinearity. Many researchers lately have been addressing this issue by using data-driven techniques like artificial neural network, support vector regression, fuzzy logic, etc. Of these data-driven tools, fuzzy logic tool is been widely used to predict strength of concrete. Fuzzy logic can efficiently predict compressive strength of high strength concrete with silica fume than artificial neural network with three inputs: cement content, age of concrete and silica fume content with 24 fuzzy sets and centroid method for a defuzzification [2]. In a study, 7, 28 and 90 days strength values of fly ash-based concrete were predicted using fuzzy logic which yielded better results than artificial neural networks [3]. Fuzzy logic has

V. Nagarkar (✉) · P. Kulkarni · S. Londhe
Department of Civil Engineering, Vishwakarma Institute of Information Technology, Pune, India
e-mail: vardhanvn@gmail.com

P. Kulkarni
e-mail: preeti.kulkarni@viit.ac.in

S. Londhe
e-mail: shreenivas.londhe@viit.ac.in

been used for: self compacting concrete strength prediction [4], predicting concrete properties subjected to sulfate attack [5], strength prediction of concrete and cement, evaluation of concrete durability, crack diagnosis, prediction of shear strength of FRP-reinforced concrete beams and retrofit and prediction of lateral confinement coefficient for FRP-strengthened RC columns which was reviewed and evaluated in [6]. Matrix formulation of fuzzy rule-based systems was studied in which a very general and commonly used structure with p inputs, q outputs and n rules was done. The training algorithms for adaptive membership functions are also provided in matrix formulations [7]. Model tree was also used to predict strength of high performance concrete which resulted in effective use of tree-based modeling approach. It was also seen that M5P tree works well for the dataset in comparison with MLP and linear regression [8]. Trend line analysis also gives an approving result for M5P. Model tree can be efficiently used to predict recycled aggregate concrete and are characterized with series of equations which can be readily used [9]. Literature discusses the use of fuzzy logic and model tree for strength prediction. However, the development of membership functions in fuzzy logic mostly seen is triangular or trapezoidal, and its reasoning is seldom done. The rule development is majorly based on experience and domain knowledge and seldom mention about any stasticial method. This method of rule development can be a tedious activity and is not based totally on statistical approach. Thus, a need to develop rules using a statistical approach is necessary which can decrease the tedious traditional method. On the other hand, model tree technique which is efficiently used for strength prediction develops series of equations to predict an output. This characteristic of model tree can be utilized in fuzzy logic, and a hybrid model with the use of fuzzy logic and rule development using the series of equations developed by model tree can be explored. Thus, the aim of current project is to predict the 28-day strength of fly ash-based concrete using fuzzy logic (FL) with the rule development using model tree. The current method can help in developing the rules in a systematic approach. This model termed as hybrid model is developed, and its performance is judged according to the error measures utilized.

The further part of the paper is organized as follows: Sect. 2 gives an overview of fuzzy logic and model tree followed by Sect. 3 which will discuss the information about data adopted, and Sect. 4 will discuss the methodology adopted for model development in the current study. Section 5 further discusses the results. The paper ends in Sect. 6 with the conclusions followed by the references.

2 Techniques Utilized

Fuzzy Logic (FL) technique is used in the current study with model tree.

2.1 Fuzzy Logic

Fuzzy logic is a superset of conventional (Boolean) logic that has been extended to handle the concept of partial truth values between 'completely true' and 'completely false.' Fuzzy logic basically contains of three parts: membership function, fuzzy inference system and defuzzification. Fuzzification: The component forms fuzzy sets for input–output variables using membership functions. Fuzzy membership functions may take many forms, but in practical applications, there are two kinds of membership functions: (1) triangular and (2) bell-shaped (Gaussian). Triangular functions are mostly used membership functions. Intuition, rank ordering and inductive reasoning can be among the many ways to assign membership functions to fuzzy variables. The intuitive approach is commonly used because it is simple and derived from the innate intelligence and understanding of human beings. Readers are referred to Tayfur for further details [10]. Fuzzy Inference System: The fuzzy inference system is a popular computing framework based on the concepts of fuzzy set theory, fuzzy if-then rules and fuzzy reasoning. There are two types of inference systems in fuzzy logic Mamdani inference system and Sugeno inference system. A typical fuzzy rule in a Sugeno fuzzy model has the form. If x is A and y is B, then $z = f(A, B)$, where A and B are fuzzy sets in the antecedent, while $z = f(A, B)$ is a crisp function in the consequent. Usually, $f(A, B)$ is a polynomial in the input variables A and B, but it can be any function as long as it can appropriately describe the output of the model within the fuzzy region specified by the antecedent of the rule. Defuzzification: Defuzzification converts the resulting fuzzy outputs from the fuzzy inference engine to a number. There are many defuzzification methods, such as center of gravity (COG), bisector of area (BOA), mean of maxima (MOM), leftmost maximum (LM) and rightmost maximum (RM). Readers are referred to Tayfur for further details [10].

2.2 Model Tree

MT utilizes divide-and-conquer approach, partitions the data and provides rules for reaching the models at the leaf nodes. The linear models are then used to quantify the contribution of each attribute to the overall predicted value. M5P, a reconstruction of Quinlan's M5 algorithm, is used for inducing trees of regression models and combines a conventional decision tree with the possibility of linear regression functions at the nodes. First, a decision tree induction algorithm is used to build a tree, and a splitting criterion is used that minimizes the intra-subset variation in the class values down each branch. The splitting procedure in M5 stops if the class values of all instances that reach a node vary very slightly, or only a few instances remain. Second, the tree is pruned back from each leaf. When pruning, an inner node is turned into a leaf with a regression plane. In comparison with classical regression trees, model trees deliver better compactness and prediction accuracy [8, 11].

Table 1 Concrete compressive strength real-time data set

Parameter	Min–max values	Average	Std-dev
Cement (kg/m^3)	130–460	302.38	73.12
Fly ash (kg/m^3)	0–120	25.38	31.05
Fine aggregate (kg/m^3)	398–1011	837.47	97.57
Coarse aggregate 10 mm (kg/m^3)	0–958	390.67	143.93
Coarse aggregate 20 mm (kg/m^3)	482–1242	790.45	135.25
Water (kg/m^3)	127–202	167.12	15.46
Admixture (kg/m^3)	0–5.2	2.68	1.31
Strength (MPa)	12–65	34.2	10.63

3 Data Utilized

Two hundred and forty-one instances of fly ash-based concrete are collected from Ready Mix concrete plant situated in Pune. The concrete mix parameters present are proportions in kg/m^3 of fly ash, cement, fine aggregate, coarse aggregate 10 mm, coarse aggregate 20 mm, water and admixture in concrete. 28-day strength of concrete in MPa is the output in the models developed. The characteristics of the data are shown in Table 1. The table shows the presence of variety or pattern of data which helps the models to learn pattern and give meaningful results with unseen data.

4 Methodology Adopted

Concrete is a complex material, and its strength characteristics depend on mix proportions of materials used and their properties [1]. To predict 28-day compressive strength of fly ash-based concrete, fuzzy logic model with rules defined using model tree was developed. The fuzzy logic model was developed with input parameters as proportions in kg/m^3 of fly ash, cement, fine aggregate, coarse aggregate 10 mm, coarse aggregate 20 mm, water and admixture in concrete and 28-day strength of concrete in MPa as output parameter. The membership function developed for the model is Gaussian type and is used for each input as the data is discrete, and there is no fixed pattern in data. Each of the input parameter is divided into six membership functions having different ranges in which whole data set is included. Membership function for one of the parameter, i.e., water is seen in Fig. 1.

Sugeno type of fuzzy interference system is used in the model with centroid method of defuzzification which is shown in Fig. 2.

Further, the rules of the fuzzy system were designed using model tree. The rules are designed as follows: For model tree technique, M5P algorithm was used for calibrating the model, and WEKA was used for the same [8, 11]. The input parameters as discussed in the current section and the output are presented to WEKA with M5
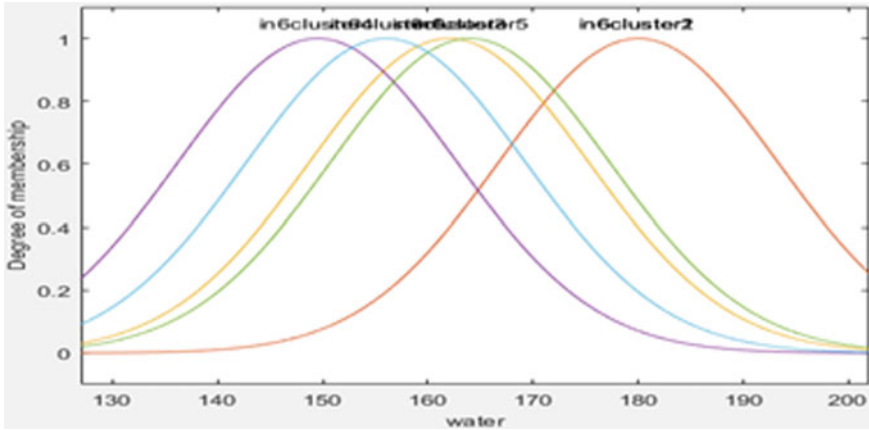
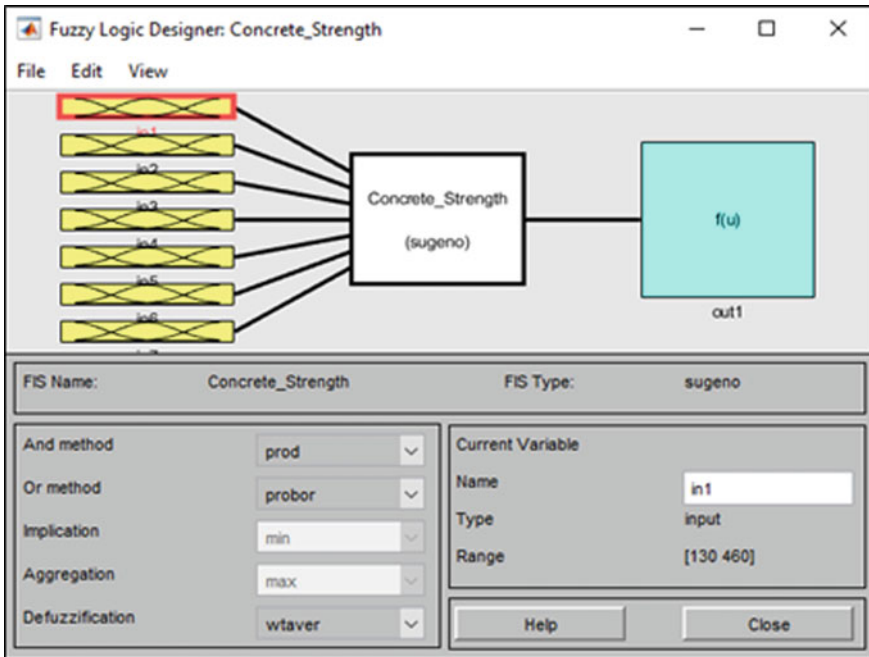**Fig. 1** Membership function for water parameter

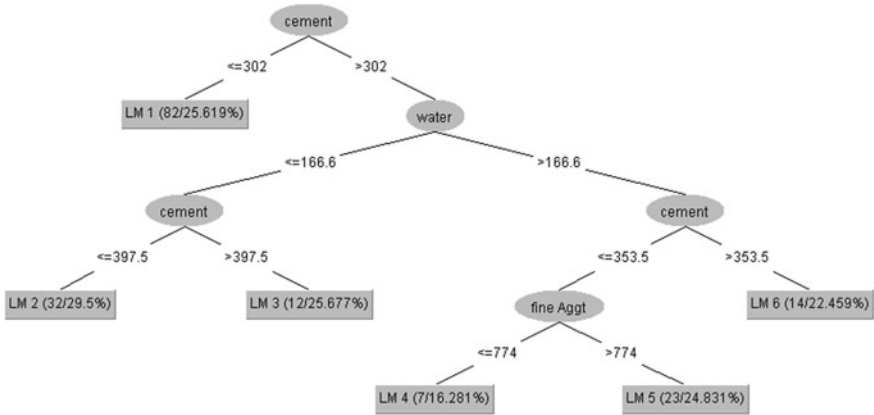**Fig. 2** Fuzzy interference system for concrete strength

Fig. 3 Model tree developed

algorithm. The tree developed for the same is as shown in Fig. 3. Total eight linear model equations (LM) developed as shown below.

$$\text{LM num: 1: strength} = 0.0925 * \text{cement} + 0.0288 * \text{fly ash} - 0.0112 * \text{fine Aggt}$$
$$- 0.0085 * 10\,\text{mm} - 0.0012 * 20\,\text{mm} - 0.0294 * \text{water}$$
$$+ 0.1888 * \text{admixture} + 20.5771$$

$$\text{LM num: 2: strength} = 0.0693 * \text{cement} + 0.0215 * \text{fly ash} - 0.0087 * \text{fine Aggt}$$
$$+ 0.0069 * 10\,\text{mm} - 0.0011 * 20\,\text{mm} - 0.1368 * \text{water}$$
$$+ 0.9255 * \text{admixture} + 42.8644$$

$$\text{LM num: 3: strength} = 0.0849 * \text{cement} + 0.0215 * \text{fly ash} - 0.0109 * \text{fine Aggt}$$
$$+ 0.0023 * 10\,\text{mm} - 0.0011 * 20\,\text{mm} - 0.426 * \text{water}$$
$$+ 1.2815 * \text{admixture} + 88.6687$$

$$\text{LM num: 4: strength} = 0.0648 * \text{cement} + 0.0499 * \text{fly ash} - 0.0349 * \text{fine Aggt}$$
$$- 0.0191 * 10\,\text{mm} - 0.0139 * 20\,\text{mm} - 0.1013 * \text{water}$$
$$+ 0.4494 * \text{admixture} + 76.2583$$

$$\text{LM num: 5: strength} = 0.0837 * \text{cement} + 0.0652 * \text{fly ash} - 0.0174 * \text{fine Aggt}$$
$$- 0.0142 * 10\,\text{mm} - 0.0007 * 20\,\text{mm} - 0.1013 * \text{water}$$
$$+ 0.4494 * \text{admixture} + 41.8827$$

$$\text{LM num: 6: strength} = 0.0837 * \text{cement} + 0.0678 * \text{fly ash} - 0.0174 * \text{fine Aggt}$$
$$- 0.0142 * 10\,\text{mm} - 0.0063 * 20\,\text{mm} - 0.1013 * \text{water}$$
$$+ 0.4494 * \text{admixture} + 46.5108$$

$$\text{LM num: 7: strength} = 0.0906 * \text{cement} + 0.0595 * \text{fly ash} - 0.0155 * \text{fine Aggt}$$
$$- 0.0136 * 10\,\text{mm} - 0.0063 * 20\,\text{mm} - 0.1013 * \text{water}$$
$$+ 0.4494 * \text{admixture} + 42.7007$$

$$\text{LM num: 8: strength} = 0.0731 * \text{cement} + 0.0398 * \text{fly ash} - 0.018 * \text{fine Aggt}$$
$$- 0.0342 * 10\,\text{mm} - 0.0195 * 20\,\text{mm} - 0.1152 * \text{water}$$
$$+ 0.4494 * \text{admixture} + 73.8673$$

The fuzzy logic model with the rules is developed using MATLAB 2017. Thus, this fuzzy model using model tree is termed as a hybrid model. To check the accuracies and robustness of the model, the experimental dataset is divided for training and testing purposes. From the available data, 70% is randomly selected to be used for training purposes, and the remaining 30% is used for model validation. The performance of the model is compared with experimental data reported by the author and assessed by statistical measures like correlation coefficient (R), root mean squared error (RMSE), mean absolute error (MAE) and Nash–Sutcliffe Efficiency (E) [12].

5   Results and Discussion

A fuzzy logic model with Gaussian membership function and rules derived through model tree is developed to predict 28-day strength of fly ash-based concrete. Gaussian membership function was selected in the current work as the data was discrete, and no fixed pattern in the data. The model tree equations developed show a high influence toward cement content (as per the coefficient) followed by fly ash content. This is in tune with the fundamental knowledge of concrete technology [1]. Negative coefficient toward water parameter indicates its increase in the mix after a certain limit can decrease the strength of concrete which agrees with the domain knowledge. Thus, it is seen that model tree develops LM models which are in tune with domain knowledge and thus have a statistical approach toward strength prediction. The concrete strength hybrid model for one of unseen output is seen in Fig. 4.

Table 2 presents the performance of developed model in terms of error measures.

As Table 2 shows correlation coefficient 'r' of 0.96, the model performs in an excellent way. This is also endorsed by the other error measures shown in Table 2. The crux of the model is the rules developed using model tree. Model tree with M5P algorithm, the basic tree is formed based on a splitting criterion. It uses the standard deviation of the class values for each node as a measure of the error at
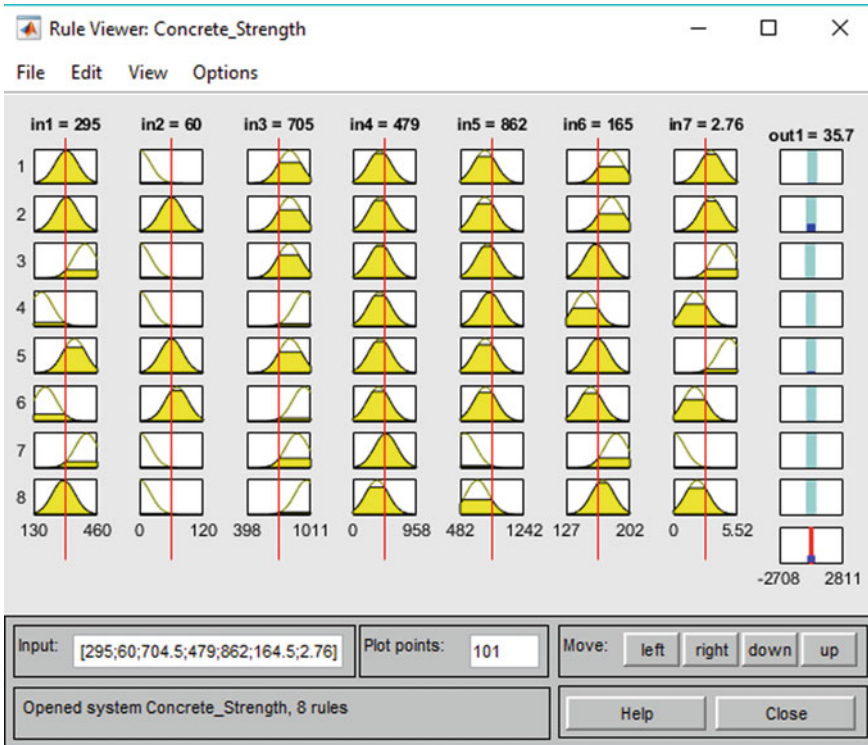
Fig. 4 Hybrid model output

Table 2 Performance of hybrid model

Correlation coefficient 'r'	Root mean square error 'RMSE'	Mean absolute error 'MAE'	Nash efficiency 'E'
0.96	2.48	1.88	0.95

that node and then calculates the expected error reduction as a result of testing each attribute at that node. Thus, in spite of linear equations at the end of nodes, due to the splitting criteria, model trees can address the nonlinearity in the problem. In comparison with classical regression trees, model trees with smoothing and pruning deliver better compactness and prediction accuracy. Thus, the equations developed can be applied to fuzzy model as rules, which can also reduce the tedious activity of forming rules through experience and observation. This concept also allows a systematic method of forming rules. Figure 5 shows the observed and predicted values of 28-day compressive strength of concrete. The graph clearly speaks that results of hybrid model are much closer to the observed values and follow the same trend.
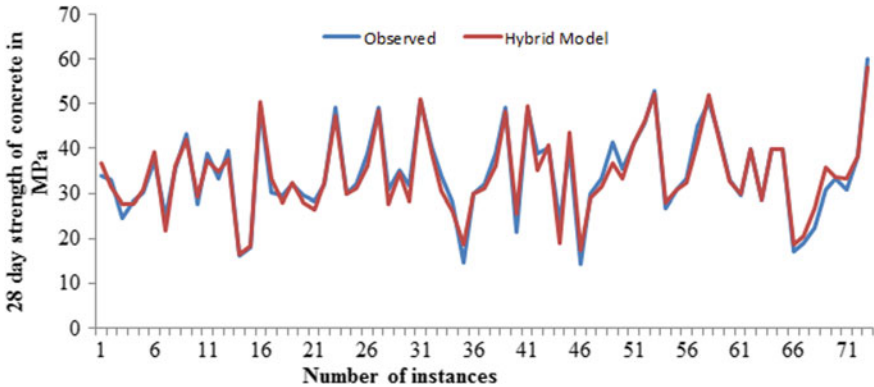
Fig. 5 Observed and predicted values of concrete strength

6 Conclusion

In the current work, a hybrid model, i.e., fuzzy logic model with rules developed using model tree is developed to predict 28-day strength of fly ash-based concrete in MPa with input parameters as kg/m^3 proportions of materials used in concrete. The developed hybrid model displays an excellent performance with a correlation coefficient of 0.96. The excellent performance is also endorsed by other error measures as RMSE, MAE and CE. The equations developed using model tree show a statistical approach and also can avoid the tedious activity of rule formation the traditional way.

References

1. Shetty, M. S. (2005). *Concrete technology* (17th ed.). New Delhi: S. Chand and Company.
2. Tayfur, G., Erdem, K. T., & Kırca, O. (2014). Strength prediction of high strength concrete by fuzzy logic and artificial neural networks. *Journal of Materials in Civil Engineering, 26*(11), 401–407.
3. Topcu, B. L., & Sarıdemir, M. (2008). Prediction of compressive strength of concrete containing fly ash using artificial neural networks and fuzzy logic. *Computational Materials Science, 41*(3), 305–311.
4. Vakhshouri, B., & Nejadi, S. (2018). Prediction of compressive strength of self-compacting concrete by ANFIS models. *Neurocomputing, 280*(6), 13–22.
5. Diab, A. M., Elyamany, H. E., Elmoaty, A. E. M. A., & Shalan, A. H. (2015) Comparison between neural network and fuzzy logic on assessment of long term concrete compressive strength and expansion due to sulfate attack. *International Journal for Research in Applied Science and Engineering Technology, 3*, 175–192.
6. Seyed, A. A., & Naderpour, H. (2015). Application of fuzzy logic in reinforced concrete structures. https://doi.org/10.4203/ccp.109.10.
7. Lotfi, A., Andersen, H. C., & Tsoi, A. C. (1996). Matrix formulation of fuzzy rule-based systems. *IEEE Transactions on Systems, Man, and Cybernetics, Part B (Cybernetics), 26*(2), 332–340.

8. Deepa, C., SathiyaKumari, K., & Sudha, K. P. (2010). Prediction of the compressive strength of high performance concrete mix using tree based modeling. *International Journal of Computers and Applications, 6*(5), 18–24.
9. Deshpande, N., Londhe, S., & Kulkarni, S. (2014). Modeling compressive strength of recycled aggregate concrete by artificial neural network, model tree and non-linear regression. *International Journal of Sustainable Built Environment, 3,* 187–198.
10. Tayfur, G. (2012). *Soft computing in water resources engineering*. WIT Press.
11. Quinlan, J. R. (1992). Learning with continuous classes. In A. Adams & L. Sterling (Eds.), *Proceedings of 5th Australian Joint Conference on Artificial Intelligence*. Singapore: World Scientific.
12. David, R. L., Jr., & Gregory, J. (1999). Evaluating the use of "goodness of fit" measures in hydrological and hydro climatic model validation. *Water Resources Research, 35*(1), 233–241.